Analysen ausgewählter Wirk- und Impfstoffkandidaten gegen COVID-19 und künftige Diseases X

von Arne Sven Auste

Inaugural-Dissertation zur Erlangung der Doktorwürde der

Tierärztlichen Fakultät der Ludwig-Maximilians-Universität München

Analysen ausgewählter Wirk- und Impfstoffkandidaten gegen COVID-19 und künftige Diseases X

von Arne Sven Auste

aus Speyer

München 2024

Aus dem Veterinärwissenschaftlichen Department der Tierärztlichen Fakultät

der Ludwig-Maximilians-Universität München

Lehrstuhl für Virologie

Arbeit angefertigt unter der Leitung von Univ.- Prof. Dr. Dr. h.c. Gerd Sutter †

Angefertigt am Paul-Ehrlich-Institut, Langen

Bundesinstitut für Impfstoffe und biomedizinische Arzneimittel

Mentor: PD Dr. Michael D. Mühlebach

Gedruckt mit Genehmigung der Tierärztlichen Fakultät der Ludwig-Maximilians-Universität München

Dekan:	Univ.-Prof. Dr. Reinhard K. Straubinger, Ph.D.
Berichterstatter:	Univ.-Prof. Dr. Reinhard K. Straubinger, Ph.D.
Korreferent/en:	Univ.-Prof. Dr. Hermann Ammer

Tag der Promotion: 10. Februar 2024

Die vorliegende Arbeit wurde gemäß § 6 Abs. 2 der Promotionsordnung für die Tierärztliche Fakultät der Ludwig-Maximilians-Universität München in kumulativer Form verfasst.

Folgende wissenschaftliche Arbeiten sind in dieser Dissertationsschrift enthalten:

Henss, L., Auste, A., Schürmann, C., Schmidt, C., von Rhein, C., Mühlebach, M. D., Schnierle, B.S.: **„The green tea catechin epigallocatechin gallate inhibits SARS-CoV-2 infection“** erschienen in Journal of General Virology 2021, unter doi: 10.1099/jgv.0.001574 online verfügbar.

Hörner, C., Schürmann, C., Auste, A., Ebenig, A., Muraleedharan, S., Dinnon 3rd, K. H., Scholz, T., Herrmann, M., Schnierle, B. S., Baric, R. S., Mühlebach, M. D.: **„A highly immunogenic and effective measles virus-based Th1-biased COVID-19 vaccine“** erschienen in Proceedings of the National Academy of Sciences of the United States of America 2020, unter doi: 10.1073/pnas.2014468117 online verfügbar.

Ebenig, A., Muraleedharan, S., Kazmierski, J., Todt, D., Auste, A., Anzaghe, M., Gömer, A., Postmus, D., Gogesch, P., Niles, M., Plesker, R., Miskey, C., Gellhorn Serra, M., Breithaupt, A., Hörner, C., Kruip, C., Ehmann, R., Ivics, Z., Waibler, Z., Pfaender, S., Wyler, E., Landthaler, M., Kupke, A., Nouailles, G., Goffinet, C., Brown, R. J. P., Mühlebach, M. D.: **„Vaccine-associated enhanced respiratory pathology in COVID-19 hamsters after T_H2-biased immunization”** erschienen in Cell Reports 2022, unter doi: 10.1016/j.celrep.2022.111214 online verfügbar.

Auste, A., Mühlebach, M. D.: **„Concentrating all helper protein functions on a single entity allows rescue of recombinant measles virus by transfection of just two plasmids”** erschienen in Journal of General Virology 2022, unter doi: 10.1099/jgv.0.001815 online verfügbar.

Weitere Arbeiten, die nicht in der Dissertationsschrift enthalten sind:

Leidenberger, S., Schröder, C., Zani, L., Auste, A., Pinette, M., Ambagala, A., Nikolin, V., de Smit, H., Beer, M., Blome, S.: **„Virulence of current German PEDV strains in suckling pigs and investigation of protective effects of maternally derived antibodies“** erschienen in Scientific reports 2017, unter doi: 10.1038/s41598-017-11160-w online verfügbar.

Inhaltsverzeichnis

1. Einführung

COVID-19, das aktuelle Beispiel einer sogenannten „Disease X“

In den Jahren 1830 und 1847 wüteten in Europa Choleraepidemien, in deren Folge die erste internationale Gesundheitskonferenz 1851 in Paris ins Leben gerufen wurde. So gehen damit schon die Anfänge der internationalen Gesundheitspolitik auf die Bekämpfung von Infektionskrankheiten zurück (McCarthy 2002). Mit steigenden Hygienestandards und wachsendem Wohlstand in einigen Regionen der Erde wurden viele Krankheitserreger zurückgedrängt und Zivilisationskrankheiten (z. B. koronare Herzkrankheit, Schlaganfall) lösten dort Infektionskrankheiten als häufigste Todesursache ab (McMichael 2001; World Health Organization 2020b). Nichtsdestotrotz bleibt die Kontrolle übertragbarer Krankheiten bis heute eine der wichtigsten Aufgaben der Weltgesundheitsorganisation (WHO), vor allem in Ländern mit mittleren und niedrigen Einkommen (World Health Organization 2020c). Dazu sollte auch das Konzept für „Globale Öffentliche Güter für Gesundheit“ dienen, das eine multinationale Anstrengung vorsieht für die Erforschung und Entwicklung von Präventions- und Kontrollmaßnahmen gegen globale Gesundheitsrisiken (Weltgesundheitsorganisation 2002). Das gleichzeitige Auftreten des *Severe acute respiratory syndrome-related coronavirus* (SARS-CoV) im Jahr 2002 gab nicht nur zusätzliches Momentum für dieses Konzept (Fidler 2004), sondern spätestens nach der sogenannten Schweinegrippe-Pandemie 2009 auch den Anstoß für einzelstaatliche Maßnahmen wie der Schaffung der *Thematic Translational Unit Emerging Infections* (TTU EI) innerhalb des Deutschen Zentrum für Infektionsforschung (DZIF). Deren Ziel ist unter anderem die Erforschung und Weiterentwicklung von Vektorimpfstoffplattformen zur Bekämpfung von neu oder verändert auftretenden Infektionserregern. Nach Auftreten des *Middle East respiratory syndrome-related coronavirus* (MERS-CoV) im Jahr 2012 konnte auf Basis dieser DZIF-geförderten Vektorimpfstoffplattformen bereits die Schutzwirkung von Impfstoffkandidaten gegen MERS-CoV nachgewiesen werden (Volz et al. 2015; Malczyk et al. 2015). Darüber hinaus zeigte die Ebola-Epidemie in Westafrika 2014-2015, dass die Vorbereitung der internationalen Staatengemeinschaft auf solche Epidemien noch ausbaufähig war. Als direkte Folge dieser Krise verabschiedete die WHO auf ihrer Weltgesundheitsversammlung im Mai 2015 einen Entwurf zur Beschleunigung von Forschung und Entwicklung (F&E) in Ausbruchssituationen. Dieser zielt darauf ab, ein förderliches Forschungsumfeld aufzubauen, Standards für klinische Studien in Ausbruchszenarien zu entwickeln und bedenkliche Pathogene zu definieren und zu priorisieren (World Health Organization 2016). Als Pathogene dieser „Blueprint“-Liste werden unter anderem neben den bekannten Erregern wie dem Ebolavirus und neu-

auftretenden hochpathogenen Coronaviren (SARS-CoV, MERS-CoV) auch ein „neuartiges Agens“ gelistet, was eine neue, schwere Infektionskrankheit auslöst, die so genannte „Disease X“. „Disease X repräsentiert das Wissen, dass eine schwere internationale Epidemie durch ein Pathogen verursacht werden könnte, von dem derzeit nicht bekannt ist, dass es menschliche Krankheiten verursacht.“ (World Health Organization)

Die Eindämmung solcher länderübergreifender Epidemien wird in Zukunft an Bedeutung gewinnen, da sie sehr wahrscheinlich immer häufiger auftreten (Jones et al. 2008), vor allem aus drei Gründen: (1) Aufgrund einer wachsenden Weltbevölkerung dringt der Mensch zur Gewinnung neuer Flächen in bis dahin unberührte Habitate vor (Patz et al. 2004). (2) Die Erde erwärmt sich (National Centers for Environmental Information 2023) und die damit einhergehenden Veränderungen der Klimazonen verschieben endemische Gebiete von Erregern und deren Vektoren (Beyer et al. 2021). (3) Die Globalisierung treibt die Vernetzung voran und Krankheiten können schneller größere Distanzen überwinden, wie schon am Beispiel des SARS-Ausbruchs 2002/2003 deutlich wurde (Peiris et al. 2003).

Ein bis dahin unbekanntes Pathogen war es dann schließlich im Dezember 2019, welches eine lokale Häufung von Lungenentzündungen im chinesischen Wuhan verursachte (Zhu et al. 2020b). Am 9. Januar 2020 wurde dieses Pathogen als neuartiges Coronavirus identifiziert (Hu et al. 2020), dessen schnelle Verbreitung über alle 34 Provinzen Chinas die WHO dazu veranlasste, am 30. Januar 2020 den internationalen Gesundheitsnotstand auszurufen (World Health Organization 2020a). Das *Severe Acute Respiratory Syndrome Coronavirus 2* (SARS-CoV-2), wie es final aufgrund seiner Verwandtschaft zu SARS-CoV genannt wurde, breitete sich schließlich weltweit aus (Fisher und Heymann 2020), sodass die WHO die Verbreitung dieser COVID-19 *(Coronavirus disease 2019)* genannten Erkrankung am 11. März 2020 zur Pandemie erklärte (Cucinotta und Vanelli 2020). Nur wenige Tage später erklärte Marion Koopmans, Mitglied der wissenschaftlichen Beratergruppe der WHO, COVID-19 als „Disease X“:

„Whether it will be contained or not, this outbreak is rapidly becoming the first true pandemic challenge that fits the disease X category, listed to the WHO's priority list of diseases for which we need to prepare in our current globalized society.”(The Novel Coronavirus Outbreak: What We Know and What We Don't 2020).

Bislang (Stand 25.04.2023) wurden weltweit mehr als 670 Millionen Infektionen mit SARS-CoV-2 und dabei mehr als 6,8 Millionen Todesfälle diagnostiziert (Johns Hopkins University 2023), wobei die tatsächlichen Zahlen deutlich höher liegen dürften. Eine beträchtliche Dunkelziffer wird auch aufgrund mangelnder diagnostischer Infrastruktur in vielen Ländern mit niedrigen und mittleren Einkommen angenommen (Levin et al. 2022).

Zur Infektion kommt es, nachdem SARS-CoV-2 mithilfe des viralen Spike Glykoproteins über den Zelleintritts-Rezeptor Angiotensin-konvertierendes Enzym 2 (*Angiotensin-converting enzyme 2*, ACE2) an Zellen der oberen Atemwege bindet und in diese eintritt. In diesen Zellen vermehrt es sich, setzt neue Tochterviren frei, die in die unteren Atemwege gelangen und dort weitere Vermehrungszyklen durchlaufen. Während ein Drittel der Infizierten symptomlos bleibt, treten bei den übrigen nach einer Inkubationszeit von durchschnittlich fünf Tagen erste Symptome auf (Hu et al. 2020; Oran und Topol 2021). 80 % der Erkrankten haben einen milden Verlauf, 20 % leiden jedoch in den folgenden acht Tagen nach Beginn der Symptome unter deren Verschlimmerung und damit einem schweren Verlauf, dessen Risiko mit dem Alter zunimmt (Hu et al. 2020; Long et al. 2022). Im Vergleich zu diesem durch die ursprünglichen Virusvarianten ausgelösten Krankheitsverlauf zeigt die im November 2021 aufgekommene und seitdem dominante Variante Omicron einen milderen Verlauf (Chatterjee et al. 2023). Grundsätzlich geht eine Infektion mit SARS-CoV-2 mit generalisierter (Fieber, Müdigkeit) und respiratorischer Symptomatik (trockener Husten, Dyspnoe) einher, häufig sind auch die Muskeln (Myalgie), der Gastrointestinaltrakt (Durchfall) oder das Nervensystem (Kopfschmerzen) betroffen (Krishnan et al. 2021). Als Komplikationen sind thrombotische Ereignisse in 16 % der hospitalisierten Erkrankten beschrieben (Bilaloglu et al. 2020), sowie die als Zytokinsturm bezeichnete Entgleisung des Immunsystems. Diese Überreaktion ist mit besonders schweren Verläufen assoziiert und stellt eine häufige Todesursache unter COVID-19-Erkrankten dar (Hu et al. 2021). 10 % aller Infizierten entwickeln ein Long COVID-Syndrom (Davis et al. 2023). Dabei bleiben auch über den Zeitraum der akuten Krankheitsphase hinaus gesundheitliche Beeinträchtigungen bestehen, wie solche des Herz-Kreislauf-, Atmungs- oder Nervensystems (Davis et al. 2023).

Die Prognosen über eine Häufung von Epidemien und Pandemien werden allein durch die Beispiele der drei Coronavirus-Ausbrüche zu Beginn des 21. Jahrhunderts (SARS-CoV, MERS-CoV, SARS-CoV-2) bestätigt, ebenso wie das Konzept des bis dahin gänzlich unbekannten Krankheitserregers, der eine schwere Erkrankung auslöst, die Disease X. COVID-19 trat als solch eine Disease X auf und die mittlerweile für globale Gesundheitsrisiken sensibilisierte Staatengemeinschaft zeigte schnell Bemühungen zur Entwicklung von effektiven Wirk- und Impfstoffen gegen COVID-19. Die vorliegende Arbeit beschreibt die Analyse eines Wirkstoffkandidaten, Epigallocatechingallat (EGCG), sowie eines Impfstoffkandidaten auf Basis eines rekombinanten Masernimpfstoffes gegen COVID-19 und dessen Optimierung.

2. Literaturübersicht

2.1 Wirkstoffe gegen COVID-19

Die Behandlung von COVID-19 erfolgt vorwiegend symptomatisch, nur wenige kausaltherapeutische Medikamente wurden von der Europäischen Arzneimittel-Agentur (*European Medicines Agency*, EMA) bisher zugelassen (Stand 24.03.2023). Unter diesen befinden sich vier biologische Therapeutika auf Basis monoklonaler Antikörper, sowie zwei klassisch pharmazeutische Therapeutika auf Basis niedermolekularer Wirkstoffe, Veklury (Wirkstoff Remdesivir) und Paxlovid (Wirkstoffe Nirmatrelvir, Ritonavir) (Europäische Arzneimittel-Agentur 2023b). Alle vier in der EU zugelassenen Antikörper haben allerdings nur noch eine reduzierte Wirksamkeit gegen die Omicron-Variante, die sich unter anderem durch mehrere Mutationen im Spike auszeichnet und damit der Erkennung und der Abwehr durch das Immunsystem entgeht (Immunevasion) (Liu et al. 2022b; VanBlargan et al. 2022). Von den niedermolekularen Wirkstoffen wurde für das Nukleosidanalogon Remdesivir bereits vor der SARS-CoV-2-Pandemie eine hemmende Wirkung auf die RNA-abhängige RNA-Polymerase (*RNA-dependent RNA-polymerase*, RdRp) unterschiedlicher RNA-Viren nachgewiesen (Tchesnokov et al. 2019). Studien belegten dessen Wirksamkeit schließlich auch gegen die RdRp von SARS-CoV-2: So verkürzt sich die Krankheitsdauer um durchschnittlich fünf Tage bei mit Remdesivir behandelten COVID-19-Erkrankten (Beigel et al. 2020; Shrestha et al. 2021), wenn deren Behandlung innerhalb von drei Tagen nach positivem Testergebnis beginnt (Paranjape et al. 2021). Ein Nukleosidanalogon als Monotherapie gegen ein schnell-mutierendes RNA-Virus lässt aber auch Sorgen vor der Entwicklung von antiviralen Resistenzen aufkommen: Am Beispiel des HIV (Humanes Immundefizienz-Virus) konnte das Entstehen von resistenten Quasispezies erst durch die Einführung der antiretroviralen Kombinationstherapie effizient unterdrückt werden (Schmit et al. 1996; Mocroft et al. 2003). Ebenso erhöhten Kombinationstherapien die Behandlungserfolge für Hepatitis C deutlich (Shiffman 2014; Solbach und Wedemeyer 2015). Im Kontext der SARS-CoV-2-Pandemie gibt es für das monotherapeutisch eingesetzte Remdesivir bereits einzelne Fallberichte von immundefizienten COVID-19-Erkrankten, in denen sich unter Behandlung resistente SARS-CoV-2-Varianten entwickelten (Gandhi et al. 2022; Hogan et al. 2022). Auch für den 2022 durch die EMA zugelassenen Proteaseinhibitor Nirmatrelvir besteht das Risiko der Resistenzentwicklung, da *in vitro* bereits Virusvarianten gefunden wurden, deren Mutationen in der viralen Protease 3CLpro (3C-like protease, 3C-ähnliche Proteinase) bei gleichbleibender Replikationsfähigkeit die Wirksamkeit von Nirmatrelvir reduzieren (Zhou et al. 2022).

Um einer möglichen Ausbreitung resistenter SARS-CoV-2-Varianten etwas entgegenzusetzen, ist die Identifikation zusätzlicher Wirkstoffe notwendig. Neben den drei Nukleosidanaloga Favipiravir, VV116

und Azvudine, die außerhalb der EU zugelassen sind, befinden sich ungefähr 30 weitere Wirkstoffe bereits in der klinischen Phase III (Lei et al. 2022). Darunter ist auch Previfenon, ein Arzneimittelkandidat, der auf dem sekundären Pflanzenstoff EGCG des grünen Tees basiert (U. S. National Library of Medicine 2020).

2.2 Impfstoffe gegen COVID-19

Obgleich Medikamente zur Behandlung neu-auftretender Infektionskrankheiten wie COVID-19 dringend benötigt werden, geht deren Anwendung jedoch wie beschrieben mit dem Risiko der Resistenzentwicklung einher. Gleichzeitig sind es weniger die antiviralen Wirkstoffe, die die Dynamik einer Epidemie bestimmen, als Maßnahmen des öffentlichen Gesundheitswesens. Von diesen Maßnahmen zählen Impfungen zu den wirtschaftlichsten und effektivsten (Rodrigues und Plotkin 2020), sodass ihnen auch in der Bekämpfung SARS-CoV-2-Pandemie die entscheidende Rolle zukam. Bislang (Stand 18.01.2023) hat die EMA sieben Impfstoffe der folgenden Hersteller gegen COVID-19 zugelassen: BioNTech, Moderna, AstraZeneca, Janssen, Novavax, Valneva und Sanofi Pasteur (Europäische Arzneimittel-Agentur 2023f).

Die erste Marktzulassung in der EU, zu diesem Zeitpunkt noch konditional, erhielt das Vakzin Comirnaty von BioNTech am 21.12.2020 (Europäische Arzneimittel-Agentur 2023a). Comirnaty besteht aus in Lipid-Nanopartikel (LNP) verkapselter mRNA mit modifizierten Nukleosiden. Die mRNA kodiert für eine Variante des SARS-CoV-2 Spike Glykoproteins, die zur erhöhten Immunogenität in seiner Konformation vor der Fusion (Präfusion-Konformation) stabilisiert wurde (Lamb 2021). Nach Injektion gelangt die mRNA mit Hilfe der Lipid-Nanopartikel in antigenpräsentierende Zellen (*antigen-presenting cells*, APC) (Sahin et al. 2021), in denen das Spikeprotein transient exprimiert wird. Da die mRNA gleichzeitig über Pathogen-assoziierte molekulare Muster (*pathogen-associated molecular patterns*, PAMP) von Mustererkennungsrezeptoren (*pattern recognition receptors*, PRR) im Endosom oder Zytosol erkannt wird, wird eine Typ-I-Interferon-Antwort ausgelöst und die APC aktiviert (Teijaro und Farber 2021). Das zu Peptiden prozessierte Spike wird über MHC-I oder MHC-II-Moleküle zusammen mit Kostimulatoren Antigen-spezifischen T-Zellen präsentiert (Rauch et al. 2018). Das native, nicht prozessierte Spike wird B-Zellen präsentiert (Rauch et al. 2018). Auf diese Weise induziert Comirnaty zelluläre und humorale Immunantworten (Sahin et al. 2020), sodass ein Schutz von 95 % vor symptomatischer COVID-19 sieben Tage nach der zweiten Impfung vermittelt wird bei gleichzeitig hohem Sicherheitsprofil (Polack et al. 2020).

Am 06.01.2021 wurde Spikevax von Moderna zugelassen (Europäische Arzneimittel-Agentur 2023e). Er besteht wie Comirnaty aus in LNP verkapselter mRNA mit modifizierten Nukleosiden, die ebenfalls für ein stabilisiertes Spike kodiert. In Phase I-Studien konnte seine hohe Sicherheit und Immunogenität gezeigt werden (Jackson et al. 2020; Anderson et al. 2020). Spikevax vermittelt einen Schutz von 94 % vor symptomatischer COVID-19 14 Tage nach der zweiten Impfung (Baden et al. 2021).

Als ersten Vektorimpfstoff hat die EMA am 29.01.2021 das Vakzin von AstraZeneca zugelassen, Vaxzevria (Europäische Arzneimittel-Agentur 2023j). Vaxzevria ist ein nicht-replizierender Vektor, der sich vom Schimpansen-Adenovirus ChAdY25 ableitet (Dicks et al. 2012). Dieser Vektor kodiert für das nicht-stabilisierte Spikeprotein, dem die Signalsequenz des gewebespezifischen Plasminogenaktivators (*tissue plasminogen activator*, tPA) zwecks erhöhter Protein-Expression vorangestellt wurde (van Doremalen et al. 2020). Anders als die thermolabileren mRNA-Impfstoffe (Lagerung bei -90 °C bis -60 °C) besitzt Vaxzevria eine hohe Haltbarkeit auch bei Kühlschranktemperaturen (2 °C bis 8 °C). In ersten klinischen Studien zeigte es ein akzeptables Sicherheitsprofil, gute Immunogenität (Folegatti et al. 2020) und ein aus zwei unterschiedlichen Dosisgruppen gemittelter Schutz von 70 % vor symptomatischer COVID-19 nach über 14 Tagen nach zweiter Impfung (Voysey et al. 2021). Nach Berichten über Thrombosen und Thrombozytopenien pausierten im März 2021 einige europäische Länder die Verabreichung von Vaxzevria (Europäische Arzneimittel-Agentur 2021c, 2021b). Dieses „Thrombosen mit Thrombozytopenie-Syndrom“ (TTS) betrifft überwiegend Frauen unter 55 Jahren (Greinacher et al. 2021; Schultz et al. 2021; Scully et al. 2021), tritt aber bei weniger als einer Person von 100.000 Geimpften auf, sodass die EMA aufgrund des höheren Nutzens gegenüber den Risiken weiterhin die Verabreichung von Vaxzevria empfiehlt (Europäische Arzneimittel-Agentur 2021a).

Am 11.03.2021 wurde als zweiter Vektorimpfstoff Jcovden von Janssen-Cilag zugelassen (Europäische Arzneimittel-Agentur 2023d). Hierbei handelt es sich um ein nicht-replizierendes Adenovirus vom Serotyp 26 (Ad26), das ebenfalls bei Kühlschranktemperaturen gelagert wird (Europäische Arzneimittel-Agentur 2023d). Ein in der Präfusion-Konformation stabilisiertes Spike mit homologer Signalsequenz zeigte in präklinischen Versuchen den höchsten Schutz aller innerhalb dieses Vektors verglichenen Antigen-Varianten (Mercado et al. 2020), sodass dieser Impfstoffkandidat für klinische Studien ausgewählt und schließlich zugelassen wurde. Sicherheit und Immunogenität konnten auch nach Verabreichung nur einer einzigen Dosis festgestellt werden (Sadoff et al. 2021), sodass dieses Impfschema aufgrund logistischer und praktischer Vorteile angestrebt wurde. Das einmalig applizierte Vakzin erzielte eine Wirksamkeit von 67 % bzw. 66 % vor einer Erkrankung mindestens 14 Tage bzw. 28 Tage nach Impfung (Europäische Arzneimittel-Agentur 2023d). In retrospektiven Studien konnten jedoch vermehrt Impfdurchbrüche bei mit Jcovden geimpften Personen festgestellt werden (Yi et al.

2022; Uschner et al. 2022; Dingemans et al. 2022), sodass die EMA eine Booster-Impfung mindestens zwei Monate nach der ersten Impfung empfiehlt (Europäische Arzneimittel-Agentur 2021d).

Als erster Protein-Impfstoff innerhalb der EU wurde am 20.12.2021 Nuvaxovid von Novavax zugelassen (Europäische Arzneimittel-Agentur 2023h). Als Antigen dient auch hier das rekombinante und stabilisierte Spike, das sich in Mizellen zusammenlagert und mit dem Wirkverstärker Matrix-M adjuvantiert ist. In klinischen Studien konnte seine hohe Sicherheit und eine Schutzwirkung von 90-93 % vor symptomatischer COVID-19 sieben Tage nach der zweiten Impfung belegt werden (Heath et al. 2021; Dunkle et al. 2022).

Mit dem COVID-19-Impfstoff von Valneva wurde am 24.06.2022 der erste Inaktivat-Impfstoff in der EU zugelassen (Europäische Arzneimittel-Agentur 2023c). Zur Herstellung des Impfstoffs wurde das vollständige Virus mit Propiolacton inaktiviert und mit den Wirkverstärkern CpG 1018 und Aluminiumhydroxid adjuvantiert, sodass in diesem Impfstoffkonzept potenziell alle Proteine von SARS-CoV-2 als Antigene wirken können. So führt beispielsweise eine zweifache Impfung mit dem nicht in der EU zugelassenen Inaktivat-Impfstoff „CoronaVac“ zwar zur Ausbildung von Antikörpern gegen das Nukleokapsidprotein, eine zelluläre Immunantwort gegen das Nukleokapsidprotein oder andere Proteine konnte aber nicht dargestellt werden (Chen et al. 2022). Zur Untersuchung der Immunogenität des Valneva-Impfstoffs wurde eine randomisierte, doppelt-blinde Vergleichsstudie durchgeführt, in der die Impflinge entweder den Valneva-Impfstoff oder Vaxzevria insgesamt zweimal im Abstand von 28 Tagen erhielten (Lazarus et al. 2022). Dabei stimulierte der Valneva-Impfstoff nicht nur gleiche oder höhere neutralisierende Antikörperspiegel gegen SARS-CoV-2 als Vaxzevria, sondern er stimulierte auch die Reaktivität von mononukleären Zellen des peripheren Blutes (peripheral blood mononuclear cells, PBMC) gegen das Nukleokapsidprotein in 45,9 % der Geimpften und gegen das Membranprotein in 20,3 % der Geimpften (Lazarus et al. 2022). Der lediglich für Spike kodierende Adenovirus-Impfstoff konnte entsprechend keine Immunantwort gegen das Nukleokapsid- oder Membranprotein auslösen (Lazarus et al. 2022).

Am 10.11.2022 wurde mit VidPrevtyn Beta von Sanofi Pasteur der zweite Proteinimpfstoff in der EU zugelassen, jedoch zur Boosterimpfung nach vorheriger Immunisierung mit einem mRNA- oder Adenovirus-Vektorimpfstoff (Europäische Arzneimittel-Agentur 2023k). VidPrevtyn Beta besteht aus mit dem Wirkverstärker AS03 adjuvantiertem Spike Protein. Um die Immunogenität von VidPrevtyn Beta zu bestimmen, wurde eine randomisierte, einfach-blinde Vergleichsstudie durchgeführt, in der die bereits zweifach homolog mit Comirnaty geimpften Personen entweder eine VidPrevtyn Beta- oder eine Comirnaty-Auffrischungsimpfung erhielten. Dabei führte die heterologe Boosterimpfung mit VidPrevtyn

Beta zu durchschnittlich 2,53-fach höheren Antikörperspiegeln in Geimpften als die homologe Boosterimpfung mit Comirnaty (Europäische Arzneimittel-Agentur 2023g).

Kurz vor dem offiziell verkündeten Ende der COVID-19-Pandemie im Mai 2023 befanden sich weltweit noch ungefähr 180 weitere Impfstoffkandidaten in der klinischen Entwicklung (World Health Organization 2023) und ungefähr 50 weitere Impfstoffe waren in wenigstens einem Land zugelassen (McGill COVID19 Vaccine Tracker Team 2023) (Stand 04.04.2023). Von diesen setzt Afrika (als Kontinent mit den niedrigsten Impfquoten (Our World in Data 2023)) neben den bereits genannten in der EU zugelassenen Impfstoffen auch auf die Inaktivatimpfstoffe der chinesischen Impfstoffhersteller Sinopharm und Sinovac: Mit 20,8 % der bezogenen Impfstoffe haben diese einen ähnlich hohen Anteil wie die mRNA-Impfstoffe von Biontech und Moderna mit zusammengenommen 26,7 %, während die übrigen 52,5 % überwiegend auf Adenovirus-basierte Impfstoffe entfallen (Africa Centres for Disease Control and Prevention 2023). Wesentliche Gründe, warum der Anteil mRNA-basierter Impfstoffe in der EU mit 68 % deutlich höher liegt als in Afrika (European Centre for Disease Prevention and Control 2023), sind deren relativ hohe Kosten (Ang 2021), die logistischen Anforderungen einer -70 °C-Tiefkühlkette aufgrund der Instabilität der RNA, sowie ein Mangel an Produktionsstätten außerhalb von einkommensstarken Ländern. Demgegenüber stehen beispielsweise Masernimpfstoffe, für die aufgrund weltweiter Impfprogramme und internationaler Förderung Produktionsstätten auf allen Kontinenten existieren, die eine kostengünstige und breite Distribution ermöglichen (Rey-Jurado et al. 2018; Weltgesundheitsorganisation und MI4A 2020). Diese Masernimpfstoffe dienen seit 1999 als Grundlage für Vektorimpfstoff-Kandidaten, die durch gentechnisches Einfügen von Fremdantigenen in das Genom des Vektorvirus neben einer Immunantwort gegen das Vektorvirus auch eine gegen das Fremdantigen auslösen können. Solche gentechnischen Modifikationen werden so durchgeführt, dass das Wachstumsverhalten des parentalen Virus erhalten bleibt, sodass ein Masernimpfstoff-basierter Vektorimpfstoff potenziell die bereits bestehenden Produktionswege von Masernimpfstoffen nutzen könnte, um einer globalen Bedrohung durch eine Pandemie eine globale, schnelle Antwort folgen zu lassen.

2.3 Impfstoffplattform rekombinante Masernimpfviren

Der Erreger der Masern, das Masernvirus (*measles virus*, MeV), ist das Prototyp-Virus der Gattung der Morbilliviren in der Familie der *Paramyxoviridae*. Die behüllten, pleomorphen Partikel haben einen Durchmesser von 100 - 300 nm. Das Masernvirusgenom umfasst ca. 16 kb einzelsträngiger, nicht-

segmentierter RNA negativer Polarität und enthält insgesamt sechs Gene, die für acht Proteine kodieren (Modrow 2021) (Abb. 1).

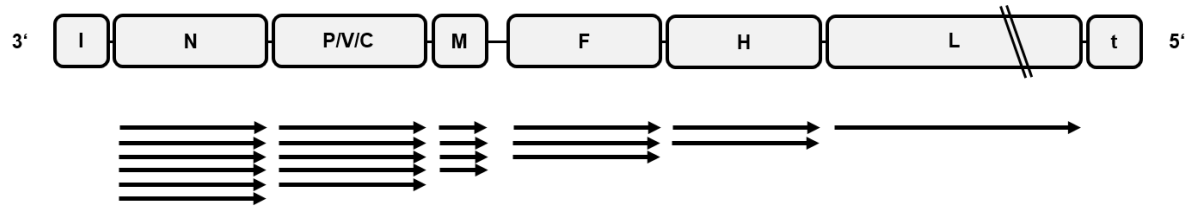

Abb. 1. Schema des Masernvirusgenoms mit der *leader*-Sequenz (l), den Genen für das Nukleoprotein (N), Phosphoprotein (P), V-Protein (V), C-Protein (C), Matrixprotein (M), Fusionsprotein (F), Hämagglutinin (H), *Large* Protein (L) und der *trailer*-Sequenz, darunter das Schema des Transkriptionsgradienten der viralen mRNA.

Das Nukleoprotein (N) formt durch Anlagerung an die virale RNA das helikale Nukleokapsid, das zusammen mit der viralen RNA-Polymerase (*Large* Protein, L) und deren Co-Faktor, dem Phosphoprotein (P), den Ribonukleoproteinkomplex (RNP) bilden. Die Nichtstrukturproteine C und V werden in überlappenden offenen Leserahmen der Genkassette für P kodiert. Das Matrixprotein (M) dient der Morphogenese der Viruspartikel, in deren Lipid-Hülle die Glykoproteine F (Fusionsprotein) und H (Hämagglutinin) eingelagert sind (Modrow 2021).

Der erste Schritt der Masernvirusreplikation, die Rezeptorbindung der MeV-Partikel an eine menschliche Zelle, wird durch die Bindung von H an einen der zellulären Rezeptoren vermittelt: SLAM (Tatsuo et al. 2000) oder Nectin-4 (Mühlebach et al. 2011; Noyce et al. 2011). Für Masern-Impfstämme dient zusätzlich auch CD46 als Rezeptor (Dörig et al. 1993; Naniche et al. 1993). Diese Bindung führt zu einer Änderung der Konformation von H, die wiederum den Fusionsprozess durch F auslöst (Navaratnarajah et al. 2011). Nach Verschmelzung der Membranen wird der RNP in das Zytoplasma der frisch infizierten Wirtszelle entlassen. Ausschließlich im Zytoplasma findet dann die Transkription und Replikation der MeV-Genome statt. Die virale Polymerase L bindet an den Promotor der Leadersequenz der viralen RNA. L erkennt dann Motive in den folgenden konservierten, intergenischen Sequenzen, die Genanfang und -ende der einzelnen viralen Genkassetten signalisieren. An der Anfangssequenz der Genkassetten startet L die Transkription, die sie am Gen-Ende mit der Polyadenylierung des Transkripts abschließt (Parks et al. 2001a). Der sich an jedem intergenischen Abschnitt wiederholende Prozess aus Stoppen, Überspringen eines nicht transkribierten RNA-Tripletts und Re-Initiation der Transkription gelingt nicht immer, sodass L mit einer gewissen Wahrscheinlichkeit vom RNA-Strang abfällt und den Transkriptionsprozess an der Leadersequenz des Genoms neu beginnen muss. Daraus resultiert ein Transkriptionsgradient der einzelnen viralen mRNAs, mit der höchsten Anzahl an mRNA, die für das am

3‘ Terminus lokalisierte N Protein kodiert, und deutlich weniger mRNA (ca. 1,5 % der Menge der N mRNA), die für das am 5‘ Terminus lokalisierte L Protein kodiert (Cattaneo et al. 1987) (Abb. 1). Die von L gecappten und mit poly(A)-Schwanz ausgestatteten mRNAs werden von der zellulären Translationsmaschinerie in Proteine translatiert. Es wird angenommen, dass der Wechsel von L in den Replikationsmodus durch die Menge an N Protein in der Zelle ausgelöst wird, wie es auch für das Vesikuläre Stomatitis-Virus (VSV), ebenfalls ein Virus aus der Ordnung der Mononegavirales, gezeigt werden konnte (Patton et al. 1984; Wertz et al. 1987). Für die Replikation transkribiert L durch *read-through* auch der intergenischen Sequenzen einen Volllängen-RNA-Strang, das Antigenom, das mit seiner positiven Polarität als Matrize in einem weiteren Transkriptionsschritt zur Erzeugung neuer viraler Genome dient. Dabei bindet L an die am 3‘ Terminus lokalisierte Trailersequenz dieses Antigenoms und transkribiert genomische Volllängen-RNA-Stränge von negativer Polarität (Plumet et al. 2005). An die virale RNA lagern sich noch während der Transkription Protomere von N und bilden das helikale Nukleokapsid aus, an das die virale Polymerase bindet. Das Nukleokapsid wiederum bindet an der Zellmembran M, das dort mit Fettsäuren in der Zellmembran interagiert (Norris et al. 2022). Die Polymerisierung von M ist schließlich für die Morphogenese neuer Virionen verantwortlich (Norris et al. 2022). In der Zellmembran sind bereits die viralen Glykoproteine F und H verankert, die über ihren jeweiligen zytoplasmatischen Schwanz mit M interagieren (Cathomen et al. 1998; Tahara et al. 2007). Dadurch sind F und H Teil der Virushülle, wenn neue MeV-Virionen durch Knospung von den infizierten Zelle freigesetzt werden (Modrow 2021).

Die Masernviren verbreiten sich über die Atemwege und sie sind mit einer Basisreproduktionszahl R_0 von 12-18 hochkontagiös (Durrheim et al. 2014). Die Erkrankung geht mit einer Fallsterblichkeit von geschätzt 2,2 % einher (Portnoy et al. 2019), sodass in den Zeiten vor Einführung der Masernimpfung jährlich geschätzt 2,6 Millionen Menschen an den Masern starben, davon überwiegend Kinder (Naniche 2009; Weltgesundheitsorganisation 2023).

Im Jahr 1954 wurde das Masernvirus aus dem Patienten David Edmonston isoliert (ENDERS und PEEBLES 1954). Dieser „Edmonston“ genannte Virusstamm wurde fortan in der Grundlagenforschung als auch zur Entwicklung des ersten lebend-attenuierten Masernimpfstoffs Edmonston B genutzt, indem er in Hühnerembryo-Fibroblasten wiederholt passagiert wurde (Griffin 2018). Die Verimpfung dieser ersten lebend-attenuiertem Masernimpfstoffe ging noch regelmäßig mit Fieber einher (KATZ et al. 1960). Edmonston B und andere Isolate wurden durch Passagierung in Zellkultur weiter attenuiert und die daraus entstandenen Nachfolger (u.a. die Impfstämme Moraten und Schwarz) werden noch heute weltweit verimpft (Parks et al. 2001b).

Mit Aufkommen der reversen Genetik, welche die Erzeugung von Negativ-Strang RNA-Viren aus DNA ermöglicht, konnten auch rekombinante Masernviren generiert werden (Radecke et al. 1995). So wurden als erste Impfantigene die Strukturproteine des Hepatitis-B-Virus (HBV) in das Masernimpfvirusgenom eingefügt (Singh et al. 1999). Nach Applikation der rekombinanten Impfviren konnten Immunantworten nicht nur gegen MeV, sondern auch gegen HBV in MeV-suszeptiblen IFNAR™-CD46Ge Mäusen (Singh et al. 1999) und nicht-humanen Primaten (Del Valle et al. 2007) induziert werden. Bisher wurden rekombinanten Masernimpfviren mit Antigenen von 22 Infektionserregern ausgestattet (Ebenig et al. 2022a). In präklinischen Studien konnte für alle Impfviren eine humorale Immunantwort gegen diese Antigene nachgewiesen werden und in den Studien, in denen die entsprechenden Analysen publiziert sind, auch eine zelluläre Immunantwort (Ebenig et al. 2022a). Nachdem die zelluläre Immunität auch Jahrzehnte nach Masernimpfung im Menschen nachgewiesen werden kann (Ovsyannikova et al. 2003; Naniche et al. 2004), wurden kürzlich erste Hinweise im Mausmodell gefunden, dass sich diese langandauernde Immunität auch auf das zusätzliche Antigen-Transgen im rekombinanten Masernimpfvirus übertragen kann (Hörner et al. 2023). Diese Erkenntnisse zur Immunogenität aus präklinischen Studien und dem Wissen über das hohe Sicherheitsprofil des parentalen Masernimpfvirus ermöglichten bereits die weitere Untersuchung von fünf rekombinanten Masernimpfviren in klinischen Studien (United States National Library of Medicine 2012; Reisinger et al. 2018; Vanhoutte et al. 2022; United States National Library of Medicine 2022a, 2022b).

Für die Herstellung solcher Impfkandidaten auf Basis rekombinanter Masernimpfviren zeichneten sich alle zu Beginn dieser Arbeit verfügbaren reverse Genetik-Systeme durch hohe Komplexität (mindestens 3 verschiedene Bestandteile) und niedrige bis moderate Effizienz aus. Gerade für die Anwendung als Impfstoffplattform gegen eine neu auftretende Disease X, bei der Herstellungszeit und -effizienz äußerst kritisch sind, kann die Optimierung der Herstellung rekombinanter Masernimpfviren eine Schlüsselrolle für die potenzielle Anwendung dieser Impfstoffplattformtechnologie spielen.

3. Ziele

3.1 In vitro-Untersuchung der anti-coronaviralen Eigenschaften von EGCG

Wie im vorherigen Abschnitt dargelegt ist bisher lediglich eine sehr überschaubare Anzahl an Therapeutika zur Behandlung von COVID-19 zugelassen, sodass durch Resistenzentwicklung diese Optionen schnell zunichte gemacht werden können. Als Lösungsansätze stehen neben dem Repositionieren (*repurposing*) bereits vorhandener Wirkstoffe in einem neuen Indikationsgebiet auch die Suche nach gänzlich neuen pharmakologischen Leitstrukturen (*lead compounds*) zur Verfügung. Das Catechin Epigallocatechingallat aus dem grünen Tee ist eine solch vielsprechende Leitstruktur, da in *in vitro*-Studien bereits seine hemmende Wirkung auf unterschiedliche Viren festgestellt werden konnte. Ob für EGCG daneben auch eine Wirkung gegen Coronaviren nachgewiesen werden kann, sodass es als Leitstruktur in der Medikamentenentwicklung gegen COVID-19 dienen könnte, wurde im Rahmen dieser Doktorarbeit in der beiliegenden Studie (Henss et al. 2021) untersucht.

3.2 Charakterisierung zweier unterschiedlicher Impfstoffkonzepte gegen COVID-19

Auf Basis rekombinanter Masernimpfviren wurde bereits ein Impfstoffkandidat gegen MERS-CoV hergestellt und dessen hohe Immunogenität im Mausmodell nachgewiesen (Malczyk et al. 2015). Nach Auftreten von SARS-CoV-2, das wie MERS-CoV in die Gattung der Betacoronaviren einzuordnen ist, wurde daher die gleiche, bei MERS-CoV bewährte Strategie angewendet, um auf Basis rekombinanter Masernimpfviren einen Impfstoffkandidaten gegen COVID-19 zu entwickeln. Die Immunogenität und Wirksamkeit wurde im direkten Vergleich mit einem Aluminiumhydroxid-adjuvantierten Proteinimpfstoff analysiert (Hörner et al. 2020).

Vor der Wirksamkeit ist die absolut essenzielle Anforderung an einen Impfstoff dessen Sicherheit. Aufbauend auf Hörner *et al.* wurden daher dieselben zwei Impfstoffkonzepte gegen SARS-CoV-2 wieder im hoch-suszeptiblen syrischen Goldhamster eingesetzt, doch dieses Mal mit Hilfe weitergehender Analysen auf eine potenzielle Verstärkung der Erkrankung durch von der Impfung stimulierte Immunzellen oder Antikörper (*Vaccine Associated Enhanced Respiratory Disease*, VAERD) untersucht (Ebenig et al. 2022b).

3.3 Vereinfachung der Herstellung rekombinanter Masernimpfviren

Wie in Kapitel 2 dargestellt erfolgt die Erzeugung (*rescue*) neuer rekombinanter Masernimpfviren wie die in Kapitel 3.2 beabsichtigten COVID-19-Impfstoffkandidaten *in vitro* mit Hilfe sogenannter reverser Genetik-Systeme. Dazu stehen verschiedene Systeme zur Verfügung, welche die Ko-Transfektion von mindestens vier Plasmiden in MeV-suszeptible Zellkulturen erfordern (Martin et al. 2006), auf einer transgenen, empfindlichen Helferzelllinie beruhen (Radecke et al. 1995), oder Transfektion von Helferplasmiden und Überinfektion mit einem MVA-abgeleiteten Helfervirus notwendig machen (Schneider et al. 1997). Deren Komplexität in der Anwendung ist hoch und ihre Effizienz niedrig bis moderat. In der im Rahmen dieser Doktorarbeit angefertigten, beiliegenden Studie wurden alle Helferfunktionen auf einem Plasmid kombiniert (Auste und Mühlebach 2022). Damit wurde in einem ersten Schritt nachgewiesen, dass durch die Verringerung der Zahl der essenziellen Elemente in der Virus-herstellenden Zelle die Komplexität des Systems signifikant reduziert werden kann. Durch weitere Optimierung dieses Systems steht auch die erhöhte Effizienz der Erzeugung rekombinanter Masernimpfviren in Aussicht.

4. Ergebnisse

Die folgenden Publikationen wurden entsprechend ihrer Thematik geordnet. Das Literaturverzeichnis jedes Manuskripts wird im Stil des jeweiligen Fachjournals dargestellt und ist nicht Teil des Literaturverzeichnisses am Ende dieses Dokuments. Die Nummerierung der Abbildungen und Tabellen entspricht der veröffentlichten Darstellung des jeweiligen Manuskripts.

4.1 The green tea catechin epigallocatechin gallate inhibits SARS-CoV-2 infection

Lisa Henss[1,†], Arne Auste[2,3,†], Christoph Schürmann[2,†], Christin Schmidt[1], Christine von Rhein[1], Michael D. Mühlebach[2,3], Barbara S. Schnierle[1]

[1]Department of Virology, [2]Department of Veterinary Medicine, Paul-Ehrlich-Institut, Paul-Ehrlich Strasse 51-59, 63225 Langen, Germany

[3]German Center for Infection Research, Gießen-Marburg-Langen, Germany.

[†] These authors contributed equally to this work

Journal of General Virology 2021

doi: 10.1099/jgv.0.001574

Abstract

The severe acute respiratory syndrome coronavirus-2 (SARS-CoV-2) infection has caused a pandemic with tens of millions of cases and more than a million deaths. The infection causes COVID-19, a disease of the respiratory system of divergent severity. No treatment exists. Epigallocatechin-3-gallate (EGCG), the major component of green tea, has several beneficial properties, including antiviral activities. Therefore, we examined whether EGCG has antiviral activity against SARS-CoV-2. EGCG blocked not only the entry of SARS-CoV-2, but also MERS- and SARS-CoV pseudotyped lentiviral vectors and inhibited virus infections *in vitro*. Mechanistically, inhibition of the SARS-CoV-2 spike–receptor interaction was observed. Thus, EGCG might be suitable for use as a lead structure to develop more effective anti-COVID-19 drugs.

Keywords

Green tea, EGCG, SARS-CoV-2, pseudotype, MERS-CoV, SARS-CoV

Introduction

The major constituent and most important polyphenolic catechin in green tea is epigallocatechin-3-gallate (EGCG). Other catechins are also found in green tea extract, such as epigallocatechin (EGC), epicatechin gallate (ECG) and epicatechin (EC). They all have a basic flavan-3-ol structure, but EC does not contain a galloyl side chain, which is thought to contribute to the biological activities of EGCG [1]. EGCG has been described to have antiviral activities towards a variety of viruses, although the exact mechanism of these inhibitory effects is not yet understood. It inhibits the cell entry of several viruses, such as human immunodeficiency virus (HIV) [2–4], influenza virus [5], hepatitis C virus (HCV) [6–9], and chikungunya virus [10]. On the other hand, inhibitory effects on viral transcription have been reported for viruses like hepatitis B virus (HBV), adenoviruses, or herpesviruses. For a review, see [11, 12].

The severe acute respiratory syndrome coronavirus-2 (SARS-CoV-2) belongs to the *Coronaviridae* family and is the causative agent of mainly pneumonias, defined as Corona Virus Disease-2019 (COVID-19), which first emerged in the Hubei province in China [13]. After only about 4 months, the virus had spread worldwide and the SARS-CoV-2 pandemic was declared in March 2020 by the World Health Organization. SARS-CoV-2 infection can cause severe life-threatening disease with high mortality rates in older patients and patients with comorbidities [14, 15].

The Coronaviruses are enveloped positive-strand RNA viruses with large genomes. They cause disease in diverse animal species and in humans. The human coronaviruses hCoV-OC43, hCoV-229E, hCoV-HKU1, and hCoV-NL63 are the causative agents of common colds. However, the severe acute respiratory syndrome virus (SARS-CoV) and the Middle East respiratory syndrome virus (MERS-CoV) have a high pathogenic potential with 10–30 % lethality in humans [16].

Currently, with the exception of remdesivir, there is no approved, specific treatment of the SARS-CoV-2 infection available. Traditional medicine and plant extracts are currently screened for their antiviral activities and for instance the antimalarial drug artemisinin, produced from the medicinal plant, Artemisia annua L., has been described to have anti-SARS-CoV-2 activity *in vitro*. In China, 85 % of SARS-CoV-2 infected patients have received in addition to conventional therapies also Traditional Chinese Medicine (TCM) treatment and current knowledge was recently summarized [17–19].

Therefore, we were interested in the influences of EGCG on SARS-CoV-2 infection.

Methods

Cell culture

HEK293T-hACE2 [20] cells were cultured at 37 °C under 5 % CO2 and grown in Dulbecco's modified Eagle medium (DMEM; Sigma-Aldrich, Taufkirchen, Germany) supplemented with 10% foetal bovine serum (Sigma-Aldrich, Taufkirchen, Germany), 5 % l-glutamine (200 mM; Lonza, Verviers, Belgium), and 1% penicillin/streptavidin (Fisher Scientific, Schwerte, Germany). Vero cells (ATCC CCL-81) and Huh7 cells (CSC-C9441L) were cultured in DMEM supplemented with 10 % foetal bovine serum and 1 % l-glutamine. SARS-CoV-2 (isolate MUC-IMB-1) was a kind gift of G. Dobler, Bundeswehr Institute for Microbiology, Germany. MERS-CoV strain EMC/2012 was provided by Ron Fouchier (Erasmus University, Rotterdam, The Netherlands [21]) and SARS-CoV strain Frankfurt-1 by Christian Drosten (Institute of Virology, Charite, Berlin, Germany [22]). Epigallocatechin gallate (EGCG) and epicatechin (EC) were purchased from Sigma-Aldrich (Taufkirchen, Germany).

Pseudotype-based neutralization assay

Lentiviral vectors were prepared in HEK293T cells by co-transfection using Lipofectamine 2000 (Thermo Fisher, Darmstadt, Germany), as described previously [23]. Plasmids encoding HIV-1 gag/pol, rev, and the luciferase-encoding lentiviral vector genome (pMDLg/pRRE, pRSVrev, pRRLsinCMV-GFPpre [18], pCSII-Luc [19]) were transfected together with the SARS-CoV-2 delta 19 spike gene cloned into the plasmid pcDNA (Genbank #MN908947; synthesized by Eurofins, Ebersberg, Germany). In addition,

other spike encoding plasmids were used: The SARS-CoV spike gene in pcDNA (#AY278741.1, codon-optimized); the plasmid pGAGGS-MERS-CoV-S encoding a codon-optimized MERS-S gene (AFY13307.1; generous gift of Nigel Temperton, University of Kent, UK [24]), the codon-optimized NL63 delta 19 spike gene (#AFV53148.1) cloned into the plasmid pcDNA [25] or the pHIT-G plasmid encoding the VSV-G gene [26]. Cell culture supernatants containing the vectors were concentrated by ultracentrifugation for 1 h at 50000 r.p.m. and stored at –80 °C. Pseudotyped vectors and serially diluted EGCG or EC (20–0.625 µg ml–1) were incubated in triplicate for 30 min at 37 °C and used to transduce 6000 HEK293T-hACE2 cells in 384-well plates. After 24 and 48 h, the luciferase substrate BriteLite (PerkinElmer, Rodgau, Germany) was added to measure luciferase activities. The 50% inhibitory value (IC_{50}) calculated for each sample corresponds to the neutralization activity. IC_{50} was calculated using the GraphPad Prism 7.04 software (La Jolla, CA, USA).

Plaque reduction assay

The green tea compounds were two-fold serially diluted in DMEM supplemented with 2 mM l-glutamine in duplicate and mixed with 50 µl medium containing 1×10^2 $TCID_{50}$ SARS-CoV-2 (isolate MUC-IMB-1) in a total volume of 100 µl. The virus–compound mixture was incubated at 37 °C for 30 min, added to 8×10^5 Vero cells that had been seeded in 6-well plates the day before, and then incubated for 1 h at 37 °C. After removal of the inoculum, cells were overlaid with DMEM supplemented with 2 mM l-glutamine, 1.5% microcrystalline cellulose Avicel RC-591NF (FMC BioPolymer, Co. Cork, Ireland), and 2% foetal bovine serum and EGCG or EC of the indicated concentrations. After 3 days, the overlay medium was removed and the cells were fixed with 4% formalin in PBS and then stained with crystal violet to visualize plaques in the confluent cell monolayer. The plaques were counted and the IC_{50} was calculated using the GraphPad Prism 7.04 software (La Jolla, CA, USA).

Surrogate neutralization test (sVNT)

The SARS-CoV-2 sVNT Kit (Genscript, Leiden, Netherlands) is a blocking ELISA that mimics the virus receptor-binding process. Inhibition of the protein–protein interaction between a horseradish peroxidase (HRP)-conjugated recombinant SARS-CoV-2 spike receptor-binding domain fragment (HRP-RBD) and hACE2 is measured as a surrogate for neutralization. The assay was performed with different concentrations of EGCG or EC following the manufacturer's instructions. The negative (non-inhibiting) and positive (inhibiting) controls of the sVNT kit were included. Inhibition was calculated following the manufacturer's protocol using the following equation: Inhibition in % = (1 – OD of sample/OD of negative control)×100. The cutoff was set to 0, the value of the negative control.

Cell toxicity assay

Toxicity of the compounds was determined by using the ATPlite 1step Luminescence Assay System of Perkin Elmer (Rodgau, Germany). Cells were incubated with EGCG or EC at different dilutions for 24 or 48 h in triplicate and analysed by adding 7.5 µl ATPlite-substrate per well, followed by detection of luciferase units with PHERAstar (BMG LABTECH, Ortenberg, Germany). The viability data are given as % relative light units of solvent (DMEM)-treated cells.

Statistical analysis

Statistical analyses were performed using the GraphPad Prism 7.04 software (La Jolla, CA, USA). IC_{50} and CC_{50} values were calculated as nonlinear regression: Log (inhibitor) vs response (three parameter) constrain equal to 0. P-values were calculated as column analyses: Student's t-test (and nonparametric test) unpaired.

Time-of-drug-addition assay

Vero cells (2×10^4), which had been seeded into 96-wells the day before, were infected with SARS-CoV-2 (isolate MUC-IMB-1, MOI=1.5). After 1 h of incubation at 37 °C, cells were washed once with ice-cold PBS and fresh DMEM supplemented with 2 mM l-glutamine and 10% foetal bovine serum was added. Then 1 h before start of infection, 1 h or 6 h after the start of the infection, medium was changed either with medium containing 10 µg ml^{-1} EGCG or medium only. After 11 h post-infection, cells were lysed and analysed using RT-qPCR. The RNA was isolated from infected Vero cells using TRIzol Reagent (Ambion, Thermo Fisher Scientific, Dreieich Germany) and Direct-zol RNA MiniPrep kit (Zymo research, Freiburg im Breisgau, Germany) according to manufacturer's instructions. RNA was resuspended in 50 µl RNase-free water. SARS-CoV-2 RNA was quantified using Superscript III one step RT-PCR system with Platinum Taq Polymerase (Invitrogen, Darmstadt, Germany) detecting the E gene as described by Corman et al. [27]. Reactions were performed in 96-wells with 5 µl of RNA in a total volume of 25 µl and run in triplicates on a CFX 96 qPCR cycler (Bio-Rad Laboratories, Hercules, CA). For analysis of samples, RNA of a SARS-CoV-2 infected hamster was used as internal standard, which had been validated with reference standard (NIBSC 19/304) before (linear range, 4.5×10^6 to 4.5×10^2 copies [28]). The cycling conditions were as follows: reverse transcription for 10 min at 55 °C, followed by denaturation for 3 min at 94 °C, and 45 cycles of 15 s at 94 °C and 30 s at 58 °C. Quantified sample copy numbers were normalized to cell count and are presented as mean – standard error of three independent experiments.

Results

EGCG inhibits pseudotyped vectors and has broad antiviral activity

The first steps of infection by SARS-CoV-2 are mediated by its spike glycoprotein, which consists of two subunits, S1 and S2. S1 facilitates the attachment of the virus to cells via its receptor-binding domain (RBD), and the S2 domain mediates the fusion of viral and cellular membranes. SARS-CoV-2 utilizes the host protein, angiotensin-converting enzyme 2 (ACE2) for binding and entry into human cells. In addition, proteolytic cleavage of S1 by the serine protease TMPRSS2 is required [29]. Antibodies that bind to the spike RBD can neutralize SARS-CoV-2 [30, 31].

To determine if EGCG blocks SARS-CoV-2 cell entry, we transduced HEK293T-ACE2 cells [20] with SARS-CoV-2 spike protein-pseudotyped lentiviral vectors encoding luciferase in the presence of different amounts of EGCG or EC. Pseudotyping of lentiviral vectors with the SARS-CoV-2 protein is a useful tool to study SARS-CoV-2 entry at a low biosafety level [32]. Inhibition of vector entry is indicated by a reduced luciferase activity of the transduced cells [25]. A clear, dose-dependent inhibition of SARS-CoV-2-pseudotyped vectors by EGCG was observed after 24 and 48 h incubation, while EC had no effect (Fig. 1a). In addition, potential toxicity of EGCG and EC was tested by monitoring ATP with a luminescence assay. Cell viability after 24 h incubation with EGCG, as relative light units in percent of untreated control, is depicted in grey and viability after 48 h in black (Fig. 1b). As indicated in Fig. 1b, only high concentrations of EGCG reduced cell viability after 48 h incubation. Inhibition of SARS-CoV-2-pseudotyped vector entry is specific, because 5 µg ml^{-1} EGCG hardly affected cell viability, but reduced the transduction rate to 16% compared to the untreated control. EC had no effect on cell viability (data not shown). The IC_{50} values for the inhibition of SARS-CoV-2-pseudotyped vectors were 2.47 µg ml^{-1} for EGCG and >20 µg ml^{-1} for EC, suggesting that EGCG interferes with SARS-CoV-2 entry processes while EC is ineffective. Similarly, EGCG interference with vectors pseudotyped with VSV-G and the receptor-binding proteins of SARS-CoV and the common cold human coronavirus NL63 or MERS-CoV were tested and the IC_{50} values were calculated as before (Fig. 1c). In contrast to the other coronaviruses tested, MERS-CoV does not use ACE2 as a receptor and vector inhibition was tested in Huh7 cells. Huh7 cell viability was not affected by EGCG or EC (CC_{50} >20 µg ml^{-1}; Fig. 2b). EGCG treatment inhibited the ACE2 receptor using coronavirus-pseudotyped vectors with IC_{50} values of 4.28 µg ml^{-1} EGCG for SARS-CoV and 2.62 µg ml^{-1} for NL63. MERS-CoV and the VSV-G control were inhibited to a lesser extent (11.21 and 5.20 µg ml^{-1} EGCG respectively); however, a broad antiviral activity of EGCG was confirmed (Fig. 1c).

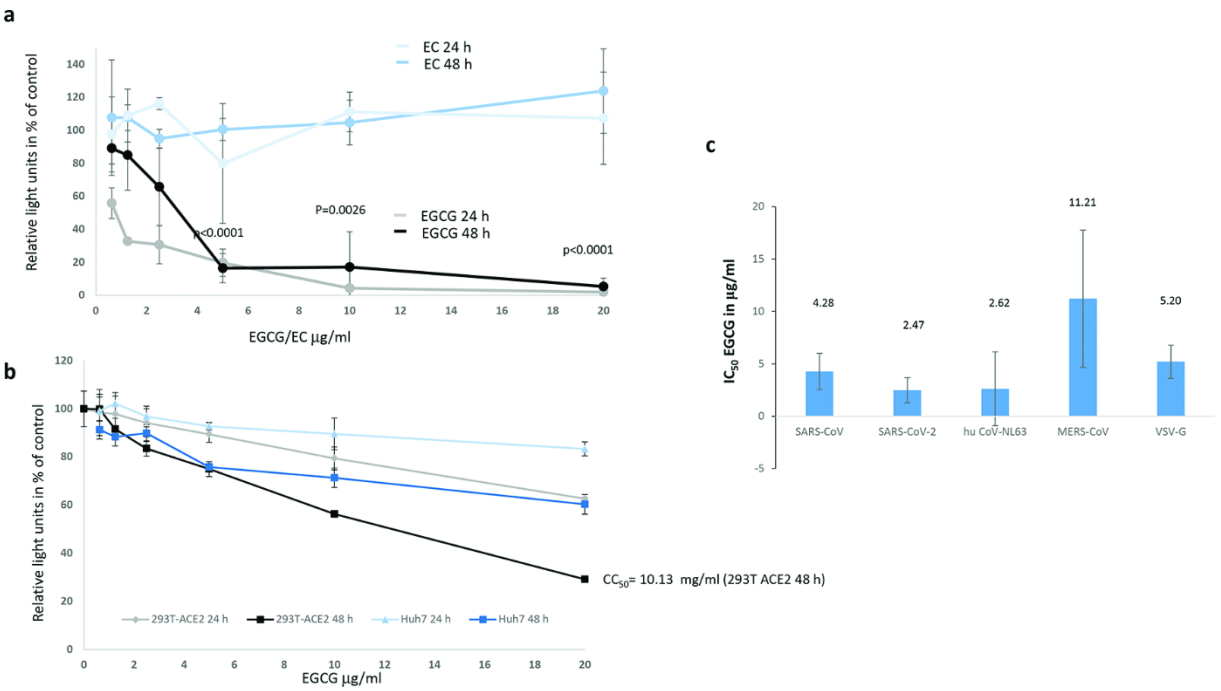

Fig. 1. EGCG inhibits transduction with SARS-CoV-2-pseudotyped lentiviral vectors. (a) EGCG or EC were added at the indicated concentrations to SARS-CoV-2-pseudotyped vectors encoding luciferase, incubated for 30 min at 37 °C and then added to HEK293T-ACE2 cells. Gene transfer into HEK293T-ACE2 cells was analysed after 24 and 48 h by measurement of luciferase activity indicated as % of the untreated control. The values for EGCG are depicted in black and grey, and those for EC in blue and light blue. The 24 h incubation was done in triplicate. The values for the 48 h incubation are mean values of three experiments done in triplicate. Significant differences between the untreated control and EGCG treatment for 48 h at the indicated concentrations are shown by the p-values, which were calculated using Student's t-test. The -values for EGCG concentrations lower than 5 µg ml^{-1} were not significant. (b) Toxicity of EGCG and EC on HEK293T-ACE2 and Huh7 cells was tested by monitoring ATP with a luminescence assay. Cell viability (as relative light units) after 24 h incubation with EGCG is depicted in grey and viability after 48 h in black for 293T-ACE2 cells and in dark blue and light blue for Huh7 cells. The values for both assays are mean values of three experiments done in triplicate (Huh7 cells: one experiment in triplicate). (c) Gene transfer by SARS-CoV-, NL63-,and VSV-G-pseudotyped vectors into HEK293T-ACE2 cells and MERS-CoV vectors into Huh7 cells, was analysed in triplicate after 48 h by measurement of luciferase activity in five independent experiments. The corresponding mean IC_{50} values and their standard deviations are depicted and were calculated using the GraphPad Prism 7.04 software (La Jolla, CA, USA).

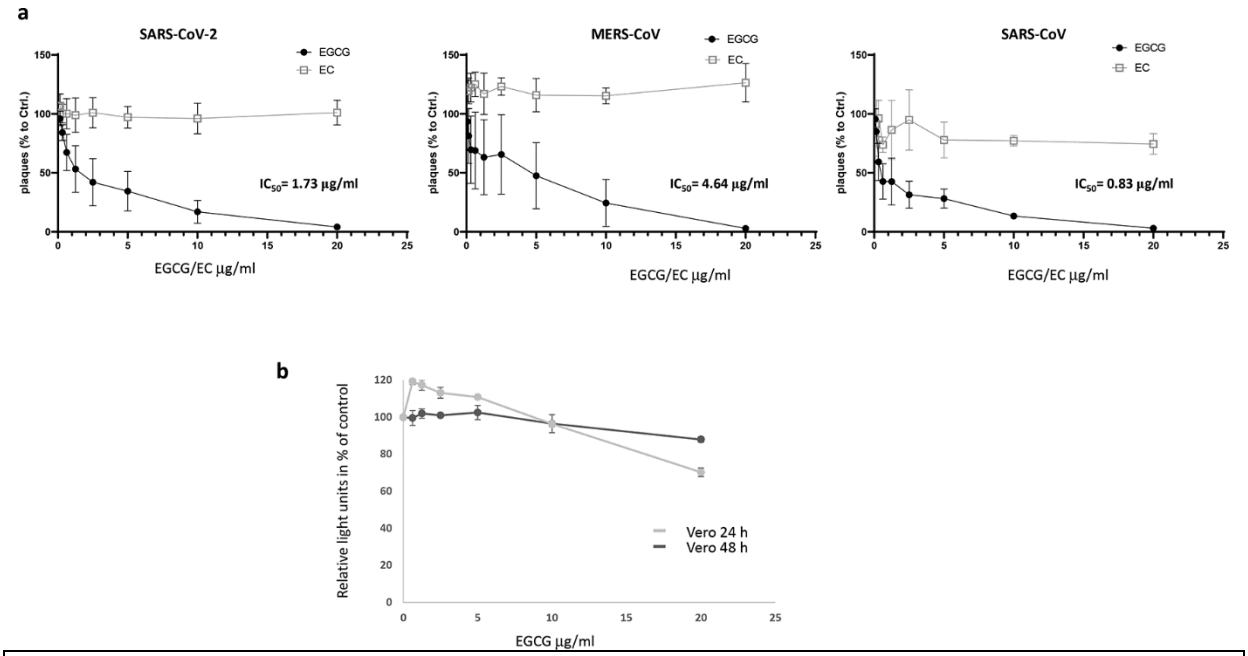

Fig. 2. EGCG inhibits coronavirus infections. (a) Vero cells were infected with SARS-CoV-2, MERS- or SARS-CoV in the presence of EGCG or EC. The values are mean values of three experiments (MERS-CoV n=4) performed in duplicate. Significant differences between EC and EGCG treatments are indicated as p-values 0.0009 for SARS-CoV-2,<0.0001 for MERS-CoV and 0.0023 for SARS-CoV. P-values were calculated with Student's t-test, using the GraphPad Prism 7.04 software (La Jolla, CA, USA). (b) Toxicity of EGCG and EC on Vero cells was tested by monitoring ATP with a luminescence assay. Cell viability (as relative light units) after 24 h incubation with EGCG is depicted in grey and viability after 48 h in black. The values for both assays are mean values of two experiments done in triplicate.

EGCG inhibits SARS-CoV-2 virus replication

To validate the potential effect of EGCG, we tested its influence on the infection of Vero cells with three emerging pathogenic coronaviruses: SARS-CoV-2, MERS- and SARS-CoV [33–35]. The green tea compounds EGCG and EC were two-fold serially diluted in DMEM and preincubated at 37 °C for 30 min with 1×10^2 $TCID_{50}$ of each of the three coronaviruses. The virus mixture was then used to infect Vero cells. After 3 days, the cells were fixed and stained with crystal violet to visualize plaques in the confluent cell monolayer, which were subsequently counted. Fig. 2a shows the results of three to four independent experiments, indicating that the infection rate was 50% of that observed in the absence of the compound at a concentration of 1.73 µg ml^{-1} EGCG (95% confidence interval (CI) 1.18 to 2.54) for SARS-CoV-2, 4.64 µg ml^{-1} EGCG (95% CI 2.37–9.29) for MERS-CoV and 0.83 µg ml^{-1} EGCG (95% CI 0.30–2.41) for SARS-CoV. The green tea compound EC had only a marginal effect on coronavirus infections (IC_{50} >20 µg ml^{-1}). The data clearly show that EGCG also has an inhibitory effect on SARS-CoV-2, MERS- and SARS-CoV infection when the replicating virus is used. In addition, similar to Huh7 cells, Vero cells

were less sensitive to the residual toxicity of EGCG (Fig. 2b). The cells were only marginally affected at high concentrations of EGCG after 24 or 48 h. Compared to the inhibition of pseudotyped vector entry, slightly lower IC_{50} values were obtained using a virus plaque reduction assay. Nevertheless, the inhibition data obtained with pseudotyped vectors were thus verified with replicating virus.

EGCG interferes with SARS-CoV-2 receptor binding

Next, the molecular mechanism of the antiviral activity was investigated. The SARS-CoV-2 RBD, which is located in the S1 protein, interacts strongly with hACE2. The SARS-CoV-2 sVNT Kit is a blocking ELISA that mimics this virus–receptor binding process. The ACE2 protein is coated onto ELISA plates and binding of the horseradish peroxidase-conjugated SARS-CoV-2 RBD is measured as optical density (OD) elicited by a substrate. Neutralizing antibodies or compounds that bind to RBD compete with ACE2 binding and the consequent reduction in OD can be quantified as a surrogate for neutralization. EGCG or EC were applied at different concentrations and only EGCG exhibited a dose-dependent neutralization activity (Fig. 3). Adding EC at the same concentration did not inhibit the ACE2–RBD interaction. The negative (non-inhibiting) and positive (inhibiting, 95% inhibition) controls of the sVNT kit were included in the assay and performed as expected. This suggests that EGCG, at least partially, interferes directly with SARS-CoV-2 receptor binding.

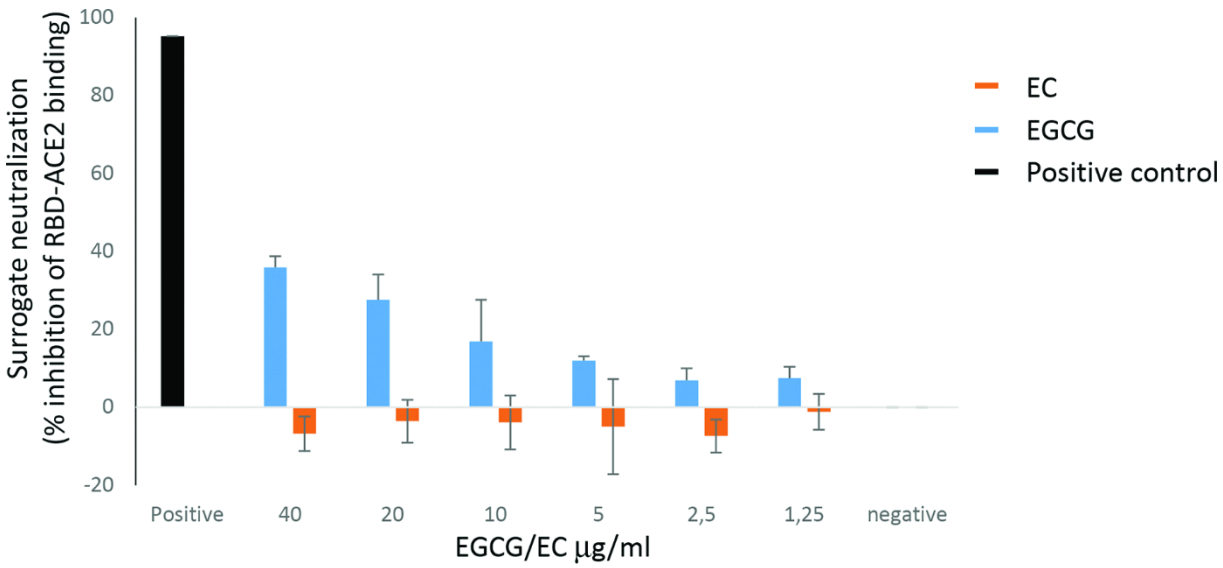

Fig. 3. EGCG inhibits attachment of SARS-CoV-2 RBD to ACE2. The sVNT assay was performed with the indicated concentrations of EGCG (black) or EC (grey) according to the manufacturer's protocol (SARS-CoV-2 sVNT Kit; Genscript, Leiden, Netherlands). Mean values and standard deviations of three independent experiments done in duplicate are given. The negative (non-inhibiting) and positive (inhibiting) controls of the sVNT kit were included. Inhibition was calculated following the manufacturer's protocol using the following equation: Inhibition in % = (1 – OD of sample/OD of negative control) ×100.

EGCG has inhibitory effects when added early during infection

The mode of EGCG action on SARS-CoV-2 infections was further evaluated by time-of-drug-addition experiments. Vero cells were infected with SARS-CoV-2 and 10 µg ml^{-1} EGCG was added either 1 h before the infection, 1 h after or 6 h after the start of the infection. SARS-CoV-2 was left on the cells for 1 h and was removed and medium was changed to either medium containing 10 µg ml^{-1} EGCG or medium only (Fig. 4a). After 11 h of infection, cells were lysed and analysed using RT-qPCR. Fig. 4b represents the results obtained as mean values of three independent experiments. Only when EGCG was added 1 h before the infection an inhibitory effect could be observed. While, this effect was not statistically significant, it also indicates that EGCG mainly interferes with early steps in SARS-CoV-2 infection.

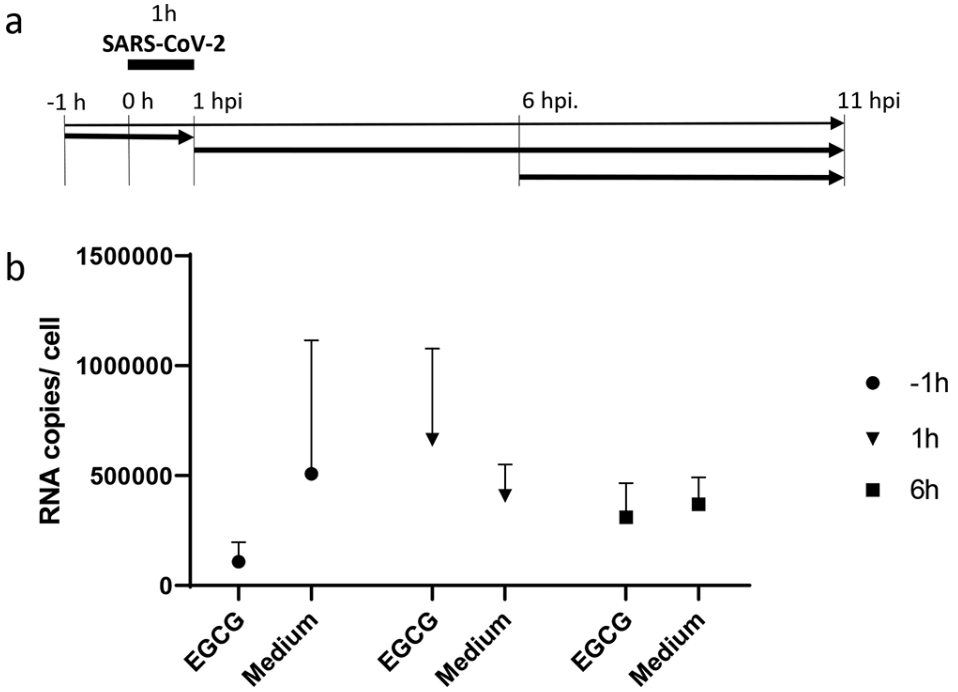

Fig. 4. Time-of-drug-addition experiment. (a) Vero cells were infected with SARS-CoV-2 and 10 µg ml^{-1} EGCG was added either 1 h before the infection, 1 h after or 6 h after the start of the infection. SARS-CoV-2 was left on the cells for 1 h (black bar), was removed and medium was changed to either medium containing 10 µg ml^{-1} EGCG or medium only. Bold arrows represent incubation with 10 µg ml^{-1} EGCG. After 11 h of infection, cells were lysed and analysed using RT-qPCR. (b) Mean values and standard deviation of SARS-CoV-2–specific RNA copies of three independent experiments at different time points of infection.

Discussion

In summary, we have shown that the most biologically active compound of green tea extract, EGCG, significantly inhibits SARS-CoV-2 and other coronavirus infections. In contrast, the less biologically active green tea catechin, EC, had no inhibitory effect. This inhibition was also observed with

pseudotyped lentiviral vectors. Moreover, EGCG used at concentrations that inhibit the virus did not display toxicity to the target cells. Toxicity of EGCG towards HEK293T-ACE2 cells was much higher than towards Vero and Huh7 cells. This might be caused by the anti-tumour activity of EGCG, which has more effect on these highly transformed cells compared to Vero cells or other cell lines, as has been described before [10, 36, 37]. Correspondingly, binding of SARS-CoV-2 RBD to its receptor ACE2 was inhibited in a surrogate neutralization assay and in time-of-drug-addition experiments, only adding EGCG before the SARS-CoV-2 infection, reduced the infection rate. This indicates that EGCG at least partially blocks the entry of SARS-CoV-2 into the target cells. However, also MERS- and SARS-CoV infections and pseudotyped vectors were inhibited by EGCG, which indicates that a more general effect on virus entry is involved.

EGCG has a broad antiviral effect against many unrelated viruses and has been described to act by competing with heparan sulphate or sialic acid on the target cells for virion binding [9]. It has been described before for other viruses, that EGCG acts directly on the virions and EGCG interacts with viral surface proteins to inhibit the attachment of herpes simplex virus-1, HCV, influenza virus A, vaccinia virus, adenovirus, reovirus, and VSV [9]. These studies showed that EGCG inhibits these unrelated viruses by competing with heparan sulphate or sialic acid for the initial binding of virus particles to cells [9]. Coronaviruses use glycans for the initial attachment to target cell [38]. In addition, it has been described that the SARS-CoV-2 spike protein interacts with cellular heparan sulphate as well as ACE2 through its RBD and heparin blocks the infection of cells by virus and pseudotyped vectors [39]. Therefore it is highly likely that EGCG also inhibits cell attachment and at least for SARS-CoV-2, additionally the RBD-ACE2 interaction. The lower inhibition rate in the *in vitro* sVNT assays compared to the cell based assays might reflect the additional effect of EGCG on interfering with heparin binding.

However, different modes of action have been described for other viruses. EGCG inhibited hepatitis B virus (HBV) by ERK1/2-mediated downregulation of hepatocyte nuclear factor 4α, resulting inhibited HBV gene expression and replication [40, 41]. But effects of EGCG on HBV have also been described to involve enhanced lysosomal acidification, which was unfavourable for HBV replication [42] or having a function as a potent entry inhibitor [43]. Moreover, inhibition of Epstein-Barr virus (EBV) by EGCG has been attributed to MEK/ERK1/2 and PI3-K/Akt pathways, which are involved in the reactivation of EBV into the lytic cycle [44]. But also, a block of binding of EBNA1 to oriP-DNA by EGCG has been described, which inhibited episomal EBV maintenance and transcriptional enhancement [45]. A summary of the pathways involved in EGCG mode of action can be found in Xu et al. (2017) [12]. Green tea extracts have been proposed before by *in silico* modelling and in *in vitro* assays as inhibitors of the SARS-CoV-2 chymotrypsin-like protease [46, 47]. However, the IC_{50} values for EGCG mediated inhibition were lower

for virus compared to pseudotyped vectors, which suggests that a dominate effect of EGCG on SARS-CoV-2 protease is not very likely.

This broad antiviral effect was also seen here for coronavirus- and VSV-G-pseudotyped vectors, although for VSV-G with slightly less efficacy. Inhibition of VSV or pseudotyped vector entry by EGCG has been described previously and is now confirmed by our results [9, 10].

The IC_{50} of the inhibitory effect observed with SARS-CoV-2 was 1.72 µg ml^{-1}. This corresponds to 3.14 µmol, which is within the range commonly described for the antiviral effects of EGCG [11]. However, EGCG might have additional beneficial effects for COVID-19 patients due to its anti-inflammatory effects [48]. Cytokine storm and inflammation are the main causes of severe COVID-19 and anti-inflammatory drugs like dexamethasone have shown promise as a treatment for COVID-19 [48, 49]. However, treatment of SARS-CoV-2 infections by oral tea consumption does not seem to be a realistic perspective. The consumption of two cups of green tea has been reported to result in a peak EGCG plasma level of <1 µM [50]. However, as a small compound with broad antiviral activity, EGCG could potentially be used as a lead structure to further develop highly effective antiviral drugs.

Funding information

This work was supported by the German Ministry of Health (BMG) by a grant to M.D.M. (CHARIS 6b) and B.S.S. (CHARIS 6a) and by the German Centre for Infection Research (DZIF; TTU 01.802) to M.D.M.

Acknowledgements

We thank Heike Baumann for excellent technical support.

Author contributions

L. H., Methodology, formal analysis, validation, data curation, project administration. A. A., Methodology, formal analysis, validation, data curation. C. S., Methodology, formal analysis, validation, data curation. C. S., Methodology, formal analysis, validation, data curation. C.v. R., Methodology, formal analysis, validation, data curation. M.D.M., Conceptualization, writing-original draft preparation, supervision, funding. B. S. S., Conceptualization, validation, formal analysis, writing-original draft preparation, visualization, project administration, supervision, funding.

Conflicts of interest

The authors declare that there are no conflicts of interest.

References

[1] Nagle DG, Ferreira D, Zhou YD. Epigallocatechin-3-gallate (EGCG): chemical and biomedical perspectives, Phytochemistry 2006;67:1849–1855.

[2] Yamaguchi K, Honda M, Ikigai H, Hara Y, Shimamura T. Inhibitory effects of (-)-epigallocatechin gallate on the life cycle of human immunodeficiency virus type 1 (HIV-1), Antiviral Res. 2002;53:19–34.

[3] Fassina G, Buffa A, Benelli R, Varnier OE, Noonan DM et al. Polyphenolic antioxidant (-)-epigallocatechin-3-gallate from green tea as a candidate anti-HIV agent, Aids 2002;16:939–941.

[4] Williamson MP, McCormick TG, Nance CL, Shearer WT. Epigallocatechin gallate, the main polyphenol in green tea, binds to the T-cell receptor, CD4: Potential for HIV-1 therapy, J.Allergy Clin.Immunol. 2006;118:1369–1374.

[5] Kim M, Kim SY, Lee HW, Shin JS, Kim P et al. Inhibition of influenza virus internalization by (-)-epigallocatechin-3-gallate, Antiviral Res. 2013;100:460–472.

[6] Ciesek S, von HT, Colpitts CC, Schang LM, Friesland M et al. The green tea polyphenol, epigallocatechin-3-gallate, inhibits hepatitis C virus entry, Hepatology 2011;54:1947–1955.

[7] Calland N, Albecka A, Belouzard S, Wychowski C, Duverlie G et al. (-)-Epigallocatechin-3-gallate is a new inhibitor of hepatitis C virus entry, Hepatology 2012;55:720–729.

[8] Chen C, Qiu H, Gong J, Liu Q, Xiao H et al. (-)-Epigallocatechin-3-gallate inhibits the replication cycle of hepatitis C virus, Arch.Virol. 2012;157:1301–1312.

[9] Colpitts CC, Schang LM. A small molecule inhibits virion attachment to heparan sulfate- or sialic acid-containing glycans, J. Virol. 2014;88:7806–7817.

[10] Weber C, Sliva K, Rhein C von, Kümmerer BM, Schnierle BS. The green tea catechin, epigallocatechin gallate inhibits chikungunya virus infection, Antiviral Research 2015;113:1–3.

[11] Steinmann J, Buer J, Pietschmann T, Steinmann E. Anti-infective properties of epigallocatechin-3-gallate (EGCG), a component of green tea, Br.J.Pharmacol. 2013;168:1059–1073.

[12] Xu J, Xu Z, Zheng W. A Review of the Antiviral Role of Green Tea Catechins, Molecules 2017;22.

[13] Wu F, Zhao S, Yu B, Chen Y-M, Wang W et al. A new coronavirus associated with human respiratory disease in China, Nature 2020;579:265–269.

[14] Wiersinga WJ, Rhodes A, Cheng AC, Peacock SJ, Prescott HC. Pathophysiology, Transmission, Diagnosis, and Treatment of Coronavirus Disease 2019 (COVID-19): A Review, JAMA 2020;324:782–793.

[15] Petersen E, Koopmans M, Go U, Hamer DH, Petrosillo N et al. Comparing SARS-CoV-2 with SARS-CoV and influenza pandemics, The Lancet Infectious Diseases 2020;20:e238-e244.

[16] Cui J, Li F, Shi Z-L. Origin and evolution of pathogenic coronaviruses, Nat Rev Microbiol 2019;17:181–192.

[17] Yang Y, Islam MS, Wang J, Li Y, Chen X. Traditional Chinese Medicine in the Treatment of Patients Infected with 2019-New Coronavirus (SARS-CoV-2): A Review and Perspective, Int J Biol Sci 2020;16:1708–1717.

[18] Li C, Wang L, Ren L. Antiviral mechanisms of candidate chemical medicines and traditional Chinese medicines for SARS-CoV-2 infection, Virus Res 2020;286:198073.

[19] Huang J, Tao G, Liu J, Cai J, Huang Z et al. Current Prevention of COVID-19: Natural Products and Herbal Medicine, Front Pharmacol 2020;11:588508.

[20] Glowacka I, Bertram S, Herzog P, Pfefferle S, Steffen I et al. Differential downregulation of ACE2 by the spike proteins of severe acute respiratory syndrome coronavirus and human coronavirus NL63, J. Virol. 2010;84:1198–1205.

[21] Zaki AM, van Boheemen S, Bestebroer TM, Osterhaus ADME, Fouchier RAM. Isolation of a novel coronavirus from a man with pneumonia in Saudi Arabia, N Engl J Med 2012;367:1814–1820.

[22] Drosten C, Günther S, Preiser W, van der Werf S, Brodt H-R et al. Identification of a novel coronavirus in patients with severe acute respiratory syndrome, N Engl J Med 2003;348:1967–1976.

[23] Henss L, Yue C, Kandler J, Faddy HM, Simmons G et al. Establishment of an Alphavirus-Specific Neutralization Assay to Distinguish Infections with Different Members of the Semliki Forest complex, Viruses 2019;11:pii:E82.

[24] Grehan K, Ferrara F, Temperton N. An optimised method for the production of MERS-CoV spike expressing viral pseudotypes, MethodsX 2015;2:379–384.

[25] Henss L, Scholz T, Rhein C von, Wieters I, Borgans F et al. Analysis of humoral immune responses in SARS-CoV-2 infected patients, J INFECT DIS 2020.

[26] Dull T, Zufferey R, Kelly M, Mandel RJ, Nguyen M et al. A third-generation lentivirus vector with a conditional packaging system, J.Virol. 1998;72:8463–8471.

[27] Corman VM, Landt O, Kaiser M, Molenkamp R, Meijer A et al. Detection of 2019 novel coronavirus (2019-nCoV) by real-time RT-PCR, Euro Surveill 2020;25.

[28] Hörner C, Schürmann C, Auste A, Ebenig A, Muraleedharan S et al. A highly immunogenic and effective measles virus-based Th1-biased COVID-19 vaccine, Proc. Natl. Acad. Sci. U.S.A. 2020:202014468.

[29] Hoffmann M, Kleine-Weber H, Schroeder S, Krüger N, Herrler T et al. SARS-CoV-2 Cell Entry Depends on ACE2 and TMPRSS2 and Is Blocked by a Clinically Proven Protease Inhibitor, Cell 2020;181:271-280.e8.

[30] Wang C, Li W, Drabek D, Okba NMA, van Haperen R et al. A human monoclonal antibody blocking SARS-CoV-2 infection, Nat Commun 2020;11:2251.

[31] Chi X, Yan R, Zhang J, Zhang G, Zhang Y et al. A neutralizing human antibody binds to the N-terminal domain of the Spike protein of SARS-CoV-2, Science 2020;369:650–655.

[32] Schmidt F, Weisblum Y, Muecksch F, Hoffmann H-H, Michailidis E et al. Measuring SARS-CoV-2 neutralizing antibody activity using pseudotyped and chimeric viruses, J Exp Med 2020;217:doi: 10.1084/jem.20201181.

[33] Rothe C, Schunk M, Sothmann P, Bretzel G, Froeschl G et al. Transmission of 2019-nCoV Infection from an Asymptomatic Contact in Germany, N Engl J Med 2020;382:970–971.

[34] Wölfel R, Corman VM, Guggemos W, Seilmaier M, Zange S et al. Virological assessment of hospitalized patients with COVID-2019, Nature 2020;581:465–469.

[35] Scheuplein VA, Seifried J, Malczyk AH, Miller L, Höcker L et al. High secretion of interferons by human plasmacytoid dendritic cells upon recognition of Middle East respiratory syndrome coronavirus, J. Virol. 2015;89:3859–3869.

[36] Singh BN, Shankar S, Srivastava RK. Green tea catechin, epigallocatechin-3-gallate (EGCG): mechanisms, perspectives and clinical applications, Biochem Pharmacol 2011;82:1807–1821.

[37] Gan R-Y, Li H-B, Sui Z-Q, Corke H. Absorption, metabolism, anti-cancer effect and molecular targets of epigallocatechin gallate (EGCG): An updated review, Crit Rev Food Sci Nutr 2018;58:924–941.

[38] Koehler M, Delguste M, Sieben C, Gillet L, Alsteens D. Initial Step of Virus Entry: Virion Binding to Cell-Surface Glycans, Annu Rev Virol 2020;7:143–165.

[39] Clausen TM, Sandoval DR, Spliid CB, Pihl J, Perrett HR et al. SARS-CoV-2 Infection Depends on Cellular Heparan Sulfate and ACE2, Cell 2020;183:1043-1057.e15.

[40] Wang Z-Y, Li Y-Q, Guo Z-W, Zhou X-H, Lu M-D et al. ERK1/2-HNF4α axis is involved in epigallocatechin-3-gallate inhibition of HBV replication, Acta Pharmacol Sin 2020;41:278–285.

[41] He W, Li L-X, Liao Q-J, Liu C-L, Chen X-L. Epigallocatechin gallate inhibits HBV DNA synthesis in a viral replication - inducible cell line, World J Gastroenterol 2011;17:1507–1514.

[42] Zhong L, Hu J, Shu W, Gao B, Xiong S. Epigallocatechin-3-gallate opposes HBV-induced incomplete autophagy by enhancing lysosomal acidification, which is unfavorable for HBV replication, Cell Death Dis 2015;6:e1770.

[43] Huang H-C, Tao M-H, Hung T-M, Chen J-C, Lin Z-J et al. (-)-Epigallocatechin-3-gallate inhibits entry of hepatitis B virus into hepatocytes, Antiviral Res 2014;111:100–111.

[44] Liu S, Li H, Chen L, Yang L, Li L et al. (-)-Epigallocatechin-3-gallate inhibition of Epstein-Barr virus spontaneous lytic infection involves ERK1/2 and PI3-K/Akt signaling in EBV-positive cells, Carcinogenesis 2013;34:627–637.

[45] Chen Y-L, Tsai H-L, Peng C-W. EGCG debilitates the persistence of EBV latency by reducing the DNA binding potency of nuclear antigen 1, Biochem. Biophys. Res. Commun. 2012;417:1093–1099.

[46] Upadhyay S, Tripathi PK, Singh M, Raghavendhar S, Bhardwaj M et al. Evaluation of medicinal herbs as a potential therapeutic option against SARS-CoV-2 targeting its main protease, Phytother Res 2020.

[47] Chiou W-C, Chen J-C, Chen Y-T, Yang J-M, Hwang L-H et al. The inhibitory effects of PGG and EGCG against the SARS-CoV-2 3C-like protease, Biochem. Biophys. Res. Commun. 2021.

[48] Menegazzi M, Campagnari R, Bertoldi M, Crupi R, Di Paola R et al. Protective Effect of Epigallocatechin-3-Gallate (EGCG) in Diseases with Uncontrolled Immune Activation: Could Such a Scenario Be Helpful to Counteract COVID-19?, Int J Mol Sci 2020;21:5171.

[49] Horby P, Lim WS, Emberson JR, Mafham M, Bell JL et al. Dexamethasone in Hospitalized Patients with Covid-19 - Preliminary Report, N Engl J Med 2020.

[50] Lee M-J, Maliakal P, Chen L, Meng X, Bondoc FY et al. Pharmacokinetics of tea catechins after ingestion of green tea and (-)-epigallocatechin-3-gallate by humans: formation of different metabolites and individual variability, Cancer Epidemiol Biomarkers Prev 2002;11:1025–1032.

4.2 A highly immunogenic and effective measles virus-based Th1-biased COVID-19 vaccine

Cindy Hörner[1,2,†], Christoph Schürmann[1,†], Arne Auste[1,2], Aileen Ebenig[1], Samada Muraleedharan[1], Kenneth H. Dinnon III[3], Tatjana Scholz[4], Maike Herrmann[5], Barbara S. Schnierle[4], Ralph S. Baric[3], and Michael D. Mühlebach[1,2]

[1]Product Testing of IVMPs, [5]Pathogenesis of Respiratory Viruses, Div. of Veterinary Medicine, [4]Div. of Virology, Paul-Ehrlich-Institut, Paul-Ehrlich-Str. 51-59, 63225 Langen, Germany

[2]German Center for Infection Research, Gießen-Marburg-Langen, Germany.

[3]Department of Microbiology & Immunology, University of North Carolina at Chapel Hill, Chapel Hill, NC, USA

[†]These authors contributed equally

Proceedings of the National Academy of Sciences of the United States of America 2020

doi: 10.1073/pnas.2014468117

Significance

The COVID-19 pandemic has already caused over 1 million deaths. Therefore, effective vaccine concepts are urgently needed. In search of such a concept, we have analyzed a measles virus-based vaccine candidate targeting SARS-CoV-2. Using this well-known, safe vaccine backbone, we demonstrate here induction of functional immune responses in both arms of adaptive immunity, yielding antiviral efficacy *in vivo* with the desired immune bias. Consequently, no immunopathologies became evident during challenge experiments. Moreover, the candidate still induces immunity against the measles, recognized as a looming second menace, when countries are forced to stop routine vaccination campaigns in the face of COVID-19. Thus, a bivalent measles-based COVID-19 vaccine could be the solution for two significant public health threats.

Abstract

The COVID-19 pandemic is caused by severe acute respiratory syndrome coronavirus-2 (SARS-CoV-2) and has spread worldwide, with millions of cases and more than 1 million deaths to date. The gravity of the situation mandates accelerated efforts to identify safe and effective vaccines. Here, we generated measles virus (MeV)-based vaccine candidates expressing the SARS-CoV-2 spike glycoprotein (S). Insertion of the full-length S protein gene in two different MeV genomic positions resulted in modulated S protein expression. The variant with lower S protein expression levels was genetically stable and induced high levels of effective Th1-biased antibody and T cell responses in mice after two immunizations. In addition to neutralizing IgG antibody responses in a protective range, multifunctional $CD8^+$ and $CD4^+$ T cell responses with S protein-specific killing activity were detected. Upon challenge using a mouse-adapted SARS-CoV-2, virus loads in vaccinated mice were significantly lower, while vaccinated Syrian hamsters revealed protection in a harsh challenge setup using an early-passage human patient isolate. These results are highly encouraging and support further development of MeV-based COVID-19 vaccines.

Keywords

SARS-CoV-2; COVID-19; measles vaccine platform; functional immunity; Th1 immune bias.

Introduction

Severe acute respiratory syndrome coronavirus-2 (SARS-CoV-2) belongs to *Coronaviridae* family and emerged toward the end of 2019 as causative agent of pneumonia in the Hubei province in China (1). The World Health Organization named the disease Corona Virus Disease-2019 (COVID-19), and officially declared the pandemic state on March 11, 2020. Human coronaviruses have been known for decades as one of the causative agents of the common cold, but two previous coronavirus outbreaks, caused by the severe acute respiratory syndrome virus (SARS-CoV-1) and the Middle East respiratory syndrome virus (MERS-CoV), have demonstrated the remarkable pathogenic potential of human beta coronaviruses. Around 10,000 people have been infected by SARS and MERS, which has resulted in a death toll of about 1,500 patients, but the outbreaks remained largely confined in terms of time or spread, respectively. In contrast, SARS-CoV-2 spreads effectively and at a rapid pace by direct transmission, with a reproductive number R_0 of at least 2 to 2.5 (2, 3). Due to high transmissibility and extensive community spread, this novel coronavirus has already caused over 36.2 million infections and over 1 million deaths (as of October 9, 2020; https://www.who.int/emergencies/diseases/novel-coronavirus-2019), while worldwide shutdowns of social life and economy to confine the spread of this respiratory virus have considerable impacts.

After the emergence of SARS in 2002 and then MERS in 2012, vaccine development efforts have been initiated, including the use of recombinant measles virus (MeV) vaccine as a platform concept (4), to develop vector vaccine candidates against both agents, and showed promising results. Recombinant MeV vectors encoding the unmodified SARS-CoV Spike protein induced high titers of neutralizing antibodies as well as IFN-γ T cell responses (5, 6) and conferred protection to immunized animals upon pathogen challenge by lowering virus titers more than 100-fold (5). For MERS, we have demonstrated that high titers of neutralizing antibodies as well as effective and polyfunctional T cell responses were induced in vaccinated animals (7, 8) and conferred protection (7). Based on these data, an MeV-based MERS vaccine candidate has been selected by the Coalition for Epidemic Preparedness Initiative for further clinical development (http://www.cepi.net/research_dev/our-portfolio).

Here, we explored the potential of recombinant MeV as vectors for the expression of the SARS-CoV-2 spike protein (S) as successfully applied for the development of MERS (7, 8) and SARS (5, 6) vaccine candidates, as well as numerous other pathogens (4). The S glycoprotein was chosen as antigen for its role as primary target of neutralizing antibodies (6, 7) and the exemplary capability of MERS-CoV S protein to trigger strong cell-mediated immune responses when expressed by MeV in our front-runner MERS vaccine candidate (7, 8). The SARS-CoV-2 S protein-encoding gene was inserted into two different

positions of the MeV genome to modulate antigen expression, and both recombinant MeVs were successfully rescued. The virus expressing lower S protein levels resulted in stable amplification over at least 10 passages, while impairment of replication was insignificant. Indeed, immunization of IFNAR$^{-/-}$-CD46Ge mice induced strong and functional humoral and cellular immune responses directed against both MeV and SARS-CoV-2 S protein biased for Th1-type T cell and antibody responses. The induced immunity translated in antiviral efficacy in two different challenge models, that is, vaccinated hamsters and mice, thereby illustrating the potential of MeV platform-based COVID-19 vaccine candidates.

Results

Generation and characterization of SARS-CoV-2-S by recombinant MeV$_{vac2}$

Since the SARS-CoV and MERS-CoV S proteins have been shown to potently induce humoral and cellular immune responses, the SARS-CoV-2 S protein was chosen as an appropriate antigen to be expressed by the recombinant MeV vaccine platform. A codon-optimized full-length gene encoding SARS-CoV-2 S protein was cloned into two different additional transcription units (ATUs) in the vaccine strain MeV$_{vac2}$ genome, either downstream of the P (post P) or H (post H) gene cassettes (Fig. 1A). Recombinant viruses were successfully generated and amplified up to P10 in Vero cells with titers of up to 4×10^7 50 % tissue culture infectious doses (TCID$_{50}$)/mL. The stability of the viral genomes was demonstrated via sequencing after RT-PCR of viruses in P2 or P10. In parallel to Sanger sequencing of the ATU region encompassing the SARS-CoV-2-S gene, the full genome was sequenced using next-generation sequencing (NGS) with a coverage of 4 to 29,683 reads of each position (SI Appendix, Fig. S1) in P2. Both methods revealed no mutations across the whole vaccine genomes but a single A to G substitution on position 9 of the noncoding trailer region of the MeV$_{vac2}$-SARS2-S(H) clone used for *in vivo* studies (GenBank accession no. MW090971).

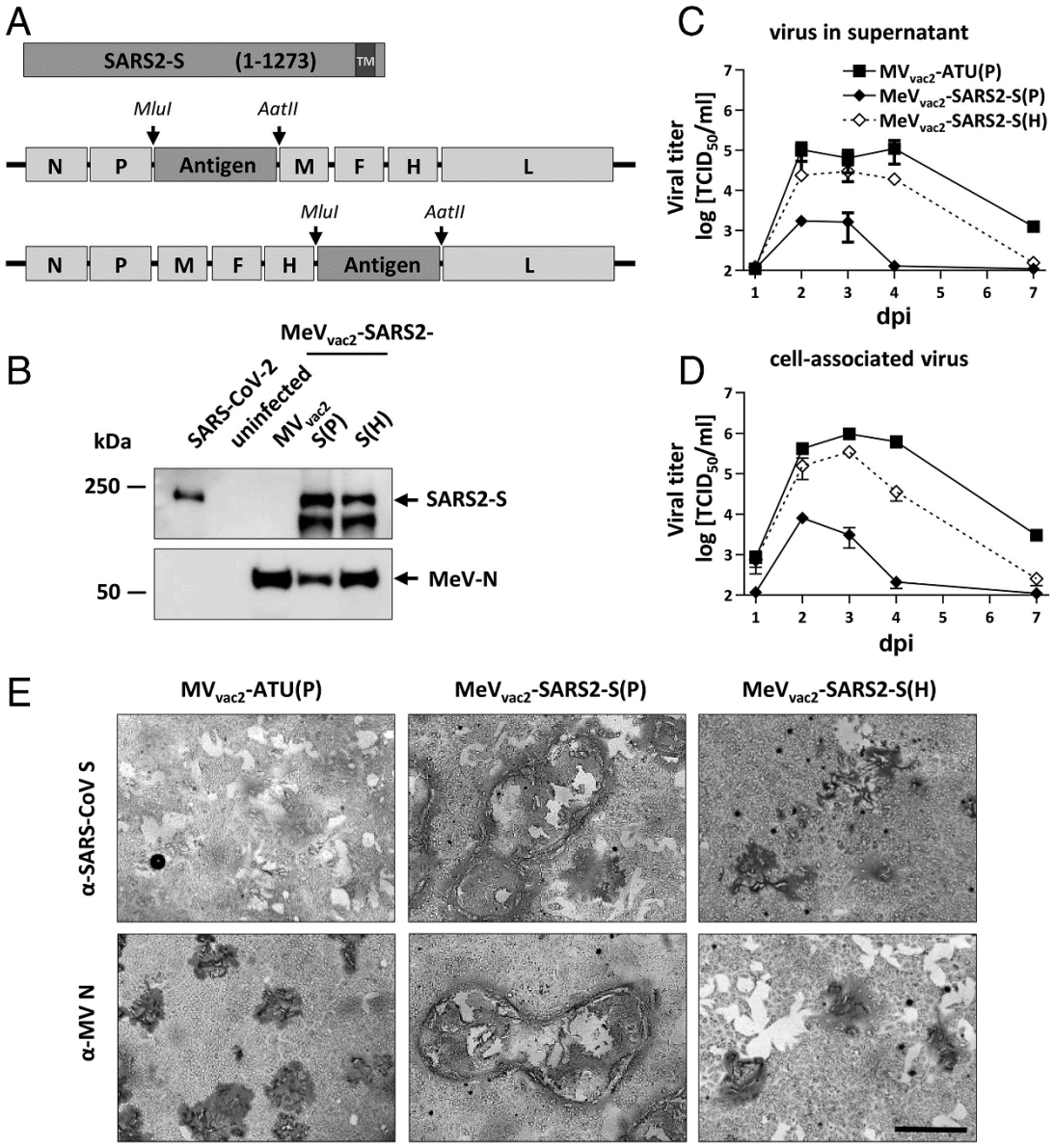

Fig. 1. Generation and *in vitro* characterization of MeV_{vac2}-SARS2-S(P) and MeV_{vac2}-SARS2-S(H). (A) Schematic depiction of full-length SARS-CoV-2 S and recombinant MeV_{vac2} genomes used for expression of this antigen (lower schemes). Antigens or antigen-encoding genes are depicted in dark gray; MeV viral gene cassettes (in light gray) are annotated. MluI and AatII restriction sites used for cloning of antigen genes into post-P or post-H ATU are highlighted. (B) Immunoblot analysis of Vero cells infected at an MOI of 0.01 with MeV_{vac2}-SARS2-S(P), MeV_{vac2}-SARS2-S(H), or MV_{vac2}-ATU(P) (MV_{vac2}) as depicted above lanes. Uninfected cells served as mock. Blots were probed using rabbit polyclonal anti-SARS spike antibody (upper blot) or mAb reactive against MeV-N (lower blot). Arrows indicate specific bands. (C and D) Growth kinetics of recombinant MeV on Vero cells infected at an MOI of 0.03 with MV_{vac2}-ATU(P) or MeV_{vac2}-SARS2-S encoding extra genes in post H or post P. Titers of samples prepared at indicated time points post infection (days post infection, dpi) were titrated on Vero cells. Means and SDs of three to five independent experiments are presented. (E) SARS-CoV-2 S protein expression in Vero cells was verified via immunoperoxidase monolayer assay; 50× magnification. (Scale bar, 500 µm.)

To verify SARS-CoV-2 S protein expression levels, Western blot analysis of Vero cells infected with the MeV_{vac2}-SARS2-S was performed. The S protein expression was slightly attenuated when cells were infected with viruses encoding the antigen in the ATU post-H compared to the post-P constructs (Fig. 1B). However, there was less overall viral protein expression in cells infected with post-P construct. Comparative growth kinetics with the vaccine viruses containing the SARS-CoV-2 S gene and the MV_{vac2}-ATU(P) control virus revealed that the MeV_{vac2} encoding full-length SARS-CoV-2 S gene in post-P position grew remarkably different than the control virus, with ~100-fold reduced maximal titers. In contrast, growth of MeV_{vac2}-SARS2-S(H) was much closer to MV_{vac2}-ATU(P), with only a slight trend for lower titers (Fig. 1 C and D).

The impaired growth of MeV_{vac2}-SARS2-S(P) was accompanied by a hyperfusogenic phenotype (Fig. 1E and SI Appendix, Fig. S2A), which was also observed for the post-H vaccine candidate, but to a lesser extent. Therefore, fusion activity was quantified and compared to the parental MV_{vac2}-ATU(P) as well as the MV_{NSe}-GFP(N), which is known for its hyperfusogenic phenotype due to a V94M substitution in the F2 subunit of the MeV fusion protein (9). MV_{vac2}-ATU(P) induced fusion of 16.8 ± 0.8 (mean± SD) Vero cells 30 h after infection. MeV_{vac2}-SARS2-S(P) revealed approximately fourfold enhanced fusion activity (syncytia including 70 ± 8 cells), while MeV_{vac2}-SARS2-S(H) just fused 41 ± 6 cells, thereby representing an intermediate phenotype. However, fusion activity of the latter was surpassed by MV_{NSe}-GFP(N) that fused 56 ± 4 cells in 30 h under the same conditions (SI Appendix, Fig. S2B).

To investigate whether this increased fusion activity is due to SARS-CoV-2 S protein-mediated cell-to-cell fusion, we expressed the SARS-CoV-2 S protein by transfection of the eukaryotic expression plasmid pcDNA3.1-SARS2-S into SARS-CoV-2 receptor hACE2-negative 293T as well as into receptor-positive Vero cells. Indeed, expression of SARS-CoV-2 S protein induced syncytia of Vero, but not of 293T cells (SI Appendix, Fig. S3).

These data demonstrate that the hyperfusogenic phenotype of the SARS-CoV-2 S-encoding MeV is linked to expression of a fusion-active form of the SARS-CoV-2 S protein, indicating that cells infected by the vaccine candidates express a functional S protein. Thus, cloning and rescue of MeVs expressing correctly folded SARS-CoV-2 S was achieved successfully. Since higher S protein expression levels impaired viral replication, MeV_{vac2}-SARS2-S(H) was chosen for further characterization *in vivo*.

MeV_{vac2}-SARS2-S(H) Induces Neutralizing Antibodies against MeV and SARS-CoV-2.

To test the efficacy of MeV_{vac2}-SARS2-S(H) *in vivo*, genetically modified $IFNAR^{-/-}$-CD46Ge mice were used, since they are the prime small animal model for analysis of MeV-derived vaccines (10). Groups of six to seven animals were immunized via the intraperitoneal route on days 0 and 28 with 1×10^5 $TCID_{50}$ of

MeV_{vac2}-SARS2-S(H) or empty MV_{vac2}-ATU(P) as a control. As positive control, recombinant SARS-CoV-2 S protein adjuvanted with aluminum hydroxide gel (Alum) was injected subcutaneously, and medium-inoculated mice served as mock controls. Twenty-one days after the second immunization, sera of immunized mice were analyzed in comparison to prebleed and postprime immunization sera, by ELISA on antigen-coated plates, for total IgG antibodies binding to MeV bulk antigens (Fig. 2 G–I) or SARS-CoV-2 S protein (Fig. 2 A–C). Sera of mice vaccinated with MeV_{vac2}-SARS2-S(H) contained IgG antibodies that bound to SARS-CoV-2 S protein (Fig. 2 B and C), whereas no antibodies were found in mice before vaccination (Fig. 2A), or in MeV or mock-immunized control mice. Moreover, final sera of mice vaccinated with any recombinant MeV had IgG in the serum binding to MeV bulk antigens, indicating at least one successful vaccination with MeVs and general vector immunogenicity (Fig. 2 G–I). The control S protein vaccine did induce higher levels of S protein-binding IgG than MeV_{vac2}-SARS2-S(H) (Fig. 2C).

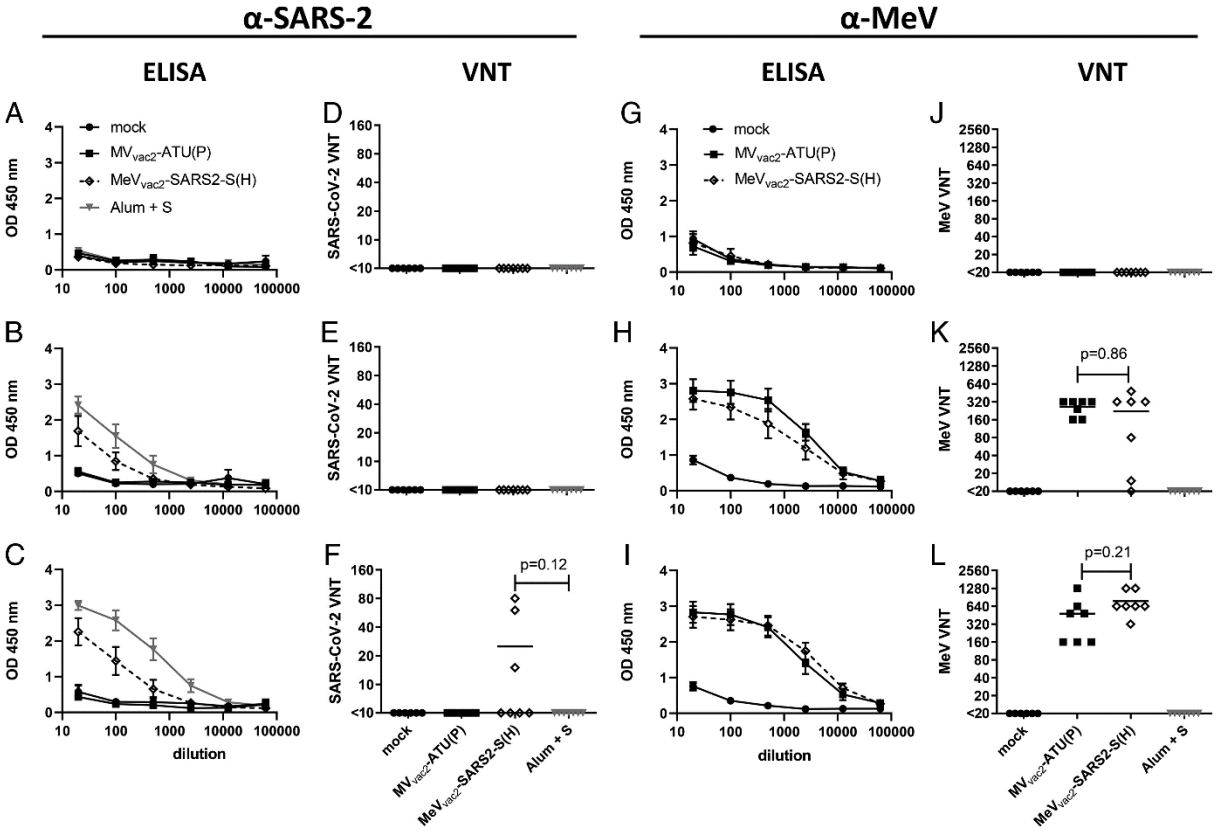

Fig. 2. Induction of α-SARS-CoV-2 S and α-MeV specific antibodies. Sera of mice vaccinated on days 0 and 28 with indicated viruses or Alum-adjuvanted S protein were sampled on day 0 (A, D, E, F), day 28 after prime immunization (B, E, H, K), and day 49 after boost immunization (C, F, I, L) and analyzed for antibodies specific for SARS-CoV-2 S or MeV. Medium-inoculated mice served as mock. Pan-IgG binding to recombinant SARS-CoV-2 S (A–C) or MeV bulk antigens (G–I) were determined by ELISA via the specific optical density (OD) 450 nm value. Depicted are

means and respective SD of the mean (SEM) of each group (n = 5 to 7). VNT in vaccinated mice for SARS-CoV-2 (D–F) or MeV (J–L) were calculated as reciprocal of the highest dilution abolishing infectivity.

We next determined the neutralizing antibody responses against SARS-CoV-2 (Fig. 2 D–F) or MeV (Fig. 2 J–L). Most mice immunized with recombinant MeV, including those receiving the control virus, had developed MeV neutralizing antibody titers (virus neutralization titer [VNT]) after the first immunization (Fig. 2K). However, two mice of the MeV_{vac2}-SARS2-S(H) cohort initially reacted only weakly, and another mouse reacted not at all, reflecting individual differences in response to immunization. All animals had developed neutralizing antibodies after the second immunization, and a threefold increase was observed upon the second immunization (220 to 762 VNT; Fig. 2 K and L). Neutralizing antibodies against SARS-CoV-2 were detected in mice vaccinated with MeV_{vac2}-SARS2-S(H) after the second immunization, and reached a titer of 15 to 80 in three out of seven mice (Fig. 2F). These titers were in the range of human reconvalescent sera tested in parallel (VNT 10 to 60; SI Appendix, Fig. S4). No VNTs against MeV or SARS-CoV-2 were detected in control mice inoculated with medium alone. Interestingly, the Alum-adjuvanted recombinant S protein did not induce any neutralizing antibodies despite higher binding IgG levels in ELISA, indicating that these antibodies bind to other epitopes of S or with lower affinity than those induced by the MeV-based vaccine candidate. In summary, the SARS-CoV-2 S protein-expressing MeV elicited robust neutralizing antibody responses against MeV and SARS-CoV-2.

Splenocytes of Animals Vaccinated with MeV_{vac2}-SARS2-S(H) React to SARS-CoV-2 S Protein-Specific Stimulation.

To assess the ability of MeV_{vac2}-SARS2-S(H) to induce SARS-CoV-2–specific cellular immune responses, splenocytes of vaccinated animals were analyzed for antigen-specific IFN-γ secretion by Enzyme-Linked Immunosorbent Spot (ELISpot) assay. Toward this, antigen-specific T cells were restimulated by cocultivation with the syngeneic murine dendritic cell (DC) cell lines JAWSII or DC2.4 stably expressing the SARS-CoV-2 S protein. For JAWSII cells, bulk cultures of transduced cells were obtained by flow cytometric sorting. For DC2.4 cells, single-cell clones were generated by limiting dilution of sorted bulk cultures. Antigen expression by transduced DCs was verified by Western blot analysis and flow cytometry (SI Appendix, Fig. S5).

ELISpot assays using splenocytes of vaccinated animals in coculture with DC2.4-SARS2-S cells revealed more than 1,400 IFN-γ secreting cells per 1×10^6 splenocytes after immunization with MeV_{vac2}-SARS2-S(H) (Fig. 3). In contrast, coculture with splenocytes of control mice resulted in a background response of less than 50 IFN-γ producing cells per 1×10^6 splenocytes. As expected, restimulation of T cells by DC2.4 presenting no exogenous antigen revealed only reactivity in the range

of background (Fig. 3). To rule out clonal or cell line-associated artifacts, antigen-specific IFN-γ secretion by splenocytes of MeV_{vac2}-SARS2-S(H)–vaccinated mice was confirmed by stimulation with transgenic JAWSII-SARS2-S bulk cells. These cells also stimulated in excess of 1,400 IFN-γ secreting cells per 1×10^6 splenocytes in animals receiving the recombinant SARS-CoV-2 vaccines, whereas only slight background stimulation was observed by the respective controls. The differences between MeV control and MeV_{vac2}-SARS2-S(H) vaccinated mice were statistically significant for both cell lines. Mice vaccinated with Alum-adjuvanted S protein showed no specific reactivity in IFN-γ ELISpot.

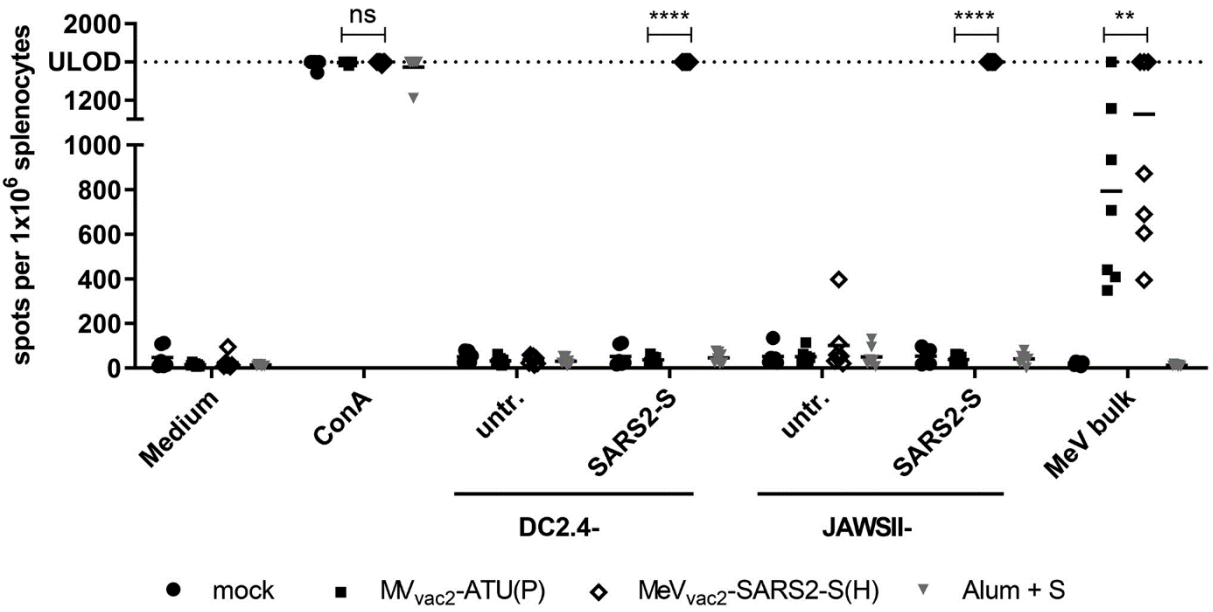

Fig. 3. Secretion of IFN-γ after antigen-specific restimulation of splenocytes. IFN-γ ELISpot analysis using splenocytes of mice vaccinated on days 0 and 28 with indicated vaccines, isolated 21 d after boost immunization, and after coculture with DC2.4 or JAWSII dendritic cell lines transgenic for SARS-CoV-2 S (SARS2-S) or untransduced controls (untr.). To analyze cellular responses directed against MeV, splenocytes were stimulated with 10 µg/mL MeV bulk antigens or were left unstimulated as controls (medium). The reactivity of splenocytes was confirmed by ConA treatment (10 µg/mL). The number of cells per 1×10^6 splenocytes represents the amount of cells expressing IFN-γ upon restimulation. Dots represent individual animals; horizontal bars are mean per group (n = 6 to 7). Samples above the upper detection limit (ULOD) were displayed as such. For statistical analysis of grouped ELISpot data, two-way ANOVA analysis was applied with paired Tukey's multicomparison test used as post hoc test; ns, not significant; ($P > 0.05$); **$P < 0.01$; ****$P < 0.0001$.

Cellular immune responses upon stimulation with MeV bulk antigens were detected in animals that had been vaccinated with any recombinant MeV virus, as expected. While MeV bulk antigens stimulated about 300 to 1,400 IFN-γ secreting cells per 1×10^6 splenocytes of MV_{vac2}-ATU(P)–vaccinated animals, splenocytes of MeV_{vac2}-SARS2-S(H)–vaccinated animals were in a similar range of 400 to 1,400 IFN-γ

secreting cells per 1×10^6 splenocytes. Splenocytes of all animals revealed a similar basic reactivity to unspecific T cell stimulation, as confirmed by numbers of IFN-γ secreting cells upon concanavalin A (ConA) treatment at the limit of detection. Remarkably, stimulation of splenocytes by DC2.4 expressing SARS-CoV-2-S resulted in at least similar or even higher numbers of IFN-γ^+ cells than after stimulation by MeV bulk antigens, indicating an extremely robust induction of cellular immunity against this antigen. Taken together, these data show that MeV_{vac2}-SARS2-S(H) induces not only humoral but also strong SARS-CoV-2 S protein-specific cellular immune responses.

SARS-CoV-2 S-Reactive T Cells Are Multifunctional.

To gain more detailed insights into the quality of the observed T cell responses, we further characterized the responsive T cell populations by flow cytometry, determining the expression of IFN-γ, TNF-α, and IL-2 in CD8- and CD4- positive $CD3^+$ T cells upon restimulation with SARS-CoV-2 S-presenting DC2.4-SARS2-S cells by intracellular cytokine staining (ICS). As a positive stimulus for T cell activation, ionomycin and phorbol myristate acetate (Ionomycin/PMA) were used. Exocytosis of cytokines was blocked by addition of brefeldin A (10 µg/mL) during stimulation. Cells were permeabilized, labeled, and fixed for flow cytometry. The gating strategy excluded duplicates (SI Appendix, Fig. S6, Middle, first row), selected for living cells (SI Appendix, Fig. S6, Right, first row), and separated $CD8^+$ and $CD4^+$ T cells on $CD3^+$ cell populations (SI Appendix, Fig. S6, second row). Selected T cells were then analyzed for their expression of IFN-γ, TNF-α, or IL-2, double-positive (SI Appendix, Fig. S6, third row), or triple-positive (SI Appendix, Fig. S4, fourth row) cells as exemplarily shown for $CD4^+$ T cells after restimulation with PMA and ionomycin (SI Appendix, Fig. S6).

Vaccination with MeV_{vac2}-SARS2-S(H) induced a significant amount of SARS-CoV-2 S-specific $CD8^+$ T cells expressing either IFN-γ (Fig. 4 B, Left), IL-2 (Fig. 4 B, Middle), or TNF-α (Fig. 4 B, Right), with means between 0.02 % and 0.5 % of positive cells for each of these cytokines. Among those, a significant fraction of cells proved to be multifunctional, with a mean of 47 % of the reactive $CD8^+$ cells expressing two cytokines or 13 % of responsive $CD8^+$ cells being positive for TNF-α, IL-2, and IFN-γ (SI Appendix, Fig. S7). A much lower portion of responsive $CD4^+$ T cells was observed, varying between 0.01 % and 0.07 % of $CD4^+$ T cells. Among the responsive $CD4^+$ cells, 40 % expressed two cytokines and 11 % were positive for TNF-α, IL-2, and IFN-γ. Moreover, vaccination induced a significant fraction of vector-specific $CD4^+$ T cells expressing IFN-γ (Fig. 4 A, Left), IL-2 (Fig. 4 A, Middle), or TNF-α (Fig. 4 A, Right) upon restimulation with MeV bulk antigen. Among those, multifunctional $CD4^+$ T cells expressing two or all three cytokines were induced with a mean of about 23 % and 6 % polyreactive T cells (SI Appendix, Fig. S7), respectively. To conclude, vaccination with MeV_{vac2}-SARS2-S(H) induces not only IFN-γ, TNF-α, or IL-2 expressing

T cells directed against SARS-CoV-2 and MeV but also a significant fraction of multifunctional cytotoxic T cells specific for SARS-CoV-2 S and $CD4^+$ T cells specific for MeV antigens, illustrating that a broad and robust SARS-CoV-2–specific immune response is induced by vaccination with MeV_{vac2}-SARS2-S(H).

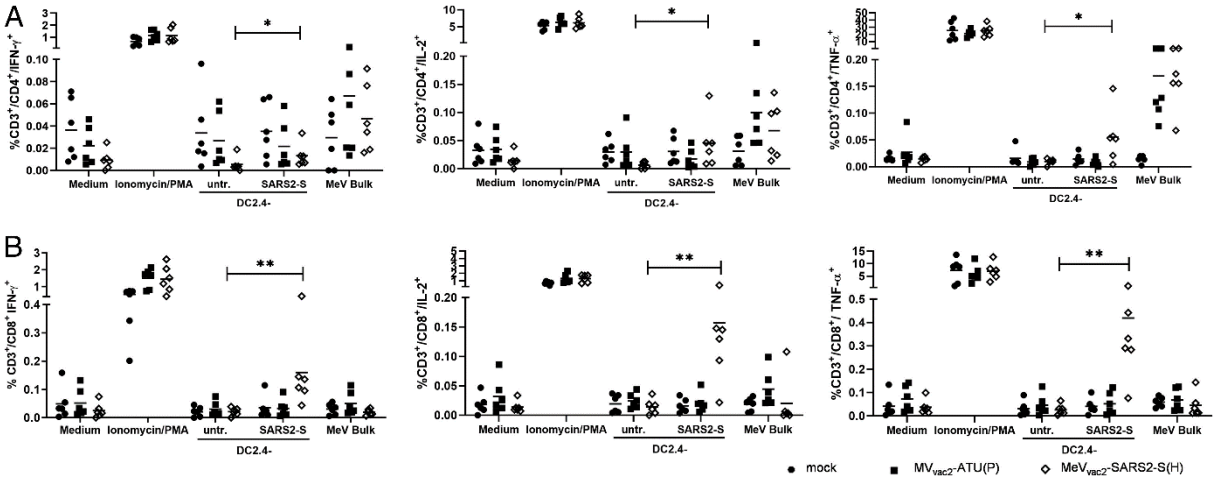

Fig. 4. Detection of multifunctional T-cell responses induced by vaccination with MeV_{vac2}-SARS2-S(H). Harvested splenocytes of MeV_{vac2}-SARS2-S(H)–vaccinated mice (same as depicted in Fig. 3) were restimulated and subjected to intracellular staining (ICS) for IFN-γ (Left), TNF-α (Right), and IL-2 (Middle), and stained for extracellular T-cell markers CD3, CD4, and CD8 for flow cytometry analysis. Quantification of flow cytometry data of (A) CD4- and (B) CD8-positive T cells after coculture with antigen-presenting DC2.4-SARS2-S or parental DC2.4 control cells, or after incubation with indicated stimuli (MeV bulk antigen [MeV bulk], or untreated cells [mock]); reactivity of splenocytes was confirmed by Ionomycin/PMA treatment (10 µg/mL). Dots represent individual animals; horizontal bars are mean. Mann–Whitney test was used to compare cytokines levels between DC2.4 and DC2.4-SARS2-S restimulated splenocytes in the MeV_{vac2}-SARS2-S(H) vaccine group without correction for multiple testing, because of the exploratory character of the study. *P < 0.05; **P < 0.01.

The reactivity of these T cells also reflected on a proliferative response to antigen-specific stimulation. Using CFSE-labelled splenocytes and flow cytometry, we detected significant proliferation of both $CD4^+$ and $CD8^+$ T cells upon stimulation with S-presenting DCs only among the splenocytes of MeV_{vac2}-SARS2-S(H)-vaccinated animals (Suppl. Fig. S8).

Induced T cells reveal antigen-specific cytotoxicity.

To demonstrate the effector ability of induced cytotoxic T lymphocytes (CTLs), a killing assay was performed to directly analyse antigen-specific cytotoxicity (Fig. 5). Splenocytes of immunized mice isolated 21 days post boost vaccination were co-cultured with DC2.4-SARS2-S or parental DC2.4 cells for 6 days to re-stimulate antigen-specific T cells. When these re-stimulated T cells were co-incubated with a defined mixture of EL-4_{green}-SARS2 S target and EL-4_{red} control cells (ratio approximately 1:1), only T

cells from MeV_{vac2}-SARS2-S(H) vaccinated mice significantly shifted the ratio of live SARS-CoV-2 S protein-expressing target cells to control cells in a dose-dependent manner (Fig. 5B). This antigen-dependent killing was also dependent on re-stimulation with DC2.4-SARS2-S cells, since unstimulated T cells did not significantly shift the ratios of target to non-target cells (Fig. 5A).

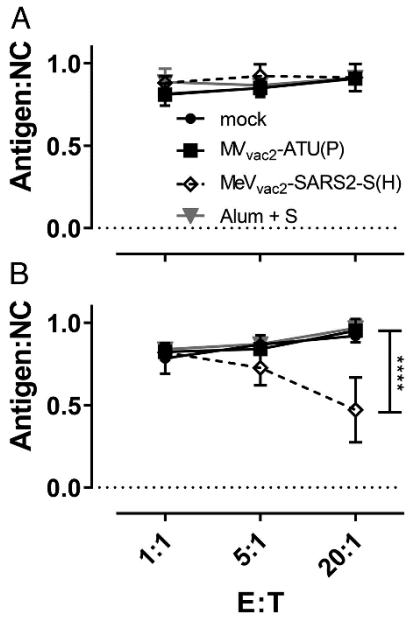

Fig. 5. Antigen-specific killing activity of SARS-CoV-2 S-specific T cells. Killing assay using splenocytes of mice vaccinated on days 0 and 28 isolated 21 d after the second immunization. Splenocytes were cocultured (A) with DC2.4 or (B) with antigen-presenting DC2.4-SARS2-S cells for 6 d. Activated CTLs were then cocultured with EL-4_{green}-SARS2-S target cells (Antigen) and EL-4_{red} control cells (NC) at indicated E:T ratios for 4 h. Ratio of living target to nontarget cells (Antigen:NC) was determined by flow cytometry. Depicted are means and SD of each group (open diamonds, MeV_{vac2}-SARS2-S(H); filled circles, mock; filled squares, MV_{vac2}-ATU(P); gray triangles, S protein + Alum) (n = 4 to 6). For statistical analysis, two-way ANOVA analysis was applied with paired Tukey's multicomparison test used as post hoc test. E:T, effector cell : target cell ratio; ****$P < 0.0001$.

These results indicate that CTLs isolated from MeV_{vac2}-SARS2-S(H)–vaccinated mice are capable of lysing cells expressing SARS-CoV-2 S. Neither splenocytes of control mice restimulated with DC2.4-SARS2-S nor splenocytes of SARS-CoV-2 S protein vaccinated mice restimulated with control DC2.4 cells showed such an antigen-specific killing activity, demonstrating that MeV_{vac2}-SARS2-S(H) induces fully functional antigen-specific $CD8^+$ CTLs.

Induced Immunity Is Skewed toward Th1-Biased Responses.

While the functionality of both humoral and cellular anti-SARS-CoV-2 immune responses elicited by MeV_{vac2}-SARS2-S(H) is reassuring, the SARS-CoV-2 vaccine development has to proceed with some

caution because of the potential risk of immunopathogenesis observed in some animal models, such as antibody-dependent enhancement (ADE) and enhanced respiratory disease (ERD) which seem to correlate with a Th2-biased immune response. Since, in mice, IgG1 is a marker for Th2 bias and risk of ADE development, whereas IgG2a antibodies indicate a favorable Th1 bias, IgG subtype-specific ELISA was performed with the sera collected at different time points. Animals vaccinated with Alum-adjuvanted SARS-CoV-2 S protein, a vaccine concept known for its Th2 bias (11, 12), developed high levels of S protein-specific IgG1 antibodies, whereas few S-specific IgG2a antibodies were detected (Fig. 6A). In comparison, MeV_{vac2}-SARS2-S(H) induced 100-fold fewer IgG1 antibodies, but at least 10-fold higher IgG2a levels (Fig. 6A), indicating a favorable Th1 bias in animals immunized with the MeV-derived vaccine candidate.

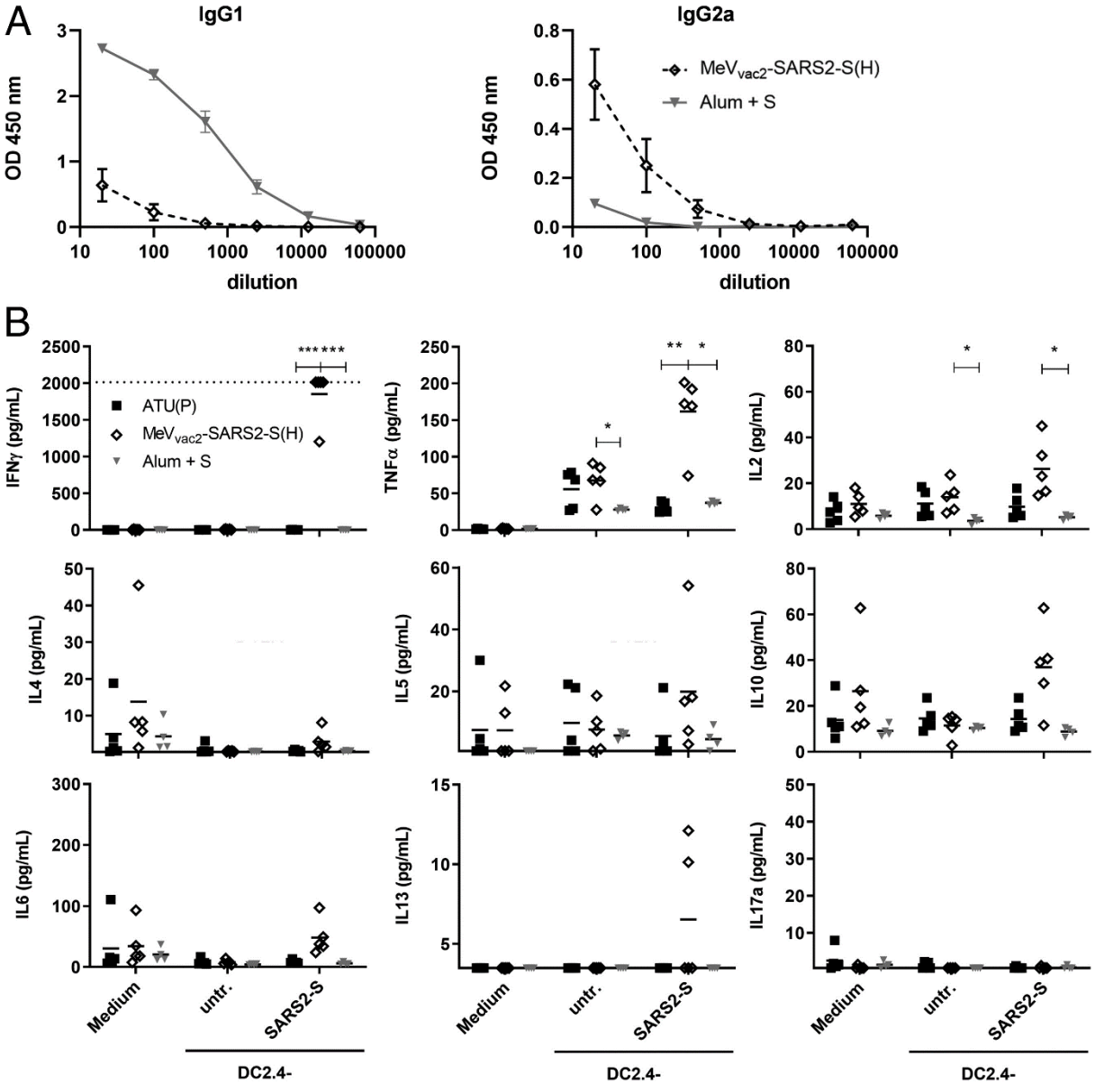

Fig. 6. Immune bias of induced responses. To analyze skewing of immune responses toward Th1- or Th2-biased immunity, (A) sera and (B) splenocytes of vaccinated mice depicted before were analyzed. (A) Sera of mice vaccinated on days 0 and 28 with MeV_{vac2}-SARS2-S(H) or Alum-adjuvanted S protein already shown in Fig. 2 were analyzed for IgG1-or IgG2a-type antibodies specific for SARS-CoV-2 S. IgG1 (Left) or IgG2a (Right) binding to recombinant SARS-CoV S were determined by ELISA via the specific optical density (OD) 450-nm value. Depicted are means and respective SD of the mean (SEM) of each group (n = 6 to 7). (B) Splenocytes of the same mice already shown in Figs. 3–5 and SI Appendix, Fig. S8 were analyzed by multiplex cytokine analysis for secretion of typical marker cytokines in the supernatant after restimulation by coculture with antigen-presenting DC2.4-SARS2-S cells. DC2.4 cells served as nonspecific control stimulus. Dots represent individual animals; horizontal bars are mean per group (n = 4 to 5). IFN-γ: upper limit of detection (ULOD): 2,015.2 pg/mL; IL-6: ULOD: 3,992.4 pg/mL; IL-17a lower limit of detection (LLOD): 0.473 pg/mL; IL-4 LLOD: 0.095 pg/mL; IL-5 LLOD: 0.685 pg/mL; IL-13 LLOD: 3.463 pg/mL. For statistical analysis of grouped multiplex data, two-way ANOVA analysis was applied with paired Tukey's multicomparison test as post hoc test. *P < 0.05; **P < 0.01; ***P < 0.001.

These findings were confirmed by multiplex cytokine analysis of the cytokine profile in the supernatants of splenocytes from vaccinated animals, which were restimulated using DC2.4 or DC2.4-SARS2-S cells. All splenocytes of representative animals revealed secretion of all cytokines after stimulation with ConA, demonstrating general reactivity of cells and assay (SI Appendix, Fig. S9). Most likely due to the low number of S-reactive T cells in animals that had been vaccinated with recombinant SARS-CoV-2 S protein and Alum, no, or minimal, constant cytokine levels were measurable in the supernatants of restimulated splenocytes (Fig. 6B). In contrast, splenocytes of animals immunized with MeV_{vac2}-SARS2-S(H) reacted specifically with the secretion of IFN-γ, TNF-α, and IL-2 upon restimulation by DC2.4-SARS2-S (Fig. 6B), in accordance with ELISpot (Fig. 3) and ICS data (Fig. 4). However, we could observe no or minimal up-regulation of IL-4, IL-5, IL-13, or IL-10, which would have been indicative for a Th2-biased response (Fig. 6B). Also, IL-17a or IL-6 indicative of a Th17 or general inflammatory response, respectively, showed minimal changes (Fig. 6B).

Thus, both humoral and cellular responses reveal a Th1-biased immunity induced by MeV_{vac2}-SARS2-S(H), which indicates a relatively low risk for putatively Th2-mediated immunopathologies.

MeV-COVID-19 Vaccine-Induced Immune Responses Are Effective *In Vivo*.

To finally test antiviral efficacy and the protective capacity of the immune responses induced by our COVID-19 vaccine candidate, two different animal models of COVID-19 were used. On the one hand, we established the Syrian golden hamster model for SARS-CoV-2–induced disease, which revealed remarkably severe outcome. Using an available low-passage SARS-CoV-2 patient isolate for intranasal

challenge of 6- to 12-wk-old hamsters, the infected animals developed severe pneumonia with an impressive gross pathology (SI Appendix, Fig. S10 A and B) that necessitated killing four out of six animals within 5 d to 6 d post infection (SI Appendix, Fig. S10C). To take advantage of this model, hamsters were vaccinated with MeV_{vac2}-SARS2-S(H), MV_{vac2}-ATU(H) as vector control, Alum-adjuvanted SARS-CoV-2 Spike protein as vaccine control, or medium (mock) in a prime–boost scheme for challenge. These hamsters showed induction of anti-MeV and anti-SARS-CoV-2 humoral immune responses with neutralizing antibody titers against SARS-CoV-2 between 15 and 80 VNT corresponding to 20 to 213 $PRNT_{50}$ (50 % plaque reduction neutralization titer), exceeding those of the Alum-S vaccine control group (SI Appendix, Fig. S11 F and M). Upon challenge, the initial weight loss observed in all groups was stopped in the MeV_{vac2}-SARS2-S(H) cohort on day 3 post infection, and animals started to gain weight, whereas all other groups revealed progressive weight loss (Fig. 7A). The experiment was stopped 4 d post infection to determine live virus titers (Fig. 7B) as well as virus genome copy numbers (Fig. 7C) in relevant tissues, that is, lungs and nasal turbinates. The corresponding data reflected the observations on gross pathology (Fig. 7A and SI Appendix, Fig. S12): The hamsters vaccinated with MeV_{vac2}-SARS2-S(H) had a more than 10-fold reduction in virus genomes in lungs and nasal turbinates than all other groups (Fig. 7C), corresponding to absence of live virus in the lungs of five out of six and nasal turbinates of one out of six vaccinated animals (Fig. 7B). Thus, vaccination with MeV_{vac2}-SARS2-S(H) significantly ameliorated virus loads in infected animals and protected them against severe pathology in this remarkably aggressive challenge model. In this model, SARS-CoV-2 neutralization antibody titers in MeV_{vac2}-SARS2-S(H)–vaccinated hamsters showed a tendency to reversely correlate with weight loss and RNA copy numbers in lung and nasal turbinates, indicating some role of neutralizing antibodies in fighting disease progression (Fig. 7D)

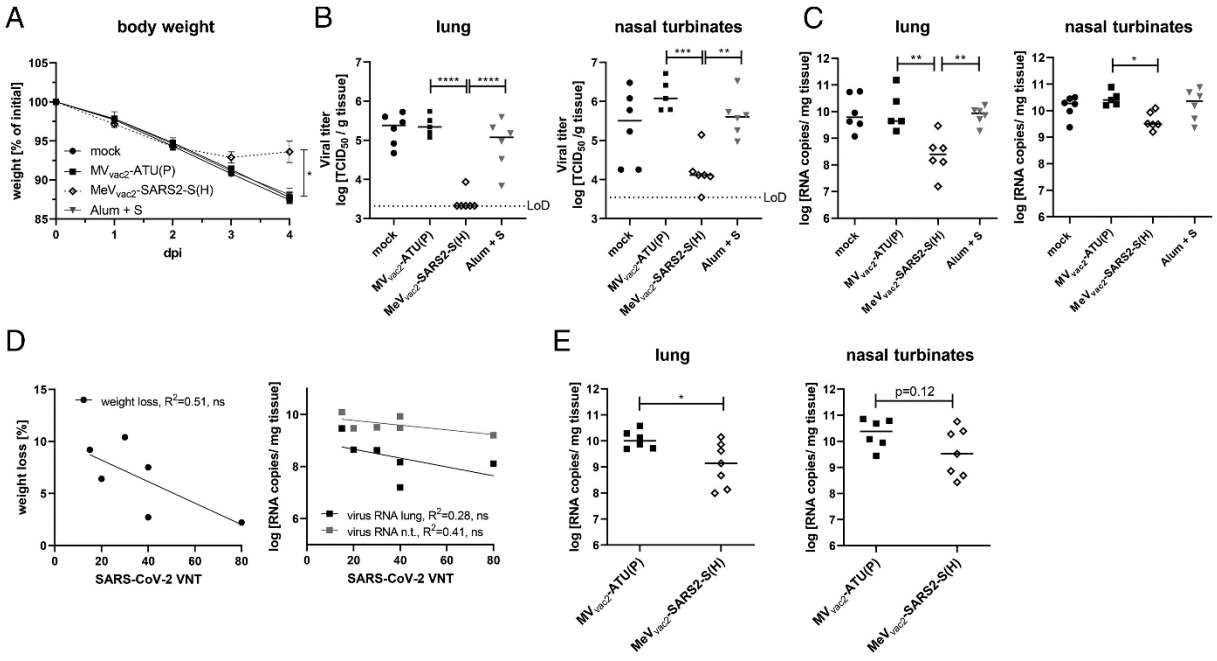

Fig. 7. Vaccine efficacy in Syrian hamster and mouse challenge models. Fully immunized Syrian golden hamsters (A–D) and IFNAR$^{-/-}$-CD46Ge mice (E) were intranasally challenged with SARS-CoV-2 or mouse-adapted SARS-CoV-2 MA, respectively, and protection was analyzed by quantifying weight loss (A), live virus titration in lungs or nasal turbinates (B), or SARS-2 E gene copy numbers via qRT-PCR (C and E). The limit of detection (LoD) is indicated. (D) For the correlation analysis comparing humoral immunity (VNT) of hamsters vaccinated with MeV$_{vac2}$-SARS2-S(H) on days 0 and 21 (sampled on day 35) and challenge outcome, linear regression was performed with the indicated challenge outcome parameters to determine Pearson correlation coefficient (R2). For statistical analysis of hamster data, one-way ANOVA was performed in combination with Tukey's multicomparison test to compare all pair means. For comparison of mouse data between the two groups, unpaired two-tailed t test was applied; ns, not significant; ($P > 0.05$); *$P < 0.05$; **$P < 0.01$; ***$P < 0.001$; ****$P < 0.0001$.

Our second animal model confirmed these observations. Virus loads of the mouse-adapted SARS-CoV-2 MA (13) were significantly reduced in the lungs of vaccinated mice (corresponding immunity data in SI Appendix, Fig. S13), and revealed a tendency for reduced titers in nasal turbinates, as well (Fig. 7E), in the absence of gross pathology in both groups. Therefore, both challenge models show protective efficacy of the immune responses induced by MeV$_{vac2}$-SARS2-S(H).

Discussion

In this study, we aimed to analyze the efficacy of MeV-derived vaccine candidates encoding the Spike glycoprotein S of SARS-CoV-2 to induce functional immune responses to protect against COVID-19. We show that MeV$_{vac2}$-SARS2-S(H) replicated comparably to MeV vaccine strain viruses and was genetically

stable over extended passaging. Upon vaccination of mice, it induced robust humoral immune responses of the IgG2a subtype directed against the SARS-CoV-2 spike glycoprotein S with neutralizing activity in a range already shown to be protective by others. In addition, considerable amounts of SARS-CoV-2 S-specific $CD4^+$ and $CD8^+$ T cells were induced, the major fraction of which were secreting two or even all three cytokines when analyzing for IFN-γ, TNF-α, or IL-2 upon antigen-specific restimulation. These T cells proliferated and specifically depleted antigen-positive target cells in a mixed population. Importantly, all responses were skewed toward Th1-biased immunity. In parallel, the capacity to induce measles-specific immune reactivity remained conserved. Finally, the induced immunity conferred protection in two different animal models of SARS-CoV-2 infection, Syrian golden hamsters inoculated with a low-passage patient isolate and mice challenged with a mouse-adapted recombinant SARS-CoV-2 MA.

This effective MeV Moraten strain-derived recombinant vaccine MeV_{vac2}-SARS2-S(H) is a live-attenuated vaccine that encodes the full-length, functional version of the SARS-CoV-2 S protein as the main target for functional antibodies, but also for induction of T cell responses. Vero cells revealed homogenous expression of the SARS-CoV-2 S antigen by Western blot analyses and positive immunostaining of syncytia after infection by MeV_{vac2}-SARS2-S(H). Stable antigen expression is a prerequisite for the immune system to encounter the specific antigen to mount robust immune responses and for industrial production of a vaccine. Indeed, $IFNAR^{-/-}$-CD46Ge mice vaccinated with MeV_{vac2}-SARS2-S(H) in a prime–boost protocol showed uniform induction of antibodies directed against MeV bulk antigens or SARS-CoV-2 S, which had considerable neutralizing activity against both pathogens. We observe antibody responses in these animals at a level that correlates with protection in mouse challenge models (14), as well as with neutralizing activity we found in the serum of four reconvalescent human patients. These responses were triggered despite the knockout of the type I IFN receptor, which is necessary to allow propagation of MeV in mice (10, 15). This knockout usually should impair the induction of especially humoral immune responses (16). This highlights the remarkable immunogenicity of the MeV vaccine platform technology that also works in this model with partially impaired immune responses.

However, why did not all immunized animals develop neutralizing activity detectable in our assay? Firstly, determination of the VNT relying on 100 % pathogen neutralization is obviously a rather harsh assay in the context of SARS-CoV-2, as evidenced by the modest VNT titers published so far, in general, and absence of VNT in the S+Alum vaccinated group despite high amounts of S-binding antibodies. This means that just detectable VNT already indicates considerable neutralizing activity. Indeed, when testing the sera of mice that were later on challenged with SARS-CoV-2 MA in parallel for VNT and $PRNT_{50}$ titers, two animals negative for VNT became positive in $PRNT_{50}$. Secondly, we realized that three of the four

animals which did not show a VNT of >10 did not respond well to the prime vaccination, at all. These animals developed no or only a minor VNT against MeV after the first vaccination. This observation is rather unusual, and argues for technical issues during the first vaccination in these animals. Since none of the animals showed VNT against SARS-CoV-2 after one vaccination with the vaccine, it is tempting to speculate that a prime–boost protocol is associated, in this animal model, with maturation of antibodies to generate better neutralizing responses. In hamsters, which fully responded to each vaccination, all six MeV_{vac2}-SARS2-S(H)–vaccinated animals developed VNT. On the other hand, all mice, including the three improperly immunized ones, revealed significant, multifunctional T cell responses against SARS-CoV-2 S, which were still recordable 3 wk after the second vaccination, when we already expect constriction of antigen-specific T cell effector populations. These data suggest that anti-S antibody responses mature after repeated vaccination, but, on the other hand, that a one-shot vaccination regime will already induce especially functional memory T cell immune responses, the protective efficacy of which, as well as their duration, has to be demonstrated in future challenge experiments. Moreover, anti-measles immunity is generally stable (17) also after pediatric vaccination (18) and might be a specific advantage of the measles vaccine platform technology, which could transfer also to the additionally encoded antigens.

Also, extended passaging of the vaccine candidate did not result in changes of the vaccine, as revealed by sequencing of the virus after 10 passages starting with a low multiplicity of infection (MOI). This genetic stability indicates that the slight impairment seen in multistep growth curves when compared to a vaccine-strain MeV is not critical for the vaccine's amplification and therefore crucial for product safety. In accordance with its genetic stability, the minor enhancement of fusion activity can also be regarded as noncritical, especially when considering the fusion activity of MeV used in clinical trials for treatment of tumors. These so-called oncolytic MeV have been used in 15 phase 1 and phase 2 clinical trials, so far. Thereby, advanced-stage tumor patients suffering from different tumor entities have been treated. Despite constituting, in principle, a vulnerable patient collective, application of high doses of nontargeted, fusion-active MeV (up to 1×10^{11} $TCID_{50}$) (19) systemically or, for example, directly into the patients' brains (20) was accompanied by an acceptable safety profile (21). Therefore, the enhancement of fusion activity cannot be expected to be crucial for product safety, while the attenuation of vaccine-strain MeV is multifactorial, anyway, and not just a matter of cell entry tropism and mechanism (22). Likewise, the clinical phase 1 and 2 trials using the MeV vector platform for the generation of bivalent vaccines, which induce immunity against Chikungunya virus (CHIKV) (23, 24), have revealed an extremely beneficial safety profile of this recombinant vaccine concept also in human patients, while signs of efficacy became evident.

In any case, generation of MeV-derived COVID-19 vaccines encoding a less fusion-active variant of the SARS-CoV-2 S glycoprotein might be beneficial to enhance titers of the vaccine virus. In the meantime, stabilized S variants have become available that have attenuated or no cell–cell fusion activity. One variant has a deletion of the multibasic cleavage motif for furin-like proteases at the S1/S2 boundary that facilitates preactivation of S (25). A second variant has proline substitutions at residues 986 and 987, which are stabilizing a prefusion conformation of S (26). Vaccine candidates encoding S with one of these motifs or a combination thereof in a soluble version, as already done for DNA vaccines (27), are under development. These have to show an at least comparable capacity to induce neutralizing antibody responses also in the context of MeV infection, which might be dependent on the respective conformation of the antigen that is expressed by vaccine virus-infected cells *in situ*.

The induction of the "right" antibodies and T cell responses is especially crucial when taking potential complications into consideration that can be observed when coronavirus encounters "wrong" immune responses that can give rise to immunopathologies after infection. In some infected cats, infection with feline coronavirus causes feline infectious peritonitis, a deadly disease characterized by viral infection of macrophages during the acute phase. Interestingly, the switch of pathology after infection from a rather moderate pathogenesis into an acute, devastating disease can be triggered by vaccination of persistently infected cats and has been attributed to the induction of antibodies that mediate enhancement of the disease, a process called ADE. During COVID-19, ADE might be the cause of the severe cases currently observed. Some case reports indicate that severe disease appeared more frequently in patients with high SARS-CoV-2 IgG levels (28). ADE has been most prominent for dengue virus (DENV) infections, especially in secondary infections with a different DENV serotype where enhancement of disease correlated with the induction of non-neutralizing Abs that can mediate an efficient uptake of the virus into FcR-positive cells such as macrophages and other immune cells (29). Moreover, other immune-related adverse events were described for SARS- and MERS-CoV. When animals were immunized with vaccines that predominantly induce Th2-biased T-helper cell responses, vaccinated mice revealed significantly reduced virus loads after challenge, but also an eosinophilic infiltrate into the lungs accompanied by pathological changes of the lung tissue, so-called ERD (30). Such immunopathologies upon CoV infection are a major concern for diseases pathology and, especially, vaccine development. Thus, Th2-biased immune responses as triggered by alum-adjuvanted whole inactivated virus particles or recombinant proteins should be avoided.

Interestingly, the live-attenuated MeV vaccine is known for a balanced Th1/Th2 bias of induced immune responses, with a bias for Th1 responses at least during the acute phase after vaccination (31). In theory, this should also apply for immune responses induced against all antigens presented during an MeV

vaccine virus infection including foreign antigen(s) additionally expressed when MeV is used as vaccine platform. Indeed, our analyses provide evidence that the bias of the immune responses is in favor of Th1 responses, as revealed by the inverted IgG1/IgG2a subtype ratio of antibodies induced against SARS-CoV-2 S by MeV_{vac2}-SARS2-S(H) compared to the animals immunized with alum-adjuvanted recombinant S protein. Moreover, the cytokine profile of splenocyte cultures of immunized mice after restimulation of S-specific T cells reveals a respective preferable Th1 bias. Since SARS-CoV-2 and SARS-CoV use the same primary attachment receptor for cell entry, hACE2, and selected hACE2-transgenic mice show differential pathology after inoculation with SARS-CoV-2 (14, 32), studying the impact of the Th1-biased MeV-based immunization in hACE2-transgenic mice during challenge with SARS-CoV-2 will be a matter for future studies. In any case, our challenge data also reveal that MeV-derived COVID-19 vaccines have a low likelihood to trigger immunopathogenesis, but we show considerable antiviral efficacy, especially in the Syrian hamster model. This animal model is susceptible for SARS-CoV-2 infection and suitable for vaccination using recombinant MeV (33); reveals in our setting a moderate to severe, clearly distinguishable pathology; and shows airborne transmissibility from infected to naïve animals. Therefore, this animal model accurately reflects at least some aspects of the course of human disease and reveals the potential of our candidate to vaccinate effectively against COVID-19.

In conclusion, the bivalent MeV/SARS-CoV-2 vaccine candidate has a number of desirable properties with respect to its immunogenicity and efficacy against SARS-CoV-2. Furthermore, the concurrent induction of anti-MeV immunity would allow its use in the context of routine measles immunization schedules. Such an MeV-based COVID-19 vaccine could be included in the currently applied MMR (measles, mumps, rubella) vaccine, providing additional protection against SARS-CoV-2. While there is controversy regarding to what extent it occurs, children do become infected and shed the virus, despite them rarely being severely affected. In any case, preventing or reducing infection or virus shedding from vaccinated children can also help to contain the disease and protect vulnerable patient groups. On the other hand, the vaccinated children themselves could be protected against newly described side effects of COVID-19 infections, such as Multisystem Inflammatory Syndrome, affecting also the cohort of (very) young patients (34). Thereby, the capacity to produce large amounts of vaccine doses as well as the respective distribution network would be available more or less instantly from routine measles vaccine production, but at no impairment of production of other necessary vaccines, since the measles vaccine property is preserved in the proposed vaccine candidate. Especially since vaccination against the measles should not be impaired also during the COVID-19 epidemic, this is a considerable advantage. Otherwise, parallel epidemics with another, even more contagious respiratory virus are looming when vaccination programs

against the measles are stopped in favor of COVID-19 vaccination programs. However, while we envision primarily pediatric application for this vaccine candidate, currently available data also suggest applicability of MeV-derived recombinant bivalent vaccines also in vaccinees with preformed anti-measles immunity. The performance of measles-derived recombinant vaccine targeting HIV-1 or CHIKV has been analyzed *in vivo* in respective models in measles-vaccinated animals. In both mice and nonhuman primates, at least antibodies against the secondary target pathogen were successfully induced also in preimmune animals (35, 36). This was reflected by the outcome of phase I and phase II clinical studies of an MeV-CHIKV vaccine candidate. Also, in human vaccinees, induction of significant anti-CHIKV antibody titers independent from the preimmunity seen in the respective individuals has been observed (23, 24). Future studies have to demonstrate that this is also the case for MeV-derived COVID-19 vaccine candidates. Taken together, MeV_{vac2}-SARS2-S(H) is a promising vaccine candidate that warrants further investigation.

Materials and Methods

Detailed descriptions of the materials, methods, and equipment used in this work, including cells, plasmids, production of lentiviral vectors and generation of antigen-expressing dendritic cell lines, viruses, MeV genome sequence analysis, NGS library preparation and sequencing, RNA sequence analysis, immunoperoxidase monolayer assay, Western blot analysis, animal experiments, total IgG and IgG1-/IgG2a quantification, Th1/Th2 cytokine multiplex assay, virus neutralization test, plaque reduction neutralization test, IFN-γ ELISpot analysis, ICS, T cell proliferation assay, CTL killing assay, virus titers in organs of infected animals, RNA preparation, quantitative RT-PCR, and statistical analyses, are provided in SI Appendix, Supplementary Extended Materials and Methods.

Data Availability

All data are provided in the manuscript and supporting information. The sequence data for the vaccine candidate described in this paper have been deposited in the GenBank Data Bank (MW090971).

Acknowledgments

This work was supported by the German Center for Infection Research (DZIF; TTU 01.805, TTU 01.922_00) and the German Ministry of Health (CHARIS). The authors would like to thank Daniela Müller and Carina Kruip for excellent technical assistance, Björn Becker for assistance in multiplex

analysis, Csabas Miskey for assistance with NGS, Christel Kamp for excellent advice on statistics, and Marcel Rommel for cell sorting. The authors are indebted to Gerhard Dobler for providing SARS-CoV-2 isolate MUC-IMB1, Maria Vehreschild for human patient reconvalescent serum, Kenneth Rock for DC2.4 cells, Roberto Cattaneo for providing the pBR(+)MVvac2 construct, and Urs Schneider for providing the PolII rescue system used to generate and to rescue recombinant MeV vectors. The authors would further like to thank Bakhos Tannous for providing pCSCW2gluc-IRES-GFP. The research reagent for SARS-CoV-2 RNA (NIBSC 19/304) was obtained from the National Institute for Biological Standards and control, UK. Moreover, the authors would like to thank Roberto Cattaneo and Veronika von Messling for valuable comments on the manuscript.

References

1. F. Wu, S. Zhao, B. Yu, Y.-M. Chen, W. Wang, Z.-G. Song, Y. Hu, Z.-W. Tao, J.-H. Tian, Y.-Y. Pei, M.-L. Yuan, Y.-L. Zhang, F.-H. Dai, Y. Liu, Q.-M. Wang, J.-J. Zheng, L. Xu, E. C. Holmes, Y.-Z. Zhang, A new coronavirus associated with human respiratory disease in China. Nature 579, 265–269 (2020).

2. Q. Li, X. Guan, P. Wu, X. Wang, L. Zhou, Y. Tong, R. Ren, K. S. M. Leung, E. H. Y. Lau, J. Y. Wong, X. Xing, N. Xiang, Y. Wu, C. Li, Q. Chen, D. Li, T. Liu, J. Zhao, M. Liu, W. Tu, C. Chen, L. Jin, R. Yang, Q. Wang, S. Zhou, R. Wang, H. Liu, Y. Luo, Y. Liu, G. Shao, H. Li, Z. Tao, Y. Yang, Z. Deng, B. Liu, Z. Ma, Y. Zhang, G. Shi, T. T. Y. Lam, J. T. Wu, G. F. Gao, B. J. Cowling, B. Yang, G. M. Leung, Z. Feng, Early Transmission Dynamics in Wuhan, China, of Novel Coronavirus-Infected Pneumonia. The New England journal of medicine 382, 1199–1207 (2020).

3. R. Li, S. Pei, B. Chen, Y. Song, T. Zhang, W. Yang, J. Shaman, Substantial undocumented infection facilitates the rapid dissemination of novel coronavirus (SARS-CoV-2). 10.5281/ZENODO.3699624 (2020).

4. M. D. Mühlebach, Vaccine platform recombinant measles virus. Virus genes 53, 733–740 (2017).

5. N. Escriou, B. Callendret, V. Lorin, C. Combredet, P. Marianneau, M. Février, F. Tangy, Protection from SARS coronavirus conferred by live measles vaccine expressing the spike glycoprotein. Virology 452-453, 32–41 (2014).

6. M. Liniger, A. Zuniga, A. Tamin, T. N. Azzouz-Morin, M. Knuchel, R. R. Marty, M. Wiegand, S. Weibel, D. Kelvin, P. A. Rota, H. Y. Naim, Induction of neutralising antibodies and cellular immune responses against SARS coronavirus by recombinant measles viruses. Vaccine 26, 2164–2174 (2008).

7. A. H. Malczyk, A. Kupke, S. Prüfer, V. A. Scheuplein, S. Hutzler, D. Kreuz, T. Beissert, S. Bauer, S. Hubich-Rau, C. Tondera, H. S. Eldin, J. Schmidt, J. Vergara-Alert, Y. Süzer, J. Seifried, K.-M. Hanschmann, U. Kalinke, S. Herold, U. Sahin, K. Cichutek, Z. Waibler, M. Eickmann, S. Becker, M. D. Mühlebach, A Highly Immunogenic and Protective Middle East Respiratory Syndrome Coronavirus Vaccine Based on a Recombinant Measles Virus Vaccine Platform. Journal of virology 89, 11654–11667 (2015).

8. B. S. Bodmer, A. H. Fiedler, J. R. H. Hanauer, S. Prüfer, M. D. Mühlebach, Live-attenuated bivalent measles virus-derived vaccines targeting Middle East respiratory syndrome coronavirus induce robust and multifunctional T cell responses against both viruses in an appropriate mouse model. Virology 521, 99–107 (2018).

9. S. Heidmeier, J. R. H. Hanauer, K. Friedrich, S. Prüfer, I. C. Schneider, C. J. Buchholz, K. Cichutek, M. D. Mühlebach, A single amino acid substitution in the measles virus F_2 protein reciprocally modulates membrane fusion activity in pathogenic and oncolytic strains (2014).

10. B. Mrkic, J. Pavlovic, T. Rülicke, P. Volpe, C. J. Buchholz, D. Hourcade, J. P. Atkinson, A. Aguzzi, R. Cattaneo, Measles Virus Spread and Pathogenesis in Genetically Modified Mice (1998).

11. P. Marrack, A. S. McKee, M. W. Munks, Towards an understanding of the adjuvant action of aluminium. Nature reviews. Immunology 9, 287–293 (2009).

12. P. He, Y. Zou, Z. Hu, Advances in aluminum hydroxide-based adjuvant research and its mechanism. Human vaccines & immunotherapeutics 11, 477–488 (2015).

13. K. H. Dinnon, S. R. Leist, A. Schäfer, C. E. Edwards, D. R. Martinez, S. A. Montgomery, A. West, B. L. Yount, Y. J. Hou, L. E. Adams, K. L. Gully, A. J. Brown, E. Huang, M. D. Bryant, I. C. Choong, J. S. Glenn, L. E. Gralinski, T. P. Sheahan, R. S. Baric, A mouse-adapted model of SARS-CoV-2 to test COVID-19 countermeasures. Nature. 10.1038/s41586-020-2708-8 (2020).

14. R.-D. Jiang, M.-Q. Liu, Y. Chen, C. Shan, Y.-W. Zhou, X.-R. Shen, Q. Li, L. Zhang, Y. Zhu, H.-R. Si, Q. Wang, J. Min, X. Wang, W. Zhang, B. Li, H.-J. Zhang, R. S. Baric, P. Zhou, X.-L. Yang, Z.-L. Shi, Pathogenesis of SARS-CoV-2 in Transgenic Mice Expressing Human Angiotensin-Converting Enzyme 2. Cell. 10.1016/j.cell.2020.05.027 (2020).

15. M. Mura, C. Ruffié, E. Billon-Denis, C. Combredet, J. N. Tournier, F. Tangy, hCD46 receptor is not required for measles vaccine Schwarz strain replication in vivo: Type-I IFN is the species barrier in mice. Virology 524, 151–159 (2018).

16. A. Le Bon, G. Schiavoni, G. D'Agostino, I. Gresser, F. Belardelli, D. F. Tough, Type I Interferons Potently Enhance Humoral Immunity and Can Promote Isotype Switching by Stimulating Dendritic Cells In Vivo (2001).

17. I. J. Amanna, N. E. Carlson, M. K. Slifka, Duration of Humoral Immunity to Common Viral and Vaccine Antigens (2007).

18. S. Carryn, M. Feyssaguet, M. Povey, E. Di Paolo, Long-term immunogenicity of measles, mumps and rubella-containing vaccines in healthy young children: A 10-year follow-up. Vaccine 37, 5323–5331 (2019).

19. S. J. Russell, M. J. Federspiel, K.-W. Peng, C. Tong, D. Dingli, W. G. Morice, V. Lowe, M. K. O'Connor, R. A. Kyle, N. Leung, F. K. Buadi, S. V. Rajkumar, M. A. Gertz, M. Q. Lacy, A. Dispenzieri, Remission of disseminated cancer after systemic oncolytic virotherapy. Mayo Clinic proceedings 89, 926–933 (2014).

20. P. Msaouel, M. Opyrchal, A. Dispenzieri, K. W. Peng, M. J. Federspiel, S. J. Russell, E. Galanis, Clinical Trials with Oncolytic Measles Virus: Current Status and Future Prospects. Current cancer drug targets 18, 177–187 (2018).

21. A. Dispenzieri, C. Tong, B. LaPlant, M. Q. Lacy, K. Laumann, D. Dingli, Y. Zhou, M. J. Federspiel, M. A. Gertz, S. Hayman, F. Buadi, M. O'Connor, V. J. Lowe, K.-W. Peng, S. J. Russell, Phase I trial of systemic administration of Edmonston strain of measles virus genetically engineered to express the sodium iodide symporter in patients with recurrent or refractory multiple myeloma. Leukemia 31, 2791–2798 (2017).

22. D. E. Griffin, W.-H. W. Lin, A. N. Nelson, Understanding the causes and consequences of measles virus persistence (2018).

23. K. Ramsauer, M. Schwameis, C. Firbas, M. Müllner, R. J. Putnak, S. J. Thomas, P. Desprès, E. Tauber, B. Jilma, F. Tangy, Immunogenicity, safety, and tolerability of a recombinant measles-virus-based chikungunya vaccine: a randomised, double-blind, placebo-controlled, active-comparator, first-in-man trial. The Lancet Infectious Diseases 15, 519–527 (2015).

24. E. C. Reisinger, R. Tschismarov, E. Beubler, U. Wiedermann, C. Firbas, M. Loebermann, A. Pfeiffner, M. Muellner, E. Tauber, K. Ramsauer, Immunogenicity, Safety, and Tolerability of the Measles-Vectored Chikungunya Virus Vaccine MV-CHIK: A Double-Blind, Randomised, Placebo-Controlled and Active-Controlled Phase 2 Trial (2019).

25. M. Hoffmann, H. Kleine-Weber, S. Schroeder, N. Krüger, T. Herrler, S. Erichsen, T. S. Schiergens, G. Herrler, N.-H. Wu, A. Nitsche, M. A. Müller, C. Drosten, S. Pöhlmann, SARS-CoV-2 Cell Entry Depends on ACE2 and TMPRSS2 and Is Blocked by a Clinically Proven Protease Inhibitor. Cell 181, 271-280.e8 (2020).

26. D. Wrapp, Wang, Nianshuang, Corbett, Kizzmekia S., J. A. Goldsmith, C.-L. Hsieh, O. Abiona, B. S. Graham, J. S. McLellan, Cryo-EM structure of the 2019-nCoV spike in the prefusion conformation 60 (2020).

27. J. Yu, L. H. Tostanoski, L. Peter, N. B. Mercado, K. McMahan, S. H. Mahrokhian, J. P. Nkolola, J. Liu, Z. Li, A. Chandrashekar, D. R. Martinez, C. Loos, C. Atyeo, S. Fischinger, J. S. Burke, M. D. Slein, Y. Chen, A. Zuiani, F. J. N Lelis, M. Travers, S. Habibi, L. Pessaint, A. van Ry, K. Blade, R. Brown, A. Cook, B. Finneyfrock, A. Dodson, E. Teow, J. Velasco, R. Zahn, F. Wegmann, E. A. Bondzie, G. Dagotto, M. S. Gebre, X. He, C. Jacob-Dolan, M. Kirilova, N. Kordana, Z. Lin, L. F. Maxfield, F. Nampanya, R. Nityanandam, J. D. Ventura, H. Wan, Y. Cai, B. Chen, A. G. Schmidt, D. R. Wesemann, R. S. Baric, G. Alter, H. Andersen, M. G. Lewis, D. H. Barouch, DNA vaccine protection against SARS-CoV-2 in rhesus macaques. Science (New York, N.Y.). 10.1126/science.abc6284 (2020).

28. N. M. A. Okba, M. A. Müller, W. Li, C. Wang, C. H. GeurtsvanKessel, V. M. Corman, M. M. Lamers, R. S. Sikkema, E. de Bruin, F. D. Chandler, Y. Yazdanpanah, Q. Le Hingrat, D. Descamps, N. Houhou-Fidouh, C. B. E. M. Reusken, B.-J. Bosch, C. Drosten, M. P. G. Koopmans, B. L. Haagmans, Severe Acute Respiratory Syndrome Coronavirus 2-Specific Antibody Responses in Coronavirus Disease Patients. Emerging infectious diseases 26, 1478–1488 (2020).

29. F. A. Rey, K. Stiasny, M.-C. Vaney, M. Dellarole, F. X. Heinz, The bright and the dark side of human antibody responses to flaviviruses: lessons for vaccine design. EMBO reports 19, 206–224 (2018).

30. L. Liu, Q. Wei, Q. Lin, J. Fang, H. Wang, H. Kwok, H. Tang, K. Nishiura, J. Peng, Z. Tan, T. Wu, K.-W. Cheung, K.-H. Chan, X. Alvarez, C. Qin, A. Lackner, S. Perlman, K.-Y. Yuen, Z. Chen, Anti-spike IgG causes severe acute lung injury by skewing macrophage responses during acute SARS-CoV infection. JCI insight 4 (2019).

31. D. Naniche, Human immunology of measles virus infection. Curr Top Microbiol Immunol. (2009).

32. L. Bao, W. Deng, B. Huang, H. Gao, J. Liu, L. Ren, Q. Wei, P. Yu, Y. Xu, F. Qi, Y. Qu, F. Li, Q. Lv, W. Wang, J. Xue, S. Gong, M. Liu, G. Wang, S. Wang, Z. Song, L. Zhao, P. Liu, L. Zhao, F. Ye, H. Wang, W. Zhou, N. Zhu, W. Zhen, H. Yu, X. Zhang, L. Guo, L. Chen, C. Wang, Y. Wang, X. Wang, Y. Xiao, Q. Sun,

H. Liu, F. Zhu, C. Ma, L. Yan, M. Yang, J. Han, W. Xu, W. Tan, X. Peng, Q. Jin, G. Wu, C. Qin, The pathogenicity of SARS-CoV-2 in hACE2 transgenic mice. Nature. 10.1038/s41586-020-2312-y (2020).

33. M. Yoneda, M.-C. Georges-Courbot, F. Ikeda, M. Ishii, N. Nagata, F. Jacquot, H. Raoul, H. Sato, C. Kai, Recombinant measles virus vaccine expressing the Nipah virus glycoprotein protects against lethal Nipah virus challenge. PloS one 8, e58414 (2013).

34. C. Lorin, L. Mollet, F. Delebecque, C. Combredet, B. Hurtrel, P. Charneau, M. Brahic, F. Tangy, A single injection of recombinant measles virus vaccines expressing human immunodeficiency virus (HIV) type 1 clade B envelope glycoproteins induces neutralizing antibodies and cellular immune responses to HIV. Journal of virology 78, 146–157 (2004).

35. S. Brandler, C. Ruffié, C. Combredet, J.-B. Brault, V. Najburg, M.-C. Prevost, A. Habel, E. Tauber, P. Desprès, F. Tangy, A recombinant measles vaccine expressing chikungunya virus-like particles is strongly immunogenic and protects mice from lethal challenge with chikungunya virus. Vaccine 31, 3718–3725 (2013).

Supplementary Extended Materials and Methods

Cells

Vero (African green monkey kidney) (ATCC# CCL-81), Vero clone E6 (ATCC# CRL-1586), 293T (ATCC CRL-3216) and EL-4 (ATCC TIB-39) cell lines were purchased from ATCC (Manassas, VA, USA) and cultured in Dulbecco's modified Eagle's medium (DMEM, Biowest, Nuaillé, France) supplemented with 10 % fetal bovine serum (FBS; Biochrom, Berlin, Germany) and 2 mM L-glutamine (L-Gln; Biochrom). JAWSII mouse dendritic cells (ATCC CRL-11904) were also purchased from ATCC and cultured in MEM-α (GIBCO BRL, Eggenstein, Germany) supplemented with 20 % FBS, 2 mM L-Gln, 1 mM sodium pyruvate (Biochrom), and 5 ng/ml murine GM-CSF (Biotechne, Wiesbaden, Germany). DC2.4 mouse dendritic cells (1) were cultured in RPMI containing 10 % FBS, 2 mM L-Gln, 1 % non-essential amino acids (Biochrom), 10 mM HEPES (pH 7,4), and 50 µM 2-mercaptoethanol (Sigma-Aldrich, Steinheim, Germany). All cells were cultured at 37 °C in a humidified atmosphere containing 6 % CO2 for a maximum of 6 months of culture after thawing of the original stock.

Plasmids

The codon-optimized gene encoding full-length SARS-CoV-2 Spike glycoprotein S of isolate Wuhan-Hu-1 (Genebank accession no. MN908947.1) in plasmids pMA-RQ-SARS2-S flanked with AatII/MluI and NheI/XhoI restriction sites was obtained by gene synthesis (Invitrogen Life Technology, Regensburg,

Germany). The antigen was inserted into plasmids pBRPolIIΔ-MVvac2-GFP(P) or pBRPolIIΔMVvac2-GFP(H) via MluI/AatII to generate pBRPolII-MVvac2-SARS2-S(P) or pBRPolII-MVvac2-SARS2-S(H). pBRPolIIΔ-MVvac2-GFP(P) or pBRPolIIΔ-MVvac2-GFP(H) were generated by inserting the immediate early CMV promoter sequence from p(+)PolII-MVNSe-GFP(N) (2), which had been modified by site-directed mutagenesis for deleting the AatII restriction sites, into pBR-MVvac2-GFP(P) or pBR-MVvac2-GFP(H) (3). For construction of a lentiviral transfer vector encoding SARS-CoV-2 S directly linked to the *egfp* gene as selection marker, the ORF of SARS-CoV-2 S was inserted via NheI/XhoI into pCSCW2gluc-IRES-GFP (4) to yield pCSCW2-SARS2-S-IRES-GFP. For construction of a eukaryotic expression plasmid encoding SARS-CoV-2 S, the ORF of SARS-CoV-2 S was inserted via NheI/XhoI into pcDNA3.1(+) (Invitrogen Life Technology) to yield pcDNA3.1-SARS2-S.

Production of lentiviral vectors and generation of antigen-expressing dendritic cell lines

Lentiviral vectors were produced and used for the generation of antigen-expressing dendritic cell lines as described before (3). In short, HIV-1-derived particles pseudotyped with VSV-G were generated using a standard three plasmid system, pMD2.G, pCMVΔR8.9 (5) with the transfer vector plasmid pCSCW2-SARS2-S-IRES-GFP in combination with PEI transfection of 293T cells (6). Subsequent purification by filtration and ultracentrifugation of supernatants yielded virus stocks were used to transduce murine DC cell lines, DC2.4 and JAWSII, as well as the murine T cell line EL-4, resulting in DC2.4-SARS2-S, JAWSII-SARS2-S, and EL-4_{green}-SARS2-S, respectively, that express the SARS-CoV-2 S protein and GFP and present the respective peptides via MHC-I. Transduced cultures with 1-10 % GFP-positive cells were single cell-sorted (BD FACS AriaTM Fusion) for GFP-expressing cells and subsequently characterized for antigen expression. For JAWSII-SARS2-S, the bulk-sorted cells were used in stimulation experiments. For DC2.4-SARS2-S and EL-4_{green}-SARS2-S, clonal cell lines were generated by limiting dilution of bulk-sorted cells and characterized for marker- and antigen-expression.

Viruses

SARS-CoV-2 S-encoding vaccine candidates MeV_{vac2}-SARS2-S(P) or MeV_{vac2}-SARS2-S(H) were generated as described previously (3, 7). Single syncytia were picked and overlaid onto 50 % confluent Vero cells cultured in 6-well plates and harvested as "passage 0" (P0) by scraping and freeze-thaw cycle of cells at the time of maximal infection. Subsequent passages were generated after $TCID_{50}$ titration of infectious virus according to the method of Kaerber and Spaerman (8). Stocks were generated by infection of Vero cells at an MOI = 0.03, and passage 2 (P2) or P3 were used for *in vitro* characterization, while vaccine viruses in P3 or P4 were used for vaccination experiments. Vector control virus MV_{vac2}-ATU(P) (9) was used in P5 for vaccination. SARS-CoV-2 (isolate MUC-IMB1) (kind gift of G. Dobler, Bundeswehr Institute

for Microbiology, Germany) (10) was used for SARS-CoV-2 neutralization assays and hamster challenge. It was propagated on Vero E6 cells and was titrated via $TCID_{50}$ as described above for recombinant MeV. All virus stocks were stored in aliquots at -80 °C.

Multistep viral growth kinetics were analyzed by infecting Vero cells at an MOI of 0.03 in 96-well plates and incubated at 37 °C. At various time points, supernatants were clarified by centrifugation, and cells were scraped into OptiMEM and subjected to freeze-thaw cycles. Released and cell-associated viral titers were determined by $TCID_{50}$ limited dilution method.

Measles virus genome sequence analysis

The RNA genomes of recombinant MeV in P2 or P10 were isolated from infected Vero cells using the QIAamp Viral RNA Mini Kit (QIAgen, Hilden, Germany) according to the manufacturer's instructions and resuspended in 50 µL RNase-free water. Viral cDNA was reversely transcribed using Superscript II RT kit (Invitrogen) with 2 µL viral RNA as template and random hexamer primers, according to manufacturer´s instructions. For specific amplification of the SARS-CoV-2 S ORF, the respective genomic regions of recombinant MeV were amplified by PCR using primers binding to sequences flanking the regions of interest and the cDNA as template. Detailed description of primers and procedures are available upon request. The PCR products were directly sequenced (Eurofins Genomics, Ebersberg, Germany).

NGS library preparation and sequencing

Total RNA was isolated from Vero cells after 4 days post infection using the Direct-zol RNA isolation kit (Zymo Research). 1 µg of RNA isolate was subjected to rRNA removal with the NEBNext rRNA Depletion Kit (NEB) using the manufacturer's recommendations. The whole 10 µL of the RNA elute was used for reverse transcription with Superscript III (Invitrogen) using the recommended reaction supplemented with 0.5 µL of RiboLock RNase Inhibitor (Thermo Scientific) and 100 pmol of NNSR-RT primer with the following protocol: 45 °C 30 min; 70 °C, 15 min. The cDNA was bead-purified with 1.8 volume of SPRI Beads (Beckman Coulter), eluted in 27 µL of water and subjected to RNase-H (NEB) digestion at 37 °C for 30 min followed by heat inactivation. After bead purification the 20 µL cDNA elute was used for 2nd strand synthesis in a 50 µL reaction containing: 1x NEB Buffer 2, 25 nmol dNTP, 5 U of exo(-) Klenow Fragment (NEB), 200 pmol of NNSR-2 Primer for 30 min at 37 °C. After bead purification half of the DNA elute was used for a 50 µL PCR reaction containing the NEBNext High-Fidelity 2x Master Mix (NEB), 25 pmol, each, of NNSR-Illumina and NNSR-nest-ind primers with the following cycling conditions: 98 °C 10 sec; 5 cycles of 98 °C 10 sec, 55 °C 30 sec, 72 °C 30 sec; 20 cycles of 98 °C 10 sec, 65 °C 30 sec, 72 °C 30 sec; 72 °C 5 min. 15 µL of the PCR reaction was separated on a 1 % agarose gel and the smear of 500-

700 bp was isolated. The indexed libraries were quantified by qPCR using the NEBNext Library Quant Kit for Illumia (NEB, mixed and sequenced on a MiSeq instrument (Illumina)) with a 2x250 paired-end setup.

RNA sequencing analysis

Quality trimming and adapter removal were performed using fastp (v0.20.0 (11)). Read 1 and 2 adapter recognition sequences were provided for adapter removal (Illumina TruSeq Adapter Read 1: AGATCGGAAGAGCACACGTCTGAACTCCAGTCACNNNNNNATCTCGTATGCCGTCTTCTGCTTG, Illumina TruSeq Adapter Read 2: AGATCGGAAGAGCGTCGTGTAGGGAAAGAGTGT; NNNNNN: sample-specific index) and the leading two nucleotides were removed from each read (--trim_front1 2 --trim_front2 2). For quality trimming, bases in sliding windows with a mean quality below 30 (-5 -3 --cut_mean_quality 30) were discarded on both sides of the reads. Base correction in overlapping regions (-c) was applied. Reads with Ns and a length below-< 30 bp after trimming (-n 0 -l 30) were discarded.

Mapping was performed with BWA mem v 0.7.12-r1039 (12), using default parameters unless stated otherwise. Host-derived reads were removed by mapping quality controlled reads against the African green monkey genome (Chlorocebus sabeus, RefSeq assembly GCA_000409795.2), specifying the minimum seed length (-k 31). Unmapped reads were extracted using samtools v1.7 (13) and bamToFastq v2.17.0 (14), and subsequently mapped to the plasmid reference genomes of either MeV_{vac2}-SARS2-S(H) or MeV_{vac2}-SARS2-S(P), as appropriate. Host-free alignments were deduplicated using picard-tools MarkDuplicates (http://broadinstitute.github.io/picard) and left-aligned using GATK LeftAlignIndels v4.0 (15).

Sample majority consensus sequences were obtained by substituting minor frequency variants in the respective virus reference sequence for alternative variants with allele frequencies > 50 %. Variant calling was performed with LoFreq v2.1.3 (16) using default parameters.

Immunoperoxidase monolayer assay (IPMA)

For immunoperoxidase monolayer assay, Vero cells cultured in flat-bottom 12-well plates were fixed overnight with methanol at −20 °C two days after infection with a MOI of 0.01. The fixed cells were then washed three times with 1 mL PBS and subsequently blocked with PBS containing 2 % bovine serum albumin (BSA) (Roth, Karlsruhe, Germany) for 30 min at 37 °C. The cells were then probed for 1 h with a polyclonal rabbit anti-SARS-CoV-2-S protein antibody (1:2,250; ab252690; Abcam, Cambridge, UK) or a rabbit anti-MeV N protein antibody (1:1,000, ab23974, Abcam) in PBS with 2 % BSA. The cells were washed 3 times with 1 mL PBS and subsequently incubated with the secondary HRP-coupled donkey anti-rabbit IgG(H+L) polyclonal antibody (1:1,000; 611-7202; Rockland, Gilbertsville, USA) for 1 h at 37 °C.

Then, the cells were washed 3 times, again. For detection, the cells were stained with TrueBlue peroxidase substrate solution (SeraCare, Milford, USA).

Western Blot Analysis

Cells were lysed and immunoblotted as previously described (17). Rabbit anti-SARS-S protein antibody (1:3,000; ab252690; Abcam), rabbit anti-MeV-N protein polyclonal antibody (1:5,000; ab23974; Abcam), and a mouse anti-ß-actin antibody (1:5,000; ab6276; Abcam) were used. Donkey anti-rabbit IgG-HRP (H&L) polyclonal antibody (1:10,000; 611-7202; Rockland) and goat anti-mouse IgG-HRP (1:10,000; A2554-1ML; Merck, Darmstadt, Germany) served as secondary antibodies. Peroxidase activity was visualized with an enhanced chemiluminescence detection kit (Thermo Scientific, Bremen, Germany) on ChemiDoc MP Imaging System (Biorad, Dreieich, Germany).

Animal experiments

All animal experiments were carried out in compliance with the regulations of German animal protection laws and as authorized by the RP Darmstadt in consideration of the ARRIVE guidelines. Six- to 12-week-old old, treatment-naïve IFNAR$^{-/-}$-CD46Ge mice (18) that are deficient for type I IFN receptor and transgenically express human CD46 were bred in-house under SPF conditions and regularly controlled by animal care takers and institutional veterinarians for general signs of well-being, and animal weight was additionally controlled once a week during the experiments. For the experiments, animals were randomized for age- and sex-matched groups and housed in IVC cages in groups of 3 to 5 animals with nist packs as environmental enrichment at room temperature with regular 12 h day and night intervalls. Group sizes were calculated based on statistical considerations to yield sufficient statistical power as authorized by the respective competent authority. These animals were inoculated intraperitoneally (i.p.) with 1x10^5 $TCID_{50}$ of recombinant vaccine viruses in 200 µL volume, or subcutaneously (s.c.) with 10 µg recombinant SARS-CoV-2 S protein (Sino Biological Europe, Eschborn, Germany) adjuvanted with 500 µg aluminum hydroxide (Alhydrogel adjuvant 2 %, vac-alu-250, InvivoGen, San Diego, CA, USA) in 100 µL volume on days 0 and 28. 200 µL blood was collected on days 0, and 28, while final serum was collected on day 49 post initial immunization (p.i.). serum samples were stored at -20 °C. Mice were euthanized on day 49 p.i., and splenocytes were harvested for assessment of cellular immune responses.

For challenge experiments, 6 – 12 week old Syrian golden hamsters (Envigo RMS, Venray, Netherlands) or IFNAR$^{-/-}$-CD46Ge mice were vaccinated on days 0 and 21 as described above, but using a weight-adapted dose of 5×10^5 $TCID_{50}$ vaccine virus or 10 µg recombinant SARS-CoV-2 S protein adjuvanted with 500 µg aluminum hydroxide for the hamsters. Blood was drawn on days 0, 21 and at the day of challenge. Hamsters were challenged on day 35 applying i.n. a dose of 4×10^3 $TCID_{50}$ SARS-CoV-2 (isolate MUC-IMB1)

in passage 1 in 100 µL volume. Mice were challenged on day 37 applying i.n. a dose of 1×10^5 $TCID_{50}$ SARS-CoV-2 MA (19) in passage 2 in 30 µL volume.

Total IgG and IgG1-/IgG2a quantification

MeV bulk antigens (10 µg/mL; Virion Serion, Würzburg) or recombinant SARS-CoV-2 S protein (5 µg/mL) were coated in 50 µL carbonate buffer (Na_2CO_3 30 mM; $NaHCO_3$ 70 mM; pH 9.6) per well on Nunc Maxisorp® 96 well ELISA plates (ebioscience) and incubated overnight at 4 °C. The plates were washed three times with 200 µL ELISA washing buffer (PBS, 0.1 % Tween 20 (w/v)) and blocked with 100 µL Blocking buffer (PBS; 5 % BSA; 0.1 % Tween 20) for at least 2 h at room temperature. Mouse sera were 5-fold serially diluted in ELISA dilution buffer (PBS, 1 % BSA, 0.1 % Tween 20), and 50 µL/well were used for the assay. The plates were incubated at 37 °C for 2 h and washed three times with ELISA washing buffer, followed by incubation with 50 µL/well of HRP-conjugated rabbit anti-mouse total IgG (1:1,000 in ELISA dilution buffer; P0260, Dako Agilent, Santa Clara, CA, USA), goat-anti-mouse IgG1 (1:8,000 in ELISA dilution buffer; ab97240, Abcam, Cambridge, UK), or goat-anti-mouse IgG2a (1:8,000 in ELISA dilution buffer; ab97245, Abcam) at room temperature for 1 h. Subsequently, the plates were washed four times and 100 µL TMB substrate (ebioscience) was added per well. The reaction was stopped by addition of 50 µL/well H2SO4 (1 N) and the absorbance at 450 nm (specific signal) and 630 nm (reference wavelength) was measured.

Th1/Th2 cytokine multiplex assay

Quantification of Th1/Th2 cytokines in supernatant of splenocytes was performed using mouse high sensitivity T cell magnetic bead panel assay (MHSTCMAG-70K, Merck, Darmstadt, Germany). 5×10^5 isolated splenocytes were co-cultured with different stimuli in 200 µL RPMI + 10 % FBS, 2 mM L-Gln, and 1 % penicillin-streptomycin for 36 h. For re-stimulation of SARS-CoV-2 S protein-specific T cells, splenocytes were co-cultivated with 5×10^4 DC2.4 dendritic cells, the corresponding cell line transgenically expressing SARS-CoV-2 S protein or medium alone. After 36 h, cells were spun down and supernatants were collected and stored at -20 °C until assayed. For multiplex assay, cytokines were coupled over night to magnetic beads coated with capture antibodies, labeled with biotinylated detection antibody and incubated with Streptavidin-PE conjugate. Fluorescence was measured using MAGPIX with xPONENT software (Luminex Instruments, Thermo Scientific, Bremen, Germany).

Virus neutralization test (VNT)

Virus neutralizing titers (VNT) were quantified as described previously (3). Towards this, sera were serially diluted in 2-fold dilution steps in DMEM in duplicates. A total of 50 PFU of MV_{vac2}-GFP(P) or 100 $TCID_{50}$ of SARS-CoV-2 (isolate MUC-IMB1) were mixed with diluted sera and incubated at 37 °C for

1 h. MeV or SARS-CoV-2 virus-serum suspensions were added to 1×10^4 Vero or Vero E6 cells, respectively, seeded 4 h prior to the assay in 96-well plates and incubated for 4 days at 37 °C. VNTs were calculated as the reciprocal of the highest mean dilution that abolished infection.

Plaque reduction neutralization test ($PRNT_{50}$)

Plaque reduction neutralizing titers ($PRNT_{50}$) were determined as follows: Triplicates of sera were 2-fold serially diluted in DMEM, and 50 µL DMEM containing 100 $TCID_{50}$ SARS-CoV-2 was added per well and incubated at 37 °C for 1 h. Then, the virus-serum mixture was added to 8×10^5 Vero cells seeded in a 6-well plates 24 h before and incubated for 1 h at 37 °C while rocking plates every 15 min. After removal of the inoculum, cells were overlaid with 1.5 % Avicel RC-591NF (FMC BioPolymer, Co. Cork, Ireland) in 2 ml complete DMEM. For assay readout 3 days after infection, cells were fixed with 4 % formalin in PBS and stained with 0.1 % crystal violet. $PRNT_{50}$ was determined as the reciprocal dilution leading to at least 50 % reduction in plaque numbers relative to the mean of serum dilutions of mock mice.

IFN-γ ELISpot Analysis

Murine interferon gamma (IFN-γ) enzyme-linked immunosorbent spot (ELISpot) assays were performed using the Mouse IFN-γ ELISPOT Pair kit including capture and detection antibody (BD Bioscience, Franklin Lakes, NJ, USA) and HRP Streptavidin (BD Bioscience) for ELISpot detection in combination with multiscreen immunoprecipitation (IP) ELISpot polyvinylidene difluoride (PVDF) 96-well plates (Merck Millipore, Darmstadt, Germany) according to the manufacturer's instructions. 5×10^5 isolated splenocytes were co-cultured with different stimuli in 200 µL RPMI + 10 % FBS, 2 mM L-Gln, and 1 % penicillin-streptomycin for 36 h. For re-stimulation of SARS-CoV-2 S protein-specific T cells, splenocytes were co-cultivated with 5×10^4 JAWSII, DC2.4 dendritic cells, or the corresponding cell lines transgenically expressing SARS-CoV-2 S protein. In parallel, splenocytes were stimulated with 10 µg/mL MeV bulk antigen (Virion Serion). For general T cell stimulation, 10 µg/mL concanavalin A (ConA, Sigma-Aldrich) was used, and as negative control, splenocytes were left untreated. After 36 h, cells were spun down, supernatants were removed, and cells were lysed in the wells by hypotonic shock. Plates were incubated with biotin-conjugated anti-IFN-γ detection antibodies and streptavidin-HRP according to the manufacturer's instructions. 3-Amino-9-ethyl-carbazole (AEC; Sigma-Aldrich) was dissolved in N,N-dimethylformamide (Merck Millipore) and used for peroxidase-dependent staining. Spots were counted using an Eli.Scan ELISpot scanner (AE.L.VIS, Hamburg, Germany) and ELISpot analysis software Eli.Analyse V5.0 (AE.L.VIS).

Intracellular cytokine staining

For flow cytometry-based analysis of cytokine expression by intracellular cytokine staining (ICS), splenocytes of vaccinated mice were isolated, and 2×10^6 splenocytes per mouse were cultivated in 200 µL RPMI1640 + 10 % FBS, 2 mM L-Gln, 1× non-essential amino acids (Biochrom), 10 mM HEPES, 1 % penicillin-streptomycin, 50 µM β-mercaptoethanol, 10 µg/mL brefeldin A (Sigma-Aldrich) with DC2.4-SARS2-S cells as used for ELISpot analysis. For general T cell stimulation, 0.25 µg/mL tetradecanoylphorbol acetate (TPA, Sigma Aldrich) and 0.5 µg/mL ionomycin (Iono, Sigma-Aldrich) were used as positive control, and medium alone served as negative control. Splenocytes were stimulated for 5 h at 37 °C. Subsequently, cells were stained with fixable viability dye eFluor450 (eBioscience), α-CD4-PE (1:2,000; Cat.-No. 553049 BD, Franklin Lakes, NJ, USA), α-CD8-FITC (1:500; Cat.-No. 553031, BD), and α-CD3-PerCPCy5.5 (1:500; Cat.-No. 550763, BD). Subsequent to permeabilization with Fixation/Permeabilization Solution (BD) and Perm/Wash Buffer (BD), cells were stained with α-IFN-γ-APC (1:500; Cat.-No. 554413, BD), α-IL-2-AlexaFluor700 (1:200; Cat.-No. 503818, Biolegend, San Diego, USA) and α-TNF-α-Pe-Cy7 (1:500; Cat.-No. 557644, BD). Cells were fixed with ice-cold 1 % paraformaldehyde (PFA) in PBS and analyzed via flow cytometry using an LSRII SORP flow cytometer (BD) and DIVA software (BD).

T cell proliferation assay

Splenocytes isolated three weeks after the second immunization were labeled with 0.5 µM carboxyfluorescein-succinimidyl-ester (CFSE) (ebioscience, Life Technologies, Carlsbad, CA, USA) as previously described (20). In brief, 5×10^5 labelled cells were seeded in RPMI 1640 supplemented with 10 % mouse serum, 2 mM L-Glutamine, 10 mM HEPES, 1 % penicillin/streptomycin, and 100 µM 2-mercaptoethanol in 96-wells. 200 µL Medium containing 10 µg/ml Concanavalin A (Con A, Sigma-Aldrich), 10 µg/mL MeV bulk antigen (Virion Serion), or 5×10^3 DC2.4-SARS2-S cells were added to each well, and cultured for 6 d. Medium and wild type DC2.4 and JAWSII cells served as controls. Stimulated cells were subsequently stained with α-CD3-PacBlue (1:50; clone 500A2; Invitrogen Life Technologies), α-CD8-APC (1:100; clone 53-6.7; ebioscience) and α-CD4-PE (1:2000; Cat. 553049; BD) antibodies and fixed with 1 % PFA in PBS. Finally, the stained cells were analyzed by flow cytometry using an LSR II flow cytometer (BD) and FCS Express software (De Novo Software).

CTL killing assay

For re-stimulation of T cells isolated 3 weeks after the second immunization, 5×10^6 splenocytes were co-cultured with 5×10^4 DC2.4-SARS2-S cells for 6 days in 12-wells in RPMI 1640 supplemented with 10 % FBS, 2 nM L-Glutamin, 1 mM HEPES, 1 % penicillin/streptomycin, 100 µM 2-mercaptoethanol, and 100

U/ml murine rIL-2 (Peprotech, Hamburg, Germany). 5×10^3 EL-4_{red} cells were labeled with 0.5 µM CFSE and mixed with 5×10^3 EL-4_{green}-SARS2-S cells per well. Splenocytes were counted and co-cultured with EL-4 target cells at the indicated ratios for 4 h at 37 °C. Afterwards, EL-4 cells were labeled with Fixable Viability Dye eFluor® 780 (ebioscience), fixed with 1 % paraformaldehyde (PFA), and analyzed by flow cytometry using an LSR II flow cytometer (BD) and FCS Express. For indication of Antigen:NC EL-4 ratio the cell count of viable SARS-CoV-2 S-expressing cells was divided by the population of viable negative controls.

Determination of virus titers in organs of infected animals

Organs were snap-frozen in liquid nitrogen and were subsequently homogenized in 1 ml cold Titration Medium (Hanks' Balanced Salt solution containing 10 % glycerol, 5 mg/mL lactalbumin, 304 µg/mL Penicilin, 500 µg/mL Streptomycin, 250 µg/mL Gentamicin, 50 U/mL Nystatin) using Lysing Matrix M tubes (MP Bio) and the TissueLyser LT (QIAGEN) for 2x 1 min at 50 Hz and were kept on ice before, between and after homogenization. Vero E6 cells were inoculated with 10-fold serially diluted organ homogenates and cultivated for 4 d at 37 °C. The SARS-CoV-2 organ titer was calculated by the $TCID_{50}$ method of Kaerber and Spearman according to the virus-induced CPE and normalized to 1 g of homogenized tissue.

RNA preparation

For purification of viral RNA from hamster or mouse tissue, 25 mg frozen nasal turbinates or 90 mg of lung tissue were homogenized in 1 mL TRIzol Reagent (Ambion, Thermo Fisher Scientific) in Lysing Matrix M tubes (MP Bioscience, Hilton, UK) using the TissueLyser LT (QIAGEN) for 1x 1 min and 1x 2 min at 50 Hz while keeping samples on ice before, between and after homogenization. To remove organ debris, homogenates were centrifuged (10 min, 6,800 rpm, 4 °C) and the supernatant was subsequently used for RNA purification with the Direct-zol RNA MiniPrep kit (Zymo research, Freiburg (Breisgau), Germany) according to manufacturers instructions and RNA was eluted in 50 µL RNAse-free water.

Determination of virus genome copy numbers by qRT-PCR

SARS-CoV-2 or SARS-CoV-2 MA RNA, was quantified via multiplex quantitative reverse transcription-PCR (qRT-PCR) using Superscript III one step RT-PCR system with Platinum Tag Polymerase (Invitrogen, Darmstadt, Germany). Primer and probe sequences for the E gene were used as described (21). Reactions were performed in 96-wells with 5 µL of RNA in a total volume of 25 µL run in triplicates on a CFX 96 qPCR cycler (Bio-Rad Laboratories, Hercules, CA) . For analysis of samples, the NIBSC reference standard (NIBSC 19/304) of SARS-2-CoV RNA was spiked with hamster or mouse RNA and purified as described. For mouse samples, this standard was used directly (linear range, 2.5×10^5 to 2.5×10^2 copies).

For hamster samples, this standard was used for validation of an internal hamster reference used for quantification in subsequent runs (linear range, 4.5×10^6 to 4.5×10^2 copies). The cycling conditions were as follows: reverse transcription for 600 sec at 55 °C, followed by denaturation for 180 sec at 94 °C, and 45 cycles of 15 sec at 94 °C and 30 sec at 58 °C. Quantified sample copy numbers were normalized to mg of tissue used for preparation of 5 µL RNA.

Statistical analyses

To compare the means of different groups in growth kinetics, a non-parametric One-way ANOVA was performed. For ICS analysis, the non-parametric two-tailed Mann-Whitney test was used to compare cytokines levels between DC2.4 and DC2.4-SARS2-S-restimulated splenoycytes within the MeV_{vac2}-SARS2-S(H) vaccine group. Note, that these exploratory analyses have been done without correction for multiple testing. For proliferation assay the mean differences were calculated and analyzed using one-tailed Mann-Whitney t-test. To all three groups in CTL killing assays a linear curve was fitted for antigen vs. logarithmised effector-target ratio E:T. The p values testing for differences in slopes were calculated and populations of SARS2-S(H) compared with control ATU vaccinated cells. The p values were not adjusted for multiplicity due to the explorative character of the study. For VNT, fusion activity, organ titer, and copy number statistical analysis, one-way ANOVA was performed in combination with Tukey's Multi comparison test to compare all pair means. For comparison of mouse copy number data between two groups, unpaired two-tailed t-test was applied. For multiplex statistical analysis, two-way ANOVA analysis was applied with paired Tukey's Multi comparison test as post hoc test. For statistical analysis of grouped ELISpot data, two-way ANOVA analysis was applied with paired Tukey's Multi comparison test.

Supplementary Figures

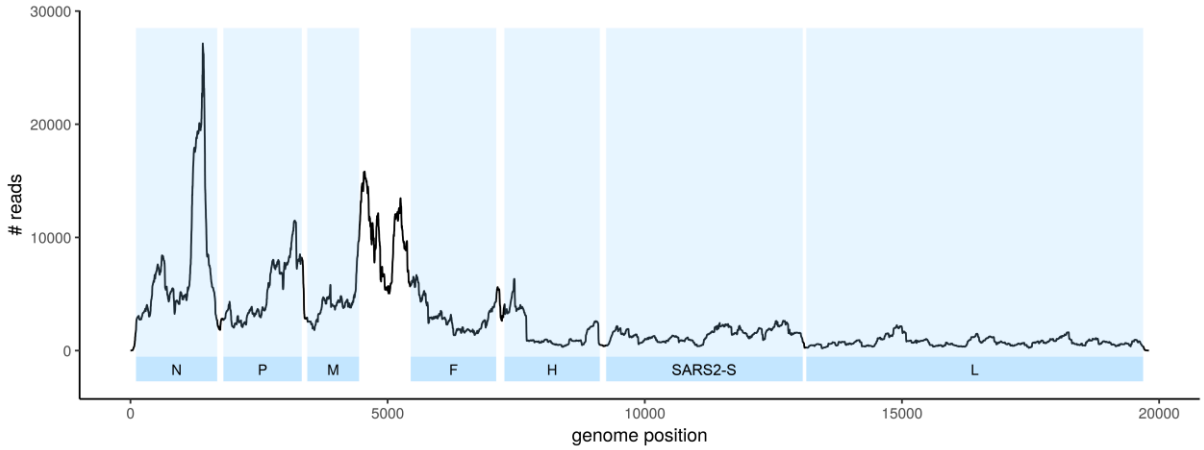

Fig. S1. Coverage of vaccine candidate MeV_{vac2}-SARS2-S(H) genome during next generation sequencing. Schematic depiction of read frequency at each position of the vaccine virus genome. Blue areas indicate respective viral coding sequences, white areas indicate intergenic regions and untranscribed terminal regions (UTRs) of the genome. Coverage across the genome was sufficient for variant detection and reflects the transcription gradient typically observed in measles virus total RNAseq data. Since the majority of reads are mRNA-derived, low read numbers decrease strongly between the coding regions and continually towards the 5' end.

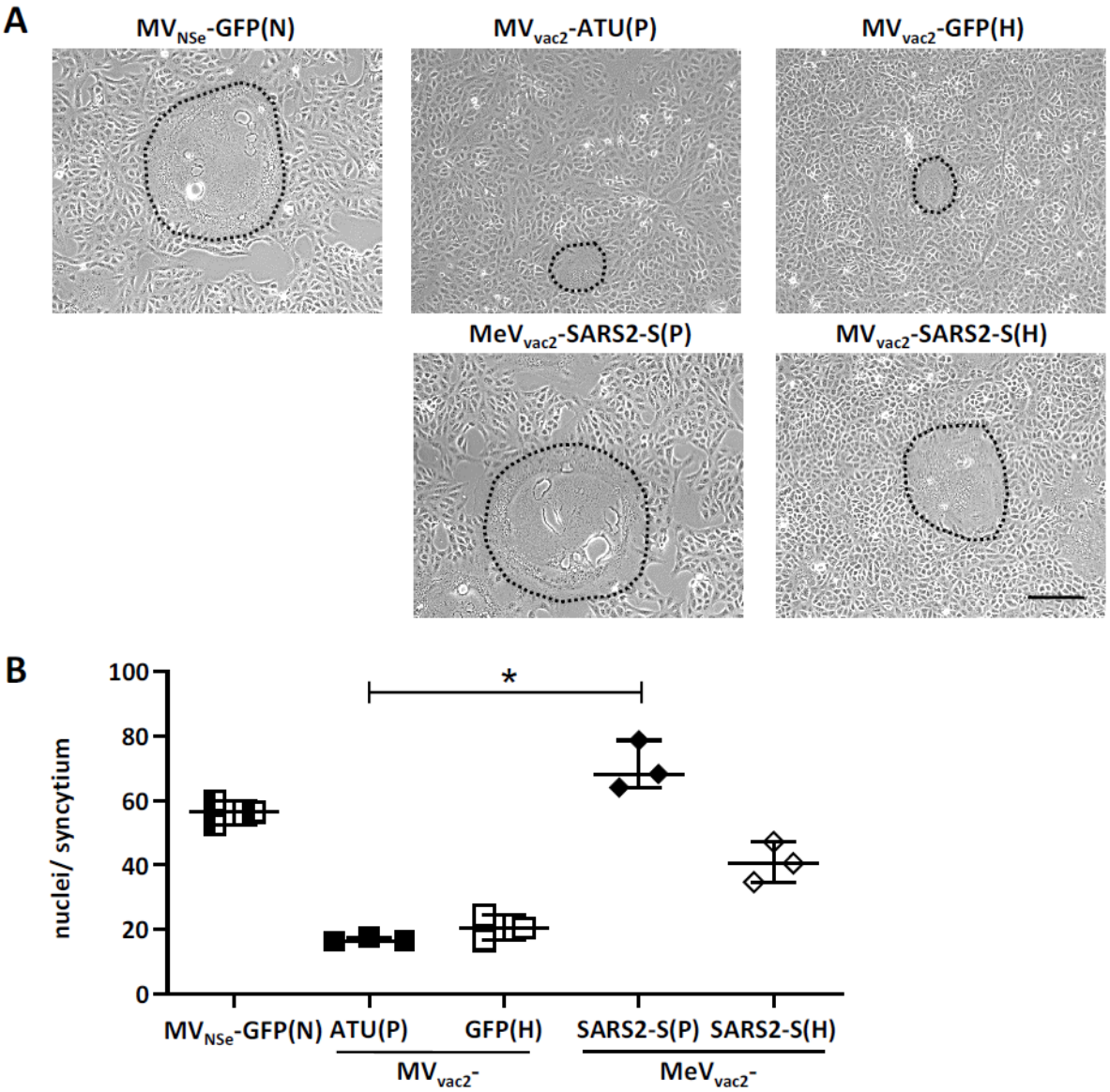

Fig. S2. Characterization of fusogenic phenotype of MeV$_{vac2}$-SARS2-S(P) and MeV$_{vac2}$-SARS2-S(H). (A) Photographs of fusion activity of Vero cells infected at an MOI of 0.01 with MeV$_{vac2}$-SARS2-S(P) or MeV$_{vac2}$-SARS2-S(H) encoding SARS-CoV-2 S in additional transcription units post-P or post-H, respectively, in direct comparison to MV$_{vac2}$-ATU(P) or MV$_{vac2}$-GFP(H) control vaccine viruses or MV$_{NSe}$-GFP(N) hyperfusogenic oncolytic MeV. Representative picture of one out of three independent experiments. Scale bar represents 200 µm. (B) Cell fusion was quantified 30 h after infection. For statistical analysis, one-way ANOVA was performed in combination with Tukey's Multi comparison test to compare all pair means. *, $p<0.05$.

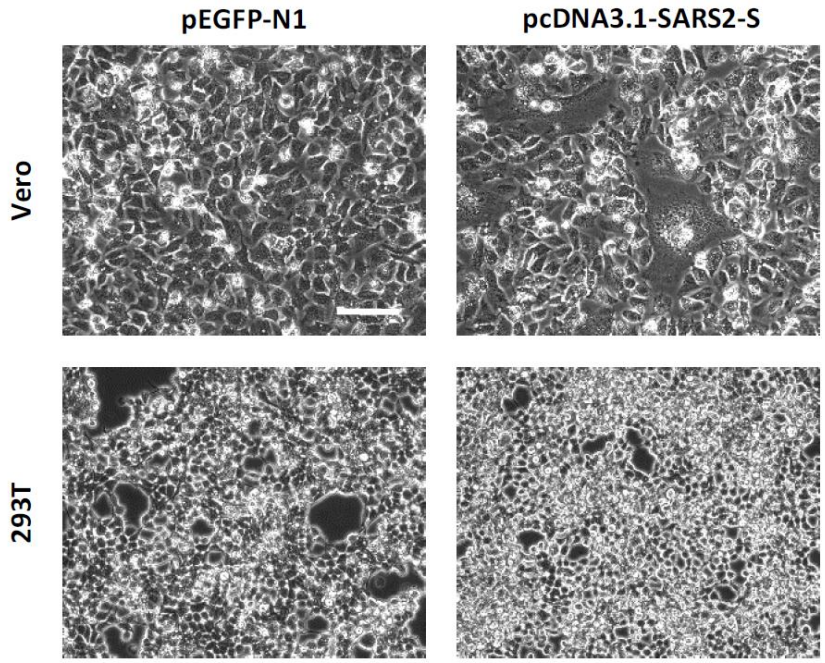

Fig. S3. Expression of SARS-CoV-2 S protein in Vero and 293T cells. Photographic depiction of fusion activity in Vero or 293T cells 48 h after transfection with 1 µg of SARS-CoV-2 S expression plasmid or control DNA. One representative out of three independent experiments is shown. Scale bar represents 100 µm.

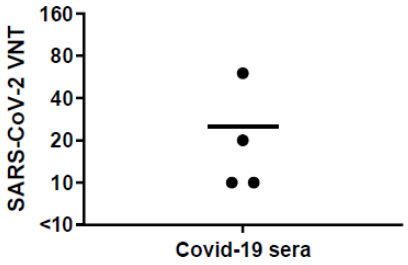

Fig. S4. SARS-CoV-2 VNT in four human COVID-19 reconvalescent patient sera. Virus neutralizing titers (VNT) were calculated as reciprocal of the highest dilution abolishing infectivity. Selected human patient sera were tested with the same assay conditions as mouse or hamster sera. Dots represent single individuals; horizontal line represents mean.

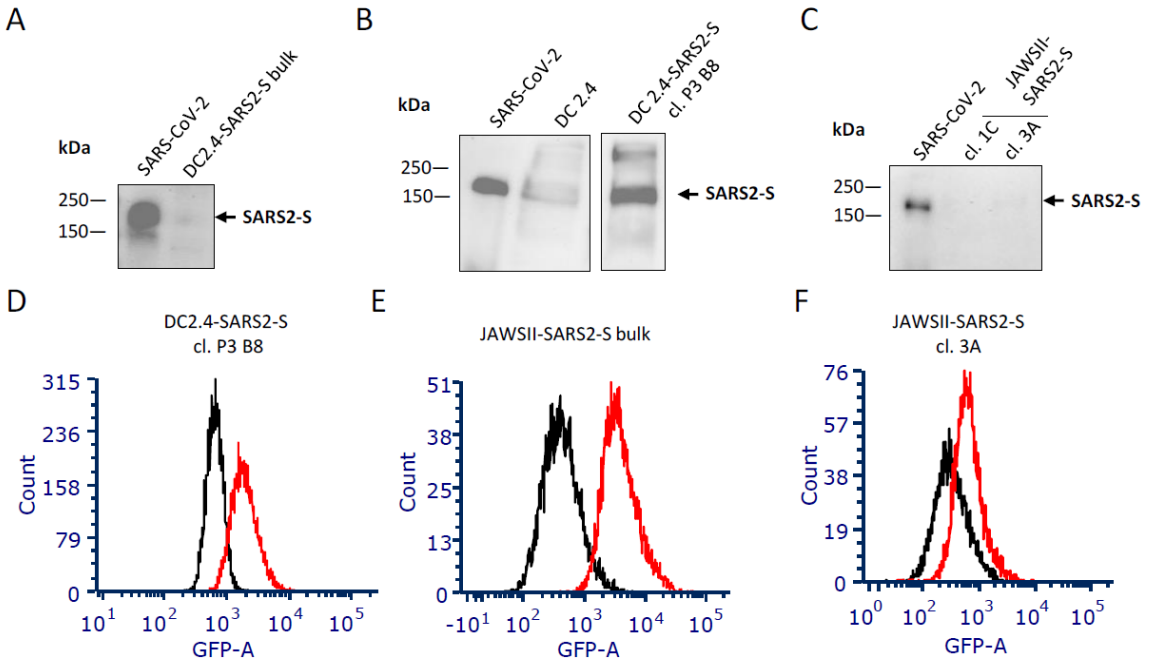

Fig. S5. Antigen expression in transduced DCs. (A-C) Immunoblot analysis of SARS-CoV-2 Spike (S) antigen expression in (A) DC2.4-SARS2-S bulk (B) the single cell clone P3 B8 of DC2.4-SARS2-S used for stimulation experiments and (C) two selected single cell clones of JAWSII-SARS2-S dendritic cell cultures stably transduced with lentiviral expression vectors encoding SARS-CoV-2 Spike glycoprotein as indicated. SARS-CoV-2, lysate of Vero cells infected by SARS-CoV-2. (D-E) flow cytometric analysis of GFP expression coupled via an IRES element on the bicistronic mRNA to the SARS-CoV-2 Spike GP ORF of (D) single cell clone P3 B8 of DC2.4-SARS2-S, (E) sorted JAWSII-SARS2-S bulk culture, and (F) single cell clone 3A of JAWSII-SARS2-S also depicted in (C). Black, parental cell line; red, transduced population.

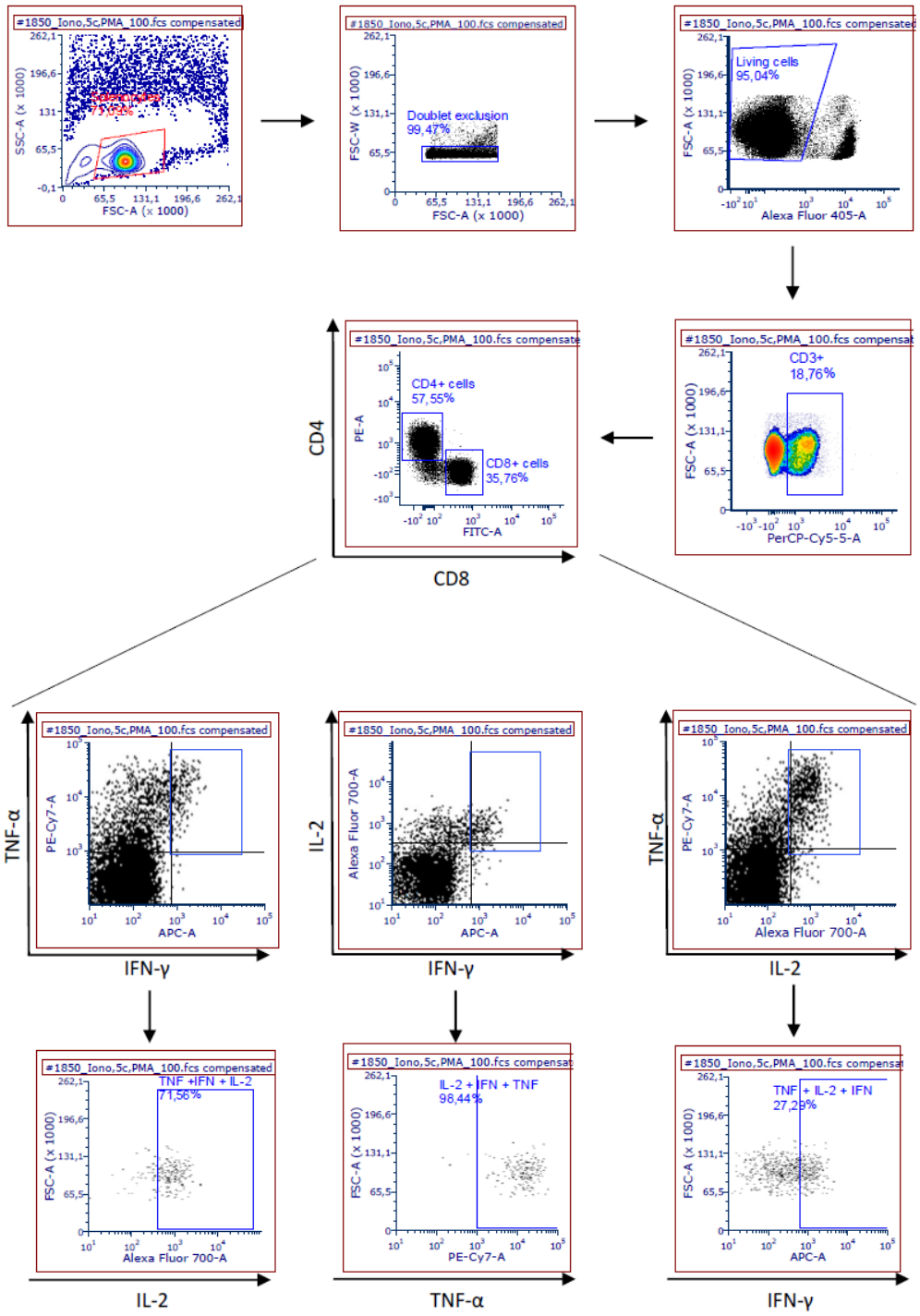

Fig. S6. Gating strategy for intracellular cytokine staining. Exemplary depiction of the gating strategy to analyze T cells after re-stimulation and staining for cytokine induction. The gating strategy includes cell doublet exclusion, selection for living cells and separation of $CD8^+$ and $CD4^+$ T cells within $CD3^+$ splenocyte populations. Respectively gated T cell populations were then analyzed for expression of IFN-γ, TNF-α, or IL-2. Multi-colour flow cytometry allows assessment of double- or triple-positive cells, exemplarily shown for $CD4^+$ T cells after stimulation with ionomycin and PMA.

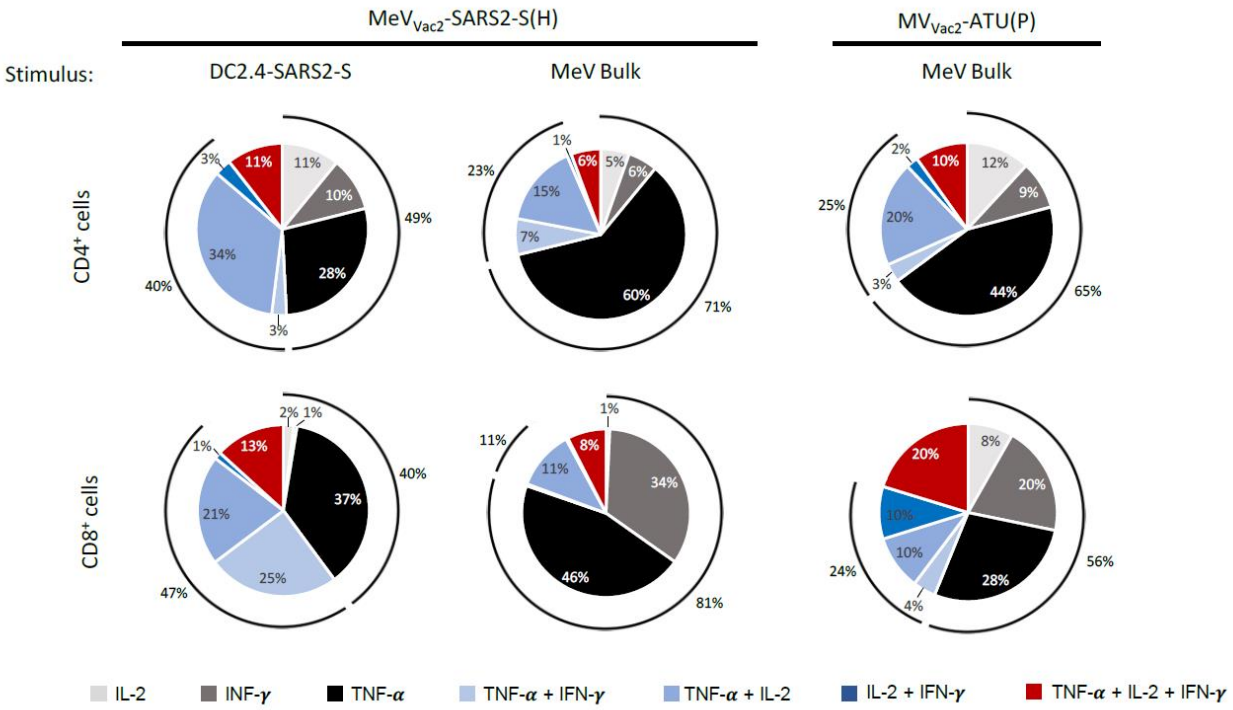

Fig. S7. Multi-functionality of induced T cell responses. Depicted are pie-charts of T cell responses induced by vaccination with MeV$_{vac2}$-SARS2-S(H) or MV$_{vac2}$-ATU(P) upon antigen specific re-stimulation. Data as depicted in Fig. 4 were analyzed for co-expression of the different cytokines. Poly-functional T cells revealed as fractions of cell populations expressing one, two, or all three of the tested cytokines and indicating the size of each fraction among all responsive T cells.

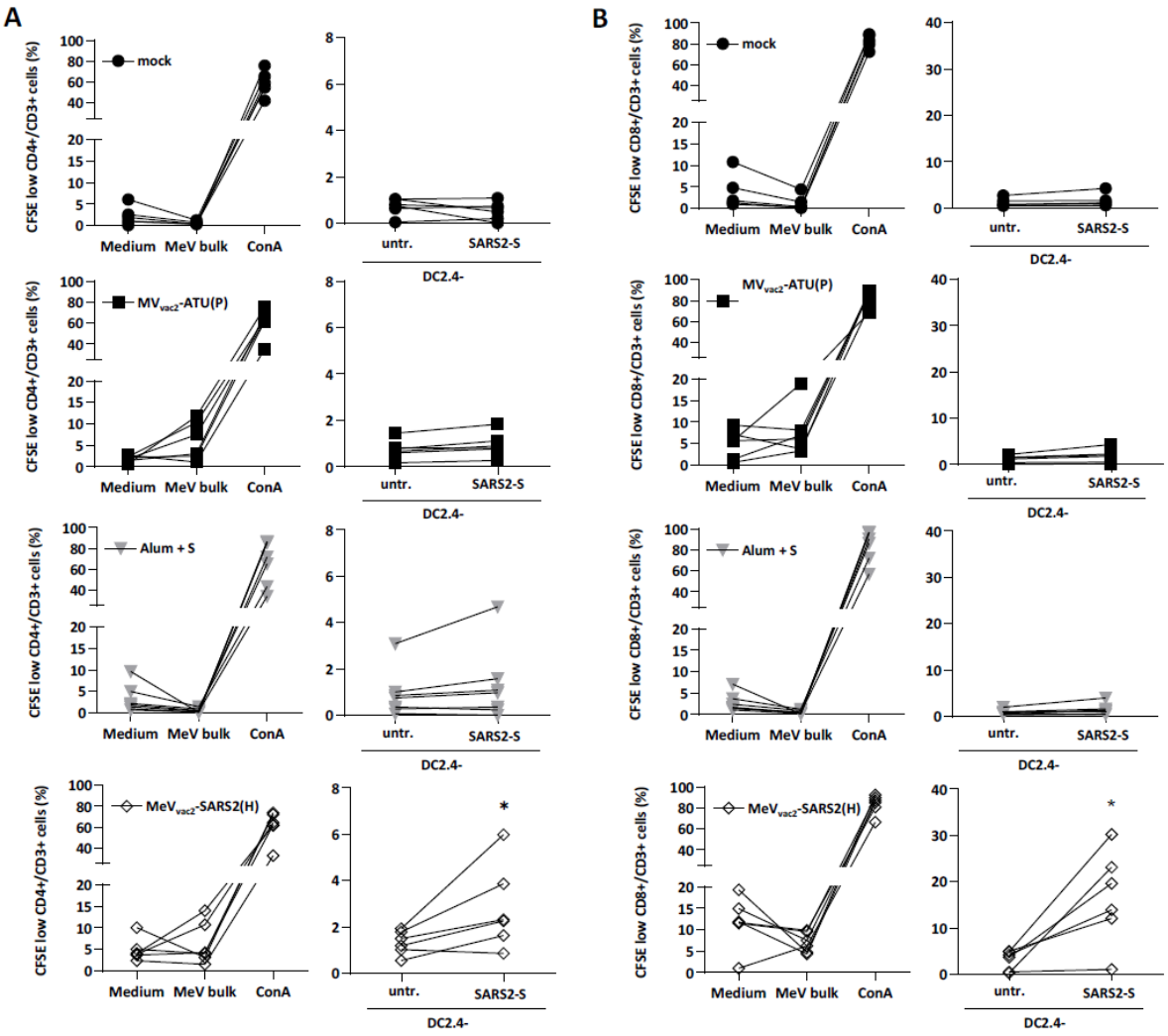

Fig. S8. Ag-specific proliferation of SARS-CoV-2 S-specific T cells. Proliferation assay using splenocytes of mice vaccinated on days 0 and 28 with indicated viruses, isolated 21 days after boost immunization, after co-culture with DC2.4 dendritic cell line transgenic for SARSCoV-2 S (SARS2-S) or untransduced controls (untr.). Depicted are the percentages of (A) $CD4^+$ or (B) $CD8^+$ T cells with low CFSE staining, indicating proliferation in the samples. To analyze cellular α-MeV responses, splenocytes were stimulated with 10 µg/mL MeV bulk antigens or were left unstimulated (medium). The reactivity of splenocytes was confirmed by Concanavalin A (ConA) treatment (10 µg/mL). Results for splenocytes of vaccinated mice are displayed individually and the trend between paired unstimulated and re-stimulated samples is outlined (n = 6-7). One-tailed Mann-Whitney t-test. *, $p<0.05$.

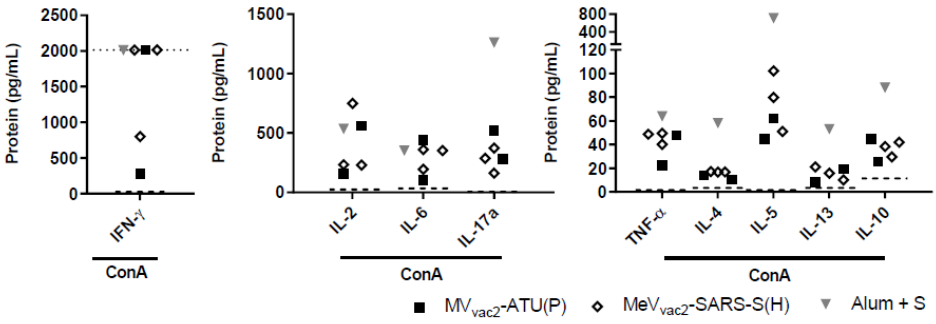

Fig. S9. Cytokine-expression by ConA-stimulated splenocytes. General reactivity of splenocytes used in multiplex cytokine assay (s. Fig. 6B) were demonstrated by Concanavalin A (ConA) treatment (10 µg/mL). Splenocytes of representative mice vaccinated with MV$_{vac2}$-ATU(P), MeV$_{vac2}$-SARS2-S(H) or Alum-adjuvanted S protein as indicated were analyzed by multiplex cytokine analysis for secretion of typical marker cytokines in the supernatant after restimulation. Dots represent individual animals. Dashed line: Median cytokine secretion of unstimulated splenocytes (medium, s. Fig. 6B) of all mice. Upper limit of detection: IFN-g: 2015.2 pg/mL (dotted line), IL-2: 4250.9 pg/mL; IL-6: 3992.4 pg/mL; IL-17a: 2108.5 pg/mL; TNF-a: 1408.1 pg/mL; IL-4: 408.4 pg/mL; IL-5: 4051.4 pg/mL; IL-13: 14196 pg/mL; IL-10: 5480.1 pg/mL.

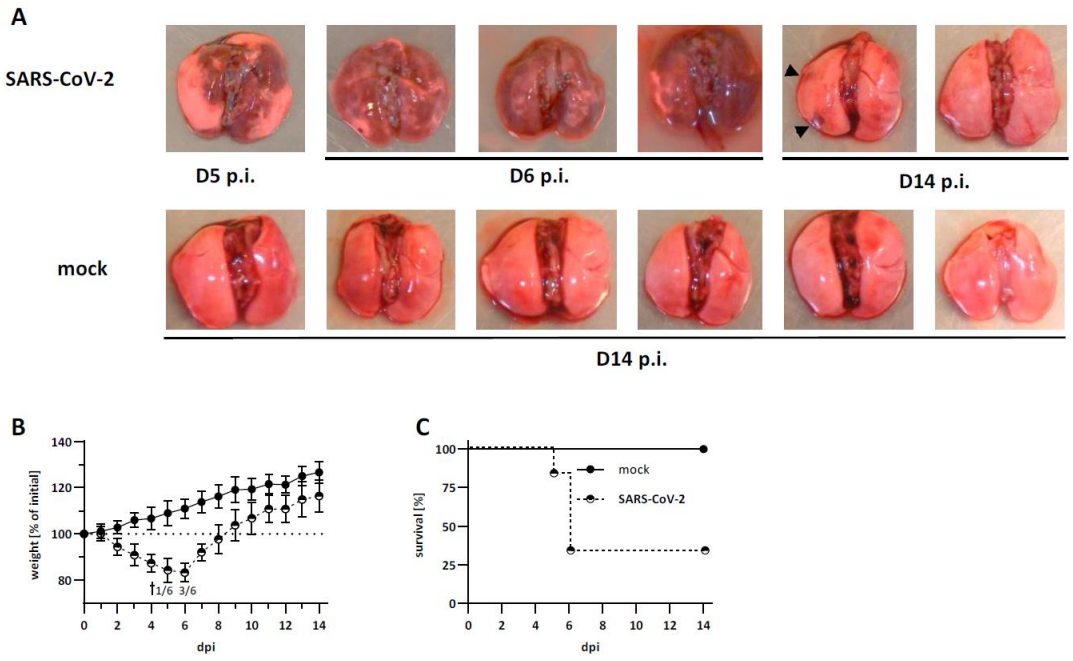

Fig. S10. SARS-CoV-2 hamster challenge model. (A) Macroscopic pictures of Syrian hamster lungs after SARS-CoV-2 or mock infection. Pictures were taken at the day of necropsy (20 % weight loss) or at the end of the experiment 14 dpi, as indicated. Arrows point at macroscopic lesions still visible in one lung 14 dpi. (B) Body weight changes of SARS-CoV-2-and mock-infected Syrian hamsters (n = 6). (C) Kaplan-Meier plot of hamster survival following SARS-CoV-2 or mock infection.

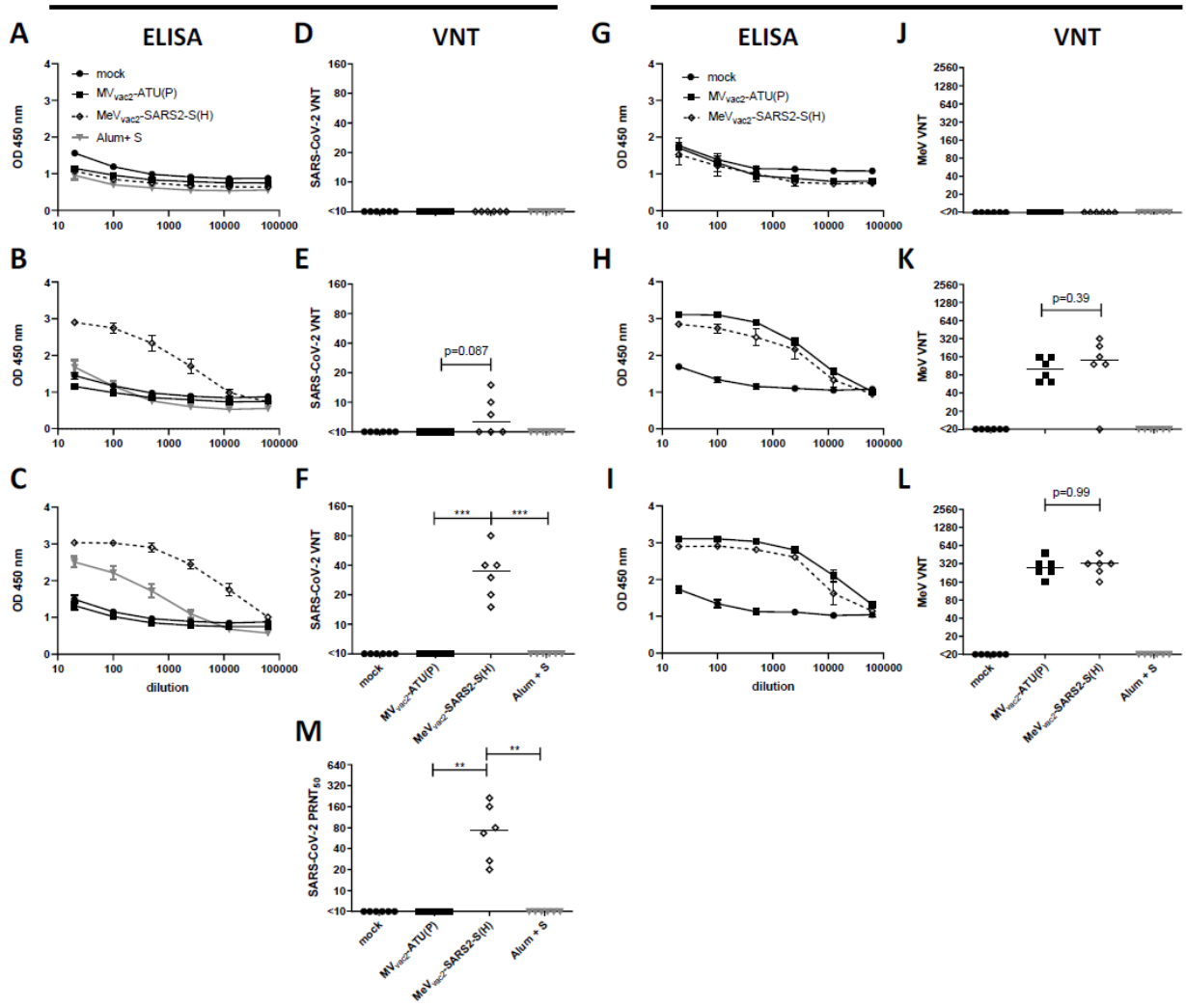

Fig. S11. Humoral immunity in vaccinated hamsters challenged with SARS-CoV-2. Sera of Syrian hamsters vaccinated on days 0 and 21 with indicated viruses or Alum-adjuvanted S protein were sampled on day 0 (A, D, G, J), day 21 after prime- (B, E, H, K) and day 35 after boost-immunization (C, F, I, L) and analyzed for antibodies specific for SARS-CoV-2 S or MeV. Medium-inoculated hamsters served as mock control. Pan-IgG binding to recombinant SARS-CoV-2 S (A – C) or MeV bulk antigens (G – I) were determined by ELISA via the specific OD 450 nm value. Depicted are means and respective standard deviation of the mean (SEM) of each group (n = 6). Virus neutralizing titers (VNT) in vaccinated hamsters for SARS-CoV-2 (D – F) or MeV (J – L) were calculated as reciprocal of the highest dilution abolishing infectivity. Dots represent single individuals; horizontal line represents median per group. All hamsters below detection limit had no detectable VNT. (M) Functional SARS-CoV-2 neutralizing antibodies (nAb) were determined in the post boost sera via plaque reduction neutralization assay of SARS-CoV-2 ($PRNT_{50}$) on Vero cells. For statistical analysis of VNT and $PRNT_{50}$ data, oneway ANOVA was performed in combination with Tukey's Multi comparison test to compare all pair medians.

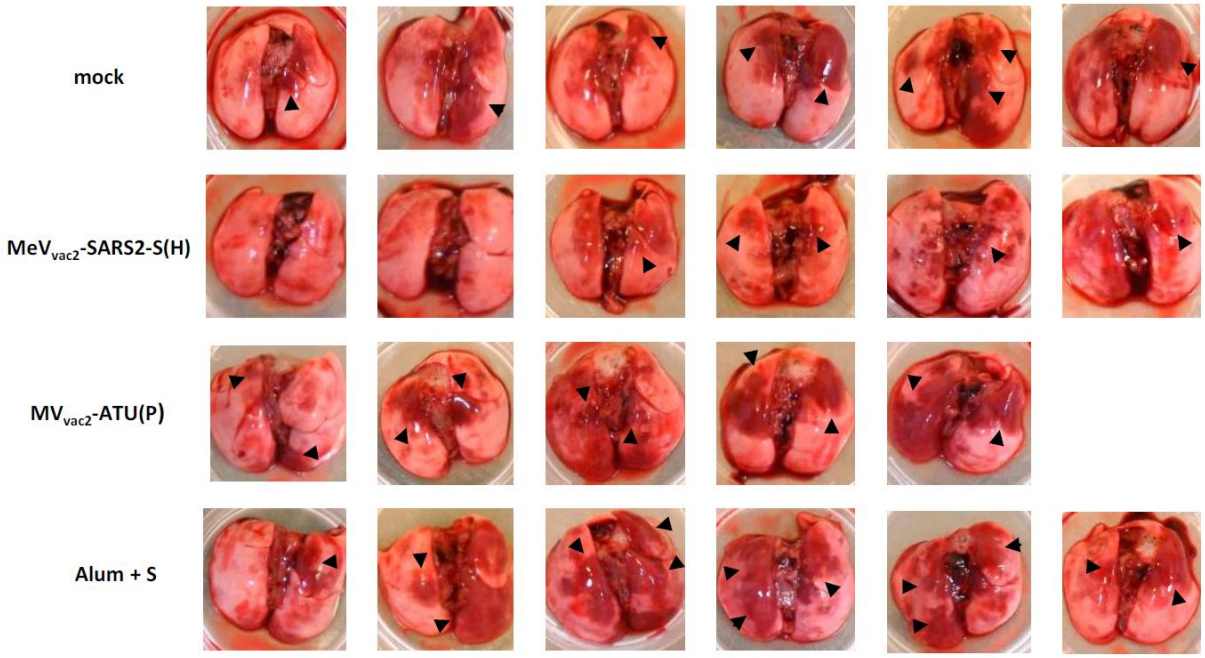

Fig. S12. Gross pathology in lungs of Syrian golden hamsters challenged with SARS-CoV-2. Hamsters were vaccinated on days 0 and 21 with indicated viruses or Alum-adjuvanted S protein and challenged at day 35 with SARS-CoV-2. Pictures were taken at necropsy on day 4 pi (n = 5 - 6). Arrow heads point at macroscopic lesions in infected lungs.

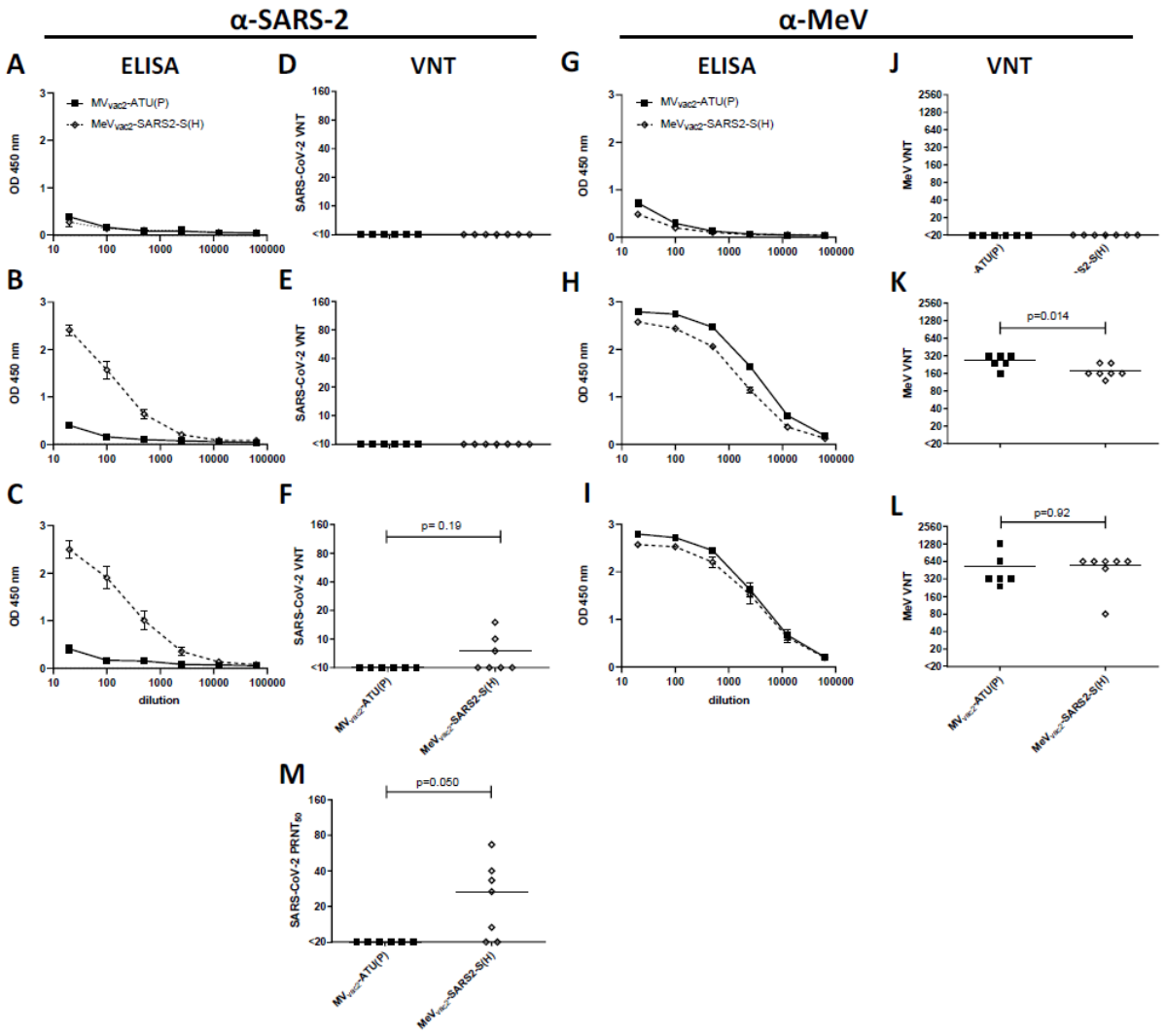

Fig. S13. Humoral immunity in mice challenged with SARS-CoV-2 MA. Sera of mice vaccinated on days 0 and 21 with indicated viruses or Alum-adjuvanted S protein were sampled on day 0 (A, D, G, J), day 21 after prime- (B, E, H, K) and day 35 after boost immunization (C, F, I, L) and analyzed for antibodies specific for SARS-CoV-2 S or MeV. Medium-inoculated mice served as mock. Pan-IgG binding to recombinant SARS-CoV-2 S (A – C) or MeV bulk antigens (G - I) were determined by ELISA via the specific OD 450 nm value. Depicted are means and respective standard deviation of the mean (SEM) of each group (n = 6 - 7). Virus neutralizing titers (VNT) in vaccinated mice for SARS-CoV-2 (D - F) or MeV (J – L) were calculated as reciprocal of the highest dilution abolishing infectivity. Dots represent single individuals; horizontal line represents mean per group. All mice depicted on the detection limit had no detectable VNT. (M) Functional SARS-CoV-2 neutralizing antibodies (nAb) were determined in the post boost sera via plaque reduction neutralization assay of SARS-CoV-2 ($PRNT_{50}$) on Vero cells. For statistical analysis of VNT and $PRNT_{50}$, one-way ANOVA was performed in combination with Tukey's Multi comparison test to compare all pair medians.

SI References

1. Z. Shen, G. Reznikoff, G. Dranoff, K. L. Rock, Cloned dendritic cells can present exogenous antigens on both MHC class I and class II molecules. Journal of immunology (Baltimore, Md. : 1950) 158, 2723–2730 (1997).

2. K. Friedrich, J. R. Hanauer, S. Prüfer, R. C. Münch, I. Völker, C. Filippis, C. Jost, K.-M. Hanschmann, R. Cattaneo, K.-W. Peng, A. Plückthun, C. J. Buchholz, K. Cichutek, M. D. Mühlebach, DARPin-targeting of measles virus: unique bispecificity, effective oncolysis, and enhanced safety. Molecular therapy : the journal of the American Society of Gene Therapy 21, 849–859 (2013).

3. A. H. Malczyk, A. Kupke, S. Prüfer, V. A. Scheuplein, S. Hutzler, D. Kreuz, T. Beissert, S. Bauer, S. Hubich-Rau, C. Tondera, H. S. Eldin, J. Schmidt, J. Vergara-Alert, Y. Süzer, J. Seifried, K.-M. Hanschmann, U. Kalinke, S. Herold, U. Sahin, K. Cichutek, Z. Waibler, M. Eickmann, S. Becker, M. D. Mühlebach, A Highly Immunogenic and Protective Middle East Respiratory Syndrome Coronavirus Vaccine Based on a Recombinant Measles Virus Vaccine Platform. Journal of virology 89, 11654–11667 (2015).

4. J. W. Hewett, B. Tannous, B. P. Niland, F. C. Nery, J. Zeng, Y. Li, X. O. Breakefield, Mutant torsinA interferes with protein processing through the secretory pathway in DYT1 dystonia cells. Proceedings of the National Academy of Sciences of the United States of America 104, 7271–7276 (2007).

5. R. Zufferey, D. Nagy, R. J. Mandel, L. Naldini, D. Trono, Multiply attenuated lentiviral vector achieves efficient gene delivery in vivo (1997).

6. R. C. Münch, M. D. Mühlebach, T. Schaser, S. Kneissl, C. Jost, A. Plückthun, K. Cichutek, C. J. Buchholz, DARPins: an efficient targeting domain for lentiviral vectors. Molecular therapy : the journal of the American Society of Gene Therapy 19, 686–693 (2011).

7. A. Martin, P. Staeheli, U. Schneider, RNA polymerase II-controlled expression of antigenomic RNA enhances the rescue efficacies of two different members of the Mononegavirales independently of the site of viral genome replication. Journal of virology 80, 5708–5715 (2006).

8. G. Kaerber, Beitrag zur kollektiven Behandlung pharmakologischer Reihenversuche (1931).

9. J. R. del Valle, P. Devaux, G. Hodge, N. J. Wegner, M. B. McChesney, R. Cattaneo, A vectored measles virus induces hepatitis B surface antigen antibodies while protecting macaques against measles virus challenge. Journal of virology 81, 10597–10605 (2007).

10. M. M. Böhmer, U. Buchholz, V. M. Corman, M. Hoch, K. Katz, D. V. Marosevic, S. Böhm, T. Woudenberg, N. Ackermann, R. Konrad, U. Eberle, B. Treis, A. Dangel, K. Bengs, V. Fingerle, A. Berger, S. Hörmansdorfer, S. Ippisch, B. Wicklein, A. Grahl, K. Pörtner, N. Muller, N. Zeitlmann, T. S. Boender, W. Cai, A. Reich, M. an der Heiden, U. Rexroth, O. Hamouda, J. Schneider, T. Veith, B. Mühlemann, R. Wölfel, M. Antwerpen, M. Walter, U. Protzer, B. Liebl, W. Haas, A. Sing, C. Drosten, A. Zapf, Investigation of a COVID-19 outbreak in Germany resulting from a single travel-associated primary case: a case series. The Lancet Infectious Diseases 20, 920–928 (2020).

11. S. Chen, Y. Zhou, Y. Chen, J. Gu, fastp: an ultra-fast all-in-one FASTQ preprocessor. Bioinformatics (Oxford, England) 34, i884-i890 (2018).

12. H. Li, R. Durbin, Fast and accurate short read alignment with Burrows-Wheeler transform. Bioinformatics (Oxford, England) 25, 1754–1760 (2009).

13. H. Li, B. Handsaker, A. Wysoker, T. Fennell, J. Ruan, N. Homer, G. Marth, G. Abecasis, R. Durbin, The Sequence Alignment/Map format and SAMtools. Bioinformatics (Oxford, England) 25, 2078–2079 (2009).

14. A. R. Quinlan, I. M. Hall, BEDTools: a flexible suite of utilities for comparing genomic features. Bioinformatics (Oxford, England) 26, 841–842 (2010).

15. A. McKenna, M. Hanna, E. Banks, A. Sivachenko, K. Cibulskis, A. Kernytsky, K. Garimella, D. Altshuler, S. Gabriel, M. Daly, M. A. DePristo, The Genome Analysis Toolkit: a MapReduce framework for analyzing next-generation DNA sequencing data. Genome research 20, 1297–1303 (2010).

16. A. Wilm, P. P. K. Aw, D. Bertrand, G. H. T. Yeo, S. H. Ong, C. H. Wong, C. C. Khor, R. Petric, M. L. Hibberd, N. Nagarajan, LoFreq: a sequence-quality aware, ultra-sensitive variant caller for uncovering cell-population heterogeneity from high-throughput sequencing datasets. Nucleic acids research 40, 11189–11201 (2012).

17. S. Funke, A. Maisner, M. D. Mühlebach, U. Koehl, M. Grez, R. Cattaneo, K. Cichutek, C. J. Buchholz, Targeted cell entry of lentiviral vectors. Molecular therapy : the journal of the American Society of Gene Therapy 16, 1427–1436 (2008).

18. B. Mrkic, J. Pavlovic, T. Rülicke, P. Volpe, C. J. Buchholz, D. Hourcade, J. P. Atkinson, A. Aguzzi, R. Cattaneo, Measles Virus Spread and Pathogenesis in Genetically Modified Mice (1998).

19. K. H. Dinnon, S. R. Leist, A. Schäfer, C. E. Edwards, D. R. Martinez, S. A. Montgomery, A. West, B. L. Yount, Y. J. Hou, L. E. Adams, K. L. Gully, A. J. Brown, E. Huang, M. D. Bryant, I. C. Choong, J. S. Glenn,

L. E. Gralinski, T. P. Sheahan, R. S. Baric, A mouse-adapted model of SARS-CoV-2 to test COVID-19 countermeasures. Nature. 10.1038/s41586-020-2708-8 (2020).

20. A. B. Lyons, C. R. Parish, Determination of lymphocyte division by flow cytometry. Journal of immunological methods 171, 131–137 (1994).

21. V. M. Corman, O. Landt, M. Kaiser, R. Molenkamp, A. Meijer, D. K. Chu, T. Bleicker, S. Brünink, J. Schneider, M. L. Schmidt, D. G. Mulders, B. L. Haagmans, B. van der Veer, S. van den Brink, L. Wijsman, G. Goderski, J.-L. Romette, J. Ellis, M. Zambon, M. Peiris, H. Goossens, C. Reusken, M. P. Koopmans, C. Drosten, Detection of 2019 novel coronavirus (2019-nCoV) by real-time RT-PCR. Euro surveillance : bulletin Europeen sur les maladies transmissibles = European communicable disease bulletin 25 (2020).

4.3 Vaccine-associated enhanced respiratory pathology in COVID-19 hamsters after T_H2-biased immunization

Aileen Ebenig[1], Samada Muraleedharan[1], Julia Kazmierski[2], Daniel Todt[3,4], Arne Auste[1,5], Martina Anzaghe[6], André Gömer[3,7], Dylan Postmus[2], Patricia Gogesch[6], Marc Niles[6], Roland Plesker[8], Csaba Miskey[9], Michelle Gellhorn Serra[10], Angele Breithaupt[11], Cindy Hörner[1,5], Carina Kruip[1], Rosina Ehmann[12], Zoltan Ivics[9], Zoe Waibler[6], Stephanie Pfaender[3], Emanuel Wyler[13], Markus Landthaler[13,14], Alexandra Kupke[5,10], Geraldine Nouailles[15,16], Christine Goffinet[2], Richard J.P. Brown[17], Michael D. Mühlebach[1,5]

[1]Product Testing of IVMPs, [8]Animal Facil., [17]Virus Tropism and Immunogenicity, Div. of Vet. Medicine, [6]Div. of Immunology, [9]Div. of Med. Biotechnology, Paul-Ehrlich-Institut, 63225 Langen, Germany

Charité - Universitätsmedizin Berlin, Corporate Member of Freie Universität Berlin and Humboldt-Universität zu Berlin, [2]Institute of Virology, Campus Charité Mitte, [15]Division of Pulmonary Inflammation, [16]Department of Infectious Diseases and Respiratory Medicine, 10117 Berlin, Germany

[3]Department for Molecular and Medical Virology, Ruhr-University, 44801 Bochum, Germany

[4]European Virus Bioinformatics Center (EVBC), 07743 Jena, Germany

[5]German Center for Infection Research, Gießen-Marburg-Langen, Germany.

[7]Institute of Virology, University of Veterinary Medicine Hannover, 30559 Hannover, Germany

[10]Institute for Virology, Phillipps-University, 35043 Marburg, Germany

[11]Department of Experimental Animal Facilities and Biorisk Management, Friedrich-Loeffler-Institut, Federal Research Institute for Animal Health, 17493 Greifswald-Insel Riems, Germany

[12]Institute for Microbiology, Bundeswehr, 80937 München, Germany

[13]Berlin Institute for Medical Systems Biology (BIMSB), Max Delbrück Center for Molecular Medicine in the Helmholtz Association (MDC), 10115 Berlin, Germany

[14]IRI Life Sciences, Institute for Biology, Humboldt-Universität zu Berlin, 10115 Berlin, Germany

Cell Reports 2022

doi: 10.1016/j.celrep.2022.111214

Abstract

Vaccine-associated enhanced respiratory disease (VAERD) is a severe complication for some respiratory infections. To investigate the potential for VAERD induction in coronavirus disease 2019 (COVID-19), we evaluate two vaccine leads utilizing a severe hamster infection model: a T helper type 1 (T_H1)-biased measles vaccine-derived candidate and a T_H2-biased alum-adjuvanted, non-stabilized spike protein. The measles virus (MeV)-derived vaccine protects the animals, but the protein lead induces VAERD, which can be alleviated by dexamethasone treatment. Bulk transcriptomic analysis reveals that our protein vaccine prepares enhanced host gene dysregulation in the lung, exclusively up-regulating mRNAs encoding the eosinophil attractant CCL-11, T_H2-driving interleukin (IL)-19, or T_H2 cytokines IL-4, IL-5, and IL-13. Single-cell RNA sequencing (scRNA-seq) identifies lung macrophages or lymphoid cells as sources, respectively. Our findings imply that VAERD is caused by the concerted action of hyperstimulated macrophages and T_H2 cytokine-secreting lymphoid cells and potentially links VAERD to antibody-dependent enhancement (ADE). In summary, we identify the cytokine drivers and cellular contributors that mediate VAERD after T_H2-biased vaccination.

Keywords

COVID-19 vaccines, vaccine-associated enhanced respiratory disease, VAERD, mechanism of immunopathogenesis, antibody-dependent enhancement, ADE, T_H2 immune responses, vaccine safety, dexamethasone treatment, protein vaccines

Graphical Abstract

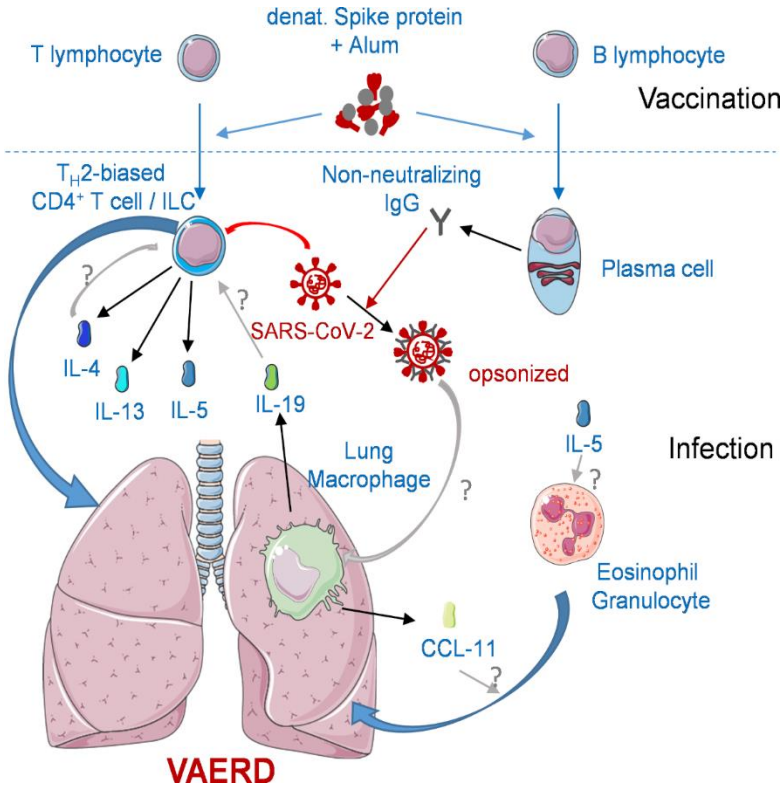

Introduction

Severe acute respiratory syndrome coronavirus 2 (SARS-CoV-2) is the etiological agent of the current coronavirus disease 2019 (COVID-19) pandemic (Wu et al., 2020; Zhu et al., 2020), resulting in more than 513 million confirmed cases (as of May 5, 2022) with an overall case fatality rate of 1.21 % (WHO, 2021). To combat this pandemic, the first vaccine candidates were developed, tested in animal models, and approved for human use within the first year after pathogen identification. To date, more than 10 billion vaccine doses have been administered of all authorized vaccines based on different vaccine technologies, namely mRNA vaccines, adenoviral vector vaccines, inactivated viruses, or proteins. Potential safety risks including the induction of a more severe or altered clinical pathology after breakthrough infection in vaccinated patients were considered, but not yet described, during their development.

One possible risk associated with immunization in the context of respiratory infections is an immunopathology termed vaccine-associated enhanced respiratory disease (VAERD) (Munoz et al., 2021). Such enhancement of disease has been well described in the context of formalin-inactivated respiratory syncytial virus (RSV) vaccines for infants and young children (Kim et al., 1969). Vaccinated children who were later exposed to circulating RSV developed an enhanced and atypical phenotype of clinical symptoms that resulted in higher hospitalization rates and even a small number of associated

fatalities (Kim et al., 1969). Lung sections of the fatal cases displayed monocytic infiltration with massive excess of eosinophils (Kim et al., 1969). Induction of low-affinity and non-neutralizing antibody (Ab) responses provoked by the formalin-inactivated virus was found to be causative for enhanced disease (Polack et al., 2002). Such a pathologic eosinophil infiltration triggered by T_H2-biased T cell responses has also been demonstrated in animal models after immunization with formalin-inactivated virus prior to RSV infection (Ruckwardt et al., 2019).

Immunopathologies such as VAERD or Ab-dependent enhancement (ADE) of disease were also reported in CoV-infected vaccinated animals or animal models for highly pathogenic human CoV. Cats immunized with a recombinant S protein-expressing vaccinia virus developed more severe disease and early death syndrome following infection with feline infectious peritonitis virus, which was linked to a low amount of vaccine-induced neutralizing Abs in the affected animals (Vennema et al., 1990). Passive transfer of Abs directed against the virus before infection was sufficient for pathology, which was correlated to accelerated virus uptake by macrophages via Fc receptor (Olsen et al., 1992; Takano et al., 2008). Such processes are considered a marker and relevant for classical ADE as described for dengue virus (DENV) (Beltramello et al., 2010). Also, animal models for the first two highly pathogenic zoonotic beta-CoVs, SARS-CoV and Middle Eastern respiratory syndrome (MERS)-CoV, revealed potential for VAERD. Entry receptor-transgenic K18-ACE2 or hDPP4 mice that were immunized with whole inactivated virus vaccines developed severe immunopathology in lung tissue with infiltration of eosinophils after infection (Bolles et al., 2011; Tseng et al., 2012; Agrawal et al., 2016).

These scenarios prompted careful evaluation of the predisposition of COVID-19 infection for disease enhancement. Induction of T_H2-biased immunity or non-functional Ab responses by the different front-runner vaccine candidates was avoided (Corbett et al., 2020a, 2020b; Ramasamy et al., 2020; Sahin et al., 2020; Sadoff et al., 2021; van der Lubbe et al., 2021). Accordingly, no ERD or ADE has been reported in vaccinated individuals to date. However, two recent publications described evidence for VAERD in per se T_H2-biased mouse models using mouse-adapted recombinant SARS-CoV-2 after immunization with alum-adjuvanted, whole-inactivated SARS-CoV-2 or adjuvanted S protein. Following virus challenge, these animals developed considerable pneumonia with infiltration of eosinophils and neutrophils, a clear sign of VAERD (DiPiazza et al., 2021; Iwata-Yoshikawa et al., 2022). Again, the pathology was linked to induction of cytokines typical for T_H2-biased immune responses, but no detailed mechanism for the pathogenesis was described.

We have previously shown in the Syrian hamster (*Mesocricetus auratus*) COVID-19 model that alum-adjuvanted spike protein failed to protect against severe disease after infection, in contrast to a measles

vaccine-derived prototypic COVID-19 vaccine (Hörner et al., 2020). Here, we report reproducible VAERD in outbred hamsters with no inbred helper cell bias. Those hamsters were vaccinated with alum-adjuvanted S protein and later infected with a low-passage human patient isolate. This model allowed us to identify the mechanisms that underlie the observed immunopathology. VAERD became evident in the respective hamsters' lungs: ISH, immunohistochemistry, staining for eosinophils, and general histopathology revealed exaggeration of pneumonia and eosinophilic infiltration, while virus load was reduced. These effects could be correlated to a broadly enhanced dysregulation of gene expression: up-regulation of the major eosinophil attractant eotaxin-1/CCL-11 combined with induction of T_H2-marker cytokines interleukin (IL)-4, IL-5, and IL-13 supported by IL-19 was evident. Furthermore, using single-cell RNA sequencing (scRNA-seq), we attributed this dysregulation to specific immune cell subsets, suggesting that ADE via Fc-receptor-mediated skewing of virion uptake drives CCL-11 and IL-19 secretion by lung macrophages. These cytokines attract eosinophils and positively feedback on the T/NK cell compartment responsible for T_H2-marker cytokine secretion. Eosinophil infiltration and pathology observed in recombinant, non-stabilized SARS-CoV-2 S protein adjuvanted with aluminum hydroxide (Alum+S)-vaccinated animals were dramatically reduced by treatment of infected animals with dexamethasone, while the whole syndrome was absent in animals that received the T helper type 1 (T_H1)-biased measles virus (MeV)-derived vaccine candidate. These data allow us to propose a detailed model of vaccine-induced immunopathogenesis, involving immune cells of the lymphoid and myeloid compartment that release pro-inflammatory cytokines, in a gold-standard animal model of COVID-19. Our data also potentially link VAERD mechanistically to ADE, which will be the focus of follow-up studies.

Results

Histological analysis and pulmonary virus load

To study the efficacy of MeV-derived COVID-19 vaccines, we vaccinated Syrian hamsters with the experimental vaccine candidate MeV_{vac2}-SARS2-S(H) and a classic protein vaccine formulation of recombinant, non-stabilized SARS-CoV-2 S protein adjuvanted with aluminum hydroxide (Alum+S). The recombinant S revealed distinct changes in secondary structural elements (31.7 % α-helices and 35.0 % β-sheets versus 19.3 % α-helices and 50.8 % β-sheets) compared with a stabilized soluble S (Figure S1), highlighting deviation (i.e., de-folding) of the vaccine protein from the native pre-fusion structure. Vaccinated animals were challenged in parallel to naive or vector-control hamsters (MV_{vac2}-ATU(P)) using the low-passage SARS-CoV-2 patient isolate BavPat1 (Hörner et al., 2020) (Figure 1A). During histological

analysis of lung necropsies, the expected pathology was observed for the control animals in hematoxylin and eosin (H&E)-stained tissue slices of the lungs (Figure 1B). In both naive and vector control hamsters, epithelia and endothelia in bronchii and vasculature, respectively, showed inflammation and hemorrhages. Between 20 % and 80 % (median 40 %) of the lung area had become dense due to cellular infiltrates of macrophages and lymphocytes; in general, no or few eosinophils or granulocytes were observed. Single foci to moderate karyorrhexis were apparent (Table S1). This pathology was significantly ameliorated in MeV_{vac2}-SARS2-S(H)-vaccinated hamsters, with reduced inflammation (median of 27.5 % dense area), very few hemorrhages, only a few eosinophils in perivascular regions, and no to minimal karyorrhexis. In contrast, animals vaccinated with Alum+S displayed a considerably intensified pathogenesis: while bronchial epithelia showed few inflammatory alterations, vascular endothelium revealed explicit inflammation. The area of dense infiltrates exceeded 50 % of the slices, with massive infiltration of eosinophils (Figures 1B and 1D). Together, this histopathology suggests induction of VAERD by the immunization of hamsters with Alum+S. Active SARS-CoV-2 infection became evident by *in situ* hybridization (ISH) of SARS-CoV-2 RNA genomes (Figures 1B, third row, and 1C) and immunohistochemistry for SARS-CoV-2 nucleocapsid protein N (Figure 1B, fourth row). MeV_{vac2}-SARS2-S(H)-vaccinated animals revealed significantly reduced staining for SARS-CoV-2 in both ISH and immunohistochemistry. These data are consistent with the previously published protective efficacy of this T_H1-biased vaccine concept. Additionally, Alum+S-vaccinated animals showed somewhat reduced staining for SARS-CoV-2 genomes and N, despite enhanced pathology. While up to 20 % of the lung tissue stained positive for SARS-CoV-2 genomes in control animals, a maximum of only 5 % did in hamsters vaccinated with MeV_{vac2}-SARS2-S(H), while Alum+S-vaccinated animals showed a split behavior (Figure 1C). Sirius red staining for eosinophils (Figure 1B, bottom row) validated H&E findings for significantly enhanced infiltration, which became evident to this extent only in this vaccine cohort. Only in 3 out of 6 animals vaccinated with MeV_{vac2}-SARS2-S(H) were some eosinophils found in perivascular regions of inflamed tissue (Figure S2). Between 84 and 155 eosinophils/mm^2 were found in lung sections of hamsters immunized with Alum+S, whereas in hamsters inoculated with MeV_{vac2}-SARS2-S(H), or the MeV vector control, eosinophil numbers remained within the same range as uninfected control hamsters (3–24 eosinophils/mm^2) (Figure 1D). Thus, the COVID-19 hamster model revealed features suggestive of VAERD for animals vaccinated using the traditional T_H2-biased alum-adjuvanted protein vaccine approach but an absence of such an effect for the T_H1-biased measles-based COVID-19 vaccine candidate (Hörner et al., 2020).

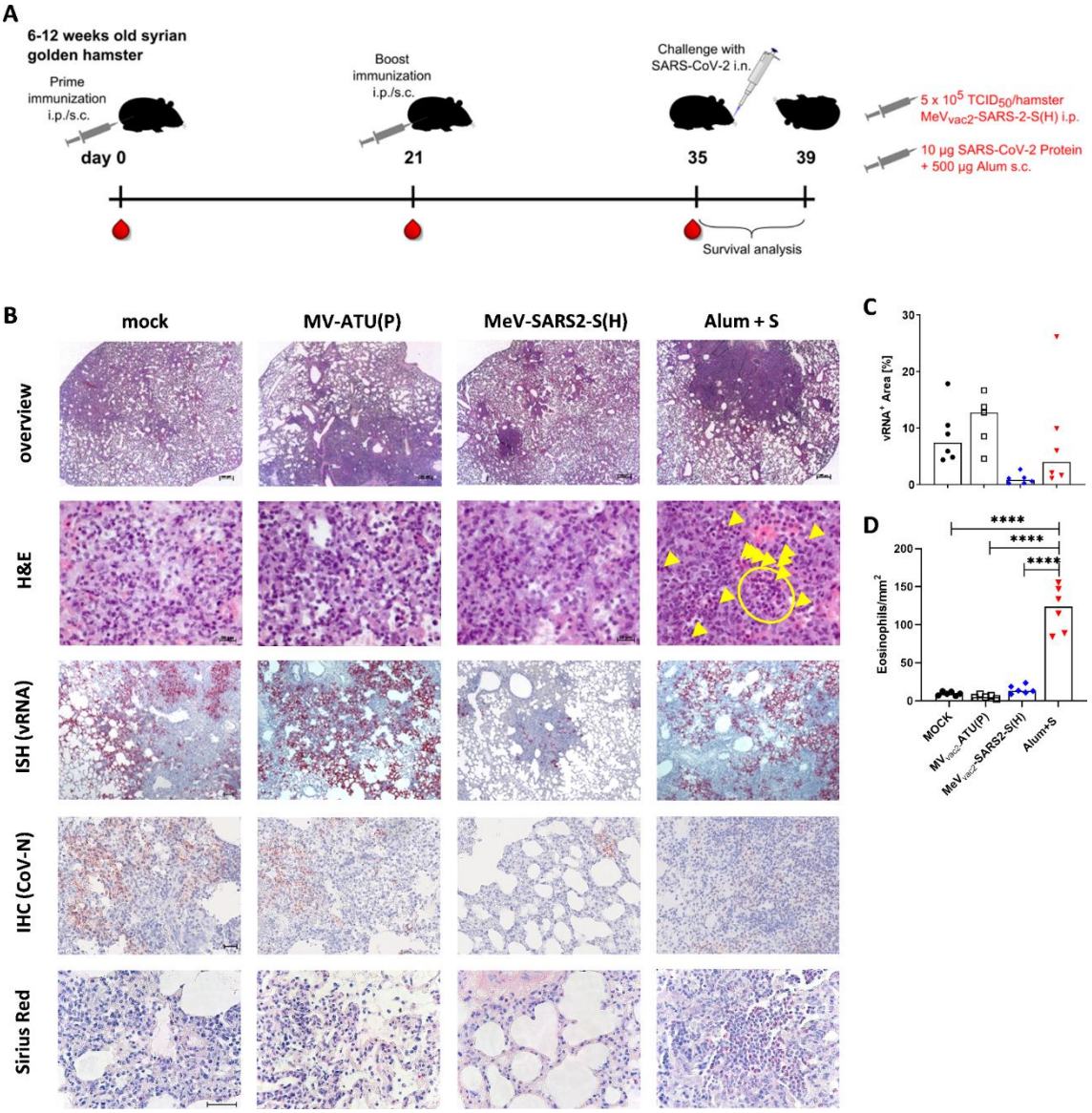

Fig. 1. Pulmonary pathology in vaccinated Syrian hamsters upon challenge with SARS-CoV-2

(A) Schematic depiction of experiment. Syrian hamsters were bled and subsequently immunized with indicated vaccines on days 0 and 21 (n = 6/cohort). On day 35, immunized hamsters were bled and intranasally challenged with low-passage SARS-CoV-2 and observed for another 4 days before sacrifice for organ preparation.

(B) Depicted are representative sections of left lobes of vaccinated hamster lungs prepared 4 days post infection (dpi) with low-passage SARS-CoV-2 (n = 6). H&E staining (two top rows) reveals histopathological changes and immune cell infiltration. In situ hybridization (ISH) for SARS-CoV-2 viral RNA (third row) and immunohistochemistry (IHC) staining for SARS-CoV-2 nucleocapsid protein N (fourth row) depict extent of infection, while Sirius red staining (bottom row) reveals infiltration of eosinophils (scale bars: top row, 500 µm; second row, 20 µm; other rows, 40 µm). Yellow arrowheads and yellow circle depict individual eosinophils or a cluster of eosinophils in H&E-stained samples, respectively.

(C) Quantification of lung infection by determining the relative area of tissue staining positive by ISH by automated image evaluation of the whole slices.

(D) Eosinophil quantification for all animals is depicted. Eosinophil numbers in 10 randomly selected fields of view at 200× magnification were counted, and means were correlated against the area of view. Each data point reveals the mean number of eosinophils per mm^2 in individual animals. For statistical analysis, ordinary one-way ANOVA was applied with Tukey's multiple comparisons test. ****$p < 0.0001$.

(C and D) Single dots represent individual animals, bars median of groups; black circles, MOCK immunized animals; open squares, MeV vector-immunized animals; blue diamonds, MeV_{vac2}-SARS2-S(H)-immunized animals; red triangles, animals vaccinated with Alum+S. ****$p < 0.0001$.

Transcriptional profiling of SARS-CoV-2-infected hamster lungs

To identify determinants underlying the observed enhanced pathology, we performed RNA-seq profiling of hamster lung tissue. Lung transcriptomes from SARS-CoV-2-infected naive hamsters were compared with infected animals previously immunized with either T_H1- or T_H2-biased vaccines. Differentially expressed genes (DEGs) in lungs were determined by comparison with baseline expression levels, derived from uninfected, unvaccinated control animals. Principal component analysis (PCA) of individual transcriptomes revealed segregation of signals according to infection and vaccination status, confirming distinct lung transcriptional responses in the different groups (Figure 2A). Significant transcriptional dysregulation was evident in infected lung tissue, with ~2,000 genes down-regulated and ~1,500 genes up-regulated in vaccine-naïve, SARS-CoV-2-infected hamsters (Figure 2B, left panel). However, prior vaccination with MeV_{vac2}-SARS2-S(H) caused a 40 % reduction in numbers of significantly dysregulated genes. In line with this, lung resident viral RNAs were also 20-fold reduced when compared with unvaccinated animals (Figure 2B, left panel). In contrast, challenge with SARS-CoV-2 after vaccination with Alum+S resulted in comparable numbers of dysregulated genes to those observed in unvaccinated animals (Figure 2B, left panel), with an increased median fold change in gene expression also apparent (Figure 2B, right panel). Only a 2-fold reduction in lung-resident viral RNAs was observed here (Figure 2B, left panel). Together, these data suggest that prior immunization with a T_H1-biased vaccine confers protection from disease, substantially reducing viral loads in hamster lungs, with a concomitant reduction in the magnitude of lung gene dysregulation. In contrast, the gene dysregulation and viral loads observed using the T_H2-biased vaccine more closely resembled patterns seen in unvaccinated animals. However, inspection of the PCA plot revealed separate clustering of unvaccinated and Alum+S groups (Figure 2A), indicating unique transcriptional signatures underlying Alum+S-associated pathology.

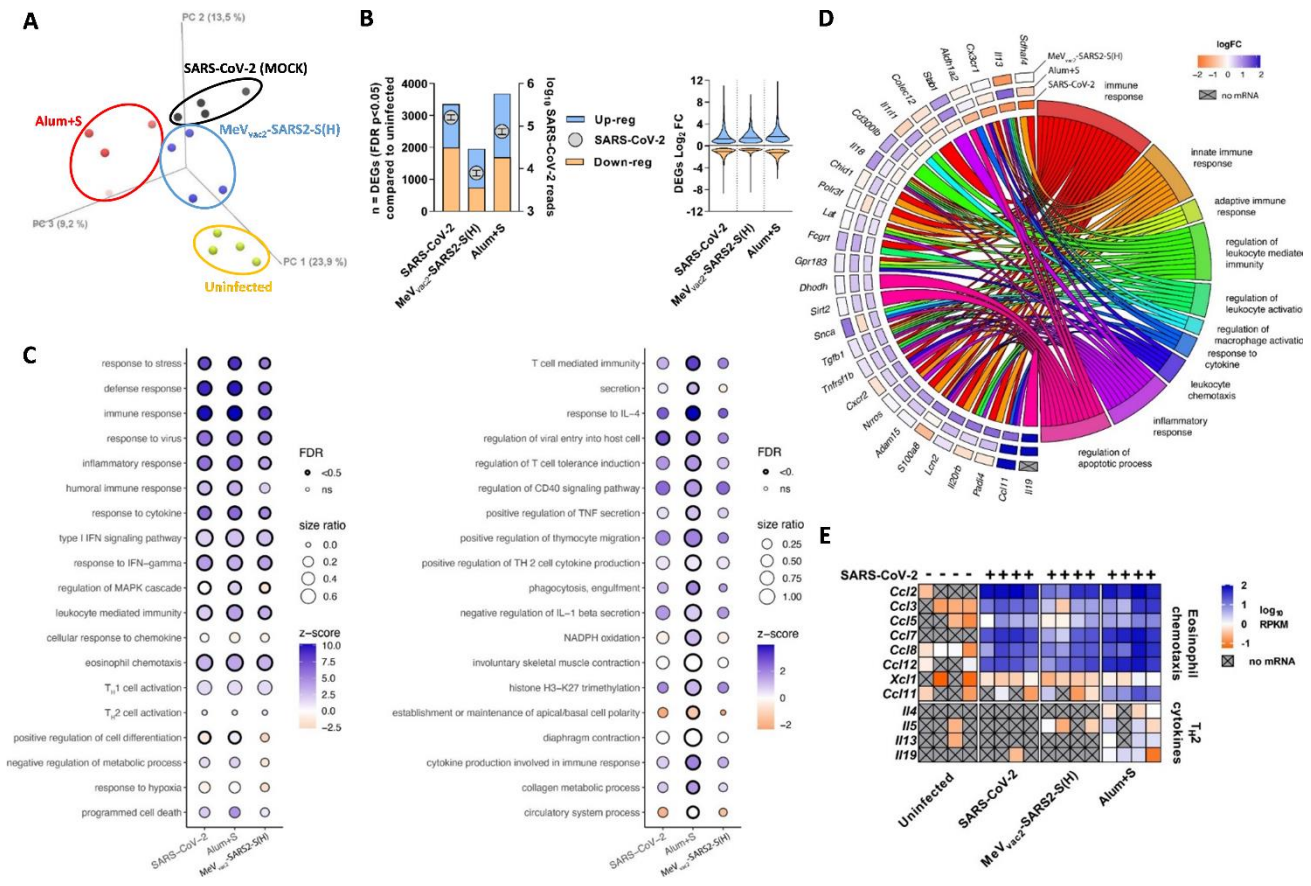

Fig. 2. Global host gene dysregulation revealed by global RNA-seq in lungs of infected, differently vaccinated hamsters

(A) Principal component analysis (PCA) of hamster lung transcriptomes. Transcriptomes from individual animals (n = 4/cohort) are represented by a single data point. Yellow, unvaccinated and not infected; blue, unvaccinated and infected; red, vaccinated with MeV$_{vac2}$-SARS2-S(H) and infected; green, vaccinated with alum-adjuvanted protein and infected.

(B) Viral RNA copies and host gene dysregulation in hamster lungs after infection and vaccination. Left panel: data plotted on the left y axis represent the number of differentially expressed genes (DEGs) (false discovery rate [FDR] $p < 0.05$) in the hamster lung under each condition, when compared with uninfected unvaccinated controls (n = 4). Blue: upregulated; orange: downregulated. Data plotted on the right y axis (gray circles) represents the number of lung-resident SARS-CoV-2 mapped reads per condition (mean ± SEM). Right panel: violin plots depict range of log$_2$ fold change in expression for all significantly dysregulated genes under each condition, when compared with uninfected unvaccinated controls. Horizontal lines, median values.

(C) Gene Ontology (GO) enrichment analysis of SARS-CoV-2-induced DEGs. GO categories are labeled on the y axes. Circle size represents the ratio of significantly dysregulated genes relative to the total gene number in a specific GO term. Circles are shaded relative to activation Z score, with significantly enriched categories highlighted. Left

panel: selected GO categories related to immune response. Right panel: significant GO categories exclusive to Alum+S-vaccinated animals.

(D) Plot depicting log_2 fold change of 28 identified genes (left) exhibiting differential expression patterns between the different conditions, and their associated cellular function (right).

(E) Dysregulation of selected cytokine genes including eosinophil chemo-attractant Ccl11 and T_H2 cytokine mRNAs in lungs of differently vaccinated hamsters upon SARS-CoV-2 infection. Heatmap represents normalized mRNA expression (reads per kilobase per million bases mapped [RPKM]) of genes. Gray cells with an X represent no detectable mRNA expression (RPKM = 0).

To investigate this in more detail, we performed Gene Ontology (GO) enrichment analyses to determine the associated biological processes (Figure 2C). In all groups, infection was associated with significant enrichment of genes associated with defense against pathogens and vigorous induction of classical antiviral and inflammatory response genes (Figure 2C, left panel). Of note, the magnitude of these responses was similar in unvaccinated and Alum+S-immunized hamsters and reduced in MeV_{vac2}-SARS2-S(H)-immunized animals. Visualizing significantly enriched GO categories that were unique to Alum+S-treated animals revealed a profile of dysregulated gene classes that likely contributes to the observed vaccine-associated pathology after superinfection (Figure 2C, right panel).

We next visualized fold change in expression of differentially induced genes, considering their associated cellular functions (Figure 2D). These analyses led us to further explore normalized expression of a refined subset of genes that exhibited unique induction profiles and likely contribute to the vaccine-associated immunopathogenesis (Figure 2E). While the suite of genes involved in eosinophil chemotaxis were similarly upregulated under all conditions, uncontrolled induction of the major eosinophil chemotaxin *Ccl11* (eotaxin-1) mRNA was unique to the Alum+S cohort (Figure 2E). Furthermore, T_H2 cytokine mRNAs *Il4*, *Il5*, *Il13*, and *Il19* were potently induced in the majority of Alum+S-vaccinated animals but largely undetectable in the other groups. These analyses pinpoint likely transcriptional mediators underlying VAERD and hyperinflammation after T_H2-biased vaccination: the specific induction of the *Il4*/*Il5*/*Il13*/*Il19* cytokine axis combined with the potent esosinophil chemotaxin *Ccl11* potentially results in uncontrolled recruitment of eosinophils to the site of infection and enhanced pathogenesis.

Induction of T_H2-biased anti-S immunity by alum-adjuvanted protein

To further demonstrate induction of T_H2-biased immunity by vaccination as the trigger of VAERD, hamsters were just immunized with Alum+S, MeV_{vac2}-SARS2-S(H), or medium (MOCK) without SARS-CoV-2 challenge (Figure 3A). We then analyzed antigen-specific cytokine responses of these animals splenocytes' in re-call experiments 14 days after the second immunization.

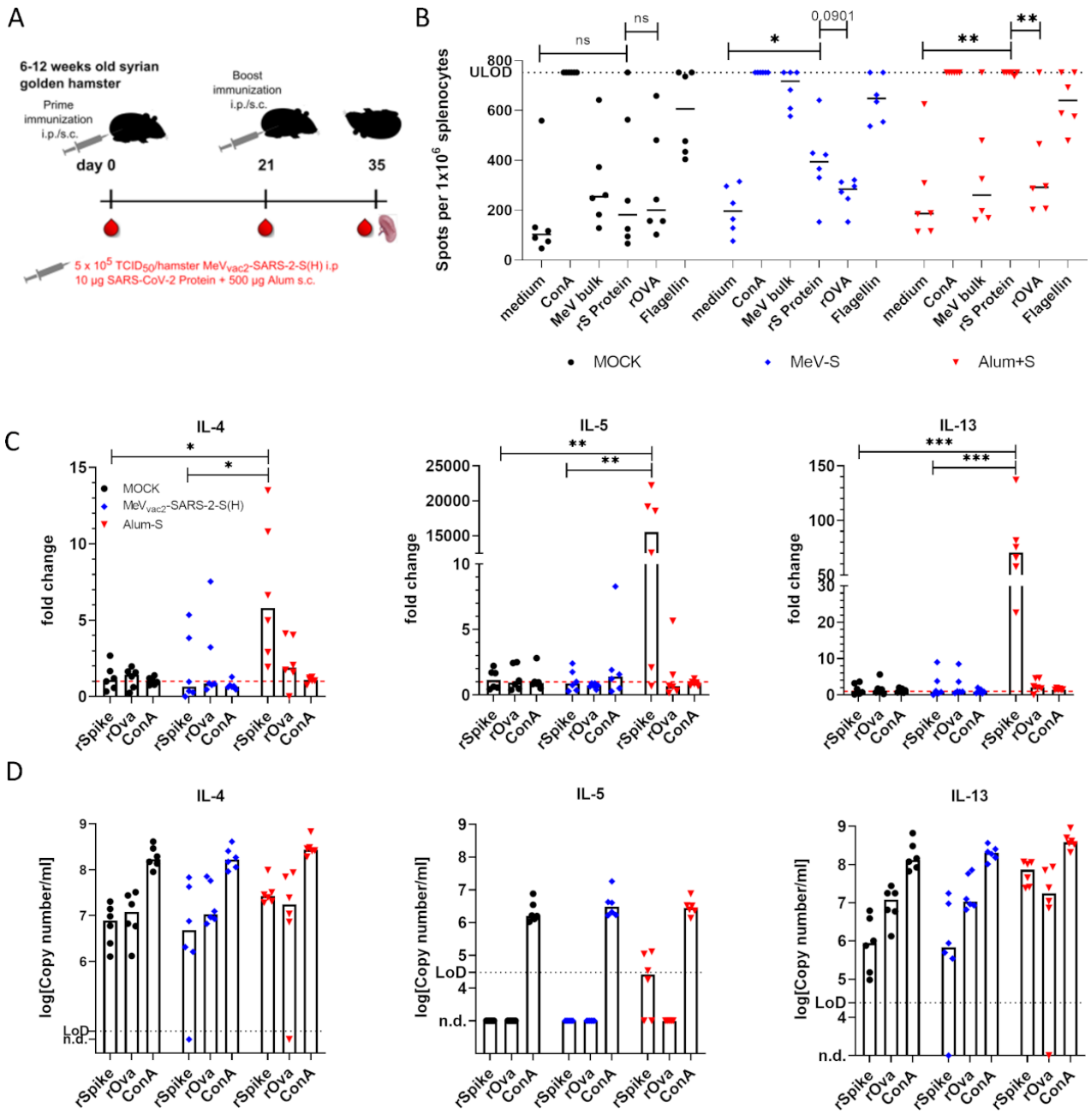

Fig. 3. Induction of T_H2-biased antigen-specific immune cells in protein-vaccinated Syrian hamsters

(A) Syrian hamsters were immunized with MeV_{vac2}-SARS2-S(H) (MeV-S) (intraperitoneally [i.p.]) or Alum+S (subcutaneously [s.c.]) on days 0 and 21 (n = 6 animals/cohort). Two weeks after immunization, hamsters were sacrificed, blood was collected, and splenocytes were isolated.

(B) IFN-γ ELISpot analysis using splenocytes of hamsters vaccinated on days 0 and 21, isolated 14 days after the boost immunization and after stimulation with recombinant S protein (rS protein) or MeV bulk antigens (MeV bulk). The reactivity of splenocytes was confirmed by Concanavalin A (ConA) (5 µg/mL) or flagellin treatment (20 µg/mL). Recombinant ovalbumin (rOva) or medium served as negative controls. The number of cells per $1×10^6$ splenocytes

represent the number of cells expressing IFN-γ upon re-stimulation. Dots represents individual animals, horizontals bars median per group (n = 6). Samples above the upper limit of detection (ULOD) were displayed as such. For statistical analysis of grouped ELISpot data, paired t test was applied. ns, not significant ($p > 0.05$); $*p < 0.05$; $**p < 0.01$.

(C) Relative fold change expression of mRNAs encoding IL-4, IL-5, or IL-13 was determined using quantitative RT-PCR and the ΔΔct method. mRNA encoding RPL18 was used as housekeeping gene for normalization. Mean of samples from mock-treated hamsters served as reference. For statistical analysis, ordinary one-way ANOVA was applied with Tukey's multiple comparisons test. ns, not significant ($p > 0.05$), $*p < 0.05$; $**p < 0.01$; $***p < 0.001$.

(D) Absolute mRNA copy numbers were determined by quantitative RT-PCR using a plasmid DNA standard for each gene. Mock-vaccinated hamsters, black circles; MeV_{vac2}-SARS2-S(H)-vaccinated hamsters, blue diamonds; protein-vaccinated hamsters, red triangles.

As a control for successful vaccination, interferon gamma (IFN-γ) secretion was determined. Splenocytes of all animals reacted with IFN-γ secretion after stimulation with the unspecific stimuli Concanavalin A (ConA) or flagellin, which triggered more than 600 spots/10^6 cells in ELISpot, thus demonstrating general functionality. On the other hand, medium- or ovalbumin-stimulated splenocytes showed a background reactivity of 100–250 IFN-γ^+ spots/10^6 cells (Figure 3B). Upon antigen-specific stimulation with recombinant S protein, only animals vaccinated with MeV_{vac2}-SARS2-S(H) or alum-adjuvanted S revealed specific reactivity with approximately 400 spots/10^6 cells or in the range of the upper limit of detection, respectively, thereby demonstrating successful induction of cellular immune responses against the SARS-CoV-2 S protein.

In the absence of suitable assays to quantify hamster IL-4, IL-5, or IL-13 protein, we determined mRNA copy numbers of these cytokines by quantitative RT-PCR in re-stimulated splenocytes and correlated the signals to the hamster housekeeping gene *RPL18* mRNA copies. The total RNA from re-stimulated splenocytes was subjected to analysis (Figure 3C). For normalization, data are presented relative to the average signal in mock-immunized hamsters' splenocytes after the respective stimulation (Figure 3D). S-specific induction of *Il4* (5-fold), *Il5* (>15,000-fold), or *Il13* (70-fold) mRNA was only detected in splenocytes of animals immunized by alum-adjuvanted S and was significantly higher than in splenocytes of MeV-vaccinated animals or naive animals that did not show relevant up-regulation of these T_H2-cytokine genes after re-stimulation.

These data demonstrate that, in contrast to the MeV-derived vaccine, the alum-adjuvanted S protein induced S-specific T_H2-biased immune cells after vaccination, corroborating the hypothesis of VAERD induction after SARS-CoV-2 challenge specifically by Alum+S.

VAERD in hamsters responds to dexamethasone treatment

To further dissect the role of individual lung cell populations during VAERD by scRNA-seq analysis and to evaluate treatment options for VAERD, the initial challenge experiment of vaccinated hamsters was replicated (Figure 4A). Cohorts of 4–6 hamsters were vaccinated as before with alum-adjuvanted S, MeV_{vac2}-SARS2-S(H), or medium (MOCK). For the cohort receiving Alum+S, the number of animals was doubled to assess the impact of treatment with the clinically used immunosuppressant dexamethasone.

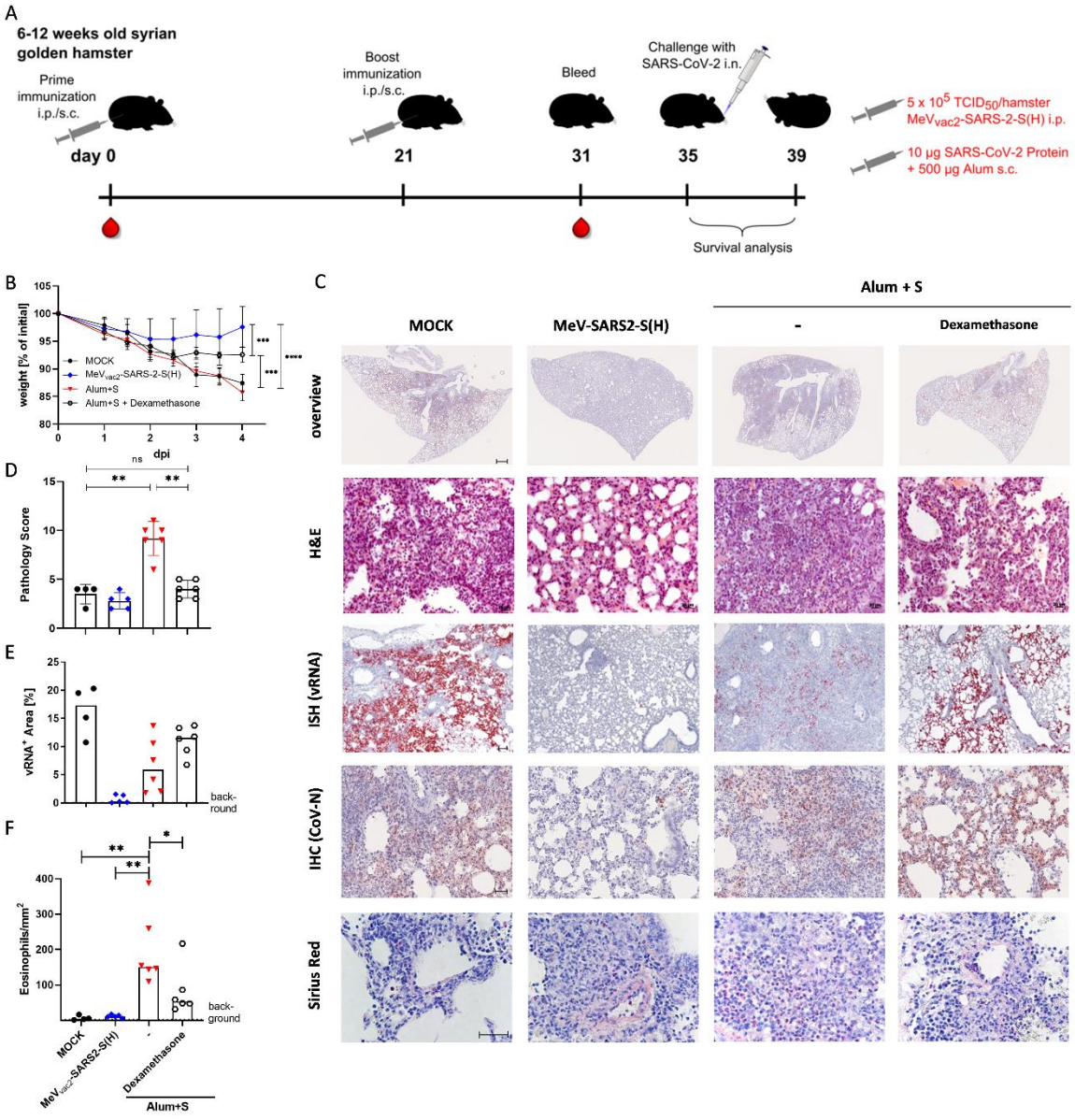

Fig. 4. Protection of vaccinated hamsters and pathology upon SARS-CoV-2 challenge in combination with dexamethasone treatment

(A) Schematic depiction of experimental setting. Syrian hamsters were bled and subsequently immunized with indicated vaccines on days 0 and 21 (n = 4 for mock, n = 5 for MeV_{vac2}-SARS2-S(H), n = 6 for both Alum+S-vaccinated

cohorts). Ten days after the second immunization, hamsters were bled again. On day 35, immunized hamsters were intranasally challenged with low-passage SARS-CoV-2 and observed for another 4 days before sacrifice for organ preparation.

(B and C) Protective efficacy of vaccination was analyzed by (B) quantifying weight loss over time and (C) histopathology of lung sections prepared 4 dpi (scale bars: top row, 1 mm; second row, 20 µm; all other rows, 40 µm). For statistical analysis, two-way ANOVA was applied with Tukey's multiple comparisons test. ***$p < 0.001$; ****$p < 0.0001$.

(D) Blinded histopathological analysis of H&E-stained lung samples (C, second row) was performed, and findings were scored. For statistical analysis, ordinary one-way ANOVA was applied with Mann-Whitney test. ns, not significant; **$p < 0.01$.

(E) Infected areas positive by ISH against SARS-CoV-2 viral RNA (C, third row) were quantified by determining the relative area of tissue staining positive for viral RNA by automated image evaluation of whole slice. Infection was confirmed by IHC against SARS-CoV-2 nucleocapsid protein (C, fourth row).

(F) Infiltration of eosinophils positive by Sirius red staining (C, bottom row) was quantified by determination of the mean number of eosinophils per mm^2 for each animal. Eosinophils of 10 randomly selected fields of view at 200× magnification were counted, and mean was correlated against the area of view. For statistical analysis, ordinary one-way ANOVA was applied with Tukey's multiple comparisons test. *$p < 0.05$; **$p < 0.01$. Mock-immunized, black circles; MeV_{vac2}-SARS2-S(H), blue diamonds; Alum+S without (red triangles) or with (open circles) dexamethasone treatment.

To control immunization and to stratify the cohorts, sera of immunized animals were tested for binding Abs by ELISA and neutralizing Abs by titration of VNT (Figure S3). As expected, immunity against MeV was detected solely after vaccination with MeV_{vac2}-SARS2-S(H). Binding Abs to SARS-CoV-2 S were detected in sera from all animals that received either adjuvanted protein or the MeV-derived vaccine (Figure S3B). However, neutralizing activity inhibiting SARS-CoV-2 was evident only in hamsters immunized with recombinant MeV_{vac2}-SARS2-S(H) (VNT of 10–80), but not in the protein-vaccinated animals (Figure S3H). The binding Ab titers targeting SARS-CoV-2 S were used together with the animals' sex to stratify both Alum+S cohorts for treatment with dexamethasone upon challenge or not. All animals were challenged 14 days after the second vaccination. During the next 4 days, one of both groups that had received Alum+S were treated twice daily with dexamethasone.

Upon infection, weight loss was initially observed in all groups (Figures 4B and S4A). Consistent with previous observations, hamsters immunized with MeV_{vac2}-SARS2-S(H) stopped losing weight by day 2 post infection (p.i.) and recovered thereafter, while naive animals revealed progressive weight loss. This

was also evident for hamsters immunized with the protein vaccine that showed comparable decay. Remarkably, the protein-vaccinated, infected animals treated with dexamethasone revealed another phenotype: weight loss stopped on day 2.5, and the animals' weights stabilized over the next 2 days. All animals were sacrificed on day 4 p.i. for subsequent necropsy.

Analysis of gross pathology replicated the phenotype observed previously (Table S2), with signs of pneumonia and inflamed areas on the lungs of naive animals, while MeV_{vac2}-SARS2-S(H)-immunized hamsters showed few lesions on the lungs' surface (Figure S4B). Moreover, this experiment replicated VAERD as evident already by the overall pathology, with large areas of inflammation on the surface of the S-protein-vaccinated animals' lungs and a swollen appearance of the entire lung. This effect was prevented in the dexamethasone-treated animals. Their lungs were comparable to the lung explants of the MeV_{vac2}-SARS2-S(H)-immunized cohort. Lungs were subjected to bronchoalveolar lavage (BAL) and subsequently sampled.

Histopathologic analyses of lung samples after H&E, ISH, immunohistochemistry, and Sirius red staining exactly replicated the VAERD phenotype for Alum+S-vaccinated animals and the absence thereof in MeV_{vac2}-SARS2-S(H)-vaccinated animals (Figure 4C). When Alum+S-immunized animals were treated with dexamethasone, the VAERD phenotype was lost. In these samples, the inflammatory phenotype was absent and lung tissue reflected the appearance of MeV_{vac2}-SARS2-S(H)-immunized hamsters, while the pathology score decreased significantly (Figure 4D). Despite this normalization of lung pathology, immunohistochemistry for SARS-CoV-2 N or ISH for SARS-CoV-2 genomes was not markedly different from naive challenged animals and was enhanced when compared with Alum+S-vaccinated, challenged hamsters without dexamethasone treatment (Figure 4C, last column).

Furthermore, live-virus titers and viral RNA copy numbers, as determined in lung tissue (Figures 5A and 5B) and BAL cells (Figure 5C), were in agreement with this phenotype. Virus RNA copy numbers in lung tissue were significantly reduced in hamsters vaccinated with MeV_{vac2}-SARS2-CoV (0.36–8.28 E-gene copies/RPL18 copy) compared with naive infected animals (110.8–235.3 E-gene copies/RPL18 copy), consistent with the absence of live virus in the lungs of all animals in the MeV group (Figure 5A). Compared with naive/unvaccinated infected hamsters, viral burden was lower in hamsters immunized

with Alum+S but increased slightly when these hamsters were treated with dexamethasone during the challenge. Comparable virus RNA copy numbers were obtained for the BAL cells studied.

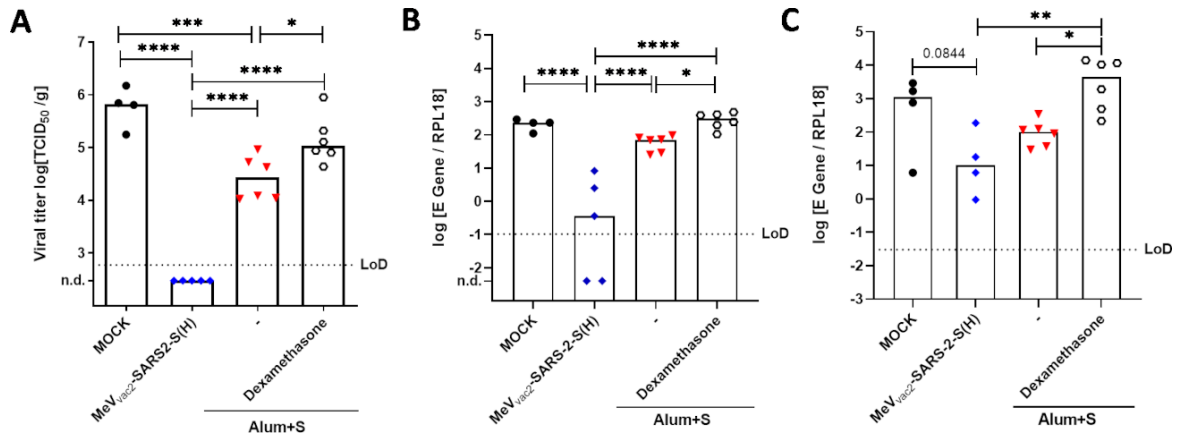

Fig. 5. Impact of vaccination or dexamethasone treatment on SARS-CoV-2 titers upon challenge of Syrian hamsters

Protection of vaccinated hamsters upon challenge with SARS-CoV-2 was analyzed 4 dpi by (A) titration of live-virus titers in lung tissue or (B and C) determination of relative SARS-CoV-2 E gene copy numbers in (B) lung tissue or (C) bronchoalveolar lavage (BAL) cells by quantitative RT-PCR. *RPL18* housekeeping gene copies were used for normalization. Lower LoDs are indicated by dotted lines. Each data point represents an individual animal vaccinated with medium (black circles), MeV_{vac2}-SARS2-S(H) (blue diamonds), or alum-adjuvanted S protein without (red triangles) or with (open circles) dexamethasone treatment. For statistical analysis, ordinary one-way ANOVA was applied with Tukey's multiple comparisons test. ns, not significant ($p > 0.05$), *$p < 0.05$; **$p < 0.01$; ***$p < 0.001$; ****$p < 0.0001$.

Thus, viral loads and extent of tissue infection did not correlate with the inflammatory phenotype of pathology, consistent with an immunopathogenesis as the basis for VAERD, which again was not observed for the T_H1-biased MeV-COVID-19 model vaccine candidate. Moreover, the responsiveness of the pathology to dexamethasone treatment indicates a role for immune cells in this process.

Dysregulation of T_H2 cytokines in lungs and BAL cells

To confirm pulmonary up-regulation of *Il4*, *Il5*, *Il13*, and *eotaxin-1* mRNAs in protein-vaccinated animals and to determine if this dysregulation was also observed in BAL cells after infection, total RNA from the respective cells was subjected to quantitative RT-PCR (qRT-PCR). These analyses revealed significant induction of all four cytokine genes in lung cells and revealed the same tendency in BAL cells after infection of protein-vaccinated animals. In contrast, vaccination with the T_H1-biased MeV_{vac2}-SARS2-S(H) down-regulated expression of these critical genes, while dexamethasone treatment did not alter the

cytokine expression pattern (Figure S5). Therefore, induction of T_H2 cytokines in protein-vaccinated animals identified by RNA-seq in the first experiment was confirmed in this second cohort of hamsters.

Assignment of dysregulation to individual cells in lungs by scRNA-seq

To delineate the role of individual cell populations, scRNA-Seq data of infected lungs were generated and first analyzed to determine cellular subsets according to individual cellular gene expression profiles, as described previously (Nouailles et al., 2021). Accordingly, 25 individual cell clusters were defined, and their transcriptional profiles identified 13 different cell populations including immune cells (Figure 6B). Minor differences between vaccine cohorts became evident in the relative cell frequencies in the infected lungs. In naive animals, and even more so in Alum+S-vaccinated animals, lung macrophages, which revealed traits of an interstitial macrophage phenotype, were overrepresented compared with the MeV-vaccinated group. In contrast, alveolar macrophages were observed at higher frequencies in MeV-vaccinated animals' lungs (Figure 6C).

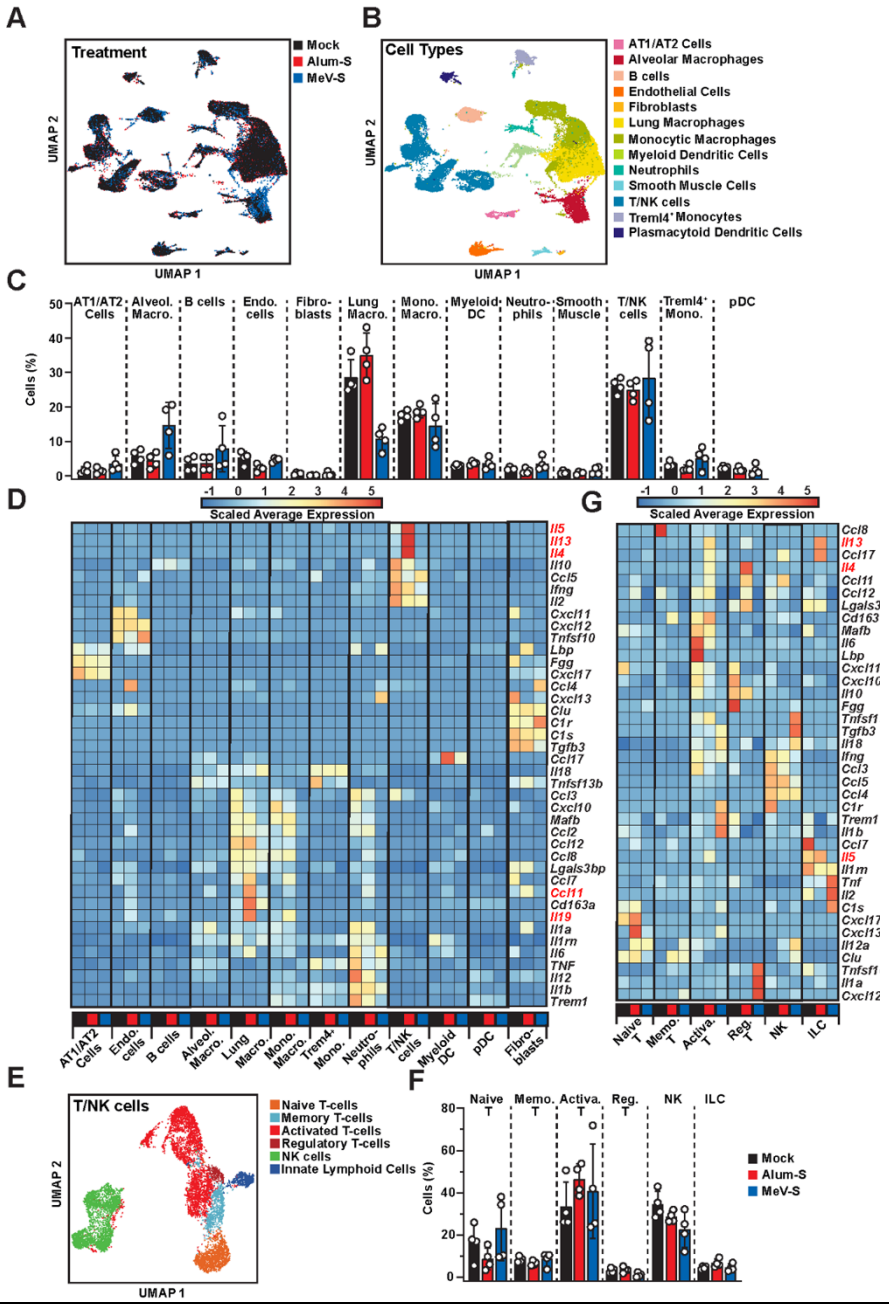

Fig. 6. Annotation of cell populations in infected hamster lungs and respective gene regulation

(A–C) Definition (A), annotation (B), and proportion (C) of specific cell populations found in the lungs of differently vaccinated hamsters 4 dpi with SARS-CoV-2 (n = 4).

(D) Differentially regulated genes of interest in these cell populations are displayed in the presented heatmap.

(E–G) To further pinpoint dysregulation of T or NK cells, the respective cell subsets were (E) annotated according to maker genes, (F) quantified, and (G) dysregulation of genes was resolved in the respective heatmap as displayed.

(A, C, D, F, and G) Black, mock-vaccinated hamsters; red, hamsters vaccinated with Alum+S; blue, hamsters vaccinated with MeV_{vac2}-SARS2-S(H) (MeV-S).

The gene-expression profiles of these distinct cell populations showed specific patterns (Figure 6D). Exclusive up-regulation of *Ccl11* expression in the Alum+S group could be assigned to the overrepresented lung macrophages (Figure 6D). Induction of *Il4*, *Il5*, and *Il13* became evident exclusively in the population of T and natural killer (NK) cells (Figure 6D, three top panels). Zooming in on specific T/NK cell subsets (Figures 6E and 6F), up-regulation of *Il4* was found in regulatory T cells, while *Il5* and *Il13* expression was assigned to cells with an innate lymphoid cell phenotype (Figure 6G) and activated T cells (Table S3). In contrast, MeV_{vac2}-SARS2-S(H)-vaccinated animals reflected a similar, but dampened, response when compared with naive infected animals, with few genes being differentially regulated. On the other hand, monitoring the distribution of SARS-CoV-2 RNA sequences indicating virus infection or uptake revealed a broad distribution of viral RNA in most cell types in naive/unvaccinated, infected animals (Figures 7A and 7B). This distribution was more focused in lung macrophages in Alum+S-vaccinated animals and correlated to some extent with the expression profiles of Fcγ receptors IIb and IV, which were found to be specifically up-regulated after infection in both naive and Alum+S-vaccinated samples (Figure 7C).

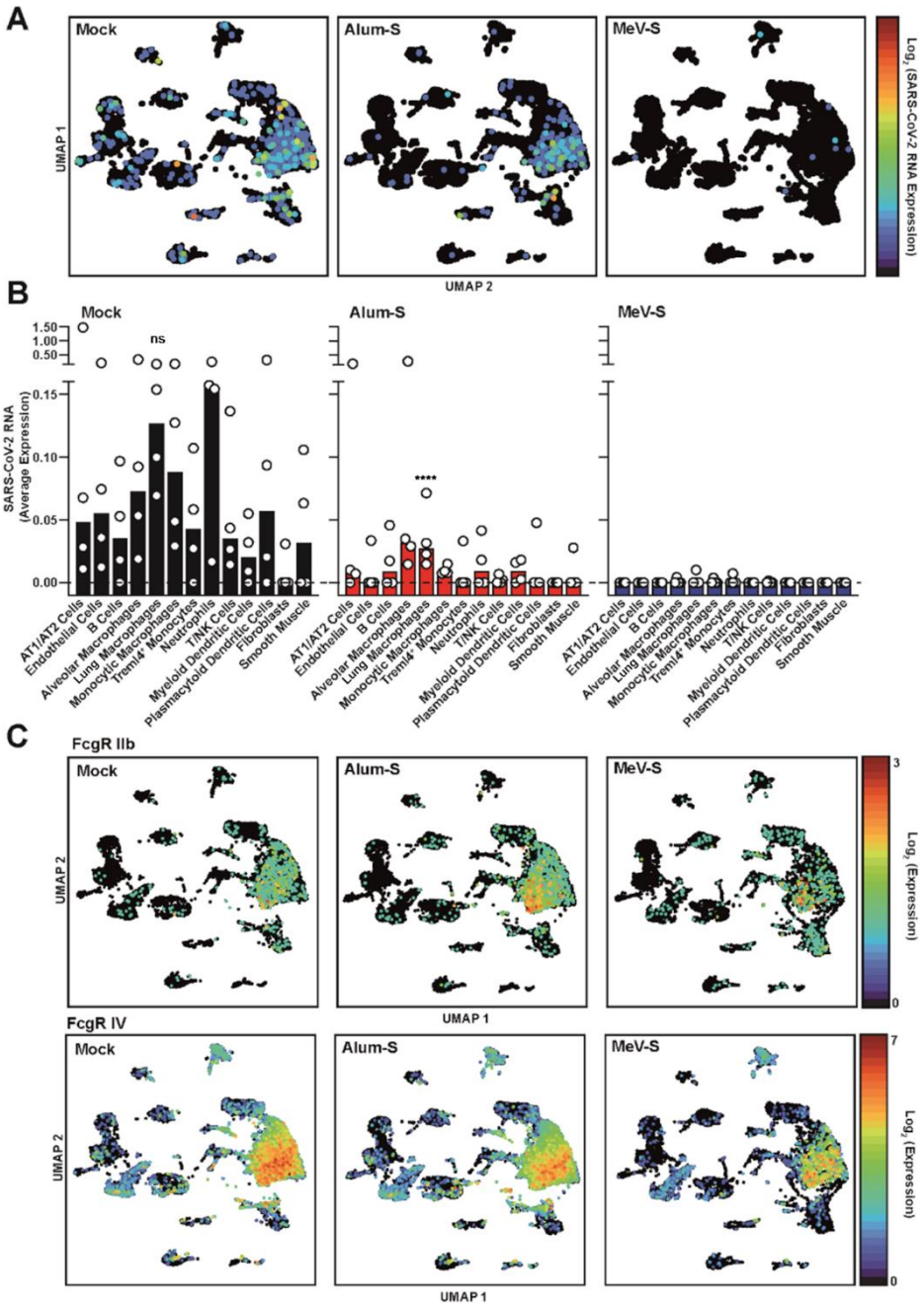

Fig. 7. Assignment of SARS-CoV-2 reads and FcR expression to cell populations in infected hamster lungs

(A and B) Assignment of SARS-CoV-2 genome reads to cell populations defined in Figure 6 (A) and quantification of respective positive cells of the different treatment groups as indicated (B). Single dots represent individual animals. Differential expression of SARS-CoV-2 RNA was analyzed using the Loupe Browser 6.0.0. Statistical significance was tested by comparison of individual cell populations with all other cells within the different treatment groups, p values were adjusted using Benjamini-Hochberg correction for multiple testings. ns, not significant; ****$p < 0.0001$.

(C) Assignment of mRNA reads encoding hamster FcγR IIb (top panel) or FcγR IV (bottom panel) to cell populations defined in Figure 6.

To further mine the scRNA-seq data, we performed both gene set variation analysis (GSVA) and gene set enrichment analysis (GSEA) using the REACTOME, KEGG, and GO databases on specific cell populations that contribute to the VAERD observed in Alum+S-vaccinated animals (Figures S6 and S7), focusing on alveolar macrophages, lung macrophages, monocytic macrophages, *Treml4*$^{+}$ monocytes, and T/NK cells. For GSVA, normalized, by-cell-population gene-expression values were used as input, while DEGs between the unvaccinated and either Alum+S- or MeV_{vac2}-SARS2-S(H)-vaccinated conditions were utilized for GSEA. These analyses highlight pathways and biological processes, which are induced by SARS-CoV-2 infection and are differentially targeted or regulated across these selected cell types, dependent on prior immune status and vaccination type. These supportive analyses of the hamster lung scRNA-seq data provide insights into how the observed transcriptional differences mediate their downstream effects, exhibiting differential targeting of a broad range of cellular process or canonical pathways in a cell-type-specific manner.

Taken together, the scRNA-seq data assigned the up-regulation of IL-4, IL-5, and IL-13 to specific T cell subpopulations induced by vaccination with Alum+S, while CCL-11 and IL-19 expression was contributed by lung macrophages, which were overrepresented, revealed up-regulation of Fcγ receptors, and were the main target population containing an excess of SARS-CoV-2 RNA. These aberrant patterns of dysregulated gene expression were not observed in animals vaccinated with the prototypic T_H1-biased MeV-COVID-19 vaccine candidate.

Discussion

Based on these data, we propose the following immune-cell-mediated mechanism for induction of VAERD: vaccination with alum-adjuvanted S protein in de-folded conformation induces low levels of non-protective S-specific binding Abs lacking neutralizing activity. In parallel, T_H2-biased S-specific T cell responses were induced as evidenced by the significant up-regulation of IL-4, IL-5, and IL-13 after recall. After infection, these immune responses lowered the virus load to some extent, but the induction of T_H2 immunity promoted VAERD via the IL-4/IL-5/IL-13 chemokine axis secreted by regulatory T cells and innate lymphoid cells. These processes are likely reinforced by IL-19 secreted by hyperstimulated lung macrophages, which, in addition, express further chemo-attractants such as CCL-11, the major attractant of eosinophils. Indeed, massive infiltration of eosinophils completed the picture of VAERD. Macrophage activity correlated with SARS-CoV-2 virus genome enrichment. It is therefore tempting to hypothesize that the enrichment of SARS-CoV-2 RNAs in macrophages is caused by Fcγ-receptor-mediated uptake of opsonized viruses as previously proposed for ADE processes and recently demonstrated for enrichment

of SARS-CoV-2 in monocytes of the peripheral blood of patients with severe COVID-19 (Junqueira et al., 2022).

While our data support such a model for induction of VAERD by sub-optimal T_H2-biased prototypic vaccines targeting SARS-CoV-2, the nature of these findings seems quite striking. VAERD had been clearly observed for both MERS-CoV and SARS-CoV in the respective transgenic mouse models after vaccination with T_H2-biased, whole-inactivated virus vaccines (Bolles et al., 2011; Tseng et al., 2012; Iwata-Yoshikawa et al., 2014; Honda-Okubo et al., 2015; Agrawal et al., 2016). Since no human vaccines had been tested against these two pathogens, the transferability of these findings to the occurrence of VAERD in humans remained unclear. Nevertheless, this potential risk was perceived also for vaccine-induced immune responses that target the closely related SARS-CoV-2 and triggered vaccine developers to aim for T_H1-biased immunity and to assess the potential of immunopathogenesis in the available animal models (Anderson et al., 2020; Corbett et al., 2020a, 2020b; Jackson et al., 2020; Polack et al., 2020; Ramasamy et al., 2020; Walsh et al., 2020; Sadoff et al., 2021; Stephenson et al., 2021; van der Lubbe et al., 2021). Despite all these efforts, only two studies have been published so far that revealed evidence for VAERD potential upon vaccination of T_H2-prone BALB/c mice with denatured antigen followed by a challenge with a mouse-adapted recombinant SARS-CoV-2 (DiPiazza et al., 2021; Iwata-Yoshikawa et al., 2022). While using an unbiased animal model and non-adapted SARS-CoV-2 and going beyond the mechanistic hypotheses expressed (Iwata-Yoshikawa et al., 2022), our study aligns well with these mouse data in the observed VAERD phenotype with T_H2 cytokine secretion and massive eosinophil attraction. However, no other studies so far have identified evidence for the risk of enhanced disease upon COVID-19 vaccination. How can this discrepancy be explained?

The sub-optimal immunization regime of vaccinating Syrian hamster subcutaneously with alum-adjuvanted, non-stabilized S protein was expected to give a rather mediocre (Nürnberger et al., 2019), but T_H2-biased, immune response (Ko et al., 2017) as a worst-case control in our earlier study describing a MeV-derived COVID-19 vaccine candidate (Hörner et al., 2020). Indeed, only binding Abs with no neutralizing activity were induced, and no antigen-specific $CD8^+$ T cell killing activity was observed by us (Hörner et al., 2020) or others (DiPiazza et al., 2021; Iwata-Yoshikawa et al., 2022). Our observations thereby closely resemble VAERD induced by inactivated RSV (Johnson and Graham, 1999; De Swart et al., 2002; Johnson et al., 2003, 2004; Moghaddam et al., 2006) or MeV in the respective animal models (Polack et al., 2003), which are quite reminiscent of the situation observed in human VAERD after RSV (Openshaw, 2001) or measles vaccination (Nader and Warren, 1968) using whole-inactivated virus vaccines. Moreover, induction of protective immune responses, or in the worst-case scenario, immunopathogenesis, represents a complex interplay of innate immune processes that set the stage for

humoral and cellular adaptive immunity. This can also be deduced from our data. While dexamethasone did not inhibit T_H2 cytokine expression, here, it clearly reduced pathology in the VAERD setting, in addition to naive infected hamsters (Wyler et al., 2022; Yuan et al., 2022). Thereby, a quite delicate process is revealed, balancing immune activities destructive against pathogen or host tissue, which may be difficult to trigger.

Limitations of the study

As already pointed out by DiPiazza *et al.*, drawing conclusions from animal models and extending these observations to the immunological situation in humans may be a difficult task (DiPiazza et al., 2021). However, we were able to replicate VAERD induced by a protein-based COVID-19 vaccine candidate with a very similar phenotype in a second animal model, Syrian hamsters, using an unmodified low-passage virus isolate. Therefore, our data strongly support the idea of monitoring vaccinated human patients that experience a break-through infection closely. In any case, while our experimental vaccines mimic, but are not the same as, the authorized vaccines, these and previously published data point to few concerns for vaccines developed to trigger T_H1-biased responses such as viral vector platform-based vaccines, mRNA vaccines, or other vaccine concepts developed for such bias by, e.g., using respective adjuvants. Moreover, even if VAERD as observed in our model should occur in human patients, this immunopathology would be treatable by dexamethasone, which was confirmed to be an effective medication for severe courses of COVID-19 anyway (Tomazini et al., 2020; Horby et al., 2021). This would be good news also for putative VAERD being mistakenly diagnosed as a variant of the usual forms of severe COVID-19 in a naive patient.

A further limitation of our study is the restriction of our analyses to a single time point of disease. It would be interesting to analyze further progression of the animals with or without VAERD. However, the applied challenge model is rather harsh. The hamsters lose weight after infection with a highly reproducible kinetics that necessitates sacrifice of 50 %–83 % of naive animals due to humane endpoints 5 to 6 days after infection (Hörner et al., 2020), and statistically significant differences cannot be expected by realistic animal numbers. Therefore, day 4 after infections was chosen as the day of analyses since this is the time point during infection when most dramatic effects can be expected (measurable weight loss starts at day 2 p.i.), but all animals are still available.

In conclusion, our data support the idea that ADE-like processes, as reported by Wan et al. for MERS-CoV, could be relevant in the mechanism of VAERD. For MERS-CoV, a monoclonal Ab binding to the RBD of the S is able to cross-link MERS-CoV S and Fc receptors. When tested in a pseudovirus assay, this monoclonal Ab mediated virus entry into CD32A-expressing (i.e., FcγRIIA-positive) cells and

macrophages (Wan et al., 2020). Such an uptake mechanism would explain the enrichment of SARS-CoV-2 genomes in macrophage populations correlating with the Fc-receptor distribution as observed in our study. Recent clinical data have demonstrated evidence that monocytes in the peripheral blood of patients with severe COVID-19 take up opsonized SARS-CoV-2 particles via this route and are impacted by this process (Junqueira et al., 2022). In any case, enrichment of SARS-CoV-2 in and stimulation of this immune cell population result in the secretion of the major eosinophil attractant CCL-11 and IL-19, which can drive regulatory T cells (T_{reg}s) into T_H2 polarization. Together with the IL-4/IL-5/IL-13 chemokine axis of such S-specific T_H2-biased CD4 helper cell populations, CCL-11 can be expected to cause infiltration of eosinophils in a process mechanistically reminiscent of allergic asthma, resulting in the immunopathogenesis observed in our study.

Key resources table

REAGENT or RESOURCE	SOURCE	IDENTIFIER
Antibodies		
HRP-conjugated goat anti-hamster IgG	Sera care KPL	Cat#5220-0371
mAb against SARS-CoV nucleocapsid protein	Bussmann *et al.*, 2006	clone 4F3C4
secondary biotinylated goat anti-mouse Ab	Vector Laboratories	Cat#BA-9200-1.5
mAb against M protein of Influenza A virus	ATCC	clone HB-64
Bacterial and virus strains		
MeV_{vac2}-SARS2-S(H)	Hörner *et al.*, 2020	N/A
MV_{vac2}-GFP(P)	Malczyk *et al.*, 2015	N/A
SARS-CoV-2 isolate MUC-IMB1	Böhmer *et al.*, 2020	GenBank# MT270101.1
Chemicals, peptides, and recombinant proteins		
SARS-CoV-2 (2019-nCoV) Spike S1+S2 ECD-His Recombinant Protein	Sino Biological Europe	Cat#40589-V08B1
SARS-CoV-2 Trimeric Spike (stabilized Spike)	NIBSC	Cat#101007
Rec. Ovalbumin	Schuelke S *et al.*, 2010	RefSeq# NM205152
Rec. Flagellin A	Schuelke S *et al.*, 2010	RefSeq# X65624
Concanavalin A	Sigma-Aldrich	Cat#11028-71-0
MeV bulk antigens	Virion Serion	Cat#BA102VS-S
Dispase	Corning	Cat#354235
DNAse	AppliChem	Cat#A3778,0100
Collagenase B	Roche	Cat#11088815001
Actinomycin D	Sigma-Aldrich	Cat#A9415-5MG
Aluminum hydroxid (Allhydrogel adjuvant 2 %)	InvivoGen	Cat#Vac-alu-250
3-Amino-9-ethyl-carbozole	Sigma-Aldrich	Cat#A5754-10G
Dexamethosone	Bela-pharm	Cat#6933074.00.00
Direktrot 80	Sigma-Aldrich	Cat#365548
Entellan	Sigma-Aldrich	Cat#107060
Papanicolaous solution 1b Hematoxylin S	Sigma-Aldrich	Cat#1.09254
RBC Lysis buffer	Santa Cruz Biotechnology	Cat#sc-296258
RNAscope® Pretreatment Reagents	Bio-Techne	Cat#322330 and 322000
RNAscope® Negative Control Probe	Bio-Techne	Cat#310043

TMB substrate	Invitrogen	Cat#00-4201-56
TRIzol Reagent	Ambion, Thermo Fisher Schientific	Cat#15596026
Critical commercial assays		
Chromium Next Gem Chip G Single Cell Kit	10x genomics	Cat#1000121
Chromium Next Gem Single cell 3' GEM, Library & Gel Bead Kit v3.1	10x genomics	Cat#1000120
Direct-zol RNA MiniPrep kit	Zymo research	Cat#R2052
Hamster IFN-γ ELISpot^{BASIC} kit	MABTECH	Cat#3102-2H
QIAseq FastSelect –rRNA HMR Kit	Qiagen	Cat#334385
RNAscope® 2.5 HD Assay – RED Kit	Bio-Techne	Cat#322360
Superscript III one step RT-PCR system with Platinum Tag Polymerase	Invitrogen	Cat#12574-026
Vectastain Elite ABC Kit	Vector Laboratories	Cat#PK6100
Deposited data		
Bulk RNA-seq	This Paper	GEO: GSE195939
scRNA seq data	This Paper	GEO: GSE196938
Experimental models: Cell lines		
Vero (African green monkey kidney)	ATCC	CCL-81
Vero clone E6	ATCC	CRL-1586
Experimental models: Organisms/strains		
Syrian golden hamster (Mesocricetus auratus); HsdHan:AURA	Envigo	Art#8903
Oligonucleotides		
s. Table S4		
Software and algorithms		
ELI.Analyse V5.0	AE.L.VIS	http://www.aelvis.de
fastp algorithm	Chen *et al.*, 2018	https://github.com/OpenGene/fastp
CLC Genomics Workbench 21.0.4	QIAGEN	https://digitalinsights.qiagen.com
CellRanger v5.0	10x genomics	https://support.10xgenomics.com/single-cell-gene-expression/software
R packages Seurat v4.0	Hao *et al.*, 2021	https://satijalab.org/seurat/
DoRothEA v3.12	Holland *et al.*, 2020	https://saezlab.github.io/dorothea/
GSVA R package	Hänzelmann *et al.*, 2013	http://bioconductor.org/packages/release/bioc/html/GSVA.html
clusterProfiler R package	Wu *et al.*, 2021	https://bioconductor.org/packages/release/bioc/html/clusterProfiler.html
Prism 9.2.0	GraphPad Software	http://www.graphpad.com
Original code used in the analysis of the single cell data	This Paper	https://github.com/Berlin-Hamster-Single-Cell-Consortium/Vaccine-associated-enhanced-respiratory-pathology-in-COVID-19-hamsters-after-T_H2-biased-immunization
Other		

Lysing Matrix M tubes	MP biosciences	Cat#6923100
J-810 Spectropolarimeter	JASCO	https://www.jasco.de/en
Eli.Scan ELISpot scanner	AE.L.VIS	http://www.aelvis.de
Qubit 4 Fluorimeter	Thermo Fisher	Cat#Q33238
Precellys24 tissue homogenizer	bertin TECHNOLOGIES	Cat#P000669-PR240-A
2100 Bioanalyzer Instrument	Agilent	Part#G2939BA
Novaseq 6000	Illumina	Cat#20013850
NextSeq 550	Illumina	Cat#SY-415-1002
Hamamatsu S60 scanner	Hamamatsu Photonics	Prod#C13210
Chromium Controller	10x Genomics	Prod# 1000204

Experimental model and subject details

Cells

Vero (African green monkey kidney; ATCC# CCL-81) and Vero clone E6 (ATCC# CRL-1586) cells were purchased from ATCC (Manassas, VA, USA) and cultured in Dulbecco's modified Eagle's medium (DMEM, Sigma Aldrich, Steinheim, Germany) supplemented with 10 % fetal bovine serum (FBS; Sigma Aldrich) and 2 mM L-glutamine (L-Gln, Sigma Aldrich). Cell cultures were incubated at 37 °C in a humidified atmosphere containing 6 % CO2 up to 30 passages after thawing of the initial stocks to ensure authentication of utilized cell lines.

Viruses

MeV_{vac2}-SARS2-S(H) (Hörner et al., 2020) and MV_{vac2}-GFP(P) (i.e. MV_{vac2}-ATU(P) (Del Valle et al., 2007) with GFP inserted in the ATU (Malczyk et al., 2015) have been described previously. Subsequent passages were generated after $TCID_{50}$ titration of infectious virus according to the method of Kaerber and Spaerman (Kärber, 1931). Stocks were generated by infection of Vero cells at an MOI = 0.03, and viruses in P3 or P4 were used for vaccination experiments. SARS-CoV-2 isolate MUC-IMB1 (Böhmer et al., 2020) was used in passage 3 on Vero-E6 cells after isolation from the patient as described before (Hörner et al., 2020).

Syrian golden hamster animal model

All animal experiments were carried out in compliance with the regulations of German animal protection laws and as authorized by the RP Darmstadt and reported according to the ARRIVE guidelines. Six to 12-weeks old Syrian hamsters (Envigo RMS, Venray, Netherlands) were randomized for age- and sex-matched groups. Male and female hamsters were used in a 1:1 ratio to ensure transferability of results to both sexes, cohort sizes (n = 6) were chosen to ensure statistical validation with an error probability of $p < 0.05$ with a power of 80 % conservatively assuming an effect size of 0.8. Animals were vaccinated

intraperitoneally (i.p.) in a prime-boost schedule (days 0 and 21) with 5×10^5 $TCID_{50}$ of recombinant MeV-derived vaccine virus in 200 µL volume or subcutaneously (s.c.) with 10 µg recombinant SARS-CoV-2 S protein (Cat-No. 40589-V08B1, Sino Biological Europe, Eschborn, Germany) adjuvanted with 500 µg aluminum hydroxide (Allhydrogel adjuvant 2 %, vac-alu-250, InvivoGen, San Diego, CA, USA) in 100 µL volume. Blood was drawn on days 0 and 21 or 31. Splenocytes of vaccinated animals were isolated 14 days after second immunization or hamsters were challenge by intranasal application of 4×10^3 $TCID_{50}$ SARS-CoV-2 (isolate MUC-IMB1) in passage 3 in 100 µL volume. Alum+S vaccinated hamsters were divided in two groups: i) a untreated group and ii) a dexamethasone treated one (1 mg/kg body weight twice daily orally or subcutaneously). Animals were euthanized 4 days after infection. Specific sections of each lung were prepared for histology (left lobe), analysis of total RNA (right middle lobe), titration of live virus (right apical lobe), and analysis of transcriptomics by scRNA-Seq (caudal lobe), where applicable.

Method details

CD spectroscopy

The secondary structure of SARS-CoV-2 Spike was analysed using circular dichroism spectroscopy and J-810 spectropolarimeter (JASCO) equipped with a quartz cuvette (0.1 cm). Spectra were recorded at room temperature from 255 nm–185 nm by accumulating 10 runs (bandwidth 1 nm, scanning speed 50 nm/min) using 0.16–0.58 µM protein solutions in 20 mM sodium phosphate buffer pH 8.0.

Bronchoalveolar lavage (BAL)

Lungs from sacrificed hamsters were inflated with 2.5 mL PBS via the trachea. The BAL fluid was collected and cells were harvested by centrifugation (1,200 rpm, 4 °C, 5 min). The cell-free fluids were removed and the cells were resuspended in 350 µL TRIzol Reagent (Ambion, Thermo Fisher Scientific).

Virus neutralization test (VNT)

Virus neutralization tests (VNT) were performed as described previously (Hörner et al., 2020). In short, serum samples were diluted in 2-fold series in DMEM. 50 PFU MV_{vac2}-GFP(P) or 100 $TCID_{50}$ SARS-CoV-2 were mixed with diluted serum samples and incubated at 37 °C for 1 h. Subsequently, the virus-serum mixture was added to 1×10^4 Vero or Vero E6 cells seeded 3 h before in 96 well plates (Thermo Fisher Scientific, Ulm, Germany). Cells were incubated for 4 days at 37 °C in a humidified atmosphere containing 6 % CO2. Virus neutralizing titers were determined as the reciprocal of the highest serum dilution that completely abrogated infectivity.

Total IgG quantification

0.5 µg MeV bulk antigens (Virion Serion, Würzburg) or 0.25 µg recombinant SARS-CoV-2 S protein were coated in 50 µL/well carbonate buffer (Na2CO3 30 mM; NaHCO3 70 mM; pH 9.6) on Nunc Maxisorp® 96 well ELISA plates (eBioscience). After overnight incubation at 4 °C, the plates were washed three times with 200 µL PBS containing 0.1 % Tween 20 (w/v) and blocked with 100 µL PBS containing 5 % BSA and 0.1 % Tween 20 for at least 2 h at ambient temperature. Hamster sera were 5-fold serially diluted in PBS containing 1 % BSA and 0.1 % Tween 20. 50 µL/well of serum dilutions were used in the assay and the plates were incubated at 37 °C for 2 h prior to washing the plates three times using PBS containing 0.1 % Tween20. Subsequently, 50 µL/well of HRP-conjugated goat anti-hamster IgG (1:1,000 in PBS containing 1 % BSA and 0.1 % Tween20; Sera care KPL, Cat. 5220-0371) were added and the plates were incubated for 1 h at room temperature. After washing the plates three times, 100 µL/well TMB substrate (Invitrogen) was added. The reaction was stopped by addition of 50 µL/well 1 N H2SO4 and the absorbance at 450 nm (specific signal) and 630 nm (reference wavelength) was measured.

IFN-γ ELISpot analysis

Hamster interferon gamma (IFN-γ) enzyme-linked immunosorbent spot (ELISpot) analysis was performed using the Hamster IFN-γ ELISpotBASIC kit (MABTECH, Nacka Strand, Sweden) in combination with multiscreen immunoprecipitation (IP) ELISpot polyvinylidene difluoride (PVDF) 96-well plates (Merck Millipore, Darmstadt, Germany) according to the manufacturer's instructions. 5×10^5 isolated splenocytes were co-cultured with different stimuli in 200 mL RPMI containing 10 % FBS, 2 mM L-Gln, 10 mM HEPES pH 7.4, 50 mM 2-mecaptoethanol and 1 % Penicillin-streptomycin. To re-stimulate SARS-CoV-2 specific T cells, isolated splenocytes were cultured with 10 mg/mL recombinant SARS-CoV-2 (2019-nCoV) Spike Protein (S1+S2 ECD, His tag) (Sino biological Europe). Recombinant Ovalbumin [10 mg/mL] served as negative protein control. In parallel, splenocytes were stimulated with 10 mg/ml MeV bulk antigen (Virion Serion, Würzburg, Germany). General stimulation of T cells was achieved using 5 µg/mL concanavalin A (ConA, Sigma-Aldrich) or recombinant 20 µg/mL Flagellin A produced in house (Schülke et al., 2011). Untreated splenocytes served as negative control. After 36 h of stimulation, cells were removed and plates were incubated with biotinylated detection antibodies and Streptavidin-HRP conjugate following the manufactures introductions using a 1 in 100 dilution for the streptavidin-HRP conjugate with 3-Amino-9-ethyl-carbazole (AEC; Sigma-Aldrich) dissolved in N,N-dimethylformamide (Merck Millipore) as substrate. Spots were counted using an Eli.Scan ELISpot scanner (AE.L.VIS, Hamburg, Germany) and analysis software ELI.Analyse V5.0 (AE.L.VIS).

Determination of infectious virus lung titers

The right apical lobe of the lungs of infected animals was snap-frozen in liquid nitrogen and homogenized in 1 mL ice-cold DMEM containing 2 mM L-Gln and 1 % Penicillin/Streptomycin in Lysing Matrix M tubes (MP Bioscience, Hilton, UK) using the Precellys24 tissue homogenizer (bertin TECHNOLOGIES, Montigny-le-Bretonneux, France) for 2 × 10 s at 6,000 rpm. Samples were kept on ice at all times. Subsequently, organ debris was removed by centrifugation (13 min, 6,800 rpm, 4 °C). Vero E6 cells were inoculated with the supernatants in a 10-fold dilution series for 7 d at 37 °C. SARS-CoV-2 organ titers were calculated by the $TCID_{50}$ method of Kaerber and Spearman according to virus-induced CPE and adjusted for 1 g of tissue.

RNA preparation

The right middle lobe of the lungs of infected animals was homogenized in 1 mL TRIzol Reagent (Ambion, Thermo Fisher Scientific) in Lysing Matrix M tubes (MP Bioscience, Hilton, UK) using the Precellys24 tissue homogenizer (bertin TECHNOLOGIES) for 2 × 15 s at 6,000 rpm. Samples were kept on ice at all times. Organ debris was removed by subsequent centrifugation (13 min, 6,800 rpm, 4 °C). Clear supernatant was used for RNA purification with Direct-zol RNA MiniPrep kit (Zymo research, Freiburg (Breisgau), Germany) according to the manufacturer's introduction.

Quantitative reverse-transcription PCR (qRT-PCR)

RNA samples were quantified by quantitative reverse transcription-PCR (qPT-PCR) using Superscript III one step RT-PCR system with Platinum Tag Polymerase (Invitrogen, Darmstadt, Germany). Primer and probe sequences for mRNA encoding the SARS-CoV-2 E gene (Corman et al., 2020), hamster RPL18 (Zivcec et al., 2011), IL-4, and IL-13 (Espitia et al., 2010) were used as described and are indicated in Table S4. Primers for detection of Eoatxin-1 (Stanelle-Bertram et al., 2020) and forward primer sequences for IL-5 (Mendlovic et al., 2015) were ordered as described. The reverse primer sequence for IL-5 was adapted according to RNA Seq results of hamster lungs as described in this manuscript. Probes for mRNA encoding Eotaxin and IL-5 were designed as shown in Table S3. Reactions were run in 96-well plates (Bio-Rad Laboratories, Hercules, CA) using CFX96 qPCR cycler (Bio-Rad Laboratories) and 5 µL RNA in a total reaction volume of 25 µL in triplicates. An internal Hamster reference (linear range, 4.5×10^6 to 4.5×10^2 copies (Hörner et al., 2020)) was used for quantification of SARS-CoV-2 E gene copy numbers. This reference was validated for copy numbers of RPL18 housekeeping gene by utilization of a PCR product DNA reference generated as described (Osterrieder et al., 2020), and was used for quantification in subsequent runs (linear range, 1.8×10^5 to 1.82×10^2 copies). The following cycling conditions were used for all analyses: reverse transcription for 10 min at 55 °C, denaturation for 180 s at 94 °C, followed by 45

cycles of 15 s at 94 °C and 30 s at 58 °C. Quantified sample copy numbers were normalized to copy numbers of the hamster housekeeping gene RPL18. If direct quantification was not possible, the ΔΔct method was used.

Total RNA-Seq

The isolated RNA samples were used for NNSR priming based RNA-Seq library preparation (Levin et al., 2010) (as described in (Brown et al., 2020), vRNA NGS section) with the following modifications. Total RNA, was subjected to rRNA removal using the QIAseq FastSelect –rRNA HMR Kit (Qiagen) in combination with reverse transcription as follows. A 35 µL reaction mixture containing 1 µg RNA, 100 pmol NNSR_RT primer (gctcttccgatctctNNNNNN), 8 µL of 5× SuperScript IV buffer (Invitrogen) 20 pmol dNTPs and 1 µL of FastSelect-rRNA mix was subjected to the following hybridization protocol: 75 °C 2 min, 70 °C 2 min, 65 °C 2 min, 60 °C 2 min, 55 °C 2 min, 37 °C 5 min, 25 °C 5 min, store at 4 °C. For cDNA synthesis the reaction above was supplemented with dithiothreitol (10 mM), 20 U of RiboLock ribonuclease inhibitor (Thermo Fisher Scientific) and 200 U of SuperScript IV reverse transcriptase in a final reaction volume of 40 µL and incubated 45 °C 5 min, 70 °C 15 min.

The smears of 200–500 base pairs of the final barcoded libraries were purified from a 1.5 % agarose gel and sequenced on a NextSeq 550 Illumina instrument using a single-end 86 bp setting. The RNS-Seq library preparation method used results in reads that start with the same two initial nucleotides. Hence, these were removed when performing quality- and minimum length- read trimming with the fastp algorithm (Chen et al., 2018) with the default parameters. Read mapping to the Hamster genome scaffold, statistical analyses of DEGs between groups and GO analyses were performed using CLC Genomics Workbench (QIAGEN).

Isolation of single cells from lung tissue

The right caudal lobe of the lung was removed from the body and transferred on ice in PBS containing 1 % BSA (w/v) and 2 mg/mL Actinomycin D (Sigma-Aldrich) for further processing. Lung tissue was incubated in 2 mL Dispase (Corning, Bedford, MA, USA) containing 2 mg DNAse (AppliChem, Darmstadt, Germany), 4.6 mg Collagenase B (Roche, Basel, Switzerland) and 2 mg/mL Actinomycin D (Sigma-Aldrich) and at 37 °C for 30 min. Digest was stopped by the addition of cold PBS containing 0.5 % (w/v) BSA and Actinomycin D. The tissue was disrupted by pipetting in a repeated pumping motion. Cell suspension was collected and filtered through 70 mm-filter to obtain a single-cell suspension. Red Blood cell were lysed by incubation with RBC lysis buffer (Santa Cruz Biotechnology, Dallas, Texas, USA) for 4 min at room-temperature. Lysis reaction as stopped by the addition of PBS containing 0.04 % BSA, the supernatant was removed by centrifugation (1,200 rpm, 6 min, 4 °C) and cells were resuspended in PBS

containing 0.04 % BSA. Barcoding of single cells and RNA isolation was performed using the Chromium controller and Chromium Next Gem Chip G Single Cell Kit and Chromium Next Gem Single cell 3′ GEM, Library & Gel Bead Kit v3.1 (10x Genomics B.V., Leiden, The Netherlands) according to the manufacturer's instructions.

Single-cell RNA-Seq

After enzymatic fragmentation and size selection, resulting double-stranded cDNA amplicons optimized for library construction were subjected to adaptor ligation and sample index PCRs needed for Illumina bridge amplification and sequencing according to the manufacturer's instruction (10x genomics). Single cell libraries were quantified using Qubit (Thermo Fisher) and quality-controlled using the Bioanalyzer System (Agilent). Sequencing was performed on a Novaseq 6000 (Illumina), aiming for 200 Million reads per library (read1: 28, read2: 150 nucleotides). Data were analysed using CellRanger v5.0 (10x Genomics) using hamster and SARS-CoV-2 genome scaffolds, and the R packages Seurat v4.0 (Hao et al., 2021) and DoRothEA v3.12 (Holland et al., 2020) were used for cell clustering, annotation, and transcription factor activity analysis. Median gene number detected per cell ranged between 2000 and 4400, with 3800–18500 median UMI counts per cell. Gene set variation analysis (GSVA) was performed using the GSVA R package (Hänzelmann et al., 2013) and gene set enrichment analysis was performed using the clusterProfiler R package (Wu et al., 2021).

Histopathology

The left lung lobe was carefully removed and immersion-fixed in 10 % neutral-buffered formalin for 7 days. The tissue was subsequently paraffin-embedded and sections of 4 µm were prepared.

Hematoxilin-eosin staining

Hematoxylin-eosin staining was carried out in accordance with standard procedures (Mulisch and Welsch, 2015). H&E-stained slices were subjected to histopathologic analyses on blinded samples.

Sirius red staining

For Sirius Red staining of lung tissue sections we followed the protocol published by Llewellyn with some modifications (Llewellyn, 1970). Briefly, sections were placed in Papanicolaous solution 1b Hematoxylin S (Sigma Aldrich) for 2 min and rinsed afterwards with water followed by ethanol, 3 % HCl in ethanol and 70 % ethanol. Subsequently, sections were stained for 90 min in alkaline Sirius red (0.5 g Direktrot 80, Sigma in 50 % ethanol containing 0.1‰ NaOH) before rinsing with water. Sections were dehydrated afterwards with increasing ethanol concentrations and xylene. Finally, sections were covered with Entellan (Merck KGaA, Darmstadt, Germany).

In situ hybridisation

To detect viral RNA in the lungs, fixed paraffin-embedded tissue sections were mounted on glass slides and analyzed by *in situ* hybridization as described previously (Halwe et al., 2021; Tscherne et al., 2021). For this, the RNAscope® 2.5 HD Assay – RED Kit (Bio-Techne, cat. no. 322360) was used according to the manufacturer's instructions. Slides were incubated at 60 °C, deparaffinized with xylene and 100 % ethanol and pretreated with RNAscope® Pretreatment Reagents (cat. no. 322330 and 322000), to enable access to the target RNA. Subsequently, the RNA-specific probe, targeting the S protein of the SARS-CoV-2 virus (cat. no. 848561) was hybridized to the RNA. After the amplification steps, Fast Red substrate was administered to the samples for signal detection. Slides were counterstained with Gill's Hematoxylin I and 0.02 % ammonia water. A RNAscope® Negative Control Probe (cat. no. 310043) was used in parallel to control background staining.

Immunohistochemistry

For SARS-CoV-2 antigen detection, a monoclonal Ab against the nucleocapsid protein (clone 4F3C4 (Bussmann et al., 2006)) was used according to standardized procedures of avidin-biotin-peroxidase complex-method (ABC, Vectastain Elite ABC Kit, Burlingame, CA, USA). Briefly, 2–3 µm sections were mounted on adhesive glass slides, dewaxed in xylene, followed by rehydration in descending graded alcohols. Endogenous peroxidase was quenched with 3 % hydrogen peroxide in distilled water for 10 min at room temperature. Antigen heat retrieval was performed in 10 mM citrate buffer (pH 6) for 20 min in a pressure cooker. Nonspecific Ab binding was blocked for 30 min at room temperature with goat normal serum, diluted in PBS (1:2). The primary Ab was applied overnight at 4 °C (1:50, diluted in TRIS buffer), the secondary biotinylated goat anti-mouse Ab was applied for 30 min at room temperature (Vector Laboratories, Burlingame, CA, USA, 1:200). Color was developed by incubating the slides with freshly prepared avidin-biotin-peroxidase complex (ABC) solution (Vectastain Elite ABC Kit; Vector Laboratories), followed by exposure to 3-amino-9-ethylcarbazole substrate (AEC, Dako, Carpinteria, CA, USA). The sections were counterstained with Mayer's haematoxylin and coverslipped. As negative control, consecutive sections were labelled with an irrelevant Ab (M protein of Influenza A virus, ATCC clone HB-64). A positive control slide was included in each run. Slides were scanned using a Hamamatsu S60 scanner (Hamamatsu Photonics, K.K. Japan).

Quantification and statistical analysis

Animal cohort or sample size per treatment was between n = 4 and n = 6 as defined in the individual figure legends. Statistical analysis of different experiments is indicated in detail in the respective figure legends. For statistical analysis of samples from animal experiments, ordinary one-way or two-way

ANOVA was applied with Tukey's multiple comparisons test using Prism. For statistical analysis of grouped ELISpot data, paired t test was applied using Prism. For statistical analysis of histopathology, ordinary one-way ANOVA was applied with Mann-Whitney test. For statistical analysis of qRT-PCR analyses, ordinary one-way ANOVA was applied with Tukey's multiple comparisons test using Prism.

Bulk RNAseq libraries from different hamster lungs (n = 4) were generated for each condition (mock uninfected, infected, Alum+S vaccinated + infected, and MeV_{vac2}-SARS2-S(H) vaccinated + infected). An average of 13,400,912.5 (range 8,468,387 to 22,180,134) reads mapped to the hamster genome scaffold MesAur1.0.102, an average of 90.1 % (range 87.95 %–92.04 %) of the total number of reads, with 98.7 % (range 97.61 %–99.27 %) representing protein-coding segments. An average 62,455.9 (range 2,649 to 205,001) reads mapped to SARS-CoV-2 reference genome (NCBI accession #LR824570), about 0.41 % (range 0.03 %–1.25 %) of the total number of reads. For statistical comparison, read counts of libraries of vaccinated animals were tested against mock animals using CLC Genomics Workbench 21.0.4 employing multi-factorial statistics based on a negative binomial Generalized Linear Model (GLM). p-values of differentially expressed genes (DEG) were corrected with FDR correction method.

Four scRNA-seq libraries from four different infected hamster lungs were generated for each condition (mock, Alum+S vaccinated, and MeV_{vac2}-SARS2-S(H) vaccinated) and an average number of 2,679 cells (range: 1,392 to 4,645) were retrieved per library with an average read count of 7,271 mapped reads per cell. Differential expression of selected cytokines in different cell type compartments between treatment groups was performed using the FindMarkers function from the Seurat R package with the default parameters (Wilcoxon Rank Sum test with Bonferroni p value correction).

Differential expression of SARS-CoV-2 RNA in scRNA-Seq experiments was analysed using the Loupe Browser 6.0.0 software. Statistical significance was tested by comparison of individual cell populations with all other cells within the different treatment groups, p values were adjusted using Benjamini-Hochberg correction for multiple testings.

We did not determine by statistical tests whether the data met assumptions of the statistical approach, also for the reason that tests were conservatively chosen for data requirements to have to meet as few pre-assumptions as possible.

Acknowledgments

The authors would like to thank Daniela Müller, Mona Lange, and Silvia Schuparis for excellent technical assistance, Bevan Sawatsky for support of BSL-3 procedures, Elke Völker for assistance with circular

dichroism (CD) spectroscopy, the team of the animal husbandry for logistic support with hamster experiments, and Christoph Schürmann for scientific discussions. The authors are indebted to Klaus Cichutek for intramural funding and support and to Stefan Schülke for providing recombinant ovalbumin and flagellin A. The SARS-CoV-2 trimeric spike (cat. no. 101007) was obtained from the National Institute for Biological Standards and Control, UK. Our thanks go to Dr. Barney S. Graham, NIAID, and Chris Ball, NIBSC, for providing this protein. This work was supported by grants from the German Center for Infection Research (DZIF; TTU 01.805 and TTU 01.922_00) and the German Ministry of Health (CHARIS) to M.D.M. and by funding of Berlin Institute of Health (BIH) to C.G. J.K. is supported by the Center of Infection Biology and Immunity (ZIBI) and Charité PhD Program. G.N. is supported by the German Federal Ministry of Education and Research and by the Agence Nationale de la Recherche (ANR) in the framework of MAPVAP (16GW0247). D.T. is supported by the (BMBF grant 01KI2106). A.G. is supported by the DFG, grant 398066876-GRK 2485/1.

Author contributions

Conceptualization, C.H., G.N., R.J.P.B., and M.D.M.; acquisition of funding, M.D.M. and R.J.P.B.; data curation, D.T., A.G., D.P., and R.J.P.B.; investigation, A.E., S.M., J.K., A.A., M.A., P.G., M.N., R.P., C.M., M.G.S., A.B., C.K., E.W., A.K., and M.D.M.; analysis of sequencing data, D.T., A.G., D.P., C.M., E.W., and R.J.P.B.; visualization, A.E., J.K., D.T., D.P., E.W., R.J.P.B., and M.D.M.; supervision, Z.I., Z.W., S.P., M.L., G.N., C.G., R.J.P.B., and M.D.M.; writing - original draft, A.E., R.J.B.P., and M.D.M.; writing - review & editing, all authors.

Declaration of interests

The authors declare no competing interests.

Inclusion and diversity

We worked to ensure sex balance in the selection of non-human subjects. The author list of this paper includes contributors from the location where the research was conducted who participated in the data collection, design, analysis, and/or interpretation of the work.

References

Agrawal, A.S., Tao, X., Algaissi, A., Garron, T., Narayanan, K., Peng, B.-H., Couch, R.B., and Tseng, C.-T.K. (2016). Immunization with inactivated Middle East Respiratory Syndrome coronavirus vaccine leads to lung immunopathology on challenge with live virus. Human Vaccines & Immunotherapeutics 12, 2351-2356.

Anderson, E.J., Rouphael, N.G., Widge, A.T., Jackson, L.A., Roberts, P.C., Makhene, M., Chappell, J.D., Denison, M.R., Stevens, L.J., and Pruijssers, A.J., et al. (2020). Safety and Immunogenicity of SARS-CoV-2 mRNA-1273 Vaccine in Older Adults. N Engl J Med 383, 2427-2438.

Beltramello, M., Williams, K.L., Simmons, C.P., Macagno, A., Simonelli, L., Quyen, N.T.H., Sukupolvi-Petty, S., Navarro-Sanchez, E., Young, P.R., and Silva, A.M. de, et al. (2010). The human immune response to Dengue virus is dominated by highly cross-reactive antibodies endowed with neutralizing and enhancing activity. Cell Host & Microbe 8, 271-283.

Böhmer, M.M., Buchholz, U., Corman, V.M., Hoch, M., Katz, K., Marosevic, D.V., Böhm, S., Woudenberg, T., Ackermann, N., and Konrad, R., et al. (2020). Investigation of a COVID-19 outbreak in Germany resulting from a single travel-associated primary case: a case series. The Lancet Infectious Diseases 20, 920-928.

Bolles, M., Deming, D., Long, K., Agnihothram, S., Whitmore, A., Ferris, M., Funkhouser, W., Gralinski, L., Totura, A., and Heise, M., et al. (2011). A double-inactivated severe acute respiratory syndrome coronavirus vaccine provides incomplete protection in mice and induces increased eosinophilic proinflammatory pulmonary response upon challenge. J Virol 85, 12201-12215.

Brown, R.J.P., Tegtmeyer, B., Sheldon, J., Khera, T., Anggakusuma, Todt, D., Vieyres, G., Weller, R., Joecks, S., and Zhang, Y., et al. (2020). Liver-expressed Cd302 and Cr1l limit hepatitis C virus cross-species transmission to mice. Science advances 6.

Bussmann, B.M., Reiche, S., Jacob, L.H., Braun, J.M., and Jassoy, C. (2006). Antigenic and cellular localisation analysis of the severe acute respiratory syndrome coronavirus nucleocapsid protein using monoclonal antibodies. Virus Research 122, 119-126.

Chen, S., Zhou, Y., Chen, Y., and Gu, J. (2018). fastp: an ultra-fast all-in-one FASTQ preprocessor. Bioinformatics (Oxford, England) 34, i884-i890.

Corbett, K.S., Edwards, D.K., Leist, S.R., Abiona, O.M., Boyoglu-Barnum, S., Gillespie, R.A., Himansu, S., Schäfer, A., Ziwawo, C.T., and DiPiazza, A.T., et al. (2020a). SARS-CoV-2 mRNA vaccine design enabled by prototype pathogen preparedness. Nature 586, 567-571.

Corbett, K.S., Flynn, B., Foulds, K.E., Francica, J.R., Boyoglu-Barnum, S., Werner, A.P., Flach, B., O'Connell, S., Bock, K.W., and Minai, M., et al. (2020b). Evaluation of the mRNA-1273 Vaccine against SARS-CoV-2 in Nonhuman Primates. N Engl J Med 383, 1544-1555.

Corman, V.M., Landt, O., Kaiser, M., Molenkamp, R., Meijer, A., Chu, D.K., Bleicker, T., Brünink, S., Schneider, J., and Schmidt, M.L., et al. (2020). Detection of 2019 novel coronavirus (2019-nCoV) by real-time RT-PCR. Euro surveillance : bulletin Europeen sur les maladies transmissibles = European communicable disease bulletin 25.

Del Valle, J.R., Devaux, P., Hodge, G., Wegner, N.J., McChesney, M.B., and Cattaneo, R. (2007). A vectored measles virus induces hepatitis B surface antigen antibodies while protecting macaques against measles virus challenge. J Virol 81, 10597-10605.

DiPiazza, A.T., Leist, S.R., Abiona, O.M., Moliva, J.I., Werner, A., Minai, M., Nagata, B.M., Bock, K.W., Phung, E., and Schäfer, A., et al. (2021). COVID-19 vaccine mRNA-1273 elicits a protective immune profile in mice that is not associated with vaccine-enhanced disease upon SARS-CoV-2 challenge. Immunity 54, 1869-1882.e6.

Espitia, C.M., Zhao, W., Saldarriaga, O., Osorio, Y., Harrison, L.M., Cappello, M., Travi, B.L., and Melby, P.C. (2010). Duplex real-time reverse transcriptase PCR to determine cytokine mRNA expression in a hamster model of New World cutaneous leishmaniasis. BMC immunology 11, 31.

Halwe, S., Kupke, A., Vanshylla, K., Liberta, F., Gruell, H., Zehner, M., Rohde, C., Krähling, V., Gellhorn Serra, M., and Kreer, C., et al. (2021). Intranasal Administration of a Monoclonal Neutralizing Antibody Protects Mice against SARS-CoV-2 Infection. Viruses 13.

Hänzelmann, S., Castelo, R., and Guinney, J. (2013). GSVA: gene set variation analysis for microarray and RNA-seq data. BMC bioinformatics 14, 7.

Hao, Y., Hao, S., Andersen-Nissen, E., Mauck, W.M., Zheng, S., Butler, A., Lee, M.J., Wilk, A.J., Darby, C., and Zager, M., et al. (2021). Integrated analysis of multimodal single-cell data. Cell 184, 3573-3587.e29.

Holland, C.H., Tanevski, J., Perales-Patón, J., Gleixner, J., Kumar, M.P., Mereu, E., Joughin, B.A., Stegle, O., Lauffenburger, D.A., and Heyn, H., et al. (2020). Robustness and applicability of transcription factor and pathway analysis tools on single-cell RNA-seq data. Genome biology 21, 36.

Honda-Okubo, Y., Barnard, D., Ong, C.H., Peng, B.-H., Tseng, C.-T.K., and Petrovsky, N. (2015). Severe acute respiratory syndrome-associated coronavirus vaccines formulated with delta inulin adjuvants provide enhanced protection while ameliorating lung eosinophilic immunopathology. J Virol 89, 2995-3007.

Horby, P., Lim, W.S., Emberson, J.R., Mafham, M., Bell, J.L., Linsell, L., Staplin, N., Brightling, C., Ustianowski, A., and Elmahi, E., et al. (2021). Dexamethasone in Hospitalized Patients with Covid-19. N Engl J Med 384, 693-704.

Hörner, C., Schürmann, C., Auste, A., Ebenig, A., Muraleedharan, S., Dinnon, K.H., Scholz, T., Herrmann, M., Schnierle, B.S., and Baric, R.S., et al. (2020). A highly immunogenic and effective measles virus-based Th1-biased COVID-19 vaccine. Proc Natl Acad Sci USA 117, 32657-32666.

Iwata-Yoshikawa, N., Shiwa, N., Sekizuka, T., Sano, K., Ainai, A., Hemmi, T., Kataoka, M., Kuroda, M., Hasegawa, H., and Suzuki, T., et al. (2022). A lethal mouse model for evaluating vaccine-associated enhanced respiratory disease during SARS-CoV-2 infection. Science advances 8, eabh3827.

Iwata-Yoshikawa, N., Uda, A., Suzuki, T., Tsunetsugu-Yokota, Y., Sato, Y., Morikawa, S., Tashiro, M., Sata, T., Hasegawa, H., and Nagata, N. (2014). Effects of Toll-like receptor stimulation on eosinophilic infiltration in lungs of BALB/c mice immunized with UV-inactivated severe acute respiratory syndrome-related coronavirus vaccine. J Virol 88, 8597-8614.

Jackson, L.A., Anderson, E.J., Rouphael, N.G., Roberts, P.C., Makhene, M., Coler, R.N., McCullough, M.P., Chappell, J.D., Denison, M.R., and Stevens, L.J., et al. (2020). An mRNA Vaccine against SARS-CoV-2 - Preliminary Report. N Engl J Med 383, 1920-1931.

Johnson, T.R., and Graham, B.S. (1999). Secreted respiratory syncytial virus G glycoprotein induces interleukin-5 (IL-5), IL-13, and eosinophilia by an IL-4-independent mechanism. J Virol 73, 8485-8495.

Johnson, T.R., Parker, R.A., Johnson, J.E., and Graham, B.S. (2003). IL-13 is sufficient for respiratory syncytial virus G glycoprotein-induced eosinophilia after respiratory syncytial virus challenge. J Immunol 170, 2037-2045.

Johnson, T.R., Teng, M.N., Collins, P.L., and Graham, B.S. (2004). Respiratory syncytial virus (RSV) G glycoprotein is not necessary for vaccine-enhanced disease induced by immunization with formalin-inactivated RSV. J Virol 78, 6024-6032.

Junqueira, C., Crespo, Â., Ranjbar, S., Lacerda, L.B. de, Lewandrowski, M., Ingber, J., Parry, B., Ravid, S., Clark, S., and Schrimpf, M.R., et al. (2022). FcγR-mediated SARS-CoV-2 infection of monocytes activates inflammation. Nature.

Kärber, G. (1931). Beitrag zur kollektiven Behandlung pharmakologischer Reihenversuche. Archiv f. experiment. Pathol. u. Pharmakol 162, 480-483.

Kim, H.W., Canchola, J.G., Brandt, C.D., Pyles, G., Chanock, R.M., Jensen, K., and Parrott, R.H. (1969). Respiratory syncytial virus disease in infants despite prior administration of antigenic inactivated vaccine. American Journal of Epidemiology 89, 422-434.

Ko, E.-J., Lee, Y.-T., Kim, K.-H., Lee, Y., Jung, Y.-J., Kim, M.-C., Lee, Y.-N., Kang, T., and Kang, S.-M. (2017). Roles of Aluminum Hydroxide and Monophosphoryl Lipid A Adjuvants in Overcoming $CD4^+$ T Cell Deficiency To Induce Isotype-Switched IgG Antibody Responses and Protection by T-Dependent Influenza Vaccine. J Immunol 198, 279-291.

Levin, J.Z., Yassour, M., Adiconis, X., Nusbaum, C., Thompson, D.A., Friedman, N., Gnirke, A., and Regev, A. (2010). Comprehensive comparative analysis of strand-specific RNA sequencing methods. Nature methods 7, 709-715.

Llewellyn, B.D. (1970). An improved Sirius red method for amyloid. The Journal of medical laboratory technology 27, 308-309.

Malczyk, A.H., Kupke, A., Prüfer, S., Scheuplein, V.A., Hutzler, S., Kreuz, D., Beissert, T., Bauer, S., Hubich-Rau, S., and Tondera, C., et al. (2015). A Highly Immunogenic and Protective Middle East Respiratory Syndrome Coronavirus Vaccine Based on a Recombinant Measles Virus Vaccine Platform. J Virol 89, 11654-11667.

Mendlovic, F., Cruz-Rivera, M., Ávila, G., Vaughan, G., and Flisser, A. (2015). Cytokine, antibody and proliferative cellular responses elicited by Taenia solium calreticulin upon experimental infection in hamsters. PLoS ONE 10, e0121321.

Moghaddam, A., Olszewska, W., Wang, B., Tregoning, J.S., Helson, R., Sattentau, Q.J., and Openshaw, P.J.M. (2006). A potential molecular mechanism for hypersensitivity caused by formalin-inactivated vaccines. Nature medicine 12, 905-907.

Mulisch, M. and Welsch, U. (2015). Romeis - Mikroskopische Technik (Berlin, Heidelberg: Springer Berlin Heidelberg).

Munoz, F.M., Cramer, J.P., Dekker, C.L., Dudley, M.Z., Graham, B.S., Gurwith, M., Law, B., Perlman, S., Polack, F.P., and Spergel, J.M., et al. (2021). Vaccine-associated enhanced disease: Case definition and guidelines for data collection, analysis, and presentation of immunization safety data. Vaccine 39, 3053-3066.

Nader, P.R., and Warren, R.J. (1968). Reported Neurologic Disorders Following Live Measles Vaccine. Pediatrics 41, 997-1001.

Nouailles, G., Wyler, E., Pennitz, P., Postmus, D., Vladimirova, D., Kazmierski, J., Pott, F., Dietert, K., Muelleder, M., and Farztdinov, V., et al. (2021). Temporal omics analysis in Syrian hamsters unravel cellular effector responses to moderate COVID-19. Nature communications 12, 4869.

Nürnberger, C., Bodmer, B.S., Fiedler, A.H., Gabriel, G., and Mühlebach, M.D. (2019). A Measles Virus-Based Vaccine Candidate Mediates Protection against Zika Virus in an Allogeneic Mouse Pregnancy Model. J Virol 93.

Olsen, C.W., Corapi, W.V., Ngichabe, C.K., Baines, J.D., and Scott, F.W. (1992). Monoclonal antibodies to the spike protein of feline infectious peritonitis virus mediate antibody-dependent enhancement of infection of feline macrophages. J Virol 66, 956-965.

Openshaw, P.J. (2001). Potential mechanisms causing delayed effects of respiratory syncytial virus infection. American journal of respiratory and critical care medicine 163, S10-3.

Osterrieder, N., Bertzbach, L.D., Dietert, K., Abdelgawad, A., Vladimirova, D., Kunec, D., Hoffmann, D., Beer, M., Gruber, A.D., and Trimpert, J. (2020). Age-Dependent Progression of SARS-CoV-2 Infection in Syrian Hamsters. Viruses 12, 779.

Polack, F.P., Hoffman, S.J., Crujeiras, G., and Griffin, D.E. (2003). A role for nonprotective complement-fixing antibodies with low avidity for measles virus in atypical measles. Nature medicine 9, 1209-1213.

Polack, F.P., Teng, M.N., Collins, P.L., Prince, G.A., Exner, M., Regele, H., Lirman, D.D., Rabold, R., Hoffman, S.J., and Karp, C.L., et al. (2002). A role for immune complexes in enhanced respiratory syncytial virus disease. Journal of Experimental Medicine 196, 859-865.

Polack, F.P., Thomas, S.J., Kitchin, N., Absalon, J., Gurtman, A., Lockhart, S., Perez, J.L., Pérez Marc, G., Moreira, E.D., and Zerbini, C., et al. (2020). Safety and Efficacy of the BNT162b2 mRNA Covid-19 Vaccine. N Engl J Med 383, 2603-2615.

Ramasamy, M.N., Minassian, A.M., Ewer, K.J., Flaxman, A.L., Folegatti, P.M., Owens, D.R., Voysey, M., Aley, P.K., Angus, B., and Babbage, G., et al. (2020). Safety and immunogenicity of ChAdOx1 nCoV-19 vaccine administered in a prime-boost regimen in young and old adults (COV002): a single-blind, randomised, controlled, phase 2/3 trial. The Lancet 396, 1979-1993.

Ruckwardt, T.J., Morabito, K.M., and Graham, B.S. (2019). Immunological Lessons from Respiratory Syncytial Virus Vaccine Development. Immunity 51, 429-442.

Sadoff, J., Le Gars, M., Shukarev, G., Heerwegh, D., Truyers, C., Groot, A.M. de, Stoop, J., Tete, S., van Damme, W., and Leroux-Roels, I., et al. (2021). Interim Results of a Phase 1-2a Trial of Ad26.COV2.S Covid-19 Vaccine. N Engl J Med 384, 1824-1835.

Sahin, U., Muik, A., Derhovanessian, E., Vogler, I., Kranz, L.M., Vormehr, M., Baum, A., Pascal, K., Quandt, J., and Maurus, D., et al. (2020). COVID-19 vaccine BNT162b1 elicits human antibody and TH1 T cell responses. Nature 586, 594-599.

Schülke, S., Burggraf, M., Waibler, Z., Wangorsch, A., Wolfheimer, S., Kalinke, U., Vieths, S., Toda, M., and Scheurer, S. (2011). A fusion protein of flagellin and ovalbumin suppresses the TH2 response and prevents murine intestinal allergy. The Journal of allergy and clinical immunology 128, 1340-1348.e12.

Stanelle-Bertram, S., Schaumburg, B., Kouassi, N.M., Beck, S., Zickler, M., Beythien, G., Becker, K., Bai, T., Jania, H., and Müller, Z., et al. (2020). SARS-CoV-2 induced CYP19A1 expression in the lung correlates with increased aromatization of testosterone-to-estradiol in male golden hamsters.

Stephenson, K.E., Le Gars, M., Sadoff, J., Groot, A.M. de, Heerwegh, D., Truyers, C., Atyeo, C., Loos, C., Chandrashekar, A., and McMahan, K., et al. (2021). Immunogenicity of the Ad26.COV2.S Vaccine for COVID-19. JAMA 325, 1535-1544.

Swart, R.L. de, Kuiken, T., Timmerman, H.H., van Amerongen, G., van den Hoogen, B.G., Vos, H.W., Neijens, H.J., Andeweg, A.C., and Osterhaus, A.D.M.E. (2002). Immunization of macaques with formalin-inactivated respiratory syncytial virus (RSV) induces interleukin-13-associated hypersensitivity to subsequent RSV infection. J Virol 76, 11561-11569.

TAKANO, T., KAWAKAMI, C., YAMADA, S., SATOH, R., and HOHDATSU, T. (2008). Antibody-dependent enhancement occurs upon re-infection with the identical serotype virus in feline infectious peritonitis virus infection. J. Vet. Med. Sci. 70, 1315-1321.

Tomazini, B.M., Maia, I.S., Cavalcanti, A.B., Berwanger, O., Rosa, R.G., Veiga, V.C., Avezum, A., Lopes, R.D., Bueno, F.R., and Silva, M.V.A.O., et al. (2020). Effect of Dexamethasone on Days Alive and Ventilator-Free in Patients With Moderate or Severe Acute Respiratory Distress Syndrome and COVID-19: The CoDEX Randomized Clinical Trial. JAMA 324, 1307-1316.

Tscherne, A., Schwarz, J.H., Rohde, C., Kupke, A., Kalodimou, G., Limpinsel, L., Okba, N.M.A., Bošnjak, B., Sandrock, I., and Odak, I., et al. (2021). Immunogenicity and efficacy of the COVID-19 candidate vector vaccine MVA-SARS-2-S in preclinical vaccination. Proc Natl Acad Sci USA 118.

Tseng, C.-T., Sbrana, E., Iwata-Yoshikawa, N., Newman, P.C., Garron, T., Atmar, R.L., Peters, C.J., and Couch, R.B. (2012). Correction: Immunization with SARS Coronavirus Vaccines Leads to Pulmonary Immunopathology on Challenge with the SARS Virus. PLoS ONE 7.

van der Lubbe, J.E.M., Rosendahl Huber, S.K., Vijayan, A., Dekking, L., van Huizen, E., Vreugdenhil, J., Choi, Y., Baert, M.R.M., Feddes-de Boer, K., and Izquierdo Gil, A., et al. (2021). Ad26.COV2.S protects Syrian hamsters against G614 spike variant SARS-CoV-2 and does not enhance respiratory disease. npj Vaccines 6, 39.

Vennema, H., Groot, R.J. de, Harbour, D.A., Dalderup, M., Gruffydd-Jones, T., Horzinek, M.C., and Spaan, W.J. (1990). Early death after feline infectious peritonitis virus challenge due to recombinant vaccinia virus immunization. J Virol 64, 1407-1409.

Walsh, E.E., Frenck, R., Falsey, A.R., Kitchin, N., Absalon, J., Gurtman, A., Lockhart, S., Neuzil, K., Mulligan, M.J., and Bailey, R., et al. (2020). RNA-Based COVID-19 Vaccine BNT162b2 Selected for a Pivotal Efficacy Study.

Wan, Y., Shang, J., Sun, S., Tai, W., Chen, J., Geng, Q., He, L., Chen, Y., Wu, J., and Shi, Z., et al. (2020). Molecular Mechanism for Antibody-Dependent Enhancement of Coronavirus Entry. J Virol 94.

WHO (2021). WHO Coronavirus (COVID-19) Dashboard. https://covid19.who.int/. 07.10.2021.

Wu, J.T., Leung, K., and Leung, G.M. (2020). Nowcasting and forecasting the potential domestic and international spread of the 2019-nCoV outbreak originating in Wuhan, China: a modelling study. The Lancet 395, 689-697.

Wu, T., Hu, E., Xu, S., Chen, M., Guo, P., Dai, Z., Feng, T., Zhou, L., Tang, W., and Zhan, L., et al. (2021). clusterProfiler 4.0: A universal enrichment tool for interpreting omics data. Innovation (New York, N.Y.) 2, 100141.

Wyler, E., Adler, J.M., Eschke, K., Teixeira Alves, G., Peidli, S., Pott, F., Kazmierski, J., Michalick, L., Kershaw, O., and Bushe, J., et al. (2022). Key benefits of dexamethasone and antibody treatment in COVID-19 hamster models revealed by single-cell transcriptomics. Molecular therapy : the journal of the American Society of Gene Therapy 30, 1952-1965.

Yuan, L., Zhou, M., Ma, J., Liu, X., Chen, P., Zhu, H., Tang, Q., Cheng, T., Guan, Y., and Xia, N. (2022). Dexamethasone ameliorates severe pneumonia but slightly enhances viral replication in the lungs of SARS-CoV-2-infected Syrian hamsters. Cellular & molecular immunology 19, 290-292.

Zhu, N., Zhang, D., Wang, W., Li, X., Yang, B., Song, J., Zhao, X., Huang, B., Shi, W., and Lu, R., et al. (2020). A Novel Coronavirus from Patients with Pneumonia in China, 2019. N Engl J Med 382, 727-733.

Zivcec, M., Safronetz, D., Haddock, E., Feldmann, H., and Ebihara, H. (2011). Validation of assays to monitor immune responses in the Syrian golden hamster (Mesocricetus auratus). Journal of immunological methods 368, 24-35.

Supplemental information

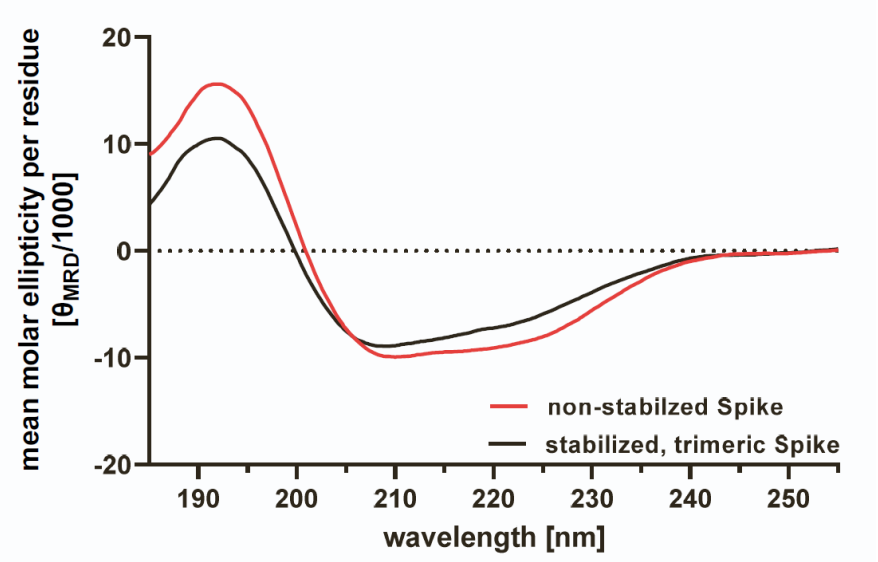

Fig. S1. Relative secondary structural elements of S determined by circular dichroism (CD). To determine misfolding of recombinant Spike used for vaccination, spectra of non-stabilized recombinant S used for vaccination (red; Sino Biological, Cat.-No. 40589-V08B1) and soluble S stabilized in the native conformation (black; NIBSC, Cat.-No. 101007), secondary structure of the proteins was determined by CD spectroscopy. CD spectra of both proteins were recorded at room temperature from 255 nm – 185 nm by accumulating 10 runs, blotted and analysed for relative content of α-helical and β-sheet secondary structural elements.

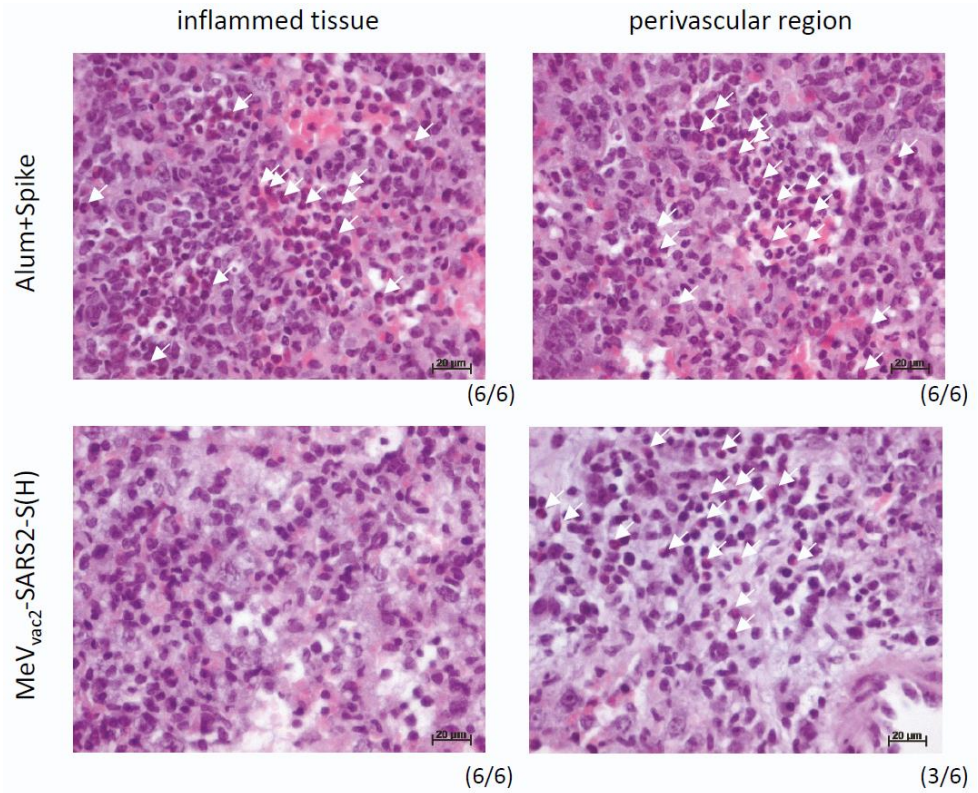

Fig. S2. Eosinophil infiltration into tissue of infected hamster lungs. Haematoxilin- and Eosin-staining of fixed lung slices of hamsters infected with SARS-CoV-2 after vaccination with Aluminum-adjuvanted Spike protein (upper panel) or MeV$_{vac2}$-SARS2-S(H) (lower panel) revealed eosinophil infiltration into inflamed tissue (left panel) of Alum+S, but not MeV$_{vac2}$-SARS2-S(H) immunized animals. While eosinophils became evident in the perivascular region of samples of all animals vaccinated with protein before infection, only half (3/6) of the MeV-vaccinated animals revealed this phenotype. N = 6; representative pictures for the fraction of animals indicated below each picture. White arrows depict single eosinophils. Scale bar, 20 µm.

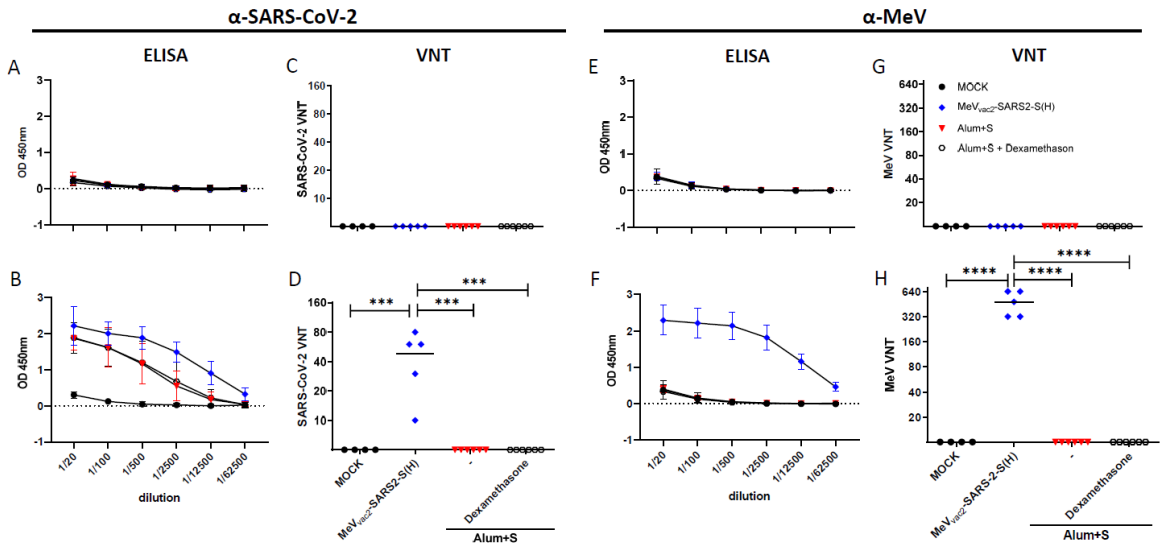

Fig. S3. Induction of α-SARS-CoV-2 S and α-MeV specific antibodies. Sera of hamsters vaccinated on days 0 and 21 with MeV_{vac2}-SARS2-S(H) (blue diamonds) or Alum-adjuvanted S protein (red triangles, open circles) were collected on days 0 (A, C, E, G) and 31 (B, D, F, H) and analyzed for antibodies specific for SARS-CoV-2 S or MeV. Medium-inoculated hamsters (black circles) served as mock. Pan-IgG binding to recombinant SARS-CoV-2 S (A, B) or MeV bulk antigen (E, F) were determined by ELISA via the specific OD 450 nm value. Depicted are means and the respective standard deviation of each group (n = 4 - 6). Virus-neutralizing titers (VNT) in vaccinated hamsters for SARS-CoV-2 (C, D) or MeV (G, H) were calculated as the reciprocal of the highest dilution abolishing infectivity. For statistical analysis, ordinary one-way ANOVA was applied with Tukey's multiple comparisons test. ns, not significant ($p>0.05$), *, $p<0.05$; **, $p<0.01$;***, $p<0.001$;****, $p<0.0001$.

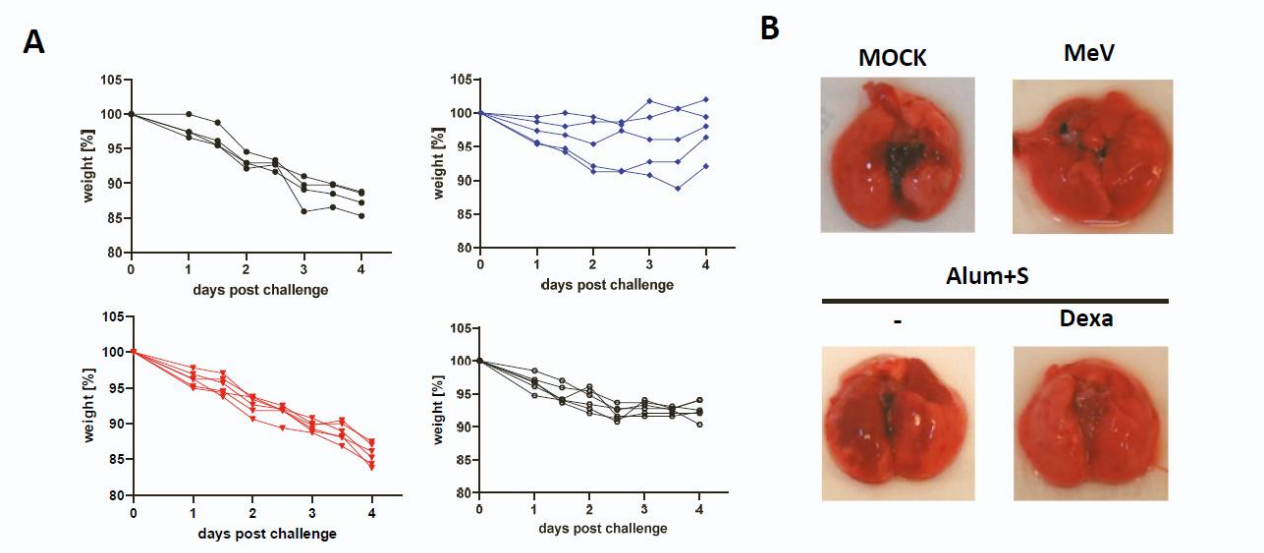

Fig. S4. Gross pathology in vaccinated hamsters after challenge. Hamster were vaccinated at days 0 and 21 and challenged on day 35 with low-passage SARS-CoV-2. (A) Body weight changes of animals vaccinated with medium (upper left, black circles), MeV_{vac2}-SARS2-S(H) (upper right, blue diamonds), Alum+S without (lower left, red triangles) or with dexamethasone-treatment after challenge (lower right, open circles). (B) Macroscopic pathology of Syrian hamster lungs after SARS-CoV-2 infection and indicated vaccination or treatment on day 4 pi.

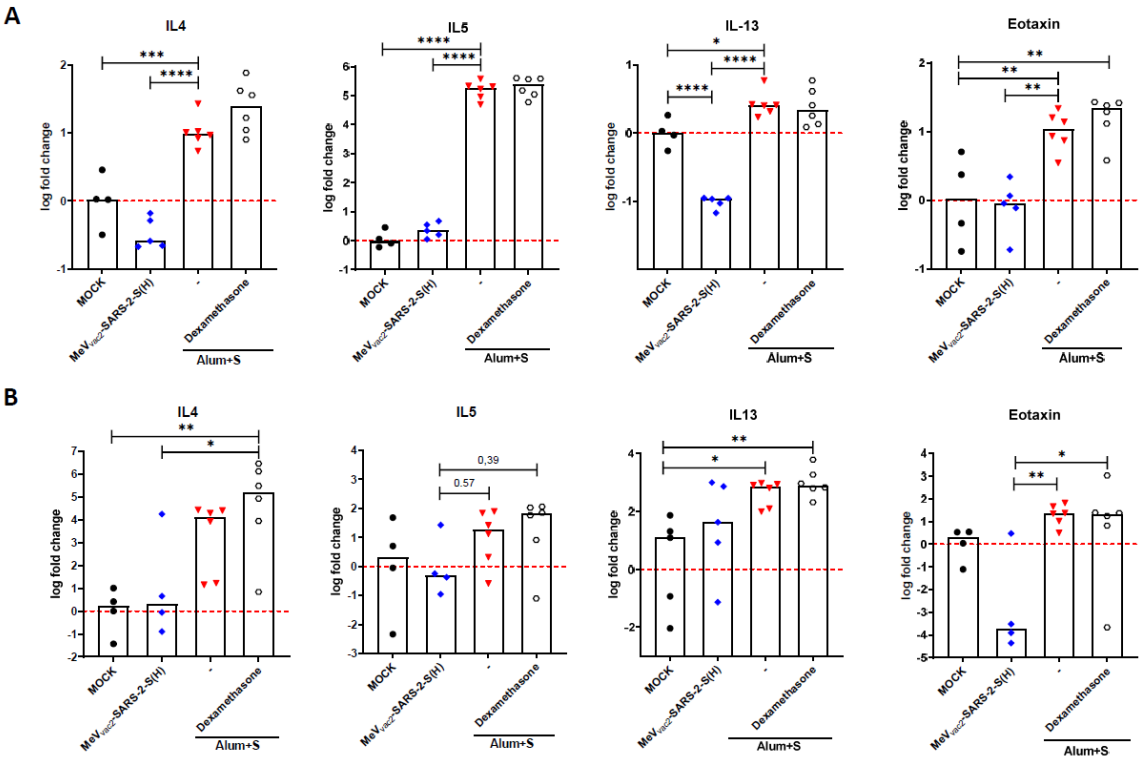

Fig. S5. Deregulation of T_H2 cytokines in lungs (A) and BAL cells (B) of SARS-CoV-2 infected, vaccinated Syrian hamsters 4 dpi. Depicted are data of animals already displayed in Fig. 4. Relative fold-change expression of mRNAs encoding IL-4, IL-5, or IL-13 was determined using quantitative RTPCR and the ΔΔct method. mRNA encoding RPL18 was used as housekeeping gene for normalization. Median of samples from mock-treated hamsters served as reference to normalize relative gene expression. Dots represent individual animals; mock-vaccinated hamsters, black circles; MeV$_{vac2}$-SARS2-S(H)-vaccinated hamsters, blue diamonds; protein-vaccinated hamsters, red triangles. For statistical analysis, ordinary one-way ANOVA was applied with Tukey's multiple comparisons test. ns, not significant (p>0.05), *, p<0.05; **, p<0.01;***, p<0.001;****, p<0.0001.

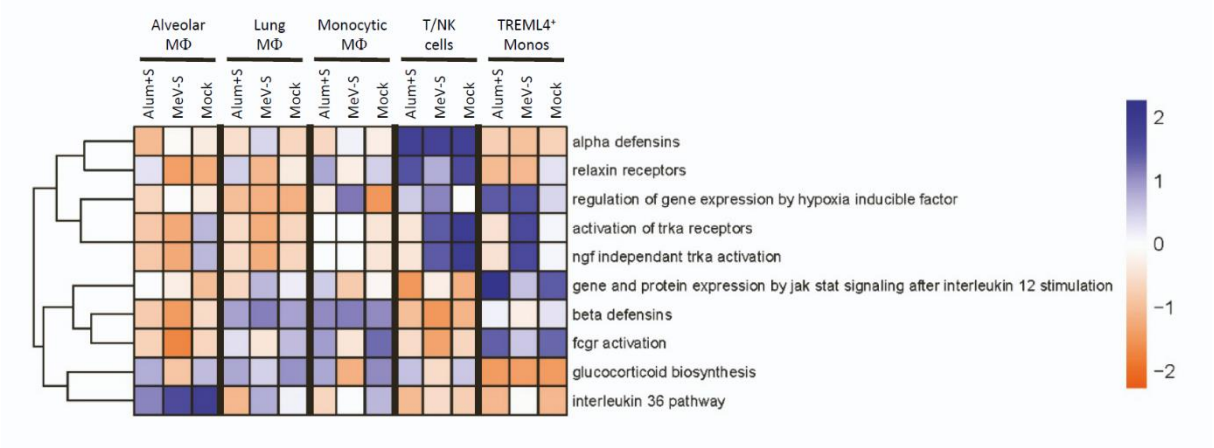

Fig. S6. SARS-CoV-2 infection triggers cell-type specific induction of REACTOME pathways which differ depending on vaccination type and prior immune status. Heat map is derived from scRNA-seq data and highlights selected REACTOME pathways which exhibit differential activation or suppression triggered by infection. Differences are dependent on prior immune status or vaccination type, and are cell-type specific. Cell population specific activation or suppression of pathways observed in alveolar macrophages (MΦ), interstitial macrophages, monocytic macrophages, Treml4^{+} monocytes, and T/NK cells is presented. Heat map is colored relative to the activation z-score gradient presented in the scale bar.


Alveolar Macrophages
tissue remodeling
T cell mediated immunity
response to ketone
response to corticosteroid
regulation of mononuclear cell migration
regulation of leukocyte migration
regulation of leukocyte chemotaxis
regulation of interleukin-1 beta production
regulation of G2/M transition of mitotic cell cycle
positive regulation of mononuclear cell migration
positive regulation of leukocyte migration
positive regulation of leukocyte chemotaxis
positive regulation of intrinsic apoptotic signaling pathway
positive regulation of immune system process
oligosaccharide metabolic process
negative regulation of myeloid cell differentiation
negative regulation of leukocyte differentiation
negative regulation of immune system process
negative regulation of hemopoiesis
negative regulation of cell growth
mononuclear cell migration
maternal process involved in female pregnancy
lymphocyte migration
lymphocyte mediated immunity
leukocyte mediated cytotoxicity
keratinocyte differentiation
inflammatory response
cellular response to ketone
cell killing
antigen processing and presentation
Alum+S
MeV-S
Lung Macrophages
translational initiation
superoxide metabolic process
substrate adhesion-dependent cell spreading
sensory perception of sound
sensory perception of mechanical stimulus
sensory perception
ribosomal large subunit biogenesis
response to ketone
response to glucocorticoid
response to corticosteroid
receptor catabolic process
protein localization to endoplasmic reticulum
positive regulation of NF-kappaB transcription factor activity
negative regulation of myeloid cell differentiation
myeloid leukocyte activation
leukocyte degranulation
inner ear development
humoral immune response
granulocyte activation
ear development
clathrin-dependent endocytosis
cellular response to ketone
antigen processing and presentation of peptide or polysaccharide antigen via MHC class II
antigen processing and presentation of peptide antigen via MHC class II
antigen processing and presentation of peptide antigen
antigen processing and presentation of exogenous peptide antigen via MHC class II
antigen processing and presentation of exogenous peptide antigen
antigen processing and presentation of exogenous antigen
antigen processing and presentation
aminoglycan biosynthetic process
Alum+S
MeV-S
FDR
<0.05
ns
size ratio
0.4
0.5
0.6
0.7
Tremi4+ Monocytes
viral entry into host cell
T cell activation
RNA splicing, via transesterification reactions with bulged adenosine as nucleophile
regulation of translational initiation
regulation of T cell activation
regulation of lymphocyte activation
regulation of leukocyte activation
regulation of DNA metabolic process
regulation of cellular response to growth factor stimulus
regulation of cell activation
regulation of B cell proliferation
recombinational repair
positive regulation of T cell activation
positive regulation of response to DNA damage stimulus
positive regulation of cold-induced thermogenesis
negative regulation of cysteine-type endopeptidase activity involved in apoptotic process
negative regulation of cell projection organization
negative regulation of cell adhesion
negative regulation of cell-cell adhesion
mRNA splicing, via spliceosome
mononuclear cell proliferation
lymphocyte proliferation
lymphocyte homeostasis
lymphocyte activation
leukocyte proliferation
icosanoid metabolic process
homeostasis of number of cells
entry into host
double-strand break repair via homologous recombination
BMP signaling pathway
Alum+S
MeV-S
T/NK cells
T cell proliferation
respiratory electron transport chain
regulation of T cell proliferation
regulation of mononuclear cell proliferation
regulation of lymphocyte proliferation
regulation of leukocyte proliferation
regulation of leukocyte activation
positive regulation of T cell proliferation
positive regulation of mRNA catabolic process
positive regulation of mononuclear cell proliferation
positive regulation of lymphocyte proliferation
positive regulation of leukocyte proliferation
oxidative phosphorylation
nuclear-transcribed mRNA catabolic process
negative regulation of T cell activation
negative regulation of lymphocyte activation
negative regulation of leukocyte cell-cell adhesion
negative regulation of leukocyte activation
negative regulation of immune response
negative regulation of cell adhesion
negative regulation of cell activation
negative regulation of cell-cell adhesion
myeloid cell development
mitochondrial respiratory chain complex assembly
mitochondrial electron transport, NADH to ubiquinone
mitochondrial ATP synthesis coupled electron transport
electron transport chain
cellular respiration
ATP synthesis coupled electron transport
anaphase-promoting complex-dependent catabolic process
Alum+S
MeV-S
z-score
2
1
0
-1
-2
Alveolar Macrophages
Toxoplasmosis
Toll-like receptor signaling pathway
Th17 cell differentiation
Synaptic vesicle cycle
Rheumatoid arthritis
Purine metabolism
Phagosome
Pertussis
PD-L1 expression and PD-1 checkpoint pathway in cancer
Pathways of neurodegeneration - multiple diseases
p53 signaling pathway
Oxidative phosphorylation
Osteoclast differentiation
Oocyte meiosis
Non-alcoholic fatty liver disease
Neutrophil extracellular trap formation
Metabolic pathways
Human T-cell leukemia virus 1 infection
Human immunodeficiency virus 1 infection
Glycolysis / Gluconeogenesis
Fluid shear stress and atherosclerosis
Epithelial cell signaling in Helicobacter pylori infection
DNA replication
Chemokine signaling pathway
Cell cycle
Carbon metabolism
C-type lectin receptor signaling pathway
Antigen processing and presentation
Amoebiasis
Amino sugar and nucleotide sugar metabolism
Alum+S
MeV-S
Lung Macrophages
Viral carcinogenesis
Toxoplasmosis
TGF-beta signaling pathway
Small cell lung cancer
Ribosome
Protein processing in endoplasmic reticulum
Phospholipase D signaling pathway
Peroxisome
PD-L1 expression and PD-1 checkpoint pathway in cancer
Pathogenic Escherichia coli infection
Natural killer cell mediated cytotoxicity
Leishmaniasis
Legionellosis
JAK-STAT signaling pathway
IL-17 signaling pathway
Huntington disease
Hippo signaling pathway
Hepatocellular carcinoma
Hematopoietic cell lineage
Glycerophospholipid metabolism
Focal adhesion
Endocytosis
Coronavirus disease - COVID-19
Chemical carcinogenesis - receptor activation
Chagas disease
Biosynthesis of nucleotide sugars
Bacterial invasion of epithelial cells
Apoptosis
Amino sugar and nucleotide sugar metabolism
Alcoholism
Alum+S
MeV-S
FDR
<0.05
ns
size ratio
0.4
0.6
0.8
Tremi4+ Monocytes
Viral carcinogenesis
Ubiquitin mediated proteolysis
Transcriptional misregulation in cancer
Toxoplasmosis
Th17 cell differentiation
Spinocerebellar ataxia
Small cell lung cancer
Signaling pathways regulating pluripotency of stem cells
Salmonella infection
RNA degradation
Proteoglycans in cancer
Prolactin signaling pathway
Platinum drug resistance
Pathogenic Escherichia coli infection
Nucleocytoplasmic transport
Natural killer cell mediated cytotoxicity
mRNA surveillance pathway
MAPK signaling pathway
Longevity regulating pathway
Leishmaniasis
JAK-STAT signaling pathway
HIF-1 signaling pathway
Fc gamma R-mediated phagocytosis
Chemokine signaling pathway
Chagas disease
Biosynthesis of cofactors
Bacterial invasion of epithelial cells
Autophagy - animal
Adherens junction
Acute myeloid leukemia
Alum+S
MeV-S
T/NK cells
Thermogenesis
TGF-beta signaling pathway
Prion disease
Platelet activation
Pathways of neurodegeneration - multiple diseases
Pathways in cancer
Parkinson disease
Oxidative phosphorylation
Non-alcoholic fatty liver disease
Melanogenesis
MAPK signaling pathway
Leukocyte transendothelial migration
Huntington disease
Growth hormone synthesis, secretion and action
Gastric cancer
FoxO signaling pathway
Focal adhesion
Endometrial cancer
Diabetic cardiomyopathy
Cushing syndrome
Colorectal cancer
Chemical carcinogenesis - receptor activation
Chemical carcinogenesis - reactive oxygen species
Carbon metabolism
cAMP signaling pathway
Breast cancer
Apelin signaling pathway
Amyotrophic lateral sclerosis
Alzheimer disease
Adherens junction
Alum+S
MeV-S
z-score
1
0
-1

Fig. S7. SARS-CoV-2 infection induces cell-type specific enrichment of GO terms and activation or suppression of KEGG pathways, which differ dependent on prior vaccination type. Dot plots highlight enriched (A) GO categories or (B) KEGG pathways that exhibit differential activation status dependent on prior vaccination with either Alum+S or MeV_{vac2}-SARS2-S(H). Individual comparison plots are derived from scRNA-seq data and represent differential enrichment observed in alveolar macrophages, interstitial macrophages, $Treml4^{+}$ monocytes and T/NK cells. Enriched categories are labelled on the y-axes. Circle size represents the ratio of significantly dysregulated genes relative to the total gene number in a specific GO term or KEGG pathway. Circles are colored relative to activation z-score gradient presented in the scale bar, with significantly enriched categories or pathways (FDR $p<0.05$) highlighted with a black boarder. ns: non-significant

Table S1. Histopathological analysis of lung tissue of vaccinated Syrian hamster batch #1 upon challenge with SARS-CoV-2. Hamsters were vaccinated with medium (MOCK), MV_{vac2}-ATU(P) as measles-only vector control (MeV), MeV_{vac2}-SARS2-S(H) (MeV-S), or Alum-adjuvanted Spike protein (Alum+S). The left lobe of vaccinated hamster lungs was dissected 4 dpi. H&E staining revealed histopathological changes and immune cell infiltration assessed by a trained pathologist in a blinded manner. DIC, disseminated intravascular coagulation.

Animal-No.	Vaccine group	% Dense Area	Bronchia	Vessels	DIC	Dense Area	Fibrosis	Syncytia
47	MOCK	< 50% dense areas, clearly bronchial-associated	Marked purulent bronchitis (granulocytes and lymphocytes in the lumen), bronchial epithelium sometimes with inflammatory infiltration.	Vascular walls with inflammatory infiltration, Single-cell necrosis in the vessel wall, multiple hemorrhages in the tissue, 2 x edema around vessels	No	mostly lymphocytes and macrophages, less with granulocytes, sporadic eosinophils, proliferation of type II pneumocytes, often karyorrhexis	No	No
48	MOCK	30% dense areas, Bronchial- and vessel- associated	Bronchitis (lymphocytes and only very few granulocytes in the lumen), bronchial epithelium with little inflammatory infiltration and damage.	Vascular walls with inflammatory infiltration, Single-cell necrosis in the vessel wall, no bleeding or edema	No	mostly lymphocytes, macrophages, pneumocytes, isolated eosinophils, often karyorrhexis	No	No
49	MOCK	approximately 50% dense areas, clearly bronchial-associated	Bronchitis (lymphocytes and granulocytes in the lumen), bronchial epithelium sporadically with inflammatory infiltration, little damage.	Vascular walls with inflammatory infiltration, multiple hemorrhages in the tissue, 2 x edema around vessels	No	mostly lymphocytes, macrophages, pneumocytes, no granulocytes, eosinophils not increased, Foci with massive karyorrhexis	No	No
50	MOCK	approximately 33% dense areas, clearly bronchial-associated	Bronchitis (lymphocytes and granulozytes in the lumen), bronchial epithelium with little inflammatory infiltration and damage (karyorrhexis).	Vascular walls with inflammatory infiltration (also eosinophils), multiple hemorrhages in the tissue, 2 x edema around vessels	No	mostly lymphocytes, macrophages, pneumocytes, isolated eosinophils, foci with karyorrhexis	No	No
51	MOCK	approximately 33% dense areas, clearly bronchial-associated	Bronchitis (lymphocytes and granulocytes in the lumen), bronchial epithelium sporadically with inflammatory infiltration, little damage.	Vascular walls with inflammatory infiltration (also eosinophils), multiple hemorrhages in the tissue, 2 x edema around vessels	No	mostly lymphocytes, macrophages, pneumocytes, isolated eosinophils, frequent karyorrhexis	No	No
52	MOCK	approximately 33% dense areas (macroscopic), bronchial- and vessel-associated, diffuse distribution	Bronchitis (only few lymphocytes and granulocytes in the lumen) bronchial epithelium with inflammatory infiltration, little damage	Vascular walls with inflammatory infiltration, clear single cell necrosis in the vessel wall, several hemorrhages in the tissue.	No	diffused distributed, mostly lymphocytes, macrophages, pneumocytes, Isolated eosinophils, frequent karyorrhexis	No	No
53	Alum+S	approximately 33% dense areas (macroscopic), bronchial- and vessel-associated, diffuse distribution	Bronchitis (only few lymphocytes, granulocytes and little karyorrhexis in the lumen) bronchial epithelium with little inflammatory infiltration, marked proliferation of the bronchial epithelium, clear damage	Vessel walls only sporadically infiltrated with inflammation, hemorrhages in the tissue	No	mostly lymphocytes, macrophages, pneumocytes, massive eosinophils, frequent karyorrhexis	No	No

Animal-No.	Vaccine group	% Dense Area	Bronchia	Vessels	DIC	Dense Area	Fibrosis	Syncytia
54	Alum+S	30% dense areas, bronchial- and vessel-associated	Bronchitis (lymphocytes and granulocytes in the lumen), bronchial epithelium: foci of inflammatory infiltration, marked proliferation of the bronchial epithelium,clear damage	Vessel walls only very slightly infiltrated, several hemorrhages in the tissue.	No	mostly lymphocytes, macrophages, pneumocytes, massive eosinophils, frequent karyorrhexis	No	Yes
55	Alum+S	40% dense areas, not bronchial- or vessel- associated	Bronchitis (Lymphocytes and granulocytes in the lumen), bronchial epithelium: foci of inflammatory infiltration, marked proliferation of the bronchial epithelium, clear damage	Vascular walls with inflammatory infiltration, significant single cell necrosis in the vascular wall, 1 x hemorrhages in the tissue, 1 x edema around vessels.	No	mostly lymphocytes, macrophages, pneumocytes, massive eosinophils, frequent karyorrhexis	No	Suspicion
56	Alum+S	80% dense areas, not clearly bronchial or vessel associated.	Bronchitis (lymphocytes and granulocytes in the lumen), bronchial epithelium: foci of inflammatory infiltration, marked proliferation of the bronchial epithelium, clear damage	Vascular walls with inflammatory infiltration, isolated single cell necrosis in the vascular wall, multiple hemorrhages in tissue, slight edema around vessels.	No	mostly lymphocytes, macrophages, pneumocytes, massive eosinophils, only sporadic karyorrhexis	No	No
57	Alum+S	50% dense areas, not clearly bronchial or vessel associated.	Bronchitis (lymphocytes, granulocytes and karyorrhexis in the lumen), bronchial epithelium with very little inflammatory infiltration, no karyorrhexis, little damage	Vascular walls with inflammatory infiltration, isolated single cell necrosis in the vascular wall, sporadic hemorrhages in the tissue.	No	mostly lymphocytes, macrophages, pneumocytes, massive eosinophils, only sporadic karyorrhexis	No	No
58	Alum+S	40% dense areas, not clearly bronchial or vessel associated.	Bronchitis (lymphocytes, granulocytes and karyorrhexis in the lumen), bronchial epithelium: Foci of inflammatory infiltration, very few karyorrhexis, little damage	Vascular walls with inflammatory infiltration, 1 x single cell necrosis in the vascular wall, 2 x hemorrhages in the tissue.	No	mostly lymphocytes, macrophages, pneumocytes, massive eosinophils, only sporadic karyorrhexis	No	No
59	MeV	50% dense areas, not clearly bronchial or vessel associated, diffuse distribution	Bronchitis (lymphocytes, granulocytes and karyorrhexis in the lumen), bronchial epithelium with focal inflammatory infiltration, no karyorrhexis, little damage	Vascular walls with inflammatory infiltration, sporadic single cell necrosis in the vascular wall, multiple hemorrhages in the tissue.	No	mostly lymphocytes, macrophages, pneumocytes, few eosinophils, more neutrophils	No	No
61	MeV	40% dense areas, bronchial associated, diffuse distribution	Bronchitis (lymphocytes, granulocytes and karyorrhexis in the lumen), bronchial epithelium: foci of inflammatory infiltration, no karyorrhexis, little damage	Vascular walls with inflammatory infiltration, sporadic single cell necrosis in the vascular walls, edema around the vascular wall, multiple hemorrhages in the tissue.	No	mostly lymphocytes, macrophages, pneumocytes, no eosinophils, more neutrophils sporadic karyorrhexis	No	No

Animal-No.	Vaccine group	% Dense Area	Bronchia	Vessels	DIC	Dense Area	Fibrosis	Syncytia
62	MeV	approximately 20% dense areas (macroscopical), bronchial and vessel associated, diffuse distribution	Bronchitis (lymphocytes, granulocytes and karyorrhexis in the lumen), Bronchial epithelium: foci of inflammatory infiltration, no karyorrhexis, little damage	Vascular walls with inflammatory infiltration, sporadic single cell necrosis in the vascular walls, multiple hemorrhages in the tissue.	No	mostly lymphocytes, macrophages, pneumocytes, eosinophile involved, sporadic karyorrhexis	No	No
63	MeV	50% dense areas, not clearly bronchial or vessel associated, diffuse distribution	Bronchitis (lymphocytes and karyorrhexis in the lumen), bronchial epithelium: foci of inflammatory infiltration, sporadic karyorrhexis, proliferation?	Vascular walls with inflammatory infiltration, sporadic single cell necrosis in the vascular walls, edema around the vascular walls, several hemorrhages in the tissue.	No	mostly lymphocytes, macrophages, pneumocytes, eosinophile involved, sporadic karyorrhexis	No	No
64	MeV	60% dense areas, not clearly bronchial or vessel associated, diffuse distribution	Bronchitis (little in the lumen), bronchial epithelium with focal inflammatory infiltration, proliferation?	Vascular walls with inflammatory infiltration (especially veins), several hemorrhages in the tissue.	No	mostly lymphocytes, macrophages, pneumocytes, no eosinophils, sporadic karyorrhexis	No	No
65	MeV-S	20% dense areas (microscopic), clearly bronchial associated	Bronchitis (little in the lumen), bronchial epithelium hardly affected.	Vascular walls with very little inflammatory infiltration, 2 x hemorrhages in the tissue.	No	mostly lymphocytes, macrophages, pneumocytes, isolated eosinophils, no karyorrhexis (1 x ?)	No	No
66	MeV-S	10% dense areas, clearly bronchial associated	Bronchitis (little in the lumen), bronchial epithelium hardly affected.	Vascular walls without inflammatory infiltration, several hemorrhages in the tissue.	No	mostly lymphocytes, macrophages, pneumocytes, isolated eosinophils, sporadic karyorrhexis	No	No
67	MeV-S	25% dense areas, clearly bronchial associated	Mild bronchitis (mostly little in the lumen), bronchial epithelium with sporadic inflammatory infiltration, otherwise not affected.	Vascular walls with infiltration of eosinophils, several hemorrhages in the tissue.	No	mostly lymphocytes, macrophages, pneumocytes, massive eosinophils around vessels, no karyorrhexis	No	No
68	MeV-S	50% dense areas, clearly bronchial-associated	Mild bronchitis (mostly little in the lumen), bronchial epithelium with focal inflammatory infiltration otherwise not affected.	Vascular walls infiltration of eosinophils, several hemorrhages in the tissue.	No	mostly lymphocytes, macrophages, pneumocytes, massive eosinophils around vessels, no karyorrhexis	No	No
69	MeV-S	30% dense areas, clearly bronchial associated	Mild bronchitis (lymphocytes and karyorrhexis in the lumen), bronchial epithelium with focal inflammatory infiltration, significant damage to the bronchial epithelium	Vascular walls with inflammatory infiltration, karyorrhexis in the vascular wall, edema around vessels, massive hemorrhage in the tissue.	No	mostly lymphocytes, macrophages, pneumocytes, significant amount of eosinophils, foci with karyorrhexis	No	Yes
70	MeV-S	60% dense areas, not clearly bronchial associated	Mild bronchitis (lymphocytes, karyorrhexis in the lumen), bronchial epithelium with focal inflammatory infiltration; significant damage to the bronchial epithelium.	Vascular walls with inflammatory infiltration, edema in the vascular wall, edema around the vessels, massive hemorrhages in the tissue.	No	mostly lymphocytes, macrophages, pneumocytes, isolated eosinophils, sporadic karyorrhexis	No	No

Table S2. Histopathological analysis of lung tissue of vaccinated Syrian hamster batch #2 upon challenge with SARS-CoV-2. Hamsters were vaccinated with medium (MOCK), MV_{vac2}-ATU(P) as measles-only vector control (MeV), MeV_{vac2}-SARS2-S(H) (MeV-S), or Alum-adjuvanted Spike protein (Alum+S). The left lobe of vaccinated hamster lungs was dissected 4 dpi. H&E staining revealed histopathological changes and immune cell infiltration assessed by a trained pathologist in a blinded manner. DIC, disseminated intravascular coagulation.

Animal-No.	Vaccine group	% Dense Area	Bronchia	Vessels	DIC	Dense Area	Fibrosis	Syncitia
#93	MOCK	about 30% dense areas, mostly bronchial associated	Bronchial epithelium with inflammatory infiltration, granulocytes in the lumen, partial erythrocytes, some bronchial epithelium in the surrounding tissue	Vascular walls sporadically infiltrated with inflammation, marked hemorrhages	No	few densed areas infiltrated with macrophages, pneumocytes, lymphocytes and granulocytes, no eosinophils, moderate karyorrhexis	No	No
#98	MOCK	max. 10%, small foci, not bronchial associated	slightly altered; low inflammatory infiltration, some inflammatory cells in the lumen	prominent endothelium, minor hemorrhage	No	with increased eosinophils; macrophages and lymphocytes	No	No
#105	MOCK	max. 10%, in a single condensed area, not bronchial associated	slightly altered; low inflammatory infiltration underneath the epithelium	prominent endothelium, minor hemorrhage	No	1 x dense area with macrophages and lymphocytes, hardly any granulocytes, no eosinophils. moderate karyorrhexis.	No	No
#109	MOCK	about 30%, dense areas not clearly bronchial associated	slightly altered; epithelium sporadically with inflammatory infiltration; granulocytes in the lumen	prominent endothelium, hemorrhage	No	Macrophages, pneumocytes, lymphocytes, hardly any granulocytes and eosinophils. Isolated foci with karyorrhexis.	No	No
#113	MOCK	max. 10%, in a single condensed area,	Epithelium clearly altered; scattered inflammatory infiltration, no granulocytes in the lumen	prominent endothelium, significant bleeding	No	Macrophages, pneumocytes, lymphocytes, hardly any granulocytes and eosinophils. Isolated foci with karyorrhexis.	No	No
#91	MeV-S	max. 10%, clear relation to bronchi.	Marked proliferation of the epithelium into the surrounding tissue. Epithelium with inflammatory infiltration	Prominent endothelium, minor hemorrhage?	No	Some eosinophils around vessels, macrophages, pneumocytes, lymphocytes and granulocytes, hardly any karyorrhexis.	No	No
#95	MeV-S	10% dense areas, small multiple foci, bronchial associated	Epithelium not signifiantly altered.	Prominent endothelium, scattered karyorrhexis in vessel walls, only 1 x hemorrhage	No	Some eosinophils in dense area, macrophages, pneumocytes, lymphocytes and granulocytes, hardly any karyorrhexis,	No	No
#99	MeV-S	minimal; only 3 small foci, strictly bronchial associated	Epithelium not significantly altered. Scattered Epithelium in the surrounding tissue.	Prominent endothelium, no hemorrhage	No	Some eosinophils in dense area, macrophages, pneumocytes, lymphocytes and granulocytes, no karyorrhexis.	No	No
#102	MeV-S	minimal; only smallest foci, bronchial associated	Regular	Prominent endothelium, no hemorrhage	No	Some eosinophils in dense area, macrophages, pneumocytes, lymphocytes and granulocytes, no karyorrhexis.	No	Suspected

Animal-No.	Vaccine group	% Dense Area	Bronchia	Vessels	DIC	Dense Area	Fibrosis	Syncitia
#114	MeV-S	30% dense areas, bronchial associated	Bronchitis, lymphocytes and a few granulocytes in the lumen; inflammatory infiltration of the epithelium. Epithelium in the surrounding tissue.	Prominent endothelium, perivasculitis with some eosinophils, hemorrhage in the surrounding area.	No	Macrophages, pneumocytes, lymphocytes. Hardly any granulocytes and eosinophils. Sporadic karyorrhexis.	No	No
#94	Alum+S / Dexa	10% dense areas, not bronchial associated	Bronchitis, epithelium with inflammatory infiltration	Vasculitis, prominent endothelium, low inflammatory infiltration of the vessel walls	No	Some eosinophils especially around vessels (poorly visible due to hemorrhages) Macrophages, pneumocytes, lymphocytes and granulocytes.	No	No
#97	Alum+S	50% dense areas, not bronchial associated	Bronchitis, epithelium with inflammatory infiltration, granulocytes and lymphocytes in the lumen, bronchial epithelium in the surrounding tissue	Marked vasculitis with inflammatory infiltration of the wall (incl. eosinophils), many eosinophils in the surrounding of the vessel walls	No	Many eosinophils especially around vessels. Macrophages, pneumocytes, lymphocytes and granulocytes.	No	No
#101	Alum+S	50% dense areas, not bronchial associated	Epithelium not infiltrated by inflammation, blood in the lumen	Marked vasculitis with inflammatory infiltration of the vessel wall, no edema around vessels, massive hemorrhage in the surrounding tissue.	No	Massive foci of eosinophils (vessels?), macrophages, pneumocytes, lymphocytes and granulocytes.	No	No
#104	Alum+S	60% dense areas, not bronchial associated	Epithelium little affected; granulocytes in the lumen	Marked vasculitis with inflammatory infiltration of the wall.	No	Massive foci of eosinophils (vessels?), macrophages, pneumocytes, lymphocytes and granulocytes.	No	No
#106	Alum+S	70% dense areas, not bronchial associated	Bronchitis, epithelium with little inflammatory infiltration, epithelium irregular, granulocytes (eosinophils) in the lumen	Marked vasculitis with low infiltration of eosinophils in the vessel wall, massive hemorrhage in the surrounding tissue.	No	Many eosinophils especially around vessels. Macrophages, pneumocytes, lymphocytes and granulocytes. Karyorrhexis.	No	No
#107	Alum+S / Dexa	30% dense areas, not bronchial associated	Bronchitis, epithelium with little inflammatory infiltration, epithelium irregular, granulocytes (eosinophils) in the lumen	Marked vasculitis with inflammatory infiltration of the vessel wall, hemorrhage in the surrounding area.	No	Some eosinophils, but more granulocytes, macrophages, pneumocytes, lymphocytes.	No	No
#111	Alum+S / Dexa	20% dense areas, bronchial associated	Epithelium hardly affected, single eosinophils in lumen	Prominent endothelium, hemorrhages.	No	Mild Infektion, Eosinophils present, often focal, Macrophages, pneumocytes, lymphocytes, granulocytes, karyorrhexis.	No	No
#112	Alum+S	60% dense areas, not bronchial-associated, highly condensed	Epithelium hardly affected, Detritus and granulocytes in the lumen	Prominent endothelium, sporadic inflammatory inflammation in the vessel wall, massive perivascular lymphatic infiltration.	No	Some eosinophils, granulocytes, macrophages, pneumocytes, lymphocytes low karyorrhexis.	No	No

Animal-No.	Vaccine group	% Dense Area	Bronchia	Vessels	DIC	Dense Area	Fibrosis	Syncitia
#116	Alum+S / Dexa	minimal; only smallest foci, strictly bronchial associated	Regular	Prominent endothelium, sporadic inflammatory infiltration.	No	Eosinophils clearly present, macrophages, pneumocytes, lymphocytes.	No	No
#117	Alum+S / Dexa	20% dense areas, not clearly bronchial associated	Epithelium appears disorganized; no infiltration of epithelium	Prominent endothelium, vessel wall infiltrated with eosinophils. Massive eosinophils in lumen + surrounding tissues.	No	Many eosinophils, macrophages, pneumocytes, lymphocytes, granulocytes.	No	No
#118	Alum+S	70% dense areas, not bronchial associated, highly condensed	Epithelium appears disorganized; no infiltration of epithelium low amount of inflammatory cell in the lumen	Prominent endothelium massive lymphatic sheath, massive eosinophils in the lumen + around the vessels, hemorrhages.	No	Massive eosinophils present, macrophages, pneumocytes, lymphocytes, granulocytes.	No	No
#120	Alum+S / Dexa	40% dense areas, not bronchial associated	Epithelium clearly altered; occasional inflammatory infiltration, granulocytes in the lumen; epithelium in the surrounding tissue	Prominent endothelium, inflammatory infiltration (eosinophils) of the wall, no hemorrhage.	No	Some eosinophils, granulocytes, macrophages, pneumocytes, lymphocytes low karyorrhexis.	No	Suspected
hamster #1	naive	Regular	Regular	Regular.	No	Regular.	No	No
hamster #2	naive	Regular	Regular	Regular.	No	Regular.	No	No

Table S3. Statistical evaluation of selected scRNA-Seq data sets. scRNA data concerning relevant selectively up-regulated gene sets in depicted annotated cell types between differently vaccinated hamster cohorts were analysed to reveal statistical significance of de-regulated genes as depicted in Fig. 6D and 6F. Differential expression of the selected cytokines in different cell type compartments between treatment groups was performed using the FindMarkers function from Seurat with the default parameters. *, p<0.05; **, p<0.01; ***, p<0.001; ****, p<0.0001. MΦ, macrophages; DC, dendritic cells; NK, natural killer cells; ILC, innate lymphoid cells.

all cells	*Il4*			*Il5*			*IL13*			*IL19*			*CCL11*		
	Alum+S vs. Mock	Alum+S vs. MeV	MeV vs. Mock	Alum+S vs. Mock	Alum+S vs. MeV	MeV vs. Mock	Alum+S vs. Mock	Alum+S vs. MeV	MeV vs. Mock	Alum+S vs. Mock	Alum+S vs. MeV	MeV vs. Mock	Alum+S vs. Mock	Alum+S vs. MeV	MeV vs. Mock
AT1/AT2															
Endothelial cells															
B cells															
Alveolar MΦ															
Lung MΦ										****	****		****	****	
Monocytic MΦ											*		***	****	
Treml4^{+} MΦ															
Neutrophils															
T/NK cells	*	****	***	****	****	****	****	****	***						
Myeloid DCs															
Plasmacytoid DC															
Fibroblasts															

T/NK cell compartment	*Il4*			*Il5*			*IL13*		
	Alum+S vs. Mock	Alum+S vs. MeV	MeV vs. Mock	Alum+S vs. Mock	Alum+S vs. MeV	MeV vs. Mock	Alum+S vs. Mock	Alum+S vs. MeV	MeV vs. Mock
Naive									
Memory									
Activated		****	*	**	****	****	****	****	**
Regulatory									
NK									
ILC					***			**	

Table S4. Primer and Probe sets used. 6-Carboxyfluorescein (6FAM), BlackBerry® Quencher (BBQ), Cyanine 5 (Cy5).

Name	Sequenz	Reference
E_Sarbeco_F	5´-ACAggTACgTTAATAgTTAATAgCgT-3´	Corman et al., 2020
E_Sarbeco_R	5´-ATATTgCAgCAgTACgCACACA-3´	Corman et al., 2020
E_Sarbeco probe	5´-(6FAM)-ACACTAgCCATCCTTACTgCgCTTCg(BBQ)-3´	Corman et al 2020
IL-5_For	5'-gCCgTAgCCATggAgATC-3'	Mendlovic et al., 2014
IL-5 Seq Rev	5'-CgATgCACAgCTggTgCT-3'	This Paper
IL-5 probe	5'-(Cy5)-AgCTgTCCACTCACCgAGCTCTACTGAC (BBQ)-3´	This Paper
RPL18 F	5'-gTTTATgAgTCgCACTAACCg-3'	Zivcec et al., 2011
RPL18 R	5'-TgTTCTCTCggCCAggAA-3'	Zivcec et al., 2011
RPL18 probe	5'-(Cy5)-TCTgTCCCTgTCCCggATgATC(BBQ)-3'	Zivcec et al., 2011
Eotaxin forward	5'- AgAgAgCCTgAgACCAACAC-3'	Stanelle-Bertram et al., 2020
Eotaxin reverse	5'-AACTgggATAgAgCCTgggTg-3'	Stanelle-Bertram et al., 2020
Eotaxin-probe	5'-(6FAM)-TTgTggCCACTgCCTTCACCTC (BBQ)-3'	This Paper
IL-4-F	5'-ACAgAAAAAgggACACCATgCA-3'	Espitia et al., 2010
IL-4-R	5'-gAAgCCCTgCAgATgAggTCT-3'	Espitia et al., 2010
IL-4 probe	5'-(6FAM)-AgACgCCCTTTCAgCAAggAAgAACTCC-(BBQ)-3'	Espitia et al., 2010
IL-13-F	5'-AAATggCgggTTCTgTgC-3'	Espitia et al., 2010
IL-13-R	5'-AATATCCTCTgggTCTTgTAgATgg-3'	Espitia et al., 2010
IL-13 probe	5'-(Cy5)-TggATTCCCTgACCAACATCTCTAgTTgC (BBQ)-3'	Espitia et al., 2010

4.4 Concentrating all helper protein functions on a single entity allows rescue of recombinant measles virus by transfection of just two plasmids

Arne Auste[1,2], Michael D. Mühlebach[1,2]

[1]Section Product Testing of IVMPs, Div. Veterinary Medicine, Paul-Ehrlich-Institut, Paul-Ehrlich-Str. 51-59, 63225 Langen, Germany

[2]German Center for Infection Research, Gießen-Marburg-Langen, Germany

Journal of General Virology 2022

doi: 10.1099/jgv.0.001815

Abstract

The generation of recombinant measles virus (MeV) from manipulated genomes on plasmid DNA is quite a complex and inefficient process. As a member of the order Mononegavirales its single-stranded RNA genome in negative sense orientation is not infectious, but requires co-availability of the viral RNA-dependent RNA polymerase L, the polymerase co-factor phosphoprotein P, and the nucleocapsid protein N in defined relative amounts to establish infectious centers in transfected cell cultures that release replication-competent recombinant MeV particles. For this so-called rescue, different rescue systems were developed that rely on at least four different components. In this work, we establish a functional MeV rescue system just being composed of two components: The plasmid encoding the (modified) viral genome, and a 1-helper-plasmid bundling all helper functions. In contrast to a rescue-system for Newcastle Disease Virus, another paramyxovirus, co-expression of all helper proteins by the same promoter failed. Instead, adaptation of the strength of the respective promoters to drive each helper gene´s expression to the relative expression found in MeV-infected cells or other rescue systems, which indeed adjusted respective mRNA and protein expression, yielded success, albeit not yet to the same efficacy as the four-component system. Thereby, our study paves the way for the development of easier and after further optimization more efficient rescue systems to generate recombinant MeV for e.g. the application as vaccine platform or oncolytic virus.

Impact Statement

Recombinant MeV is in the focus of biomedical research as vaccine platform technology or as oncolytic virus. It is a member of the order Mononegavirales and its generation is therefore dependent on the presence of the viral replication machinery in cells expressing the viral negative-sense RNA genome or the positive-sense anti-genome. Both are otherwise no suitable templates for the cellular transcription and translation processes, per se. At least four different components have been necessary to generate the viral machinery to allow virus rescue. The system established here consists of just two components – the genome and the helper plasmid – and therefore is much simpler configured and less complicated in application, but needed adaptation to specific properties of MeV biology. Options for further optimization became evident, implicating more efficient rescue systems to be expected, which would pave the way for up-graded application of recombinant MeV or other hard-to-rescue negative-stranded RNA viruses.

Introduction

Genetically engineered Measles virus (MeV) is used in basic research and developed as anti-cancer agent for oncolytic virotherapy [1]. Moreover, it is tested as vector platform expressing antigens of other pathogens for the development of novel vaccines targeting respective diseases in addition to the measles [2]. For these applications in biomedicine, genomes of authorized MeV vaccine strains or strains derived thereof have been used in the overwhelming number of cases [2,3]. Thereby, its safety and immunogenicity has been shown against more than 17 different disease targets, by now, in a considerable number of preclinical models. Also clinical trials using MeV-derived recombinant MeV have been done, and reached up to phase 2, awaiting a phase 3 trial to target CHIKV [4]. Moreover, MeV-derived vaccines have recently been tested also against COVID-19 [5–9].

For the generation of such recombinant MeV (rMeV), the genetic properties of MeV have to be considered. MeV is member of the family of *Paramyxoviridae* and the prototype virus of the genus *Morbillivirus*. Therefore, it is characterized by its single-stranded linear RNA genome in negative-sense orientation. As such, transcription and replication of MeV is dependent on the viral ribonucleoprotein complex (RNP) contained in infectious virus particles. The RNP is formed by the RNA genome, which is complexed with the viral nucleocapsid protein N, the viral phosphoprotein P, and the viral RNA dependent RNA-polymerase, the so-called large protein L [10]. This tight association of the RNA genome and other components of the RNP, especially the N protein, is assumed to be responsible for the so-called "rule-of-six": The total number of nucleotides of any MeV genome has to be a multiple of six to allow replication [11].

For the generation of infectious replicating rMeV particles from cDNA, the rescue, the technology of reverse genetics was developed, as applied first for rabies virus [12]: A full-length cDNA copy of the viral genome is transcribed into positive-sense RNA in cells expressing all three protein components of the RNP, in parallel. The viral polymerase complex assembles on this antigenomic RNA to build the fully functional RNP. This complex then transcribes the negative-sensed genomic RNA. The genomic RNA serves in turn as template for viral mRNA transcription to start also the expression of the viral structural genes, and assembly into infectious viral particles becomes possible. Hence, all four elements of the RNP have to be provided in the initial virus-producing cell in parallel in the appropriate amounts [13–15]. For MeV, few rescue systems have been established over the years [16,17]. One effective system provides the viral RNA genome and the three protein components of the RNP encoded on separate plasmids under the control of PolII-driven promoters [17]. Co-transfection of these plasmids in defined amounts turns single cells into virus factories, which release infectious recombinant virions. Albeit quite effective, the rescue

efficacy is still limited and yields approximately a few dozen independent virus factories releasing independent virus clones during each experiment. This limitation is most likely due to a low probability for the optimal amount of each component of the RNP complex, which is regulated during virus infection by the transcriptional gradient of viral mRNAs [18]. Moreover, the generation and co-transfection of four independent plasmids potentiates eventual issues (e.g. purity, content, supercoiling) with plasmid DNA quality.

For another paramyxovirus, the combination of helper functions in one plasmid considerably improved rescue efficacy. Newcastle Disease Virus (NDV) is a paramyxovirus of the genus *Avulavirus*, which can be rescued by combining the three helper genes for viral proteins NP, P, and L driven by the same PolII-promoter, the immediate-early promoter of human cytomegalovirus (CMV), in one helper plasmid, which is co-transfected with the genome plasmid also driven by P_{CMV} [19]. Application of this two-plasmid system increased the number of independent rescued clones as well as the option to rescue virus strains difficult to rescue using a formerly established four-plasmid system.

Therefore, we intended to implement a similar strategy to generate a simpler rescue system for vaccine strain-derived MeV, and constructed a helper system encoding MeV-N, -P and -L on one single plasmid, which was designated 1-helper plasmid (1HP). However, using the same strategy as for NDV with the same promoter to drive expression of helper genes and transcription of the viral antigenome failed. Therefore, we modified the single helper plasmid by using different promoters with specifically evaluated transcriptional activity to drive the individual helper functions. Indeed, expression of the helper proteins can be adapted by this strategy and gave rise to few plasmid configurations that allowed rescue of recombinant vaccine strain-derived MeV from plasmid DNA with different efficiency.

Methods

Cells and viruses

293T (ATCC# CRL-3216) and Vero (African green money kidney) (ATCC# CCL-81) cells were purchased from ATCC (Manassas, USA) and cultured in Dulbecco's modified Eagle's medium (DMEM, Sigma-Aldrich, Steinheim, Germany) supplemented with 10 % fetal bovine serum (FBS; Sigma-Aldrich, Steinheim, Germany) and 2 mM L-glutamine (L-Gln; Biochrom). All cells were cultured at 37 °C in a humidified atmosphere containing 6 % CO2 for a maximum of 6 months of culture after thawing of the original stock to ensure authenticity of the cell lines. MV_{vac2}-GFP(P) or MV_{vac2}-GFP(N) were amplified as described [20] and titrated in Vero cells according to the $TCID_{50}$ method of Kaerber and Spaerman [21].

Plasmids

Luciferase control plasmid pG-RL-Pcag was generated by cloning the renilla luciferase gene of pGL4.82 (Promega, Walldorf, Germany) into pGL3-basic (Promega) backbone using HindIII and FseI to yield pG-RL-basic. Then, P_{CAG} was cut out of pCA-MVN with SalI and EcoRI, and blunted using the Klenow fragment of DNA-polymerase I (New England Biolabs, Frankfurt, Germany) according to the manufacturer´s instructions. Finally, P_{CAG} was inserted into pG-RL-basic, which had been opened with SmaI. Luciferase candidate plasmids pGL3-Pcag, pGL3-CMV, pGL3-EF1α, pGL3-EFS, pGL3-PGK, pGL3-SFFVp or pGL3-SV40p were generated by inserting excised and blunted promoter sequences P_{CAG} (from pCA-MVN [17]), P_{CMV} (from pBRPolII-MVvac2-GFP(N) [20], EF1αp (from pBOS_hBKLF.2 [22]), EFSp (pSRS11 EFS GFPpre (gift from U. Modlich, Paul-Ehrlich-Institut, Langen, Germany)), PGKp (from VMD00.PG pRRL.PPT.PGK.mHAMpl(wt).pre (gift from U. Modlich, Paul-Ehrlich-Institut, Langen, Germany)), SFFVp (from LeGO-Cer2 (Addgene, Watertown, Massachusetts, USA) or SV40p (from pTurboFP635-C (Evrogen, Moscow, Russia), respectively, into pGL3-basic, which had been opened with SmaI. Correct direction of inserted promoters was checked by restriction pattern analyses. The construction of single helper plasmids is described in detail in the Results section. Respective modified plasmid regions were sequenced to ensure correct cloning.

PCR and primers

For generation of pBR-1HP-3CMV, fragments were amplified under the following conditions: After initial denaturation for 2 min at 94 °C, 20 cycles of PCR amplification were done with 20 s denaturation at 94 °C, 30 s annealing at 60 °C, and 45 s elongation at 68 °C. Thermocycling was finished with a final elongation phase for 7 min at 68 °C before the samples were cooled down to 4 °C.

The intermediate construct pBRPolII-MVvac2-pA(L) was generated by inserting the fragment ‘pA’, which was amplified from pGL3-basic with primer pair pANotA(+) and pANotA(-) (Tab. 1), into pBRPolII-MVvac2. The intermediate construct pBRPolII-MVvac2-pA(L)-CMVP1 was generated by inserting the fragment ‘CMVP1’, which was amplified from pBRPolII-MVvac2 with primer pair CMVP1(+) and CMVP1(-) (Tab. 1), into pBRPolII-MVvac2-pA(L). The fragment ‘CMVP2’ was amplified from pBRPolII-MVvac2 with primer pair CMVP2(+) and CMVP2(-) (Tab. 1). The Fragment ‘Plink’ was amplified from pBRPolII-MVvac2 with primer pair PlinkCMV(+) and Plink(-) (Tab. 1). The final construct pBR-1HP-3CMV was generated by fusing fragments ‘CMVP2’ and ‘Plink’ with the primer pair CMVP2(+) and Plink(-) (Tab. 1) and prolonging the elongation phase to 60 sec per circle to yield fragment ‘CMVP2-Plink’, which was inserted into pBRPolII-MVvac2-pA(L)-CMVP1.

Table 1. Primers. Depicted are nucleotide sequences of primers used 5´- 3´. (+) and (-) indicate direction of respective primers.

pANotA(+)	GCGGCCGCAGACATGATAAGATACATTGATG
pANotA(-)	GCGGCCGCTACCACATTTGTAGAGGTTTTAC
CMVP1(+)	GTCGACGCGGCCGCGTACGCCGTTACATAACTTACGGTAAATG
CMVP1(-)	ACTAGTTCGAACGGAGGCTGGATCGGTCCCG
CMVP2(+)	CCTGCAGGCGGCCGCACGCGTCCGTTACATAACTTACGGTAAATG
CMVP2(-)	CGTGCCTGCTCTTCTGCCATTTAATTAACGGAGGCTGGATCGGTCCCG
PlinkCMV(+)	CGGGACCGATCCAGCCTCCGTTAATTAAATGGCAGAAGAGCAGGCACG
Plink(-)	CCTGCAGGTGGCTCGCTCCTGTCCTG

Dual-luciferase assay

8×10^4 293T cells had been seeded in 48-well plates one day before the assay. Adherent cells were transfected the following day with 0.1 µg pG-RL-Pcag coding for P_{CAG}-driven renilla luciferase and with 0.1 µg of one of the plasmids coding for firefly luciferase driven promoters of interest, i.e. pGL3-P_{CAG}, pGL3-P_{CMV}, pGL3-P_{CMV}-AatII-1.1+2.1, pGL3-EF1α, pGL3-EFS, pGL3-PGK, pGL3-SFFVp or pGL3-SV40p, using Lipofectamine 2000 (Invitrogen Life Technology, Darmstadt, Germany) according to manufacturer´s instructions. 48 h post transfection, cells were lysed with 50 µl/well 1× Passive Lysis Buffer (Promega) and transferred to black Falcon Microtest 96-well plates (BD Bioscience, Heidelberg, Germany). 50 µl/well Dual-Glo Luciferase Reagent (Promega) were added and after 15 min, the emitted light was measured at 565 nm with a Safire 2 microplate reader (TECAN, Männerdorf, Switzerland). 50 µl/well Dual-Glo Stop & Glo Reagent (Promega) were added and the emitted light was measured after 15 min at 480 nm.

Reverse transcription quantitative RT-qPCR

1×10^6 293T cells were seeded in 6-well Nunc tissue culture plates (Thermo Fisher Scientific, Ulm, Germany). On the next day, adherent cells were transfected with 4 µg pBRPolII-MVvac2-GFP(P) and either 1.2 µg of the respective 1HP constructs (two-plasmid rescue systems) or 0.4 µg pCA-MVN, 0.1 µg pCA-MVP and 0.4 µg of pCA-MVL (four-plasmid rescue system) using Lipofectamine 2000 (Invitrogen Life Technology) according to manufacturer´s instructions. In parallel, cells were infected with MV_{vac2}-GFP(P) (MOI 0.03). 24 h post transfection, or 6 h or 24 h post infection, cells were detached by pipetting, pelleted (300 × g, 5 min, 4 °C) and stored frozen at -80 °C. After thawing on ice, cells were disrupted with 350 µl RLT Plus buffer (QIAgen, Hilden, Germany) in Lysing Matrix D 2 ml tubes (MP Bioscience, Hilton, UK) containing 1.4-mm ceramic spheres using the Precellys 24 tissue homogenizer (Bertin Technologies, Montigny-le-Bretonneux, France) for 30 sec at 6,000 rpm. RNA of cell pellets was

purified with RNeasy Plus Kit (QIAgen) according to manufacturer´s instructions, and eluted in 30 µl RNase-free water. 1 µg RNA was treated with 2 U DNaseI (Invitrogen Life Technology) for 20 min at RT and then stopped with addition of 1 µl of 25 mM EDTA for 10 min at 65 °C. To this solution, 1 µl Oligo(dT)12-18 primers (500 µg/ml, Invitrogen Life Technology), 1 µl of 10 mM dNTPs (Invitrogen Life Technology), 4 µl 5× first strand buffer, 2 µl of 0.1 m DTT (Invitrogen Life Technology), 1 µl of RNase Out (Invitrogen Life Technology) and 1 µl SuperScript II RT (Invitrogen Life Technology) were added and incubated at 42 °C for 50 min. Reverse transcription was stopped by incubation at 70° C for 15 min. 5 µl of 1:10 diluted cDNA were analyzed by real-time PCR with LightCycler SYBR Green I Master kit (Roche, Basel, Switzerland) using a LightCycler II thermocycler (Roche) and primers exactly as described [23]. Plasmids pCA-MVN, pCA-MVP or pCA-MVL of known concentration were serially diluted and applied as DNA standards for copy number calculation.

Western blot analyses

2.8×10^5 293T cells were seeded in 12-well Nunc tissue culture plates (Thermo Fisher Scientific, Ulm, Germany). Adherent cells were transfected on the next day with either 1.2 µg of the respective 1HP constructs (two-plasmid rescue systems) or 0.4 µg pCA-MVN, 0.1 µg pCA-MVP and 0.4 µg of pCA-MVL (four-plasmid rescue system) using Lipofectamine 2000 (Invitrogen Life Technology) according to manufacturer´s instructions. In parallel, cells were infected with MV_{vac2}-GFP(N) (MOI 1). 48 h post infection or transfection, cells were lysed with 200 µl/well RIPA lysis buffer containing 1 tablet cOmplete Mini Protease Inhibitor Cocktail (Roche) per 10 ml buffer as described [24]. After pelleting cell debris (13,000 rpm, 15 min, 4° C), lysates were stored frozen at -80 °C. Later, 7.5 µl of lysates were mixed with 7.5 µl 2× urea buffer (200 mM Tris-HCl (pH 6.8), 8 M urea, 5 % SDS (w/v), 0.1 mM EDTA, 0.03 % bromophenol blue (w/v), 1.5 % DTT (w/v)) and incubated at 95 °C for 10 min as described [5]. Proteins were separated on a 4-20 % Mini-PROTEAN TGX sodium dodecyl sulfate-polyacrylamide gel electrophoresis gel (Biorad, Dreieich, Germany) with a Mini-PROTEAN Tetra Vertical Electrophoresis Cell (Biorad) at 100 V and blotted onto Hybond-P PVDF membranes (Amersham Biosciences, Freiburg, Germany) by wet blotting using Mini Trans-Blot Cell (Biorad) (90 mA, a maximum of 30 V, 4 °C for 18 h). Blotted membranes were blocked with TBS-T + 5 % skim milk powder (w/v) for at least 1 h at RT. Blocked membranes were probed using rabbit polyclonal anti-MeV-N antibody (1:5,000; ab23974, Abcam, Cambridge, UK), mouse monoclonal anti-MeV-P (1:2,000; ab43820, Abcam), rabbit polyclonal anti-MeV-L (1:1,000; Roberto Cattaneo, Mayo Clinic, Rochester, USA), mouse monoclonal anti-FLAG (1:1,000; A8592, Sigma-Aldrich) or mouse monoclonal anti-α-Tubulin (1:2,000; T5168, Sigma-Aldrich) diluted in blocking buffer for at least 1 h at RT with gentle rocking. Donkey polyclonal anti-rabbit IgG peroxidase conjugated (1:5,000-1:10,000; 611-7302, Rockland, Limerick, USA) or goat polyclonal anti-mouse IgG peroxidase

conjugated (1:10,000, ab102448, Abcam) diluted in blocking buffer served as secondary antibodies as appropriate. Peroxidase activity was visualized with the enhanced chemiluminescence detection kit (Thermo Fisher Scientific) according to manufacturer´s instructions on a ChemiDoc MP Imaging System (Biorad).

MeV rescue

1×10^6 293T cells were seeded in 6-well Nunc tissue culture plates (Thermo Fisher Scientific). Adherent cells were transfected on the next day with 4 µg pBRPolII-MVvac2-GFP(P) and either 1.2 µg of the respective 1HP constructs (two-plasmid rescue systems) or 0.4µg pCA-MVN, 0.1 µg pCA-MVP, and 0.4 µg of pCA-MVL (four-plasmid rescue system) using Lipofectamine 2000 (Invitrogen Life Technology) according to manufacturer´s instructions. 48 h post transfection, the cells were detached by pipetting and overlaid on a Vero cell layer (7×10^5 Vero cells/10 cm dish, seeded 4 h before). 293T-Vero co-cultures were screened daily beginning on day 4 post overlay with Axio Observer.Z1 microscope (Zeiss, Oberkochen, Germany) for appearance of syncytia.

Results

Generation of helper plasmid using the same promoter for all helper protein genes

To generate a simple rescue system for recombinant MeV, we first adapted the strategy to generate the two-plasmid rescue system for NDV [19]. For this purpose, all three helper genes of MeV were compiled in one plasmid, which had a P_{CMV} i.e. promoter sequence driving each of them, pBR-1HP-3CMV (Fig. 1). To generate pBR-1HP-3CMV, the SV40 late polyadenylation signal of pGL3-basic (Promega) was amplified and inserted downstream of the L gene at the NotI site of pBRPolII-MVvac2 to yield pBRPolII-MVvac2-pA(L). The gene-sequences encoding M, F, and H were cut out using SaI and SpeI. Using these restriction sites, a fragment encompassing the SV40 late polyadenylation signal of pGL3-basic thus terminating the P cassette and the P_{CMV} i.e. promoter excised from pBRPolII-MVvac2 thus initiating the L cassette were inserted at this site to yield pBRPolII-MVvac2-pA(L)-CMVP1. Lacking a single-cutting enzyme between the N and P genes in pBRPolII-MVvac2-pA(L)-CMVP1, the closest single cutter in the P gene segment, SbfI, was chosen to open the plasmid and insert the SV40 late polyadenylation signal thus terminating the N cassette. A P_{CMV} i.e. promoter-encoding segment (from pBRPolII-MVvac2) was chosen to initiate the P cassette, which had been fused via overlapping PCR fragments to the coding region of P from its 5' end to its SbfI site, to complete the P gene. At its 5' terminus, the L gene was tagged by inserting a FLAG (GAC TAC AAA GAC GAT GAC GAC AAG) PCR

fragment flanked with NotI and BbsI restriction sites to yield the 1HP pBR-1HP-3CMV. In 13 independent experiments, this 1HP construct failed to rescue rMeV (Fig. 1b, c).

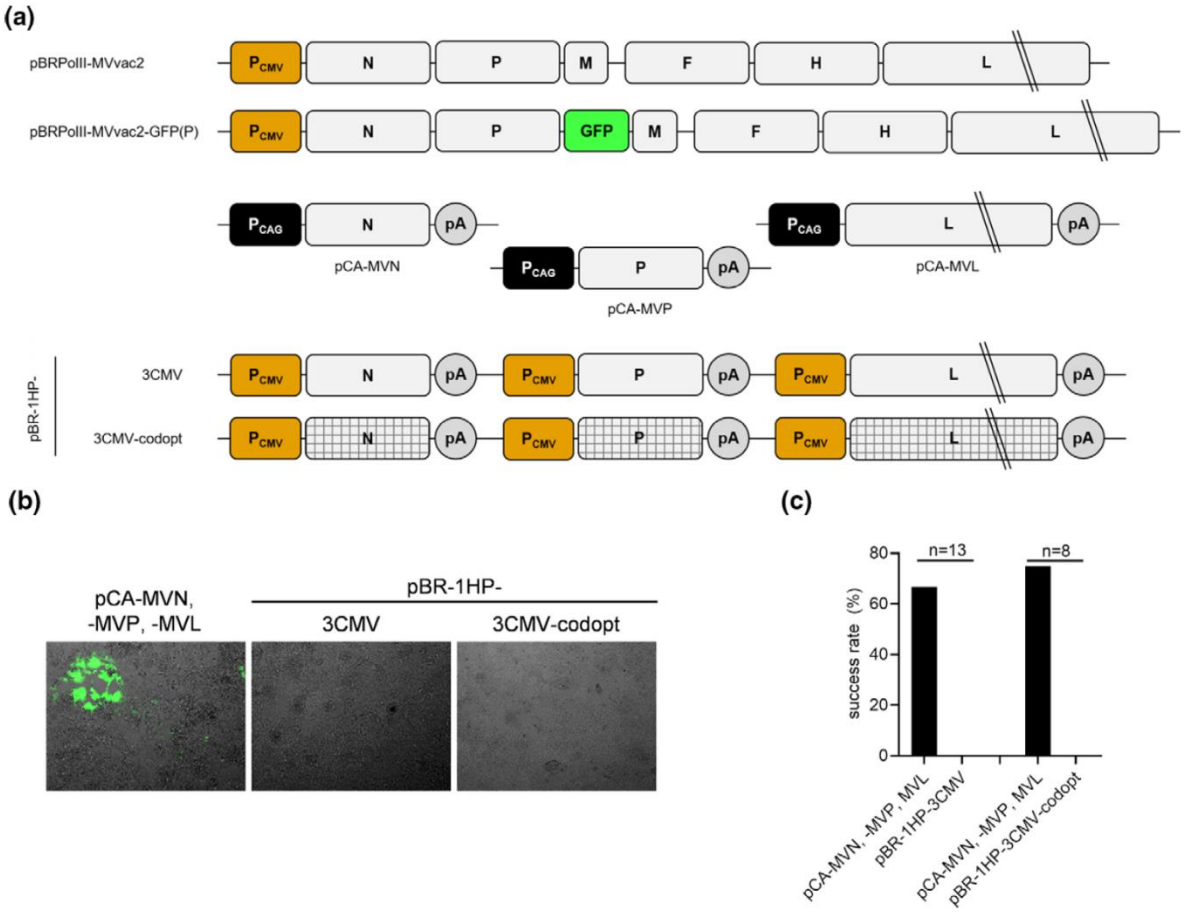

Fig. 1. MeV genome plasmids and helper plasmids. (a) Schematic depiction of two MeV genome plasmids (upper schemes), the helper plasmids of the four-plasmid rescue system (central schemes) and two 1HP constructs with the P_{CMV} promoter driving each of the three helper genes (lower schemes). (b) Overlay microscopic photographs displaying green-fluorescent syncytia of rescued MeV in overlay cultures. Pictures were taken 4-6 days post overlay. 100× magnification. (c) Number of experiments with at least one syncytium per rescue system were summed up, divided by the total number of rescue experiments per rescue system performed which equals the success rate (expressed in percentage [%]).

In a second approach, we generated a helper plasmid candidate encoding all RNP-proteins via ORFs optimized for human codon usage (pBR-1HP-3CMV-codopt). Codon-optimized genes encoding N, P, or L (including the same FLAG tag described above), which were flanked upstream by the P_{CMV} i.e. promoter and downstream by a bovine growth hormone polyadenylation signal, were obtained by gene synthesis. N was cut out with SfiI and BglII, P with BglII and SpeI, L with SpeI and NotI, and the plasmid backbone of pBR-1HP-3CMV was opened with NotI and SfI. The four fragments were ligated in a 4-point ligation to yield pBR-1HP-3CMV-codopt.

This construct aimed to compensate for potential low translation efficiency of RNP proteins due to sub-optimal viral codon use or potential cryptic splicing of plasmid-derived mRNA transcribed in the nucleus as found in pBR-1HP-3CMV. Similar to the non-optimized 1HP, this construct was not functional in rescuing rMeV in eight independent experiments (Fig. 1b, c).

Determination of promoters to simulate expression differences

In contrast to the established plasmid rescue system by Martin *et al.* [17] (Fig. 1), the helper protein expression by the tested single helper plasmids making use of P_{CMV} to drive each of the three helper genes cannot take advantage of an optimized ratio of the respective individual mRNAs´ transcription due to fixed relative gene copy numbers and same promoters driving the individual genes. Hence, we hypothesized, that graded helper protein expression is critical for MeV rescue also using single helper plasmids. To achieve this goal, the expression of individual mRNAs in the standard four-plasmid system was estimated: All three helper plasmids (pCA-MV-N, pCA-MV-P, and pCA-MV-L) utilize the P_{CAG} promoter [17,25] (Fig. 1), thus a similar transcriptional activity of the promoters in each plasmid can be assumed. Given the relative plasmid size (6.3 kb, 6.2 kb and 11.3 kb, respectively) and the amounts of plasmids transfected in the cells (0.4 µg, 0.1 µg, and 0.4 µg, respectively), an mRNA synthesis ratio of 100 : 25 : 56 (N : P : L) should result after transient transfection of the four-plasmid rescue system. This normalized ratio n_N of mRNA synthesis (100 is set for N mRNA) is calculated by equation 1, assuming that the ratio of transcribed mRNAs is directly proportional to the ratio of plasmid molecules found in the respective cells after transfection, with m indicating the amount of transfected plasmids and MW indicating the respective molecular weight:

$$n_N = \left(\frac{m(x)/MW(x)}{m(N)/MW(N)} \right) \times 100$$

To simulate this differential expression when encoding all RNP-complex proteins on one plasmid, we tested different promoters with different transcriptional activity. For this purpose, the promoters P_{CAG}, P_{CMV}, EF1αp, PGKp and SV40p were chosen as candidate promoters, since their activities span the range of promoter activities as envisioned above [26]. Additionally, the EF1α short promoter (EFSp) [27] and the promoter of the spleen focus-forming virus (SFFVp) were chosen for analyses [28].

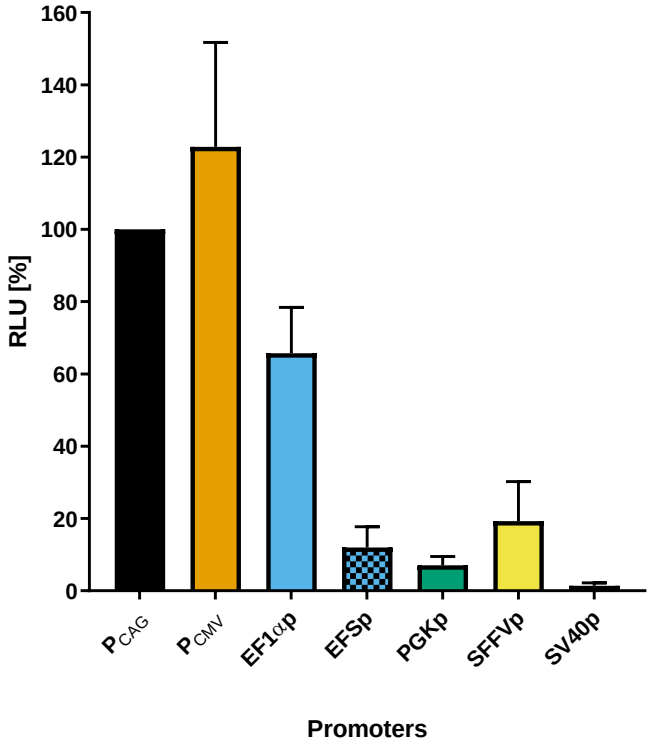

Fig. 2. Promoter activities in 293T cells. 293T cells were transfected with a plasmid coding for firefly luciferase driven by one of the eight depicted promoters and a transfection control plasmid coding for renilla luciferase. 48 h post transfection, luciferase substrate was added and the emitted light was measured. Ratios of firefly to renilla signals were normalized to reference promoter P_{CAG} (100 RLU). For this purpose, RLU of firefly signal was divided by RLU of renilla signal and ratios were normalized to ratios of reference promoter P_{CAG}. Means and SDs of four (EF1αp), five (EFSp, SFFVp, SV40p) or seven (P_{CAG}, P_{CMV}, PGKp) independent experiments presented. RLU, relative light units.

The activity of these promoters driving expression of the firefly luciferase (FLuc) reporter gene was determined in 293T cells after transient transfection in a dual luciferase assay. Thereby, pG-RL-P_{CAG} was used as control plasmid with a P_{CAG}-driven renilla luciferase (RLuc) for normalization of the transfection efficiency and to simulate promoter activity of the MeV genome plasmid during rescue. Signals of the firefly luciferase, which was driven by the respective candidate promoter, were measured. Activities of the respective promoters in 293T cells were calculated after normalization of FLuc to RLuc signals (Fig. 2). Herewith a wide variance of activities of the different promoters was identified, with P_{CMV} revealing the strongest relative promoter activity (123 RLU) in 293T cells. P_{CAG} (100 RLU) and EF1αp (66 RLU) had an intermediate activity, whereas SFFVp (19 RLU), EFSp (12 RLU), and PGKp (7 RLU) were the weakest of the tested promoters in 293T cells.

Generation of plasmids with individualized promoters to simulate expression differences

Based on these data, the promoter with the highest relative activity, i.e. P_{CMV}, was chosen to drive transcription of the MeV-N gene. To simulate the hypothetic expression ratio of MeV helper genes of 100 : 25 : 56 (N : P : L), the following two promoters were chosen: SFFVp with 16 % relative activity of P_{CMV} to drive MeV-P, and the promoter EF1αp with 54 % relative activity of P_{CMV} to drive MeV-L. On these premises, pBR-1HP-SFFVp(P) and pBR-1HP-EF1α(L) with exchange of only one promoter were generated to analyze which helper protein plays a crucial role in MeV rescue (Fig. 3). In addition, a combination of both cassettes was cloned in one plasmid (pBR-1HP-SFFVp(P)-EF1α(L)) (Fig. 3). The relative transcription of MeV-P mRNA in the four-plasmid rescue system can be estimated to be particularly low with only 25 % of the transcription of MeV-N. Therefore, we hypothesized that this ratio might be crucial for successful rescue of rMeV and generated two more 1HP, which both code for low-activity promoters (measured in 293T cells relative to P_{CMV}) for driving the MeV-P gene: pBR-1HP-EFS(P) and pBR-1HP-PGK(P) (Fig. 3). pBR-1HP-3CMV served as a basis for exchanging the respective promoters. Single-cutting enzymes MluI and PacI were used to remove the P_{CMV} i.e. promoter driving P in pBR-1HP-3CMV, to insert the promoters SFFVp (cut out of pGL3-SFFVp with XhoI and MluI), EFSp (cut out of pGL3-EFS with NcoI and SacI), or PGKp (cut out of pGL3-PGK with EcoRV and BamHI), thereby generating pBR-1HP-SFFVp(P), pBR-1HP-EFS(P), or pBR-1HP-PGK(P), respectively. Single-cutting enzymes BsiWI and BstBI were used to remove the P_{CMV} i.e. promoter driving L in pBR-1HP-3CMV or pBR-1HP-SFFVp(P) to insert the EF1αp promoter (cut out of pGL3-EF1α with NheI and NcoI) generating pBR-1HP-EF1α(L) or pBR-1HP-SFFVp(P)-EF1α(L), respectively.

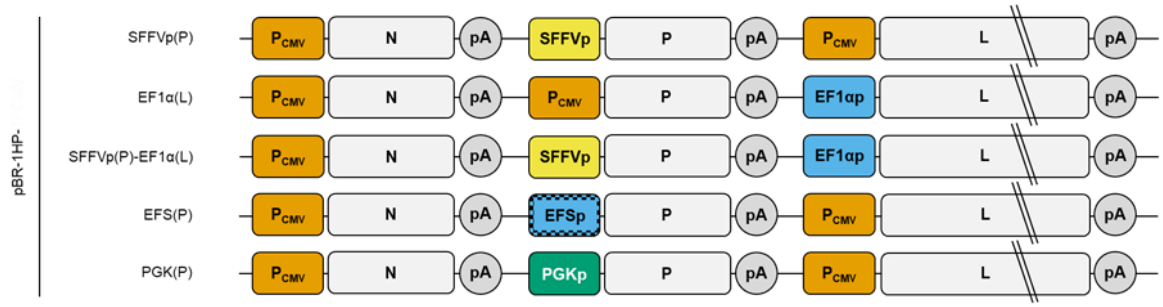

Fig. 3. 1HP constructs with modulated promoter activities. Schematic depiction of five 1HP constructs generated based on pBR-1HP-3CMV (Fig. 1) by exchanging the promoters driving the P gene, the L gene or both.

Modulation of transcriptional activities in different helper plasmids

To confirm modulation of mRNA expression by the exchange of promoters in the 1-helper plasmids and to assess their expression profiles compared to the four-plasmid system, the transcription of mRNA species for MeV-N, -P and -L was quantified by RT-qPCR (Fig. 4a). Cells infected with MeV and harvested 6 and 24 h post infection were used as further comparator for the mRNA transcription profiles. Thereby, comparison of the respective rescue systems to cells with actively replicating virus early or late after infection with active replicative centers during predominant viral gene transcription (6 h) or genome replication (24 h) becomes feasible. Copies coding for N increase from 7.7×10^5 to 3.3×10^7 copies/µg RNA, for P from 7.3×10^4 to 4.9×10^7 copies/µg RNA and for L from 2.1×10^4 to 5.5×10^6 copies/µg RNA between 6 h and 24 h after infection, respectively.

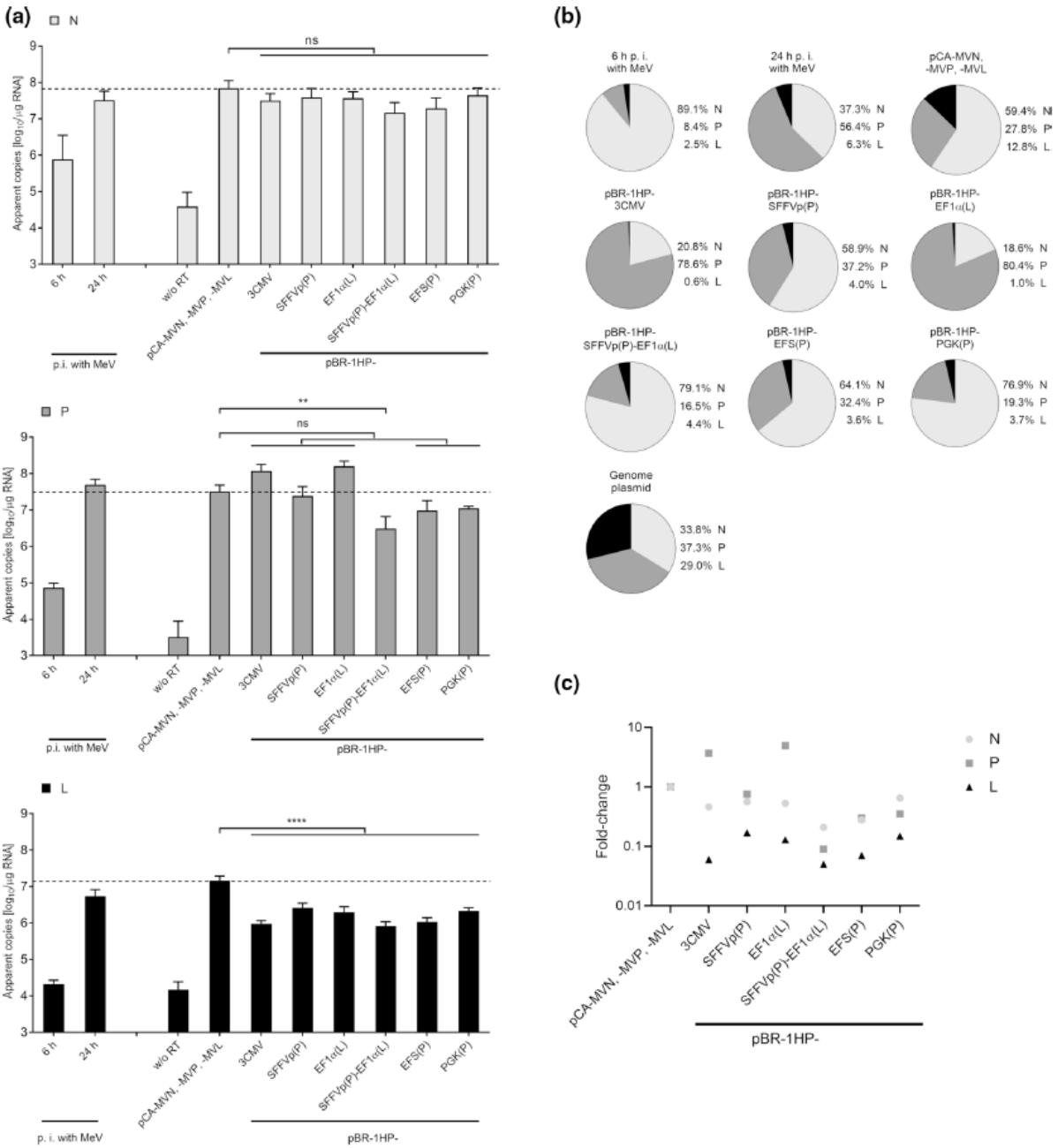

Fig. 4. mRNA expression of 1-HP plasmids during rescue. 293T cells were transfected with depicted helper plasmids or infected with MeV (MOI = 0.03). 24 h post transfection or 6 h or 24 h post infection, cells were lysed. Cellular RNA was reversely transcribed using oligo-dT primers. 1:10 diluted cDNA was analyzed in SYBR Green I-based quantitative PCR reaction. Using dilutions of plasmids of known concentration, respective mRNA copy numbers in samples were calculated. (a) Copies of mRNA coding for N (light grey bars), P (dark grey bars) and L (black bars) normalized to 1 µg cellular RNA are depicted. Sample "w/o RT" was treated like "pCA-MVN, -MVP, -MVL", but without adding enzyme for reverse transcription to reveal background signal of residual plasmid DNA carry-over. (b) Relative mRNA copies for each viral gene (N, light grey; P, dark grey; L, black) as percentage of the whole depicted in pie diagrams. Means and SDs of three independent experiments are presented. For statistical analysis one-way ANOVA analysis was applied; ns, not significant ($P>0.05$); **$P<0.01$; ****$P<0.0001$. Data are the same as displayed in Table 3.

In transfected cells, the transcription of MeV-N mRNA using pCA-MVN in combination of the four-plasmid system resulted in 6.9×10^7 mRNA copies/µg RNA). This is only slightly higher than MeV-N mRNA copies transcribed from each of the six analysed 1-HP constructs (Tab. 2). Since N ORFs are driven by the P_{CMV} Promoter in all of these constructs, these data indicate absence of interference of the other promoters for each of the 1-HP constructs.

For P, the four-plasmid system yielded 3.2×10^7 P mRNA copies / µg total cellular RNA. This was excelled by nearly an order of magnitude by pBR-1HP-3CMV (1.2×10^8 copies/µg RNA) and pBR-1HP-EF1α(L) (1.6×10^8 copies/µg RNA). Exchanging the P_{CMV} promoter of the MeV-P cassette in pBR-1HP-3CMV reduced copy numbers of P mRNA by 5-fold, when SFFVp had been inserted (pBR-1HP-SFFVp(P) 2.4×10^7 copies/µg RNA), 12-fold, when EFSp had been inserted (pBR-1HP-EFS(P) 9.7×10^6 copies/µg RNA), or 11-fold, when PGKp had been inserted (pBR-1HP-PGK(P) 1.1×10^7 copies/µg RNA) (Tab. 2). Thus, mRNA expression of MeV P was indeed regulated by the promoters driving transcription of the P gene in the different 1-HP constructs.

Table 2. Absolute numbers of MeV mRNAs in cells. Listed are absolute numbers of qRT-PCR analyses of cells after infection or transfection with respective viruses / plasmids as indicated. Depicted numbers indicate mRNA copies/µg total RNA and are graphically depicted in Fig. 4a.

mRNA	MeV infected		pCA -MVN, -MVP, -MVL	pBR-1HP-					
	6 h p. i.	24 h p. i.		3CMV	SFFVp(P)	EF1a(L)	SFFVp(P)-EF1a(L)	EFS(P)	PGK(P)
N	7.7×10^5	3.3×10^7	6.9×10^7	3.2×10^7	3.9×10^7	3.7×10^7	1.5×10^7	1.9×10^7	4.5×10^7
P	7.3×10^4	4.9×10^7	3.2×10^7	1.2×10^8	2.4×10^7	1.6×10^8	3.1×10^6	9.7×10^6	1.1×10^7
L	2.1×10^4	5.5×10^6	1.5×10^7	9.5×10^5	2.6×10^6	2.0×10^6	8.2×10^5	1.1×10^6	2.2×10^6

Finally, the transcription of MeV-L mRNA was quantified. Transfection of pCA-MVL yielded 1.5×10^7 L mRNA copies/µg total RNA), which was considerably higher than L copy numbers detected in cells, which had been transfected with any 1HP construct (8.2×10^5 copies/µg RNA - 2.6×10^6 copies/µg RNA) (Tab. 2). Thus, an exchange of the promoter P_{CMV} to EF1αp in pBR-1HP-EF1α(L) and pBR-1HP-SFFVp(P)-EF1α(L) had surprisingly little effect on the already low abundance of L encoding mRNA in the analysed cells.

To set these numbers into perspective, we calculated the relative transcription of N, P or L mRNA copies for each construct and after infection. Interestingly, cells transfected with the original four-plasmid rescue system revealed an intermediate pattern of the relative mRNA abundance of MeV-N and -P (59.4 % N, 27.8 % P, 12.8 % L) compared to those of cells harvested 6 h (89.1 % N, 8.4 % P, 2.5 % L) and 24 h (37.3 % N, 56.4 % P, 6.3 % L) after infection (Fig. 4b, Tab. 3). As already indicated above, rescue cells transfected with pBR-1HP-3CMV or pBR-1HP-EF1α(L) revealed a disturbed transcription profile with high abundance of MeV-P mRNA in relation to MeV-N or especially MeV-L mRNA (Tab. 3). This imbalance was ameliorated in the 1HP plasmids bearing SFFVp, EFSp, or PGKp to drive P mRNA transcription, as intended. There are four 1 HP plasmids, which only differ in the promoter driving the P gene, i.e. pBR-1HP-3CMV, pBR-1HP-SFFVp(P), pBR-1HP-EFS(P), and pBR-1HP-PGK(P). Their relative mRNA expression of P closely reflects the activity of the respective promoters (P_{CMV}, SFFVp, EFSp, PGKp) measured before in the dual luciferase assay: P_{CMV}, the strongest of the analyzed promoters (123 RLU), driving P in pBR-1HP-3CMV resulted in highest relative expression of P (78.6 % relative mRNA abundance). Accordingly, the weakest of the above-mentioned promoters PGKp (7 RLU) resulted in lowest relative relative mRNA expression of P (19.3 %). Plasmids containing the promoters SFFVp and EFSp revealed intermediate transcription of P mRNA, as expected from their individual strengths (Fig. 2, Fig. 4b, Tab. 3).

Table 3. Relative MeV mRNA expression in cells. This tables indicates relative abundance (%) of MeV RNP protein encoding mRNAs as calculated from absolute numbers shown in Table 2 and are graphically depicted in Fig. 4b.

mRNA	MeV infected		pCA -MVN, -MVP, -MVL	pBR-1HP-					
	6 h p. i.	24 h p. i.		3CMV	SFFVp(P)	EF1a(L)	SFFVp(P)-EF1a(L)	EFS(P)	PGK(P)
N	89.1	37.3	59.4	20.8	58.9	18.6	79.1	64.0	76.9
P	8.4	56.4	27.8	78.6	37.2	80.4	16.5	32.3	19.3
L	2.5	6.3	12.8	0.6	4.0	1.0	4.4	3.6	3.7

Expression of viral proteins after transfection of helper plasmids

After quantification of the respective mRNA species, we next controlled the amounts of translated proteins via Western blot analysis. The membranes of blotted lysates of respectively transfected 293T cells were probed with antibodies recognizing MeV-N, MeV-P, MeV-L, the FLAG tag (added to MeV-L gene in helper plasmids), or the house-keeping protein α-tubulin. The abundance of α-tubulin served as control for similar loading (Fig. 5).

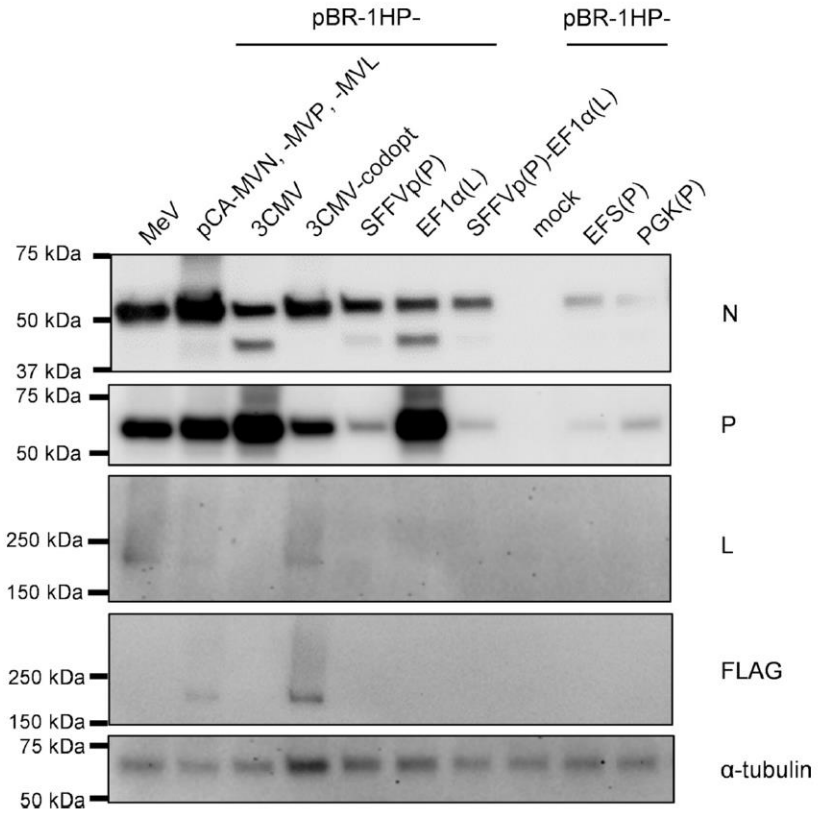

Fig. 5. Protein expression by 1HP plasmids during rescue. 293T cells were infected with MeV or transfected with depicted helper plasmids. 48 h post infection or transfection cells were lysed. Untransfected cells served as mock. Blots were probed using rabbit polyclonal anti-MeV-N antibody (first blot), mouse monoclonal anti-MeV-P (second blot), rabbit polyclonal anti-MeV-L (third blot), mouse monoclonal anti-FLAG (fourth blot) or mouse monoclonal anti-α-Tubulin (fifth blot). Expected size: N, 55 kDa; P, 70 kDa; L or FLAG: approx. 200-250 kDa; α-tubulin, 52 kDa.

MeV-N was detected in comparable amounts in cells transfected by helper plasmids pBR-1HP-3CMV (lane 3), pBR-1HP-SFFVp(P) (lane 5), pBR-1HP-EF1α(L) (lane 6), or pBR-1HP-SFFVp(P)-EF1α(L) (lane 7). Thus, the similar abundance of N mRNA was reflected by N protein expression. However, considerably more MeV-N is found in cells transfected with the single helper plasmid system. For pBR-1HP-EFS(P) and pBR-1HP-PGK(P), only weak signals were detected for MeV-N, although mRNA copy numbers were similar as for the other 1HP constructs. Codon optimization of MeV-N resulted in slightly higher

expression as evident from the direct comparison of pBR-1HP-3CMV-codopt to pBR-1HP-3CMV (Fig. 5, lanes 4 and 3, respectively). In addition to the 58 kDa band of complete MeV-N, a second band at approx. 45 kDa was detected. This band is clearly visible in lysates of cells transfected with pBR-1HP-3CMV (lane 3) or pBR-1HP-EF1α(L) (lane 6), and relatively faint in those cells transfected with pCA-MVN (lane 2), pBR-1HP-SFFVp(P) (lane 5), or pBR-1HP-SFFVp(P) EF1α(L) (lane 7). Cells expressing N from codon-optimized pBR-1HP-3CMV-codopt did not reveal this pattern despite overall high N expression (lane 4).

When the blot was probed with αMeV-P antibodies, we found unexpectedly low expression by pBR-1HP-3CMV-codopt in comparison to the intensity of the MeV-P signal in cells transfected with pBR-1HP-3CMV. As reflected already in the mRNA transcription analyses, transcription of the MeV-P gene via the i.e. P_{CMV} promoter (pBR-1HP-3CMV, pBR-1HP-EF1α(L)) is higher than in cells transfected with pCA-MVP together with pCA-MVN and pCA-MVL. Weakest signals of MeV-P were detected for constructs with attenuated P transcription (pBR-1HP-SFFVp(P), pBR-1HP-SFFVp(P)-EF1α(L), pBR-1HP-EFS(P), pBR-1HP-PGK(P)), as expected also from the mRNA profiles.

A weak signal for MeV-L, approximately 250 kDa in size, was only detectable in cells transfected with the four-plasmid system, pBR-1HP-3CMV-codopt, or in cells two days after infection with MeV. In the other rescue cells, L expression remained below the limit of detection, most likely also due to low abundance of respective mRNA.

Rescue of rMeV using different helper plasmids

Finally, functionalities of the 1HP helper plasmids were analyzed side-by-side with the standard plasmid-based rescue system. Cells were transfected with the respective helper plasmids and a plasmid encoding a Moraten vaccine strain-derived MeV genome with GFP as marker protein in an additional transcription cassette following the P gene cassette, pBRPolII-MVvac2-GFP(P) [29]. This mix should give rise to rescue of recombinant MV_{vac2}-GFP(P) that causes fluorescence of cells, which replicate this virus (Fig. 6a). The different constructs were analyzed in at least 5 independent experiments, and rates of successful rescues were calculated for each helper plasmid construct (Fig. 6b). Using the standard four-plasmid system, MV_{vac2}-GFP(P) was successfully rescued in 93 % of the experiments (n = 30). In contrast, no recombinant MeV was generated when using pBR-1HP-3CMV, pBR-1HP-3CMV-codopt, or pBR-1HP-EF1α(L) for rescue. However, all constructs with diminished expression of MeV-P, i.e. pBR-1HP-SFFVp(P), pBR-1HP-SFFVp(P)-EF1α(L), pBR-1HP-EFS(P), pBR-1HP-PGK(P), revealed the capacity to rescue rMeV. Recombinant MeV was rescued with a two-plasmid system making use of pBR-1HP-SFFVp(P) in 10 of 30 experiments (33 %), of pBR-1HP-SFFVp(P)-EF1α(L) in 4 of 17 experiments (23.5 %), of pBR-1HP-EFS(P) in 1 of 15 experiments (6.7 %), or of pBR-1HP-PGK(P) in 4 of 16 experiments (25 %). Thus, rescue of MeV was

successful with 1HP constructs that had a diminished transcription of of MeV-P, and functional two-plasmid rescue systems for MeV became available.

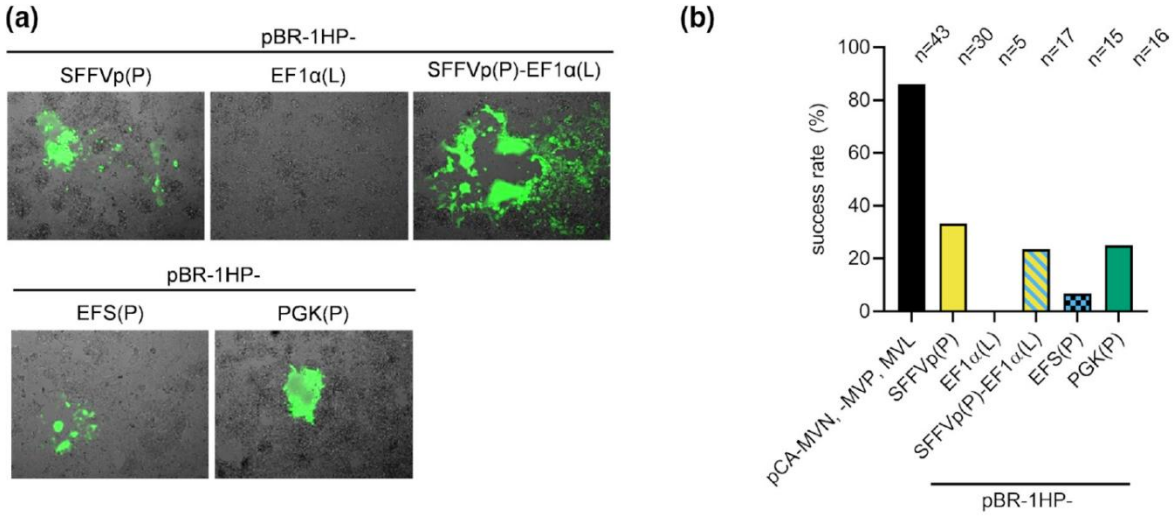

Fig. 6. Efficacy of MeV rescue experiments. 293T cells were transfected with pBRPolII-MVvac2-GFP(P) with either of the depicted helper plasmids. 48 h post transfection, transfected 293T cells were overlaid onto a Vero cell layer. 293T-Vero co-cultures were screened daily beginning on day 4 post overlay. (a) Overlay microscopic photographs displaying green-fluorescent syncytia of rescued MeV in overlay cultures. Pictures were taken 4-6 days post overlay. 100× magnification. (b) The success rate of rescues in independent experiments is indicated for the different rescue systems (in %). Above each bar, the number *n* of respective independent overlay experiments for each rescue system is indicated.

Discussion

To ease the generation of recombinant MeV, we generated a set of helper plasmids accommodating all helper functions on one single plasmid. To be able to simulate helper gene expression by the current four-plasmid system, promoter activities were analyzed in target 293T rescue cells. Based on these data, adapted helper plasmids were generated. Thereby the expression of the helper genes was modulated as intended and documented by qRT-PCR of respective mRNA species and by immunoblot analysis of protein expression in transfected cells. Down-modulation of P protein expression proved useful, and finally resulted in the generation of constructs that allowed rescue of recombinant MeV in cells using just one helper plasmid in addition to the plasmid encoding the recombinant MeV genome.

However, two factors potentially impairing gene expression needed to be considered already from the start when these helper plasmid constructs were designed: First, homologous recombination within the single plasmid DNA molecules would become feasible due to the presence of the identical genetic

sequences that were present two or even three times in the individual plasmids, e.g. the CMV i.e. promoter. Second, interference of in some cases even identical promoter sequences in the face of limited amounts of transcription factors could have impaired gene expression of the helper plasmids. Considering these potential pitfalls, the copy numbers of individual mRNAs as revealed by qRT-PCR results do not suggest such effects. Neither incidental decrease in expression of any helper protein was observed, which would result from deletion of one or more plasmid segments in between homologous sequences by recombination events, nor a systematic decrease in expression of genes, which are driven by the same promoter due to competition for binding transcription factors.

Remarkably, one helper gene consistently revealed low numbers of mRNA copies, independent of the promoter chosen to drive the respective gene: The L gene encoding the MeV polymerase. Recombination or interference between identical promoter sequences cannot explain this fact, since also 293T cells transfected with pBR-1HP-SFFVp(P)-EF1α(L) showed this phenomenon. In this construct, each helper gene is driven by a specific promoter (Fig. 3). Yet, this 1HP gives rise to fewest mRNA copies compared to all the other constructs, in which one promoter occurs more than once (Fig. 4, Tab. 2).

Strikingly, the mean copy numbers of L mRNA after transfection of 4 µg of any 1HP was 10-fold lower than after transfection of only 0.4 µg pCA-MVL (Tab. 2). This observation could be due to the relict of a Hepatitis delta virus ribozyme at the 3' terminus of the L gene upstream of the polyadenylation signal. This was a result of the selected cloning strategy on the basis of pBRPolII-MVvac2. This ribozyme cleaves its RNA sequence with about 90 % efficacy [30,31]. On the L mRNA, this cleavage would leave the poly(A) tail intact in only 10 % of the mRNA copies. As oligo(dT) primers were used for reverse transcription of mRNAs in the qRT-PCR used for quantification of mRNA species, only 10 % of transcribed L mRNA copies were detectable, which is paralleled by the observed 9.3-fold decrease of L mRNA copy numbers. Moreover, poly-A tails stabilize mRNAs and are important for translational efficacy [32]. Thus, loss of the poly-A tail of the L mRNA would significantly impair L protein expression, as such. This could also at least partially explain the difficulties to detect L protein in transfected rescue cells. Interestingly, L has already been a special case in the very first MeV rescue system. While N and P are stably expressed in 293-3-46 cells, L expression has to be introduced afresh during each rescue due to the impossibility to generate stably L-expressing cell clones [13].

Concerning the polymerase co-factor P, we found that reducing the transcription of P mRNA proved useful to generate helper plasmids that allowed rescue of MeV. In the previously described rescue systems for MeV, which is using the clonal cell line 293-3-46, both helper proteins P and N are stably expressed in addition to the T7 RNA Polymerase [13]. Here, the single cell clone with highest expression

of T7 and expression of N and P protein as high as in infected cells had been chosen. While a particularly low expression of P seems not to have been of advantage for MeV rescue with this system, this has never been tested, but adjusted to that of infected cells – an effect mirrored by our efforts to some extent.

In other previously described rescue systems for MeV - be it a transient rescue system utilizing MVA-T7 [16] or the four-plasmid system using CMV-driven helper plasmids each encoding one helper protein – the plasmids encoding P are transfected in less amounts than those encoding N to reach optimal rescue efficacy. For the MVA-T7 system, best rescue efficacies (syncytia in 60 % of transfected wells) were reached with a quantity of P plasmid, which is 50 % of the N plasmid. In the PolII-driven rescue system, the helper plasmids pCA-MVN and pCA-MVP are transfected in a ratio of 5:1, respectively, favoring the N plasmid as well. Although expression analyses of mRNA or protein were not provided by none of the two studies, these are the input ratios of MeV-N and MeV-P helper plasmids, which have proven to be most successful for rescue of MeV.

This is a clear difference from the rescue of NDV, where an equimolar ratio for NDV single helper plasmids pN and pP has been described to be most effective [19]. Therefore, it is not surprising, that the NDV-1HP worked with a P_{CMV} driving each of the three helper genes, while the corresponding approach failed for MeV in our hands. Thus, the modulated approach by the promoter exchanges that we found necessary for the rescue of MeV should reflect basic differences in viral biology among different paramyxoviruses to assemble replicative centers. Thereby, our study presents a perspective beyond just the rescue of recombinant MeV. While some negative-stranded RNA viruses as NDV [19] or VSV [33] can be rescued with considerable efficacies that even allow the generation of diversified virus libraries [34], others such as MeV are much harder to rescue. Also, some segmented negative-sense RNA viruses such as CCHFV can be a challenge to rescue [35]. Therefore, the approach used in this study to use different promoters with tailored activity in a tunable, but otherwise fixed configuration could be beneficial also for these viruses.

In summary, we present here the least complex and first two-plasmid rescue system for MeV. For its generation, it was necessary to adjust the quantity of P expressed in the cells transfected. The sensitivity of the transcription and replication process of MeV and the critical role of P in those became obvious. The present study shows, that the obstacles in this delicate system can be overcome and a rescue system for MeV with a minimum of essential components can be generated, thereby paving the road for future developments.

Conflicts of Interest

The authors declare that there are no conflict of interests

Funding Information

This work was supported by a grant of the German Center for Infection Research (DZIF; TTU 01.805) to MDM.

Author contributions

Conceptualization: MDM

Acquisition of Funding: MDM

Investigation: AA

Visualization: AA, MDM

Supervision: MDM

Writing - original draft: AA, MDM

Writing - review & editing: all authors

Acknowledgements

We thank D. Müller and C. Kruip for excellent technical assistance, V. von Messling and U. Modlich for helpful discussions, and B. Sawatsky for critically reading the manuscript. The authors are indebted to U. Modlich for providing pSRS11 EFS GFPpre and VMD00.PG pRRL.PPT.PGK.mHAMpl(wt).pre, to J. Kirberg for providing pBOS_hBKLF.2, to B. Fehse for providing LeGO-Cer2 via Addgene, and to U. Schneider for providing the three-plasmid PolII rescue system for measles viruses.

References

[1] Robinson S, Galanis E. Potential and clinical translation of oncolytic measles viruses, Expert Opin Biol Ther 2017;17:353–363.

[2] Mühlebach MD. Vaccine platform recombinant measles virus, Virus Genes 2017;53:733–740.

[3] Mühlebach MD. Measles virus in cancer therapy, Curr Opin Virol 2020;41:85–97.

[4] Reisinger EC, Tschismarov R, Beubler E, Wiedermann U, Firbas C et al. Immunogenicity, safety, and tolerability of the measles-vectored chikungunya virus vaccine MV-CHIK: a double-blind, randomised, placebo-controlled and active-controlled phase 2 trial, The Lancet 2018;392:2718–2727.

[5] Hörner C, Schürmann C, Auste A, Ebenig A, Muraleedharan S et al. A highly immunogenic and effective measles virus-based Th1-biased COVID-19 vaccine, Proc Natl Acad Sci U S A 2020.

[6] Frantz PN, Barinov A, Ruffié C, Combredet C, Najburg V et al. A live measles-vectored COVID-19 vaccine induces strong immunity and protection from SARS-CoV-2 challenge in mice and hamsters, Nat Commun 2021;12:6277.

[7] Launay O, Artaud C, Lachâtre M, Ait-Ahmed M, Klein J et al. Safety and immunogenicity of a measles-vectored SARS-CoV-2 vaccine candidate, V591 / TMV-083, in healthy adults: results of a randomized, placebo-controlled Phase I study, EBioMedicine 2022;75:103810.

[8] Lu M, Dravid P, Zhang Y, Trivedi S, Li A et al. A safe and highly efficacious measles virus-based vaccine expressing SARS-CoV-2 stabilized prefusion spike, Proc Natl Acad Sci U S A 2021;118.

[9] Vanhoutte F, Liu W, Wiedmann RT, Haspeslagh L, Cao X et al. Safety and immunogenicity of the measles vector-based SARS-CoV-2 vaccine candidate, V591, in adults: results from a phase 1/2 randomised, double-blind, placebo-controlled, dose-ranging trial, EBioMedicine 2022;75:103811.

[10] Seifried AS, Albrecht P, Milstien JB. Characterization of an RNA-dependent RNA polymerase activity associated with measles virus, J Virol 1978;25:781–787.

[11] Calain P, Roux L. The rule of six, a basic feature for efficient replication of Sendai virus defective interfering RNA, J Virol 1993;67:4822–4830.

[12] Schnell MJ, Mebatsion T, Conzelmann KK. Infectious rabies viruses from cloned cDNA, EMBO J 1994;13:4195–4203.

[13] Radecke F, Spielhofer P, Schneider H, Kaelin K, Huber M et al. Rescue of measles viruses from cloned DNA, EMBO J 1995;14:5773–5784.

[14] Parks CL, Lerch RA, Walpita P, Sidhu MS, Udem SA. Enhanced measles virus cDNA rescue and gene expression after heat shock, J Virol 1999;73:3560–3566.

[15] Chey S, Palmer JM, Doerr L, Liebert UG. Dual Promoters Improve the Rescue of Recombinant Measles Virus in Human Cells, Viruses 2021;13.

[16] Schneider H, Spielhofer P, Kaelin K, Dötsch C, Radecke F et al. Rescue of measles virus using a replication-deficient vaccinia-T7 vector, J Virol Methods 1997;64:57–64.

[17] Martin A, Staeheli P, Schneider U. RNA polymerase II-controlled expression of antigenomic RNA enhances the rescue efficacies of two different members of the Mononegavirales independently of the site of viral genome replication, J Virol 2006;80:5708–5715.

[18] Cattaneo R, Rebmann G, Schmid A, Baczko K, ter Meulen V et al. Altered transcription of a defective measles virus genome derived from a diseased human brain, EMBO J 1987;6:681–688.

[19] Liu H, Albina E, Gil P, Minet C, Almeida RS de. Two-plasmid system to increase the rescue efficiency of paramyxoviruses by reverse genetics: The example of rescuing Newcastle Disease Virus, Virology 2017;509:42–51.

[20] Bodmer BS, Fiedler AH, Hanauer JRH, Prüfer S, Mühlebach MD. Live-attenuated bivalent measles virus-derived vaccines targeting Middle East respiratory syndrome coronavirus induce robust and multifunctional T cell responses against both viruses in an appropriate mouse model, Virology 2018;521:99–107.

[21] Kärber G. Beitrag zur kollektiven Behandlung pharmakologischer Reihenversuche, Archiv f. experiment. Pathol. u. Pharmakol 1931;162:480–483.

[22] Mizushima S, Nagata S. pEF-BOS, a powerful mammalian expression vector, Nucleic Acids Res 1990;18:5322.

[23] Plumet S, Duprex WP, Gerlier D. Dynamics of Viral RNA Synthesis during Measles Virus Infection, J Virol 2005;79:6900–6908.

[24] Funke S, Maisner A, Mühlebach MD, Koehl U, Grez M et al. Targeted cell entry of lentiviral vectors, Molecular therapy : the journal of the American Society of Gene Therapy 2008;16:1427–1436.

[25] Hitoshi N, Ken-ichi Y, Jun-ichi M. Efficient selection for high-expression transfectants with a novel eukaryotic vector, Gene 1991;108:193–199.

[26] Qin JY, Zhang L, Clift KL, Hulur I, Xiang AP et al. Systematic comparison of constitutive promoters and the doxycycline-inducible promoter, PloS one 2010;5:e10611.

[27] Montiel-Equihua CA, Zhang L, Knight S, Saadeh H, Scholz S et al. The β-globin locus control region in combination with the EF1α short promoter allows enhanced lentiviral vector-mediated erythroid gene expression with conserved multilineage activity, Molecular therapy : the journal of the American Society of Gene Therapy 2012;20:1400–1409.

[28] Mao Y, Yan R, Li A, Zhang Y, Li J et al. Lentiviral Vectors Mediate Long-Term and High Efficiency Transgene Expression in HEK 293T cells, International journal of medical sciences 2015;12:407–415.

[29] Malczyk AH, Kupke A, Prüfer S, Scheuplein VA, Hutzler S et al. A Highly Immunogenic and Protective Middle East Respiratory Syndrome Coronavirus Vaccine Based on a Recombinant Measles Virus Vaccine Platform, J Virol 2015;89:11654–11667.

[30] Chadalavada DM, Cerrone-Szakal AL, Bevilacqua PC. Wild-type is the optimal sequence of the HDV ribozyme under cotranscriptional conditions, RNA 2007;13:2189–2201.

[31] Beaty SM, Park A, Won ST, Hong P, Lyons M et al. Efficient and Robust Paramyxoviridae Reverse Genetics Systems, mSphere 2017;2.

[32] Gallie DR. The cap and poly(A) tail function synergistically to regulate mRNA translational efficiency, Genes Dev 1991;5:2108–2116.

[33] Whitt MA. Generation of VSV pseudotypes using recombinant ΔG-VSV for studies on virus entry, identification of entry inhibitors, and immune responses to vaccines, J Virol Methods 2010;169:365–374.

[34] Kottke T, Errington F, Pulido J, Galivo F, Thompson J et al. Broad antigenic coverage induced by vaccination with virus-based cDNA libraries cures established tumors, Nat Med 2011;17:854–859.

[35] Bergeron É, Zivcec M, Chakrabarti AK, Nichol ST, Albariño CG et al. Recovery of Recombinant Crimean Congo Hemorrhagic Fever Virus Reveals a Function for Non-structural Glycoproteins Cleavage by Furin, PLoS Pathog 2015;11:e1004879.

5. Diskussion

5.1 EGCG als mögliches anti-coronavirales Therapeutikum

Für den sekundären Pflanzenstoffs EGCG konnte bereits eine antivirale Wirkung auf eine Reihe von DNA- und RNA-Viren gezeigt werden, sodass die Untersuchung solch einer Hemmwirkung auf das neu-aufgekommene SARS-CoV-2 vielversprechend erschien (Wang et al. 2021). Tatsächlich konnte in der im Rahmen dieser Doktorarbeit durchgeführten Studie eine Hemmung von SARS-CoV-2 *in vitro* durch EGCG gezeigt werden, ebenso wie eine Hemmung von zwei weiteren Betacoronaviren, SARS-CoV und MERS-CoV (Henss et al. 2021). Diese Hemmung wirkte sowohl auf die mit dem jeweiligen Spikeprotein pseudotypisierten, lentiviralen (LV) Vektoren (Fig. 1), als auch auf die nativen Coronaviren (Fig. 2). Die mittleren inhibitorischen Konzentrationen (IC_{50}) von EGCG auf die entsprechend pseudotypisierten LV liegen bei 2,47 µg/ml (SARS-CoV-2-Pseudotyp), 4,28 µg/ml (SARS-CoV-Pseudotyp) oder 11,21 µg/ml (MERS-CoV-Pseudotyp) (Fig. 1). Diese Daten wurden in einer anderen Studie mit Hilfe von pseudotypisierten VSV-Vektoren bestätigt, für die IC_{50}-Werte gleicher Größenordnung ermittelt wurden: für VSV mit dem Spikeprotein des SARS-CoV-2 unter 5 µM (<2,29 µg/ml) und für den jeweiligen VSV-Vektor mit SARS-CoV- oder MERS-CoV-Spikeprotein zwischen 5 µM (2,29 µg/ml) und 25 µM (11,46 µg/ml), während für das als Kontrolle mitgeführte Adenovirus vom Serotyp 5 keine Hemmung festgestellt wurde (Joseph et al. 2021). Es kann daher auf einen Zelleintritt-Effekt von EGCG geschlossen werden (Joseph et al. 2021). Auch ein Surrogat-Neutralisationsversuch, mit dem die Bindung zwischen der Rezeptorbindedomäne (RBD) und dem viralen Rezeptor Angiotensin-konvertierendes Enzym 2 (angiotensin-converting enzyme 2, ACE2) untersucht wird, stellte eine Hemmung durch EGCG auf eben diese Bindung, also auf den ersten Schritt des Zelleintritts dar: Mit der höchsten Konzentration (40 µg/ml) EGCG werden ca. 40 % der Bindung der RBD von SARS-CoV-2 an ACE2 geblockt (Fig. 3). Eine *in silico*-Studie, welche für die Interaktion von EGCG mit der RBD eine hohe Bindungsenergie von −9.7 kcal/mol über fünf Wasserstoffbrückenbindungen modellierte, weist damit auf die RBD als Zielstruktur von EGCG hin (Mhatre et al. 2021). Kurz nach Publikation von Henss *et al.* konnte diese Hemmung der Bindung von RBD am Rezeptor ACE2 auch in mehreren Studien *in vitro* bestätigt werden (Joseph et al. 2021; Ohgitani et al. 2021; Zhang et al. 2021a; Liu et al. 2021a). Neben dieser Bindung an den Zelleintrittsrezeptor ACE2 interagiert das Spikeprotein von SARS-CoV-2 auch mit Heparansulfat (HS), was ebenfalls an der Oberfläche von Zielzellen des SARS-CoV-2 exprimiert wird (Liu et al. 2021b). Die Bindung von Spike an HS begünstigt wiederum die offene Konformation des Spikeproteins, die für die RBD-ACE2-Bindung notwendig ist (Clausen et al. 2020; Kearns et al. 2022). Da HS zusammen mit ACE2 und dem Spikeprotein einen ternären Komplex eingeht und dadurch die RBD-ACE2-Bindung nicht

nur initiiert, sondern auch stabilisiert, ist HS ein Korezeptor für SARS-CoV-2 (Clausen et al. 2020; Kearns et al. 2022). Außer für SARS-CoV-2 wird Heparansulfat auch als Korezeptor für die Coronaviren SARS-CoV (Lang et al. 2011), HCoV-NL63 (Milewska et al. 2014) und das murine Coronavirus (Maus-Hepatitisvirus, MHV) beschrieben (Watanabe et al. 2007). Da EGCG mit HS um die Bindung von viralen Oberflächenproteinen konkurriert (Colpitts und Schang 2014; LeBlanc und Colpitts 2022), könnte diese Kompetition den breiten anti-coronaviralen Effekt von EGCG erklären. Für SARS-CoV-2 ist allerdings beschrieben, dass innerhalb von fünf Zellkultur-Passagen Varianten mit Mutationen im Spike selektiert werden, deren Affinität zu Heparin erhöht ist (Shiliaev et al. 2021). Studienergebnisse, die mit Hilfe von Zellkultur-adaptierten Viren gewonnen werden, könnten daher die Bedeutung von Heparin als Rezeptor überschätzen. Um eine breite, anti-coronavirale Wirkung von EGCG über das Konkurrieren mit Heparansulfat um die Bindung von viralen Oberflächenproteinen weiter zu untersuchen, sollten daher Zellkultur-Artefakte ausgeschlossen werden, indem niedrigpassagierte Coronaviren verwendet werden.

Neben diesen Zelleintritt-Effekten von EGCG wurden in der im Rahmen dieser Doktorarbeit durchgeführten Studie auch Hinweise auf Effekte identifiziert, die nach Zelleintritt (*post-entry*) wirken: Im Plaque-Reduktionstests hatte EGCG auf die replizierenden Coronaviren etwas niedrigere IC_{50}-Werte als auf die jeweiligen pseudotypisierten LV-Vektoren: 1,73 µg/ml vs. 2,47 µg/ml (SARS-CoV-2-Pseudotyp), 0,83 µg/ml vs. 4,28 µg/ml (SARS-CoV-Pseudotyp) oder 4,64 µg/ml vs. 11,21 µg/ml (MERS-CoV-Pseudotyp) (Fig. 1, 2). Solche *post-entry*-Effekte können auf eine Hemmung der viralen Replikation oder der viralen Mechanismen gegen die angeborene Immunantwort zurückzuführen sein. Tatsächlich konnte nach Veröffentlichung unserer Studie gezeigt werden, dass EGCG an die virale Papain-ähnliche Protease (PLpro) bindet (Chourasia et al. 2021; Pitsillou et al. 2021) und deren Proteaseaktivität je nach Studie mit einer IC_{50} von < 45,9 µg/ml bzw. 20,5 µg/ml hemmt (Pitsillou et al. 2021; Kawall et al. 2022). Diese ist einerseits essenziel in der Replikation von SARS-CoV-2, da es dessen Polyproteine pp1a und pp1ab zu den funktionellen Nichtstrukturproteinen (NSP) 1-3 spaltet, sodass die Hemmung der PLpro durch die chemische Leitstruktur „rac5c“ mit einer IC_{50} von 0,81 µM auch die Replikation von SARS-CoV-2 *in vitro* statistisch signifikant hemmt (Klemm et al. 2020). Andererseits wirkt die PLpro auch modulatorisch auf die antiviralen Mechanismen der Zelle. Die Konjugation des Interferon-stimulierten Gens (ISG) 15 an den interferonregulatory factor 3 (IRF3) in aktivierten Zellen verhindert die Ubiquitinierung von IRF3 und damit dessen beschleunigte Degradierung (Shi et al. 2010). Die damit erreichte verstärkte Anreicherung von IRF3 führt zu einer vermehrten Aktivierung der Transkription von Interferonen und weiteren antiviralen Zytokinen. Die PLpro von SARS-CoV-2 wiederum spaltet ISG15 von IRF3 ab und verkürzt damit die Halbwertszeit von IRF3, was sich schwächend auf die Typ-I-Interferon (IFN)-Antwort auswirkt (Shin et al. 2020; Swaim et al. 2020). Die Ausschüttung von Typ-I-IFN in IFN-I-kompetenten Zellen

fördert die Transkription hunderter verschiedener ISG, die beispielsweise die Transkription oder Translation von Viren wie dem SARS-CoV-2 unterdrücken oder dessen RNA direkt degradieren können (Kim und Shin 2021). Eine Hemmung der PLpro durch EGCG könnte daher auf die IFN-I-Antwort in infizierten Zellen unterstützend wirken, sodass die Replikation des Virus autokrin und parakrin gehemmt würde (Kim und Shin 2021). Ein solcher Effekt wäre jedoch nicht in den in unserer Studie verwendeten Vero-Zellen nachweisbar, da diese kein Typ-I-IFN mehr produzieren können (Desmyter et al. 1968; Mosca und Pitha 1986). Neben der PLpro hemmt EGCG auch die 3C-ähnliche Protease (3CLpro) verschiedener Coronaviren einschließlich SARS-CoV-2, welche die für diese Viren essenzielle Spaltung der Polyproteine pp1a und pp1ab in die Nsp 5-16 durchführt. In Protease-Aktivitätstests zeigte sich eine breite Hemmwirkung von EGCG gegen 3CLpro unterschiedlicher Alpha- und Betacoronaviren, zusammengestellt in Tab. 1:

Tab. 1: Hemmung der 3CLpro Protease ausgewählter Coronaviren *in vitro* durch EGCG. Die angegebenen IC_{50}-Werte wurden über FRET-Analysen durch Verdau von mit Fluorophor-Quencher-Paar-koppelnden Substrat-Peptiden der in der ersten Spalte angegeben Viren ermittelt.

Virus	IC_{50}	Quelle
SARS-CoV-2	7,58 µg/ml	(Jang et al. 2020)
	1,94 µg/ml	(Chiou et al. 2021)
	0,40 µg/ml	(Du et al. 2021)
	5,31 µg/ml	(Zhong et al. 2022)
SARS-CoV	11,46 µg/ml	(Chiou et al. 2021)
HCoV-OC43	14,6 µg/ml	(Jang et al. 2021)
HCoV-229E	11,7 µg/ml	(Jang et al. 2021)

Wird die Aktivität von 3CLpro gehemmt, kann beispielsweise auch weniger des Nichtstrukturproteins 12 in seine aktive Form, die für Coronaviren obligatorische RNA-abhängige RNA-Polymerase (*RNA-dependent RNA-polymerase,* RdRp), gespalten werden, sodass EGCG neben Effekten über PLpro auch über 3CLpro in die virale Replikation eingreifen könnte.

Neben diesen Effekten auf die coronaviralen Proteasen hemmt EGCG auch die virale Endoribonuklease nsp15 mit einer IC_{50} von 0,74 µg/ml (Hong et al. 2021). Nsp15 sichert einerseits über die Hemmung von Stress-Granula die ungehinderte Virusreplikation (Gao et al. 2021). Andererseits spaltet es Polyuridin-RNA, die als Pathogen-assoziierte molekulare Muster (*pathogen-associated molecular patterns*, PAMP) wirkt, und verhindert damit die Induktion einer IFN-Antwort (Hackbart et al. 2020).

Es zeigt sich somit, dass an der antiviralen Wirkung von EGCG gegen die oben genannten verschiedenen Coronaviren wahrscheinlich sowohl hemmende Effekte auf den Zelleintritt, als auch solche auf die Replikation des Virus beteiligt sein sind (Zhang et al. 2021b; Dinda et al. 2023). Die biologische Wirkung von EGCG beruht auf dessen chemische Eigenschaften: EGCG besitzt acht Phenolgruppen und damit Protonendonoren, die Wasserstoffbrücken zu Protonenakzeptoren anderer Moleküle, hier zur RdRp von SARS-CoV-2 (Singh et al. 2021) oder zu ACE2 (Ohishi et al. 2022), ausbilden können. Sind die intermolekularen Kräfte wie Wasserstoffbrückenbindungen zwischen dem Molekül und EGCG hoch genug, kann EGCG an das Molekül binden und damit andere Bindungen des Moleküls kompetitiv hemmen.

Neben den direkten, hemmenden Effekten auf die Virusinfektion könnten die anti-inflammatorischen Eigenschaften von EGCG möglicherweise auch indirekt durch die Linderung von pathologischen Prozessen wie der Sepsis als schwere COVID-19-Komplikation wirken. Während einer Sepsis werden bestimmte Moleküle durch Zelltod oder Aktivierung des Inflammasoms freigesetzt, so genannte *damage-associated molecular patterns* (DAMPs) (Denning et al. 2019). Eines dieser DAMPs ist das *high mobility group box 1* (HMGB1)-Protein, welches gleichzeitig als später Mediator in der Pathogenese einer tödlichen Sepsis gilt, sodass dessen Hemmung über anti-HMGB1-Antikörper die Überlebenschance von Mäusen mit Endotoxämie oder Sepsis erhöhte (Wang et al. 1999; Yang et al. 2004). Indem es die HMGB1-Ausschüttung aus Monozyten und Makrophagen hemmt, kann EGCG ebenfalls vor einer Endotoxämie schützen (Li et al. 2007). HMGB1 wurde während der COVID-19-Pandemie zu einer möglichen Zielstruktur für Wirkstoffe, weil es nicht nur die Expression des SARS-CoV-2-Zelleintritt-Rezeptors ACE2 induziert, sondern auch im Serum von schwer an COVID-19 Erkrankten erhöht ist (Zhu et al. 2010; Chen et al. 2020). Studien zu einer EGCG-vermittelten Reduktion der HMGB1-Freisetzung und eine dadurch vermittelte Schutzwirkung vor einer COVID-19-assoziierten Sepsis stehen allerdings noch aus.

Ebenso bleibt noch offen, ob die oben beschriebenen direkten anti-coronaviralen Effekte von EGCG auch *in vivo* nachweisbar. Gegen HCoV-OC43 wurde für EGCG parallel zum *in vitro* Befund einer IC_{50} zwischen 1 und 5 µg/ml auch in mit EGCG zugefütterten Mäusen 14 Tage nach Infektion eine signifikante Reduktion der viralen RNA in der Lunge gefunden (Park et al. 2021). Da in Henss *et al.* IC_{50}-Werte von EGCG gegen SARS-CoV, SARS-CoV-2 oder MERS-CoV zwischen 0,8 und 5 µg/ml *in vitro* ermittelt wurden, sollte jedoch in Mäusen ein hemmender Effekt von EGCG auch gegen diese Viren nachweisbar sein.

Eine Hürde auf dem Weg zu einem EGCG-basierten (anti-coronaviralen) Medikament ist die geringe orale Bioverfügbarkeit von EGCG als reinem Wirkstoff: Nur 0,3 % oral aufgenommenen EGCGs lässt sich nach

1 h im menschlichen Plasma nachweisen (Nakagawa und Miyazawa 1997). Um einen Plasma-Wirkspiegel in Höhe der in Henss *et al.* ermittelten IC_{50} gegen SARS-CoV-2 von 1,73 µg/ml (Fig. 2) zu erreichen, müsste eine 75 kg schwere Person mit ca. 5,6 l Blut 9,7 mg EGCG im Blutplasma haben. Um diesen Wirkspiegel 1 h nach Aufnahme zu erreichen, müssen 3,2 g EGCG aufgenommen werden, was 13 Tassen Grüntee entspricht (Khan et al. 2006). Diese Menge ist noch größer, wenn mit einer IC_{90} eine potentere Hemmwirkung erreicht werden soll. Die IC_{90} wurde in Henss *et al.* allerdings nicht bestimmt.

Ein Grund für die niedrige Bioverfügbarkeit von EGCG ist dessen Instabilität in leicht alkalischem Milieu, wie z.B. bei einem pH-Wert von 8 im Duodenum und Jejunum, wo ein Großteil aller Wirkstoffe aufgenommen wird. In alkalischem Milieu wird das Proton einer Hydroxylgruppe an einem Phenol-Ring des EGCG angegriffen, sodass ein hoch reaktives Phenolat-Anion entsteht (Lam et al. 2004). Die Hydroxylgruppen können geschützt werden, indem sie mit Peracetat-Resten verestert werden. Solcherart modifizierte EGCG-Derivate haben eine 6-fach höhere Stabilität unter leicht alkalischen Bedingungen *in vitro* als das native EGCG (Lam et al. 2004). Während ein ebenfalls mit Peracetat-Resten geschütztes EGCG sowohl eine höhere Bioverfügbarkeit als auch eine höhere Wirksamkeit gegen Endometriose-Läsionen in Mäusen hat (Hung et al. 2021), müsste ein solch modifiziertes EGCG allerdings nochmals hinsichtlich der Konservierung seiner anti-coronaviralen Eigenschaften überprüft werden.

Zur Erhöhung der Bioverfügbarkeit von EGCG wurden auch Nanopartikel als Wirkstoffträger erprobt: Durch das Verkapseln in 440 nm große Chitosan-Tripolyphosphat-Nanopartikel konnte die Menge an im Jejunum verfügbaren EGCG um das 2,3-fache (von 5,3 nMh auf 12,3 nMh) und die Menge an im Blutplasma verfügbaren EGCG um das 1,5-fache (von 116,4 nMh auf 179,3 nMh) gesteigert werden (Dube et al. 2011). Auch die Stabilität (24 h nach Applikation) von EGCG in Blutplasma und Gehirn konnte mithilfe von 125 nm großen PEGylierten Poly(laktid-co-glykolid) (*poly(lactic-co-glycolic acid*), PLGA)-Nanopartikel um mindestens das 6-fache (von 60 ng/mg auf 361 ng/mg im Plasma bzw. 0,11 ng/mg auf 0,66 ng/mg im Gehirn) gesteigert werden (Cano et al. 2019).

Zusammenfassend kann *in vitro* neben einem Effekt von EGCG auf die Hemmung des Zelleintritts von SARS-CoV-2 auch additive *post-entry*-Effekte festgestellt werden. Dabei wirken die gleichen Mechanismen der Virushemmung unterschiedlich stark auch auf andere Coronaviren (Tab. 1). Der großen Zahl an Studien, die eine allgemein antivirale Wirkung von EGCG *in vitro* belegen (Wang et al. 2021), stehen bisher nur drei Studien gegenüber, welche eine antivirale Wirkung von EGCG *in vivo* nachgewiesen haben: Eine Hemmung konnte gegen das Hepatitis-B-Virus (Lai et al. 2018), das Suide Herpesvirus 1 (Huan et al. 2020) sowie HCoV-OC43 (Park et al. 2021) gezeigt werden. Weitere Studien

zur Optimierung der Bioverfügbarkeit von EGCG und zur Untersuchung seiner antiviralen Wirkung *in vivo* wären daher als sehr sinnvoll anzusehen, da *in vitro* wie dargelegt bereits vielfach dessen Wirkung und Potenzial als Leitstruktur für pan-coronavirale Medikamente nachgewiesen werden konnte.

5.2 Vergleich von COVID-19-Impfstoffkandidaten auf Basis rekombinanter Masernimpfviren

Diese Arbeit trug signifikant zur Publikation des ersten auf rMeV basierenden Impfstoffkandidaten gegen SARS-CoV-2, MeV_{vac2}-SARS2-S(H), bei (Hörner et al. 2020). Als Antigen dient in diesem Kandidaten das nicht modifizierte, vollständige (native) Spikeprotein mit der ersten veröffentlichten Sequenz des SARS-CoV-2. Das gleiche Antigen in dessen nativer Form wird auch in den zugelassenen Impfstoffen der Universität Oxford / AstraZeneca (Vaxzevria), des Gamaleya Forschungsinstituts (Sputnik V) und von CanSino / der Technischen Universität Peking (Convidecia) verwendet (van Doremalen et al. 2020; Logunov et al. 2020; Zhu et al. 2020a). Das native Spikeprotein enthält zahlreiche B- und T-Zell-Epitope (Lu et al. 2021b; Lee et al. 2021). 90 % der Epitope für neutralisierende Antikörper (*neutralizing antibodies*, nAb) befinden sich auf dessen Rezeptorbindedomäne (RBD), sodass die RBD ein vielversprechendes Antigen für COVID-19-Impfstoffe darstellt (Premkumar et al. 2020; Piccoli et al. 2020). Eine Beschränkung auf die RBD als alleiniges Antigen hat dabei zum Ziel, den Fokus auf Epitope zu legen, die neutralisierende Antikörper auslösen können. Entsprechende Proteinimpfstoffe auf Basis der RBD zeigten deren Immunogenität in präklinischen und klinischen Studien (Yang et al. 2020; Thuluva et al. 2022; Jaggaiahgari et al. 2022). Obwohl die Mehrheit der nAb die RBD zum Ziel haben, verzichten solche Impfstoffe allerdings auf Effekte durch Antikörper, die andere Domänen des Spike zum Ziel haben: Beispielsweise binden die Antikörper COV2-2676 und COV2-2489 an der N-terminalen Domäne (NTD) des Spike und besitzen ebenfalls neutralisierende Eigenschaften (Suryadevara et al. 2021). Das vollständige Spikeprotein als Antigen eines COVID-19-Impfstoffes kann daher durch das Präsentieren weiterer B- und T-Zell-Epitope gegebenenfalls additive Effekte auslösen. So wurde in Makaken bereits die protektive Funktion von $CD8^+$-T-Zellen nachgewiesen, vor allem in Tieren mit niedrigen Antikörpertitern gegen SARS-CoV-2 (McMahan et al. 2021). Da zudem die S2-Untereinheit des Spikeproteins unter den Betacoronaviren höher konserviert ist als die RBD (Chan et al. 2020; Ladner et al. 2021), ist ein breiter wirksamer Impfschutz eher durch das vollständige Spike-Antigen zu erwarten als durch das RBD-Antigen allein.

Für die vorliegenden Studie wurde das vollständige Spike-Gen an zwei verschiedenen zusätzlichen Transkriptionseinheiten (*Additional Transcription Unit*, ATU) im Genom von rMeV eingefügt: nach dem

Gen kodierend für das Phosphoprotein (P) von MeV (ATU(P)), resultierend in dem Impfvirus MeV_{vac2}-SARS2-S(P), oder in die ATU nach dem Gen kodierend für das Hämagglutinin (H) von MeV (ATU(H)), resultierend in dem Impfvirus MeV_{vac2}-SARS2-S(H) (Fig. 1A) (Hörner et al. 2020). MeV_{vac2}-SARS2-S(P) erreichte im Vergleich zum parentalen MeV lediglich ca. 100-fach niedrigere maximale Titer in infizierten Vero-Zellen während einer *multi-step* Wachstumskinetik (Fig. 1C, 1D). Ursächlich dafür ist sehr wahrscheinlich der frühe Zelltod der Virus-produzierenden Zellen aufgrund einer vermehrten Bildung von Synzytien, das heißt durch Membranfusion von Einzelzellen miteinander verschmolzenen vielkernigen Riesenzellen. Masernvirus-infizierte Vero-Zellen entwickeln an sich bereits Synzytien (Makino et al. 1977). Dieser Prozess wird durch die zusätzliche Expression von SARS-CoV-2-Spike mit dessen Fähigkeit, Zellfusion in Vero-Zellen auszulösen (Fig. S3 (Hörner et al. 2020)), noch gesteigert (Hyperfusogenität) (Fig. S2). Da das Spike-Gen in MeV_{vac2}-SARS2-S(P) in die ATU(P) kloniert wurde, wird es entsprechend dem Transkriptionsgradienten von MeV höher exprimiert als das in die ATU(H) klonierte Spike-Gen (Fig. 1B). Für MeV_{vac2}-SARS2-S(H) hingegen konnte ein dem parentalen MeV ähnliches Replikationsverhalten bei stabiler Expression des Spike-Antigens festgestellt werden (Fig. 1C, 1D). Die reduzierte Replikation von MeV_{vac2}-SARS2-S(P) kann sowohl eine mögliche Beeinträchtigung des Wachstums *in vivo* implizieren als auch Hinweis für eine genetische Instabilität des Virus sein, die sich gegebenenfalls aus dem entsprechenden Selektionsvorteil von Antigen-defizienten Virus-Varianten herleitet. Daher wurde MeV_{vac2}-SARS2-S(H) für die Immunisierung von $IFNAR^{-/-}$-CD46Ge-Mäusen in einem Prime-Boost-Schema verwendet. Dabei entwickelten die geimpften Tiere Spike-spezifische T-Zellen, von denen ein überwiegender Anteil mindestens zwei oder alle drei der Zytokine IFN-γ, IL-2, TNF-α sezernierten und damit multifunktional sind (Fig. 4., S7). Eine solche Multifunktionalität kann vor allem bei Gedächtnis-T-Zellen (Westerhof et al. 2019) und in T-Zellen von COVID-19-Rekonvaleszenten gesehen werden, sodass diesen Zellen eine große Bedeutung beim Reaktivieren einer Immunantwort zukommt (Pavan Kumar et al. 2022). In allen geimpften Tieren konnten bindende Antikörper und in drei von sieben Tieren nAb im Virusneutralisationstest (VNT) gegen SARS-CoV-2 nachgewiesen werden (Fig. 2C, 2F). Von den übrigen vier Tieren, die keine nAb gegen SARS-CoV-2 entwickelten, besaßen drei ebenfalls keine oder nur niedrige Neutralisationstiter gegen MeV nach der Prime-Impfung (Fig. 2K). Dies deutet auf einen technischen Fehler bei dieser Impfung hin, da nAb gegen MeV bereits nach der ersten Impfung mit einem rekombinanten Masernimpfstoff zu erwarten sind (Malczyk et al. 2015). Auch für vier von sieben mit MeV_{vac2}-SARS2-S(H) geimpften Mäusen, die später mit dem Maus-adaptierten SARS-CoV-2 MA infiziert wurden, konnten keine nAb gegen SARS-CoV-2 im VNT nachgewiesen werden (Fig. S13F). Im Plaque-Reduktion-Neutralisationstest (PRNT) dagegen konnten für alle Tiere, außer für zwei, die auch im VNT negativ waren, nAb nachgewiesen

werden (Fig. S13M). Da für den VNT volle Neutralisation statt nur Reduktion der Virusinfektion (wie im PRNT) gegeben sein muss, stellt sich der VNT als weniger sensitiv für den Nachweis von nAb gegen SARS-CoV-2 dar. Diese methodischen Faktoren erklären allerdings nur unzureichend, warum die übrigen zwei mit MeV_{vac2}-SARS2-S(H) geimpften Tiere scheinbar gar keine nAb entwickelten (Fig. S13M), obwohl alle sieben Tiere dieser Kohorte schon nach der ersten Impfung nAb gegen MeV entwickeln (Fig. S13K), die sich in sechs Tieren auch boostern ließen (Fig. S13L). Um die Immunogenität von MeV_{vac2}-SARS2-S(H) mit der anderer Masernvirus-abgeleiteter Vektorimpfstoffkanditen gegen COVID-19 zu vergleichen, können humane Seren von COVID-19-Rekonvaleszenten als Referenz dienen: In mit MeV_{vac2}-SARS2-S(H) geimpften Mäusen, die nAb-Titer entwickelten, lagen diese im Bereich der Seren von Rekonvaleszenten (Fig. 2F, S13F, S4). Auch für einen rMeV-Impfstoffkandidaten des Pasteur-Instituts, der in ATU(H) für ein modifiziertes (siehe Tab. 2) Spike kodiert, entwickelten geimpfte $IFNAR^{-/-}$-Mäuse nach dem Prime nur niedrige oder keine nAb-Titer, welche nach Boost schließlich Rekonvaleszenten-Niveau erreichen (Frantz et al. 2021). Wird dasselbe Antigen jedoch in der ATU(P) des Impfvirus kodiert, entwickeln die geimpften Mäuse signifikant höhere nAb-Titer nach Boost (Frantz et al. 2021), sodass ein Effekt der Proteinmenge von Spike auf dessen Immunogenität abgeleitet werden kann. Derselbe Effekt wurde für das in drei unterschiedlichen ATU von rMeV kodierte Hepatitis- B-Virus-Oberflächenantigen (*Hepatitis B surface antigen*, HBsAg) gefunden: Ein rMeV, das für HBsAg in ATU(P) kodiert, induziert die höchsten anti-HBsAg-Antikörpertiter, gefolgt von einem rMeV kodierend für HBsAg in ATU(H) und schließlich dem rMeV kodierend für HBsAg in der ATU nach dem *Large* (L) Protein von MeV (Del Valle et al. 2007).

Tab. 2 COVID-19-Impfstoffkandidaten auf Basis rekombinanter Masernimpfviren. Dargestellt sind die Immunantworten, die in den folgenden Publikationen in IFNAR$^{-/-}$-CD46GE-Mäusen (Frantz et al.: IFNAR$^{-/-}$-Mäuse; Kwak et al.: B6.FVB-Tg(CD46)2Gsv/J-Mäuse) gemessen wurden, nachdem diese mit der angegeben Inokulationsdosis eines rMeV-Vektorvirus kodierend für das jeweilige Antigen in der jeweiligen Position geimpft wurden.

2P/6P = 2-/6-Prolin-Mutation; ATU = *additional transcription unit*; bAb = *binding antibodies*; ΔFurin = Deletion der Furin-Spaltstelle; F = Fusionsprotein von MeV; foldON = T4 Fibritin Trimerisierungsmotiv; H = Hämagglutinin von MeV; nAb = *neutralizing Antibodies*; NAP = Neutrophilen-aktivierendes Protein von *Helicobacter pylori*; P = Phosphoprotein von MeV; PFU = *plaque forming units*; $PRNT_{50}$ = Plaque-Reduktion-Neutralisationstest 50; PsV = Pseudovirus; S = Spikeprotein von SARS-CoV-2; SFC = *spot forming cells*; $TCID_{50}$ = *tissue culture infection dose 50*; TMD = Transmembrandomäne; VNT = Virusneutralisationstest.

MeV-Impfvirus	Antigen(e)	Antigen-Position	Inokulation mit Impfvirus	Humorale Immunantwort (Titer bindender Antikörper, neutralisierender Antikörper)	Zelluläre Immunantwort (ELISpot, Intrazelluläre Zytokinfärbung)	Quelle
Moraten	• Vollständiges, natives Spikeprotein	• ATU(H)	1×10^5 $TCID_{50}$ (1. Impfung) 1×10^5 $TCID_{50}$ (2. Impfung)	7/7 Tiere anti-S bAb positiv 3/7 nAb positiv, VNT 25 49 Tage nach 2. Impfung	7/7 Tiere am oberen Detektionslimit (1600 spot forming cells (SFC) / 1×10^6 Splenozyten), Anteil von funktionalen T-Zellen: 40 % / 47 % ($CD4^+$ / $CD8^+$ T-Zellen) bifunktional, 11 % / 13 % ($CD4^+$ / $CD8^+$ T-Zellen) multifunktional 21 Tage nach 2. Impfung	(Hörner et al. 2020)
Edmonston	• Unmodifiziertes S1 • 2P- und ΔFurin-stabilisiertes Spike (preS), dessen TMD und zytoplasmatische Domäne durch foldON ersetzt ist	• ATU(P)	8×10^5 PFU (1. Impfung) 6×10^5 PFU (2. Impfung)	• S1 1×10^4 anti-S bAb • preS 1×10^4 anti-S bAb 7 Tage nach 2. Impfung	• S1 2/6 Tiere positiv, 0 SFC / 1×10^6 Splenozyten; • preS 5/6 Tiere positiv, 50 SFC / 1×10^6 Splenozyten; keine intrazelluläre Zytokinfärbung; 7 Tage nach 2. Impfung	(Lu et al. 2021a)

Schwarz	• 2P- und ΔFurin-stabilisiertes Spike, Deletion Signalsequenz für Endoplasmatisches Retikulum	• ATU(P) • ATU(H)	1×10^5 $TCID_{50}$ (1. Impfung) 1×10^5 $TCID_{50}$ (2. Impfung)	• ATU(P) 6×10^5 anti-S bAb $PRNT_{50}$ 2×10^3 • ATU(H) 7×10^4 anti-S bAb $PRNT_{50}$ 4×10^2 80 Tage nach 2. Impfung	• ATU(P) 2.500 SFC / 1×10^6 Splenozyten (CD8-Peptide), 430 SFC / 1×10^6 Splenozyten (CD4-Peptide), Anteil von funktionalen T-Zellen: 0 % / 1,5 % ($CD4^+$ / $CD8^+$ T-Zellen) bifunktional; • ATU(H) 2.000 SFC / 1×10^6 Splenozyten (CD8-Peptide), 130 SFC / 1×10^6 Splenozyten (CD4-Peptide), keine intrazelluläre Zytokinfärbung 7 Tage nach 2. Impfung	(Frantz et al. 2021)
„Moraten Resurfaced“ (F ersetzt durch CDV-F; H ersetzt durch H von MeV Genotyp H1, deletiert um 8 immundominante Epitope)	• IgGk Leitsequenz, 6P- und ΔFurin-stabilisiertes Spike, TMD ersetzt durch foldON und NAP	• ATU(P)	1×10^5 PFU (1. Impfung) 1×10^5 PFU (2. Impfung)	5×10^4 anti-S bAb PsV-VNT 8×10^3 21 Tage nach 2. Impfung	100 SFC / 1×10^6 Splenozyten (S1-Peptide), 700 SFC / 1×10^6 Splenozyten (S2-Peptide), keine intrazelluläre Zytokinfärbung (keine Zeitangabe)	(Muñoz-Alía et al. 2022)
Moraten	• 6P- und ΔFurin-stabilisiertes Spike	• ATU(P)	1×10^6 PFU (1. Impfung) 1×10^6 PFU (2. Impfung)	5/5 Tiere anti-S bAb positiv $PRNT_{50}$ 2×10^3 14 Tage nach 2. Impfung	400 *spot forming units* / Vertiefung (keine Angabe der Zellzahl / Vertiefung) 14 Tage nach 2. Impfung	(Kwak et al. 2023)

Die erhöhte Proteinmenge, die mit Einfügen des Spike-Gens in die ATU(P) einhergeht, führt für das native Spike zur Hyperfusogenität des Impfvirus und dadurch zu dessen reduziertem Wachstumsverhalten (Hörner et al. 2020). Auch die genetische Instabilität solch eines hyperfusogenen Impfvirus mit nativem Spike in ATU(P) konnte nachgewiesen werden (Frantz et al. 2021), was retrospektiv die Entscheidung validiert, in Hörner *et al.* die weiteren Studien mit MeV_{vac2}-SARS2-S(H) statt mit MeV_{vac2}-SARS2-S(P) durchgeführt zu haben. Um ein stabileres Impfvirus zu erhalten, wurde das Spike-Gen von Frantz *et al.* mehrfach modifiziert (Frantz et al. 2021): Für einen vermehrten Transport des Spikeproteins (S) zur Zellmembran wurden die letzten elf Aminosäuren deletiert, die eine Signalsequenz für das Endoplasmatische Retikulum (*endoplasmic reticulum retention signal*, ERRS) enthalten (Frantz et al. 2021), wie bereits für das S von SARS-CoV gezeigt (Ujike et al. 2016). Darüber hinaus wurde das S durch zwei Mutationen in der Konformation vor der Fusion (Präfusion-Konformation) stabilisiert (Frantz et al. 2021). Solch eine Stabilisierung kann einerseits durch die Substitution von zwei definierten Aminosäuren (K986, V987) durch zwei Proline (2P) erreicht werden: Diese befinden sich in der Gelenkregion (*hinge*), welche in der *head*-Region des S die zentrale Helix (*central helix*, CH) mit der Heptad-Wiederholung 1 (*heptad repeat 1*, HR1) verbindet. Nach Rezeptorbindung spaltet sich die S1-Untereinheit ab und die HR1 faltet sich entlang des Gelenks in Richtung Zelle auf, um den Fusionsprozess einzuleiten. Die 2P-Substitution versteift diese *hinge* zwischen CH und HR1 und verringert dadurch die Wahrscheinlichkeit, dass sich S durch äußere Einflüsse wie Rezeptorbindung irreversibel in die Postfusion-Konformation faltet. Die Versteifung des S wurde schon am Beispiel des nahe verwandten und sehr ähnlich aufgebauten MERS-S gezeigt (Pallesen et al. 2017). Eine andere Mutation zur Stabilisierung des SARS-CoV-2-S betrifft die Furin-Spaltstelle zwischen den Untereinheiten S1 und S2: Durch die Deletion der Spaltstelle (ΔFurin) wird eine Prozessierung in S1 und S2 im Golgi-Apparat vor dem Ausschleusen aus der Zelle verhindert, sodass ein Auslösen der Fusion und damit das Auftreten des Antigens in Postfusion-Konformation unwahrscheinlicher werden (Johnson et al. 2021). Spikeproteine, die aufgrund einer oder beider dieser Mutationen stabilisiert wurden, sind also nicht mehr in der Lage eine Spike-vermittelte Zell-Zell-Fusion auszulösen. Dadurch sind virale Vektorimpfstoffe, die für solch stabilisierte Spikeproteine kodieren, weniger in ihrem Wachstumsverhalten beeinflusst als solche, die für das native, fusogene S kodieren.

Darüber hinaus sind bei SARS-CoV-2-Spike in der Präfusion-Konformation alle Epitope vorhanden, die eine Neutralisation erlauben (Wrapp et al. 2020), sodass durch einen höheren Anteil von Spikeproteinen in dieser Konformation die Immunantwort mehr auf schützende Epitope des Antigens gelenkt wird. Kodiert beispielsweise ein Ad26-Vektor für ein 2P- und ΔFurin-stabilisiertes S (Ad26.S.PP), so entwickeln damit geimpfte Tiere höhere nAb-Titer als solche, die mit dem Ad26-Vektor mit nativem S (Ad26.S) geimpft wurden, sowohl Mäuse (Bos et al. 2020), als auch Rhesusaffen (Mercado et al. 2020). Ebenso

entwickeln mit mRNA-Impfstoff (Kalnin et al. 2021) oder Protein-Impfstoff (Amanat et al. 2021) geimpfte Tiere höhere nAb-Titer, wenn die jeweiligen Impfstoffe für 2P- und ΔFurin-stabilisiertes S kodierten, als die Tiere, die den jeweiligen Impfstoff mit nativem S erhielten. Daher ist auch in fünf der sieben in der EU zugelassenen COVID-19-Impfstoffe das Antigen eine in der Präfusion-Konformation stabilisierte Version des S (Corbett et al. 2020; Vogel et al. 2021; Mercado et al. 2020; Europäische Arzneimittel-Agentur 2023i, 2023l).

Nach der 2P-Mutation wurde eine weitere stabilisierende Modifikation von SARS-CoV-2-S beschrieben, die neben den zwei beschriebenen Substitutionen noch vier weitere Proline einfügt: Die HexaPro (6P)-Mutante des S, welche in FreeStyle 293-F-Zellen 10-fach stärker exprimiert wird als die 2P-Mutante. Daneben erweist sich die 6P-Mutante als besonders thermostabil, da sie auch nach 30 min bei 55 °C noch in der Präfusion-Konformation vorliegt, während sich bei der 2P-Mutante nach 30 min bei 50 °C bereits Protein-Aggregate bilden (Hsieh et al. 2020). Auch diese Modifikation wurde bereits in zwei rMeV-basierten Impfstoffkandidaten untersucht (Tab. 2) und zeigt dabei im Vergleich zu Kandidaten mit 2P-stabilisiertem S-Antigen höhere bindende und neutralisierende Antikörper-Antworten und mehr als 500 IFN-γ-produzierenden Zellen pro $1{\times}10^6$ Splenozyten, nachdem diese mit Peptiden der S2-Untereinheit stimuliert wurden (Muñoz-Alía et al. 2022).

Entsprechend dieser positiven Effekte aus stabilisierenden Modifikationen von S und nach der Zulassung erster Impfstoffe, in denen diese Modifikationen erfolgreich genutzt werden, wurden überwiegend rMeV-basierte Impfstoffkandidaten gegen COVID-19 untersucht, die für ein stabilisiertes S kodieren (Tab. 2). Dies ist einerseits erforderlich, um ein rMeV zu generieren, welches für das S in ATU(P) kodiert und damit potenziell höhere Antikörpertiter induziert ohne dabei die Wachstumseigenschaften des Vektorvirus zu verändern. Andererseits erscheint eine solche Stabilisierung per se nützlich, um höhere Titer an nAb zu stimulieren (Pedenko et al. 2023).

Dies steht im Kontrast zu Ergebnissen aus präklinischen Studien von Impfstoffkandidaten gegen MERS-CoV: Die in über 40 präklinischen Studien untersuchten Impfstoffkandidaten nutzen das native S oder Teile davon (wie die RBD) (Zhang et al. 2020; Tai et al. 2022). Dabei wurde die Immunogenität und Schutzwirkung des nativen MERS-S auch im Kontext desselben rMeV-Vektors gezeigt, der auch in Hörner *et al.* untersucht wurde: Alle Tiere, die mit einem rMeV geimpft wurden, welches in ATU(H) für das native MERS-S kodiert, entwickelten bereits nach der ersten Impfung neutralisierende Antikörpertiter (Malczyk et al. 2015). Dabei konnte keine Hyperfusogenität der Impfviren kodierend für MERS-S beobachtet werden, auch nicht bei einem Impfstoffkandidaten, der für das native S in ATU(P) kodiert: Dieses Impfvirus wächst zu ebenso hohen Titern wie das parentale Virus (Malczyk et al. 2015).

MERS-S, welches nur eine Sequenzhomologie von 35 % zu SARS-CoV-2-S aufweist (Grifoni et al. 2020), wirkt also bereits unmodifiziert wesentlich immunogener als SARS-CoV-2-S und ist nicht fusogen in den zur Amplifikation des Impfvirus verwendeten Zellsubstraten wie beispielsweise Vero-Zellen, die den MERS-CoV-Rezeptor Dipeptidylpeptidase 4 (DPP-4) exprimieren (Eckerle et al. 2013).

Im Gegensatz zu MERS-CoV-S weist SARS-CoV-S eine höhere Sequenzhomologie von 76 % zu SARS-CoV-2-S auf (Grifoni et al. 2020). Wird SARS-CoV-S in seiner nativen Form in ATU(P) von rMeV-Impfstoffkandidaten kodiert, entwickeln alle damit geimpften Mäuse nAb-Titer (Liniger et al. 2008; Escriou et al. 2014). Trotz dieser hohen Menge an exprimiertem S wachsen die Vektorviren zu nur 10-fach verminderten bis vergleichbaren maximalen Titern im Vergleich zum parentalen Virus (Liniger et al. 2008; Escriou et al. 2014). Eine Tendenz zu mehr Zell-Zell-Fusionen wurde dabei nicht beschrieben. Während sich also die Spikeproteine von MERS-CoV und SARS-CoV bereits in deren nativer Form als Antigen für Vektorimpfstoffe offenbar nahezu uneingeschränkt eignen, stellt die Fusogenität von SARS-CoV-2-S in den Virus-produzierenden Zelllinien eine Herausforderung dar, die beispielsweise mit der Stabilisierung des S in seiner Präfusion-Konformation gelöst werden kann.

Um die Schutzwirkung eines zukünftigen Vakzins besser abschätzen zu können, wurden Studien zu Schutzkorrelaten anhand klinischer Studien der bestehenden COVID-19-Impfungen durchgeführt. Neben den oben erwähnten $CD8^+$-T-Zellen werden aufgrund der Korrelation von Antikörperantworten und Schutzwirkung auch SARS-CoV-2-S-bindende IgG-Antikörper als Schutzkorrelat beschrieben (Khoury et al. 2021; Earle et al. 2021; Feng et al. 2021; Gilbert et al. 2022; Goldblatt et al. 2022). Durch Immunflucht gelingt der SARS-CoV-2-Variante Omicron allerdings eine 11- bis 43-fache Reduktion der Neutralisation durch Antikörper, die durch das Wildtyp-Virus induziert worden waren (Cele et al. 2022; Nemet et al. 2022; Carreño et al. 2022; Cheng et al. 2022; Hoffmann et al. 2022). Der trotzdem erhaltene Immunschutz, der auch durch die ursprünglichen Impfstoffe mit S der Ursprungsvariante vermittelt wird, kann dabei auf die oben ausgeführte zelluläre Immunität vor allem durch $CD8^+$-T-Zellen zurückgeführt werden (Liu et al. 2022a).

Da also der Stimulierung der humoralen Immunantwort ein hoher prädiktiver Wert für den Erfolg eines COVID-19-Impfstoffkandidaten zugesprochen werden kann, wurden in der COVID-19-Impfstoffforschung weitere Antigenmodifizierungen getestet, die besonders diesen Arm des adaptiven Immunsystems ansprechen sollen. Da lösliche statt membrangebundene Antigene die Aufnahme durch Antikörper-produzierende B-Zellen erleichtern (Pape et al. 2007; Bajénoff und Germain 2009), wurden weitere rMeV-basierten COVID-19-Impfstoffkandidaten entwickelt, die für S-Varianten kodieren, die vor der Transmembrandomäne (TMD) trunkiert sind. In Zellen, die mit einem rMeV mit trunkiertem,

nativem S (S-dTM) infiziert wurden, konnte die Expression des S nur schwach und erst 96 h, nicht aber bereits 72 h nach Infektion nachgewiesen werden (Lu et al. 2021a). Demgegenüber war die Expression in Zellen, die mit einem rMeV infiziert wurden, das für ein S mit ΔFurin- und 2P-Mutationen und außerdem anstelle der TMD und der C-terminalen Domäne (CTD) ein Trimerisierungsmotiv kodiert (preS) die Expression des S bereits 72 h nach Infektion deutlich (Lu et al. 2021a). Baumwollratten, die mit einem preS-kodierenden rMeV geimpft wurden, bildeten signifikant höhere nAb-Titer, als Tiere immunisiert mit einem rMeV, das für das native, vollständige S kodiert (Lu et al. 2021a). Auf die Auswirkung der Trunkierung des S vor der TMD und damit des löslichen Antigens kann mangels direkten Vergleichs mit rMeV, die membranständiges S-Antigen kodieren, nicht geschlossen werden.

Mehr Hinweise auf die Wirkung eines löslichen SARS-CoV-2-S geben auch die schon zitierten Studien von Ad26-Vektoren in Rhesusmakaken (Mercado et al. 2020): Das membranständige, ΔFurin- und 2P-stabilisierte S (Ad26.S.PP) induzierte vier Wochen nach Immunisierung Pseudovirus-nAb-Titer von >400 und nAb-Titer im VNT gegen SARS-CoV-2 von >100, während das lösliche, ebenfalls ΔFurin- und 2P-stabilisierte S (Ad26.S.dTM.PP) Pseudovirus-nAb-Titer von <100 und SARS-CoV-2 nAb-Titer im VNT von ca. 30 induziert (Mercado et al. 2020). Interessanterweise provozierte Ad26.S.dTM.PP mehr (ca. 300 pro 1×10^6 Mononukleäre Zellen des peripheren Blutes (peripheral blood mononuclear cells, PBMC)) IFN-γ-sezernierende Zellen als Ad26.S.PP (<100 pro 1×10^6 PBMC) (Mercado et al. 2020). Dieser Effekt auf die zelluläre Immunantwort konnten in einem Vergleich zwischen dem löslichen, nativen (solS(H)) und dem vollständigen, nativen (S(H)) MERS-S als Antigen kodiert in rMeV nicht gesehen werden: Beide Gruppen an geimpften Mäusen entwickelten ähnlich viele Antigen-spezifische IFN-γ-produzierende Zellen (Malczyk et al. 2015). Die erwartet stärkere humorale Immunantwort induziert durch eine lösliche Form des Antigens bestätigt sich hingegen auch für MERS-CoV-S nicht: Mit MV_{vac2}-MERS-S(H) geimpfte Mäuse entwickelten im Median nAb-Titer von 874, mit MV_{vac2}-MERS-solS(H) geimpfte Mäuse nAb-Titer von 640 nach zweifacher Immunisierung (Malczyk et al. 2015). Dass die humorale Immunantwort durch die löslichen S-Antigene nicht stärker induziert wird als durch membranständige ist bemerkenswert und muss durch kommende Studien näher untersucht werden. Entsprechend wird diese Modifikation in den bisher in der EU zugelassenen Impfstoffen nicht eingesetzt.

Präklinische Studien zeigten also die Immunogenität von rMeV-basierten COVID-19-Impfstoffkandidaten. Zudem wurde vor der COVID-19-Pandemie ein auf dem Impfstamm Schwarz basierendes rMeV als Impfstoffkandidat gegen das Chikungunya Virus (CHIKV) bereits erfolgreich in einer klinischen Phase II-Studie getestet (Reisinger et al. 2018). Auf dieser Basis wurde ein MeV-abgeleiteter COVID-19-Vektorimpfstoff entwickelt, der ebenfalls auf dem Schwarz-Impfstamm basiert, der aber für ein membranständiges, ΔFurin- und 2P-stabilisiertes SARS-CoV-2-S mit ERRS kodiert: V591.

Mit V591 wurden zwei klinische Studien durchgeführt: In der Phase I-Studie entwickelten nur 17 % der Probanden in der Niedrig-Dosis-Gruppe (zweifach geimpft mit 1×10^5 $TCID_{50}$) und 61 % der Probanden in der Hoch-Dosis-Gruppe (zweifach geimpft mit 1×10^6 $TCID_{50}$) nachweisbare nAb (>10 neutralisierende Titer 50, NT_{50}), während eine Antigen-spezifische T-Zellantwort in PBMCs im intrazellulären Zytokin-Färbungs-Assay nicht messbar war (Launay et al. 2022). In der Phase I/II-Studie konnten an Tag 29 nach einfacher Immunisierung in Probanden der drei niedrigsten Dosis-Gruppen (1×10^4 $TCID_{50}$, 1×10^5 $TCID_{50}$, bzw. 1×10^6 $TCID_{50}$) weder neutralisierende noch S-bindende spezifische Antikörper nachgewiesen werden (Vanhoutte et al. 2022). In der höchsten Dosis-Gruppe (1×10^7 $TCID_{50}$) konnten zwar nAb-Titer nachgewiesen werden (im Mittel ein NT_{50} von 31,2), diese lagen aber deutlich niedriger als die nAb-Titer von Rekonvaleszenten-Seren (im Mittel 164,9) (Vanhoutte et al. 2022). Parallel entwickelten Probanden, die in Studien der mittlerweile zugelassenen Impfstoffe Spikevax, Comirnaty, Vaxzevria und Sputnik V mitwirkten, nAb-Titer, die gleich hoch oder höher lagen als die der Rekonvaleszenten (Anderson et al. 2020; Walsh et al. 2020; Voysey et al. 2021; Logunov et al. 2021). Auf Grund der im Vergleich nicht konkurrenzfähigen Immunogenität wurde die weitere Entwicklung von V591 abgebrochen (Launay et al. 2022; Vanhoutte et al. 2022).

Interessant ist jedoch in diesem Zusammenhang der Vergleich der Analysen der anti-Vektor-Immunität zu vorhergehenden Studien. In der Phase II-Studie des CHIKV-Impfstoffkandidaten MV-CHIK erhöhten sich die anti-MeV-Titer nach Impfung in der Niedrig-Dosis-Gruppe (5×10^4 $TCID_{50}$) um das 3-fache und in der Hoch-Dosis-Gruppe (5×10^5 $TCID_{50}$) um das 5-fache gegenüber dem Ausgangsniveau der größtenteils gegen Masern präimmunen Testpersonen (Reisinger et al. 2018). Dem gegenüber steht die Phase I-Studie von V591, in der sich die anti-MeV-Titer in der Niedrig-Dosis-Gruppe nur um 2-fache und in deren zwei Hoch-Dosis-Gruppen nur um das 2,5-fache erhöhten (Launay et al. 2022). Aus diesem Grund vermuten die Verfassenden der genannten Studie, dass die verhältnismäßig geringe Immunogenität von V591 eher von Vektorvirus und Antigen gemeinsam bedingt ist als vom Antigen alleine (Launay et al. 2022). Da Studienteilnehmende, die vor der ersten Impfung niedrige Maserntiter hatten, signifikant höhere Titer gegen S nach der ersten Impfung erreichten als Testpersonen mit initial hohen Maserntitern, wird als eine Ursache für das Scheitern von V591 die vor der ersten Impfung der Studie bereits bestehende Immunität gegen das Vektorvirus (Präimmunität) diskutiert (Launay et al. 2022). Da diese Präimmunität gegen den MeV-Vektor prinzipiell als mögliche Hürde für die klinische Anwendung eines rMeV-Impfstoffs erkannt wurde, wurde dieser Faktor schon zuvor in anderen präklinischen Studien betrachtet: In präimmunen Mäusen und präimmunen, nicht-humanen Primaten konnte nach Impfung mit rMeV-Konstrukten mit zusätzlichen Antigenen von HIV oder CHIKV immer noch vergleichbare Antigen-spezifische humorale Immunantworten gegen das Fremdantigen ausgelöst werden wie in

Masern-naiven Tieren (Lorin et al. 2004; Brandler et al. 2013). Vor allem stehen die Ergebnisse der V591-Studien aber in Kontrast zu vorherigen klinischen Studien, in denen ebenfalls das Schwarz-Masernimpfvirus als Vektorvirus verwendet wurde für den CHIKV-Impfstoffkandidaten MV-CHIK (Ramsauer et al. 2015; Reisinger et al. 2018). In der Phase-I-Studie wurden an Tag 28 nach der ersten Impfung vergleichbar hohe nAb-Titer gegen CHIKV induziert, unabhängig von den Ausgangstitern der Probanden gegen das MeV bei Studienstart (Ramsauer et al. 2015). In der Phase-II-Studie ging man in der Untersuchung der möglichen Auswirkung einer Präimmunität noch weiter und immunisierte zwei Kohorten entweder 28 Tage (Kohorte M1) oder 196 Tage (Kohorte M2) vor der ersten MV-CHIK-Impfung mit einem MeV-Impfstoff (Reisinger et al. 2018). 28 Tage nach zweiter MV-CHIK-Impfung wurden jeweils in der Hoch-Dosis-Gruppe durchschnittliche anti-CHIKV-Titer von 254 für Kohorte M1 bzw. 160 für Kohorte M2 im Vergleich zu 175 für die Kohorte, die nicht zu Beginn der Studie präimmunisiert wurde, erreicht (Reisinger et al. 2018). Auch in den jeweiligen Niedrig-Dosis-Gruppen entwickelten alle Probanden nAb-Titer gegen das CHIKV, die sich nicht signifikant von den Titern von nicht-präimmunisierten Probanden unterschieden. Somit konnte in keiner der beiden klinischen Studien eine Auswirkung der Präimmunität auf MV-CHIK festgestellt werden (Ramsauer et al. 2015; Reisinger et al. 2018). Mögliche Gründe für die niedrige Immunogenität von V591, insbesondere im Vergleich zu MV-CHIK, werden daher untersucht. Eine Publikation dieser Ergebnisse und der Daten der präklinischen Studien mit V591 wurde von den Verfassenden angekündigt.

Um einer möglichen Problematik der Präimmunität gegen MeV beim Einsatz von MeV als onkolytisches Virus (d.h. als Virus, das möglichst zielgerichtet Tumorzellen infiziert und abtötet) begegnen zu können, wurde bereits ein auf dem MeV-Impfstamm Moraten basierendes rMeV generiert, dessen acht immundominante nAb-Epitope im Hämagglutinin gezielt mutiert und dessen Fusionsprotein gegen das Fusionsprotein des nahe verwandten Hundestaupevirus (canine distemper virus, CDV)-F ausgetauscht wurde (Muñoz-Alía et al. 2021). Nach Verabreichung von anti-Masern-Antikörpern behält dieses Virus „MeV-MR“ (Moraten Resurfaced) weiterhin seine Replikationsfähigkeit in IFNAR$^{-/-}$-CD46Ge-Mäusen (Muñoz-Alía et al. 2021). Auf Basis von „MeV-MR“ wurde ein COVID-19-Impfstoffkandidat hergestellt, der für das lösliche, 6P-stabilisierte S kodiert, das zusätzlich mit einem T4 Fibrin Trimerisierungsmotiv sowie dem Neutrophilen-aktivierenden Protein (NAP) ausgestattet ist (Tab. 2) (Muñoz-Alía et al. 2022). Das T4 Fibrin Trimerisierungsmotiv erleichtert die Multimerisierung der löslichen S-Monomere zu Trimeren (Letarov et al. 1999). NAP wirkt zusätzlich immunogen, wenn es neben einem Antigen im rMeV-Vektor exprimiert wird (Iankov et al. 2013) und trägt über seine dodekamere Struktur zur Selbstassemblierung von Nanopartikeln bei, die mit S-Trimeren bestückt sind (Muñoz-Alía et al. 2022). Mit diesem Impfstoffkandidat geimpfte IFNAR$^{-/-}$-CD46Ge-Mäuse haben an Tag 42 nach Impfung nAb-

Titer von 8.192 gegen LV, die mit SARS-CoV-2-S pseudotypisiert (Pseudovirus, PsV) wurden, und bis zu 700 IFN-γ-sezernierende Zellen pro 1×10^6 Splenozyten. Nach vorheriger Applikation von 0,4 internationalen Einheiten anti-MeV-Antikörpern entwickeln Mäuse immer noch hohe PsV nAb-Titer von 2.048 (Muñoz-Alía et al. 2022). Dabei wurde nicht untersucht, wie sich eine vorherige Applikation von anti-MeV-Antikörpern auf die Induktion von PsV nAb-Titer auswirkt, wenn Mäuse anschließend mit einem für Spike kodierenden, aber nicht Oberflächen-modifizierten rMeV geimpft werden. Auf eine tatsächliche Verbesserung des Vektorvirus hinsichtlich eines Umgehens einer potenziellen Präimmunität kann auf Basis dieser Daten daher noch nicht endgültig geschlossen werden.

Weiterhin konnte zwar gezeigt werden, dass nach Applikation von anti-MeV-Antikörper Mäuse, die anschließend mit dem parentalen, nativen Moraten-Impfvirus geimpft wurden, niedrigere MeV-nAb-Titer entwickelten als solche, die keine anti-MeV-Antikörper erhielten. Allerdings bleibt fraglich, in welchem Maß die Mäuse durch die Applikation der anti-MeV-Antikörper tatsächlich präimmun waren, da der Nachweis der anti-MeV-Antikörper in den Tieren nach Applikation nicht gezeigt wurde und präformierte anti-MeV T-Zellantworten in diesem Modell nicht dargestellt werden, die im Fall einer Maserninfektion kritisch für eine *Clearance* des Virus sind (Lin et al. 2014). Weitere Studien zu MeV-MR bleiben daher abzuwarten, die beispielsweise die Effekte einer vollständigen Immunisierung durch ein MeV-Impfvirus mit anschließendem Nachweis einer humoralen und zellulären MeV-Immunität auf die Immunogenität von MeV-MR im direkten Vergleich mit einem nicht modifizierten rMeV untersuchen. Sollte in Studien die negativen Auswirkungen einer Präimmunität auf die Immunogenität von rMeV tatsächlich belegt werden, könnten modifizierte rMeV wie MeV-MR erste Lösungswege aufzeigen, um die Wirksamkeit von rMeV-basierten Impfstoffkandidaten in Masern-immunen Personen zu erhalten oder weiter zu erhöhen.

Noch vor der Wirksamkeit eines Impfstoffs ist dessen Sicherheit von höchster Relevanz. Bei der Entwicklung der COVID-19-Impfstoffe lag ein besonderes Augenmerk der Entwicklung auf der Vermeidung schwerwiegender Impfstoffnebenwirkungen. Insbesondere Impfstoff-induzierte Immunpathogenesen wie sie beispielsweise bei der frühen Entwicklung von Impfstoffen gegen das Respiratorische Synzytial-Virus (RSV) beobachtet wurden (Kim et al. 1969), galt es zu verhindern. Eine solche unerwünschte Wirkung eines Impfstoffs, sodass gegen ein Pathogen geimpfte Individuen nach Infektion mit diesem Pathogen eine verstärkte respiratorische Erkrankung entwickeln, wird als *Vaccine Associated Enhanced Respiratory Disease* (VAERD) beschrieben (Munoz et al. 2021). In Tiermodellen zu SARS-CoV-Impfstoffen konnte beobachtet werden, dass vor allem nach Impfung mit inaktivierten Vollvirus-Vakzinen, aber auch mit virusähnlichen Partikeln, DNA- und Protein-Vakzinen, eine nachfolgende Infektion mit SARS-CoV eosinophile Infiltrate in der Lunge auslöst (Bolles et al. 2011; Tseng

et al. 2012; Iwata-Yoshikawa et al. 2014; Honda-Okubo et al. 2015), welche mit einer überwiegenden Th2-Immunantwort assoziiert werden (Tseng et al. 2012). Ähnlich dazu löste auch ein inaktivierter MERS-CoV-Impfstoff nach Infektion von Mäusen mit MERS-CoV eosinophile Infiltrate in den Lungen aus (Agrawal et al. 2016). Solche Vakzin-induzierten Immunpathologien wurden in präklinischen Studien auch bei SARS-CoV-2 Infektionen im Rahmen dieser und anderer Arbeiten beschrieben (DiPiazza et al. 2021; Iwata-Yoshikawa et al. 2022; Ebenig et al. 2022b). Die Infektion von BALB/c-Mäusen mit einem Maus-adaptierten SARS-CoV-2 (MA10) führt zur Infiltration der Lunge mit eosinophilen Granulozyten, wenn die Tiere zuvor entweder mit einem Aluminiumhydroxid (Alum)-adjuvantiertem Inaktivat- oder Proteinimpfstoff geimpft wurden (DiPiazza et al. 2021; Iwata-Yoshikawa et al. 2022). Solch eosinophile Infiltrate sind ein klares Anzeichen für VAERD. Bemerkenswert dabei ist, dass weder Inaktivat- noch Proteinimpfstoff-geimpfte Mäuse nach Infektion Gewicht verloren (DiPiazza et al. 2021). Ähnlich dazu litten in einer weiteren Studie von den geimpften Tieren nur solche unter Gewichtsverlust, die nicht- (S-ect) oder Alum-adjuvantierten (S-ect+alum) Proteinimpfstoff bestehend aus der Ektodomäne des SARS-CoV-2-S erhielten (Iwata-Yoshikawa et al. 2022). Dagegen erleiden Mäuse, die mit einem Toll-like Rezeptor (TLR)-Agonisten adjuvantiertem Proteinimpfstoff (S-ect+TLR) geimpft wurden, keinen Gewichtsverlust (Iwata-Yoshikawa et al. 2022). Die S-ect- oder S-ect+alum-geimpften Mäuse hatten drei Tage nach Infektion beachtliche (ca. 10^6-10^8 $TCID_{50}$/g) SARS-CoV-2-Titer in der Lunge und sind daher nur partiell geschützt im Gegensatz zu den S-ect+TLR-geimpften Mäusen, die nach Infektion niedrige Virustiter (ca. 10^3 $TCID_{50}$/g) in der Lunge aufwiesen (Iwata-Yoshikawa et al. 2022). Ungeimpfte Kontrolltiere erleiden hingegen einen kontinuierlichen Gewichtsverlust, weisen hohe Virustiter in der Lunge auf (ca. 10^9 $TCID_{50}$/g) und versterben spätestens am sechsten Tag nach Infektion (Iwata-Yoshikawa et al. 2022). Der beobachtete Gewichtsverlust bei S-ect- oder S-ect+alum-geimpften Tieren kann daher aufgrund deren hohe Virustiter zumindest teilweise auf die SARS-CoV-2-Infektion zurückgeführt werden, ähnlich zu ungeimpften Tieren. Aus den Daten dieser beiden Studien lassen sich daher wenige Hinweise auf eine klinisch relevante VAERD ableiten. Demgegenüber leiden syrische Goldhamster unter einem vergleichbar hohen Gewichtsverlust nach SARS-CoV-2-Infektion, wenn sie zuvor nicht (*mock*) oder mit Alum-adjuvantiertem Spikeprotein (Alum-S) geimpft wurden (Hörner et al. 2020; Ebenig et al. 2022b). Überraschenderweise war die Viruslast in Alum-S-geimpften Hamstern signifikant mehr als 10-fach niedriger (2×10^4 $TCID_{50}$/g) als in nicht geimpften Tieren (5×10^5 $TCID_{50}$/g), während sich aber in den Lungen von Alum-S-geimpften im Unterschied zu ungeimpften Hamstern massive eosinophile Infiltrate nachweisen ließen. Somit sollte der Gewichtsverlust in der *mock*-Gruppe auf die SARS-CoV-2-Infektion und in der Alum-S-Gruppe vorwiegend auf eine VAERD zurückgeführt werden können (Ebenig et al. 2022b). Dies wurde bestätigt in einer Gruppe mit Alum-S geimpften Hamster, die parallel zur

Infektion mit Dexamethason behandelt wurden (Alum-S+Dex). In diesen Tieren waren die eosinophilen Infiltrate signifikant vermindert und auch der Gewichtsverlust an Tag 4 nach Infektion war ca. 7 Prozentpunkte niedriger. Diese mildere Symptomatik der Alum-S+Dex-Gruppe ist nicht auf eine schwächere Virusinfektion zurückzuführen, was sich sowohl aufgrund deren erhöhtem Anteil (ca. 10 %) an mit SARS-CoV-2 infiziertem Gewebe im histologischen Schnitt (Alum-S-Gruppe: ca. 5 %) als auch anhand deren erhöhter Viruslast in der Lunge von ca. 1×10^5 $TCID_{50}$/g (Alum-S-Gruppe: 2×10^4 $TCID_{50}$/g) ableiten lässt (Ebenig et al. 2022b). Sowohl der hohe Gewichtsverlust bei niedrigerem Virustiter als auch die Therapierbarkeit der Symptomatik mit Hilfe von Dexamethason lassen in diesem Modell auf eine klinische Relevanz der VAERD schließen. Da der syrische Goldhamster in der Auszucht vermehrt wird, das heißt Verwandtschaftspaarungen vermieden werden, hat er keine genetisch bedingte Tendenz der T-Helferzellen (wie die Th2-Tendenz der BALB/c-Mäuse). VAERD-Studien, die (wie Ebenig *et al.*) im ausgezüchteten Hamster durchgeführt werden, zeigen daher, dass die beobachtete Erkrankung nicht auf einen Artefakt eines auf eine bestimmte Immunantwort geprägten Tiermodells zurückzuführen ist. Während Gartlan *et al.* davor warnen, eine in geimpften, aber ungenügend geschützten Tieren gezeigte Pathologie nach Infektion ohne eine Quantifizierung der eosinophilen Infiltrate als VAERD zu interpretieren, stellen sie fest, dass zum Zeitpunkt des Verfassens des Manuskripts in keinem Tiermodell eine solche VAERD nach Infektion mit SARS-CoV-2 festgestellt wurde (Gartlan et al. 2022). Die nach Gartlan *et al.* publizierten Studien von Ebenig *et al.* zeigen damit zum ersten Mal, dass eine klinisch relevante VAERD nach SARS-CoV-2-Infektion in Tieren ausgelöst werden kann (Ebenig et al. 2022b).

Die im syrischen Goldhamster dargestellte VAERD nach Immunisierung mit Alum-Spike geht auf eine durch den Impfstoff Th2-tendierende Immunantwort mit vermehrter Ausschüttung der Zytokine IL-4, IL-5 und IL-13 durch lymphoide Zellen zurück (Ebenig et al. 2022b). Makrophagen der Lunge scheinen diese Th2-Immunantwort nach Kontakt mit opsonisiertem SARS-CoV-2 zu verstärken, indem sie IL-19 ausschütten und eosinophile Granulozyten durch die vermehrte Expression des Chemokins CCL-11 anlocken (Ebenig et al. 2022b). Tatsächlich spiegelt der von Ebenig et al. beschriebene Mechanismus der VAERD nach Infektion mit SARS-CoV-2 durch eine Impfstoff-bedingte Th2-Antwort mit vermehrter Expression von IL-4, IL-5 und IL-13 mit eosinophilen Infiltraten in der Lunge sehr genau die Situation wider, wie sie bereits für Alum-adjuvantierte Inaktivatimpfstoffe gegen das RSV nachgewiesen wurde (Johnson und Graham 1999; Swart et al. 2002). Eine solche überschießende Th2-Antwort war in den 1960er Jahren verantwortlich für entsprechende Impfstoff-induzierte Pathogenesen in geimpften Kindern. Im Kontrast dazu wurde diese vermehrte Expression der Zytokine IL-4, IL-5 und IL-13 in Immunzellen von MeV_{vac2}-SARS2-S(H)-geimpften Hamstern nicht gesehen (Ebenig et al. 2022b), was

nach Hörner *et al.* in einem zweiten Tiermodell neben den dort analysierten Mäusen bestätigt, dass der rMeV-basierte COVID-19-Impfstoffkandidat wie erwartet eine Th1-tendierende Immunantwort auslöst, die kein Risiko der Induktion einer VAERD mit sich bringt. Gleichzeitig wurde die Schutzwirkung von MeV_{vac2}-SARS2-S(H) gegen eine Erkrankung durch SARS-CoV-2 erneut bestätigt: SARS-CoV-2-Titer 4 d nach Infektion in der Lunge gemessen waren in MeV_{vac2}-SARS2-S(H)-geimpften Tieren nicht nachweisbar, während sie in nicht geimpften Tieren bei ca. 5×10^5 $TCID_{50}$/g liegen (Ebenig et al. 2022b). Diese physiologische und potente Immunantwort induziert durch den rMeV-basierten COVID-19-Impfstoffkandidaten spiegelt sich auch in der Lungenpathologie MeV_{vac2}-SARS2-S(H)-geimpfter Tiere wider, die im Vergleich zu Alum-S-geimpften Tieren wesentlich weniger entzündetes Gewebe, Hämorrhagien und eosinophile Granulozyten aufweisen (Ebenig et al. 2022b).

Es steht mit dem syrischen Goldhamster also ein aussagekräftiges Tiermodell zur Erforschung einer VAERD nach SARS-CoV-2-Infektion zur Verfügung, das im Gegensatz zu bestimmten Inzucht-Mausstämmen keine genetisch bedingte Tendenz der T-Helferzell-Antwort aufweist und in dem trotzdem eine VAERD mit klinischer Symptomatik ausgelöst wird (Ebenig et al. 2022b). Die durch den Alum-Proteinimpfstoff geprägte Immunantwort der Hamster löst hohe Titer an bindenden, jedoch nicht neutralisierenden Antikörpern aus (Hörner et al. 2020), führt dazu, dass Immunzellen hohe Mengen an Zytokinen einer Th2-Antwort exprimieren und ähnelt damit den bereits beschriebenen VAERD-Mechanismen von RSV (Ebenig et al. 2022b). Demgegenüber konnte im gleichen Tiermodell keinerlei Hinweise für eine VAERD gefunden werden, wenn die mit SARS-CoV-2 infizierten Tiere zuvor mit MeV_{vac2}-SARS2-S(H) geimpft wurden (Hörner et al. 2020; Ebenig et al. 2022b).

Zusammenfassend wurde gezeigt, dass MeV_{vac2}-SARS2-S(H), welches für ein natives S kodiert, sowohl eine humorale als auch zelluläre Immunantwort auslöst und in zwei Tiermodellen schützend wirkt. Auf MeV_{vac2}-SARS2-S(H) folgende rMeV-basierte COVID-19-Impfstoffkandidaten nutzen modifizierte Spikeproteine als Antigene, die über eine Stabilisierung des Spikeproteins in seiner Präfusion-Konformation sowohl eine Hyperfusogenität des rMeV in Zellkultur verhindern als auch potenziell immunogener sind. Einer dieser rMeV-Impfstoffkandidaten gegen COVID-19 war in klinischen Phase-I/II-Studien im Vergleich zu schon zugelassenen Impfstoffen nur moderat effektiv, sodass dessen weitere Entwicklung gestoppt wurde. Neben der Modifikation des Antigens unterliegt aber auch die rMeV-Plattform selbst einer ständigen Optimierung: Oberflächen-Proteine von MeV wurden ausgetauscht bzw. modifiziert, um die Immunogenität des Vektorimpfstoffs auch vor dem Hintergrund einer möglichen Präimmunität gegen MeV zu erhalten. Neben Studien, welche die immunogene Wirkung von rMeV verbessern sollen, wurden auch solche zur Untersuchung dessen Sicherheit durchgeführt: In einer Vergleichsstudie mit einem Alum-adjuvantiertem Spikeproteinimpfstoff löste

dieser nach SARS-CoV-2-Infektion in Hamstern eine *Vaccine Associated Enhanced Respiratory Disease* aus, die auf einer überschießenden Th2-tendierenden Immunantwort beruht. Parallel dazu vermittelte der rMeV-Impfstoffkandidat MeV_{vac2}-SARS2-S(H) eine vorteilhafte Th1-Immunantwort und schützte damit Hamster vor einer schwerwiegenden Symptomatik sowohl durch die SARS-CoV-2-Infektion als auch durch eine VAERD.

5.3 Relevante Faktoren bei der Erzeugung rekombinanter Masernimpfviren

Da die Erzeugung von rekombinanten Viren auf Basis von Masern-Impfviren wie die zuvor diskutierten MeV-abgeleiteten COVID-19 Impfstoffkandidaten komplex und damit ineffizient und fehleranfällig ist, wurde im Rahmen dieser Arbeit ein vereinfachtes System entwickelt, welches aus nur zwei Komponenten besteht: dem Genomplasmid, das für das gesamte Genom des zu erzeugenden rMeV kodiert, und einem 1-Helferplasmid, das für alle drei Helferproteine von MeV kodiert, welche notwendig sind, um infektiöse MeV auf Basis des vom Genomplasmid transkribierten viralen Genoms zu erzeugen. Es wurden in dieser Arbeit sieben verschiedene 1-Helferplasmide entwickelt, von denen ausschließlich die vier Plasmide funktionieren (das heißt, nach deren Co-Transfektion mit einem Genomplasmid von den transfizierten Zellen infektiöse rMeV freigesetzt werden), bei denen die Expression des viralen Phosphoproteins P im Vergleich zu der Expression von N reduziert ist (Auste und Mühlebach 2022).

Die Menge des Phosphoproteins scheint also in zu großen Mengen die Erzeugung der rekombinanten MeV zu inhibieren. Vergleichbar wurde für das Borna Disease-Virus (BDV) gezeigt, dass die virale Transkription eines BDV-Minigenoms durch den RNP-Komplex (bestehend aus Genom, viraler Polymerase L, Nukleokapsidprotein N, und Phosphoprotein P) beeinträchtigt wird, wenn die Menge des Expressionsplasmids für BDV-P erhöht wird (Schneider et al. 2003). Dass P zwar essenziell für die Bildung des RNP ist, es andererseits aber in größeren Mengen inhibierend auf die Transkription wirkt, kann mit dessen Bindungsverhalten mit L und N erklärt werden: MeV-P fungiert als Bindeglied zwischen der viralen Polymerase L und der mit Nukleokapsidprotein (N) eng assoziierten vRNA. Die C-terminale XD-Domäne von P bindet sowohl die C-terminale Domäne (CTD) N_{tail} von N, als auch die N-terminale Domäne (NTD) von L (Bourhis et al. 2005; Bloyet et al. 2019). Für die Bindung an L mit Hilfe der XD-Domäne muss P jedoch oligomerisieren (Bloyet et al. 2019). P bringt und hält L dadurch in der Nähe der vRNA, was die Assoziation von L an der vRNA mit Start der Transkription und Replikation des Genoms ermöglicht. Darüber hinaus binden P und N auch über ihre jeweiligen N-Termini aneinander. Bei dieser Bindung von P mit dem löslichen, monomeren N_0 hemmt P dessen inkorrekte Bindung an zelluläre statt virale RNA (Karlin et al. 2003). Bindet P an N, sodass beide im N_0-P-Komplex vorliegen,

sind die NTD und CTD von N rotiert im Vergleich zur RNA-gebundenen helikalen Form (Guryanov et al. 2015). Durch die Rotation überlappen sich die für die RNA-Bindung notwendigen Oberflächen der NTD und CTD von N, was dessen RNA-Bindung hemmen könnte (Guryanov et al. 2015).

Neben dieser Chaperonfunktion von P für N in eine wenig RNA-affine Konformation wurde auch gezeigt, dass P den helikalen Aufbau des Nukleokapsids hemmen kann, indem es die Bindestellen von nebeneinander liegenden N-Protomeren blockiert (Guryanov et al. 2015). Die Verfassenden vermuten, dass in infizierten Zellen ein Gleichgewicht zwischen der löslichen, P-gebundenen Form und der im Nukleokapsid gebundenen Form von N besteht, welches auf den relativen Mengen von N und P beruht (Guryanov et al. 2015). Dieser Gleichgewichtszustand von N und P könnte in Zellen, die mit 1-Helferplasmiden mit relativ hoher P-Expression transfiziert waren, gestört sein: 1-Helferplasmide, deren Genkassette für P nicht mit einem schwächeren Promotor ausgestattet wurde, führten nach deren Transfektion zu einem 4-fachen Überschuss an P-mRNA gegenüber N-mRNA und einem Überschuss an P-Protein gegenüber N-Protein in diesen Zellen (Fig. 4, 5 (Auste und Mühlebach 2022)).

Dieses Ungleichgewicht des P:N-Verhältnisses könnte sich auch nachteilig auswirken auf das Viroplasma (früher „Einschlusskörperchen“), den Ort in der Zelle, an dem sich neu synthetisierte Virusbestandteile ansammeln und zusammenlagern. Viren der Ordnung Mononegavirales nutzen phasengetrennte Kompartimente als solche „Virus-Fabriken“ (Su et al. 2021). Auch die Masernvirusproteine N und P führen *in vitro* zur Ausbildung von Kompartimenten einer Flüssig-Flüssig-Phasentrennung (*liquid-liquid phase separation*, LLPS), in denen sich RNA bevorzugt sammelt und dort den Aufbau von Nukleokapsiden auslöst (Guseva et al. 2020). Daher weisen diese LLPS-Kompartimente sowohl physikalische als auch funktionelle Merkmale von Viroplasma auf (Guseva et al. 2020).

Für Rhabdoviren, ebenfalls eine Familie der Ordnung Mononegavirales, wurde gezeigt, dass die dort als Negri-Körperchen bekannten Kompartimente der Ort der viralen Transkription und Replikation sind (Lahaye et al. 2009; Heinrich et al. 2010). Es wurde für diese Virusfamilie weiterhin nachgewiesen, dass die Co-Transfektion von Expressionsplasmiden, die für N oder P des Tollwutvirus kodieren, in Verhältnissen von 3:1 bis 1:3 zur Bildung von kugelförmigen Einschlüssen führt, die ähnliche physikalische Eigenschaften wie Negri-Körperchen haben (Nikolic et al. 2017). Wurde dagegen die relative Menge von P:N auf 9:1 erhöht, konnten keine Proteinaggregate mehr beobachtet werden; stattdessen verteilten sich die Proteine P und N diffus im Zytoplasma der Zelle (Nikolic et al. 2017). Sollten diese Proteinaggregate Vorläufer von funktionellen, für die Virus-Replikation essenziellen Virus-Fabriken sein, würde ein Ungleichgewicht in der Expression der viralen Proteine P und N über die Hemmung der Assemblierung solcher Kompartimente auch die Virusreplikation hemmen.

Ähnlich den Rhabdoviren würde auch die unausgewogene Expression von MeV-P die Bildung von LLPS-Kompartimenten, dem Ort der Assemblierung von MeV-Nukleokapsiden, behindern. Weitere Studien bleiben abzuwarten, welche die Rolle von im Überschuss vorhandenen MeV-P auf dessen Chaperonfunktion für N, sowie auf die Ausbildung von LLPS-Kompartimenten beleuchten. Daraus könnte abgeleitet werden, welche P:N-Verhältnisse in transfizierten Zellen vorliegen müssen, um rMeV mittels reverser Genetik effizient erzeugen zu können. Die bereits vorliegenden Ergebnisse zeigen aber bereits, dass sich das Phosphoprotein der Mononegavirales nach Virusinfektion in einem Gleichgewicht (vor allem mit dem Nukleokapsidprotein) befindet, in dem es noch fördernd und noch nicht hemmend auf die Transkription des Virus wirkt. Diese kritische Rolle von MeV-P und die besondere Empfindlichkeit des Transkriptions- und Replikationsprozesses des Masernvirus wurde auch deutlich bei der Etablierung des Zwei-Plasmid-Systems zur Herstellung von rMeV in der hier vorgelegten Arbeit: Erst nach Modulierung der Expression von P führte die Transfektion dieser 1-Helferplasmide zur Ausbildung von intrazellulären Virus-Fabriken (Auste und Mühlebach 2022).

Durch die Entwicklung des ersten Zwei-Plasmid-Systems zur Herstellung von rekombinanten Masernimpfviren innerhalb der hier vorgelegten Doktorarbeit konnte die Komplexität der Systeme zur Erzeugung rekombinanter MeV deutlich verringert werden. Die Anzahl der notwendigen Einzelkomponenten hat sich dadurch mindestens halbiert. Das Zwei-Plasmid-System hat bereits eine gute Effizienz, reicht aber noch nicht an das bisher effizienteste System von Martin *et al.* heran. Die Etablierung dieses neuen Systems eröffnet allerdings Spielraum in der weiteren Verbesserung der 1-Helferplasmide hinsichtlich einer möglichst exakten Simulierung der Expressionsprofile von N, P und L in der MeV-infizierten Zelle. Somit eröffnen sich über die Optimierung der reversen Genetik zur Nutzung der Impfstoffplattform rekombinante Masernimpfviren neue Potenziale unter anderem gegen zukünftige Diseases X.

6. Zusammenfassung

Eine Disease X ist laut Definition der WHO eine schwerwiegende Epidemie, die durch einen bis dahin nicht als humanpathogen bekannten Erreger ausgelöst wird. Knapp zwei Jahre nach Entwicklung dieses Konzepts trat SARS-CoV-2 als erstes Beispiel einer Disease X auf und löste zu Beginn des Jahres 2020 die COVID-19-Pandemie aus. Innerhalb von nur elf Monaten nach Ausrufung des internationalen Gesundheitsnotstandes durch die WHO wurde die erste Impfung gegen COVID-19 in der EU zugelassen – ein Prozess, der sonst einige Jahre dauert und zeigt, dass nach der Sicherheit dem Faktor Zeit im Kontext einer Disease X ebenfalls eine große Bedeutung zukommt. Die vorliegende Arbeit beschäftigt sich daher mit der Untersuchung von Wirk- und Impfstoffkandidaten gegen COVID-19, deren Erkenntnisse für weitere Diseases X nützlich sein können. Um als Leitstruktur in der Medikamentenentwicklung gegen COVID-19 dienen zu können, wurde die anti-coronavirale Wirkung des sekundären Pflanzenstoffes Epigallocatechingallat untersucht. Dabei zeigte sich dessen hemmende Wirkung *in vitro*, die sich nicht nur auf SARS-CoV-2 beschränkt, sondern mit SARS-CoV und MERS-CoV auch zwei weitere Betacoronaviren einschließt. Daneben wurden zwei Impfstoffkandidaten gegen COVID-19 hinsichtlich ihrer Immunogenität und Sicherheit vergleichend untersucht: ein rekombinantes Masernimpfvirus, das für das Spikeprotein von SARS-CoV-2 kodiert, und als Proteinimpfstoff das Aluminiumhydroxid-adjuvantierte Spikeprotein. Während das rekombinante Masernimpfvirus eine Th1-Immunantwort auslöst, die syrische Goldhamster vor einer schweren Erkrankung schützt, löst der Proteinimpfstoff eine Th2-Immunantwort aus, die im Hamster zu einer sogenannten *Vaccine Associated Enhanced Respiratory Disease* führt. Rekombinante Masernimpfviren zeichnen sich daher und auch durch den bereits langen Einsatz von Masernimpfstoffen im Menschen durch ihre hohe Sicherheit aus. Sie sind allerdings komplex in ihrer Herstellung, sodass eine weitere Studie auf deren Vereinfachung abzielte. Dabei konnte das erste System zur Herstellung rekombinanter Masernimpfviren entwickelt werden, welches nur aus zwei statt bisher mindestens vier essenziellen Komponenten besteht. Dies reduziert die Fehleranfälligkeit in der Anwendung und eröffnet weiteres Optimierungspotenzial hinsichtlich der Effizienz. So ist nun die Impfstoffplattform rekombinante Masernimpfviren durch ihre leichtere und potenziell schnellere Anwendung besser etabliert, um auch gegen die nächste Disease X innerhalb kurzer Zeit einen Impfstoffkandidaten hervorbringen zu können.

7. Summary

According to the WHO definition, a Disease X is a serious epidemic caused by a pathogen not previously known to be human pathogenic. Less than two years after this concept was developed, SARS-CoV-2 emerged as the first example of a Disease X and triggered the COVID-19 pandemic at the beginning of 2020. Within only eleven months of the WHO declaring an international public health emergency, the first vaccination against COVID-19 was licensed in the EU – a process that usually takes several years and shows that, after safety, time is also an important factor in the context of a Disease X. The present work therefore addresses the investigation of drug and vaccine candidates against COVID-19, the findings of which may be useful for further Diseases X. In order to be able to serve as a lead structure in drug development against COVID-19, the anti-coronaviral effect of the secondary plant metabolite epigallocatechin gallate was investigated. This showed its inhibitory effect *in vitro*, which is not only limited to SARS-CoV-2, but also includes two other betacoronaviruses, SARS-CoV and MERS-CoV. In addition, two vaccine candidates against COVID-19 were comparatively investigated with regard to their immunogenicity and safety: a recombinant measles vaccine virus encoding the spike protein of SARS-CoV-2 and, as a protein vaccine, the aluminium hydroxide-adjuvanted spike protein. While the recombinant measles vaccine virus elicits a Th1 immune response that protects Syrian golden hamsters from severe disease, the protein vaccine elicits a Th2 immune response that leads to so-called vaccine associated enhanced respiratory disease in the hamster. Recombinant measles vaccine viruses are therefore characterised by their high safety, and also because of the long use of measles vaccines in humans. However, they are complex to generate, so another study aimed to simplify their generation. The first system for the generation of recombinant measles vaccine viruses was developed, which consists of only two essential components instead of at least four. This reduces the susceptibility to errors in the application and paves the way for further potential optimisation in terms of efficiency. Thus, the vaccine platform recombinant measles vaccine virus is now better established due to its easier and potentially faster application, in order to be able to generate a vaccine candidate also against the next Disease X within a short time.

8. Literaturverzeichnis

Africa Centres for Disease Control and Prevention (2023): COVID-19 Vaccination. Online verfügbar unter https://africacdc.org/covid-19-vaccination/, zuletzt aktualisiert am 23.03.2023, zuletzt geprüft am 04.04.2023.

Agrawal, Anurodh Shankar; Tao, Xinrong; Algaissi, Abdullah; Garron, Tania; Narayanan, Krishna; Peng, Bi-Hung et al. (2016): Immunization with inactivated Middle East Respiratory Syndrome coronavirus vaccine leads to lung immunopathology on challenge with live virus. In: Human vaccines & immunotherapeutics 12 (9), S. 2351–2356. DOI: 10.1080/21645515.2016.1177688.

Amanat, Fatima; Strohmeier, Shirin; Rathnasinghe, Raveen; Schotsaert, Michael; Coughlan, Lynda; García-Sastre, Adolfo; Krammer, Florian (2021): Introduction of Two Prolines and Removal of the Polybasic Cleavage Site Lead to Higher Efficacy of a Recombinant Spike-Based SARS-CoV-2 Vaccine in the Mouse Model. In: mBio 12 (2). DOI: 10.1128/mBio.02648-20.

Anderson, Evan J.; Rouphael, Nadine G.; Widge, Alicia T.; Jackson, Lisa A.; Roberts, Paul C.; Makhene, Mamodikoe et al. (2020): Safety and Immunogenicity of SARS-CoV-2 mRNA-1273 Vaccine in Older Adults. In: The New England journal of medicine 383 (25), S. 2427–2438. DOI: 10.1056/NEJMoa2028436.

Ang, Carmen (2021): COVID-19 Vaccine Prices: Comparing the U.S. and EU. Visual Capitalist. Online verfügbar unter https://www.visualcapitalist.com/covid-19-vaccine-cost-eu-versus-us/, zuletzt geprüft am 04.04.2023.

Auste, Arne; Mühlebach, Michael D. (2022): Concentrating all helper protein functions on a single entity allows rescue of recombinant measles virus by transfection of just two plasmids. In: The Journal of general virology 103 (11). DOI: 10.1099/jgv.0.001815.

Baden, Lindsey R.; El Sahly, Hana M.; Essink, Brandon; Kotloff, Karen; Frey, Sharon; Novak, Rick et al. (2021): Efficacy and Safety of the mRNA-1273 SARS-CoV-2 Vaccine. In: The New England journal of medicine 384 (5), S. 403–416. DOI: 10.1056/NEJMoa2035389.

Bajénoff, Marc; Germain, Ronald N. (2009): B-cell follicle development remodels the conduit system and allows soluble antigen delivery to follicular dendritic cells. In: Blood 114 (24), S. 4989–4997. DOI: 10.1182/blood-2009-06-229567.

Beigel, John H.; Tomashek, Kay M.; Dodd, Lori E.; Mehta, Aneesh K.; Zingman, Barry S.; Kalil, Andre C. et al. (2020): Remdesivir for the Treatment of Covid-19 - Final Report. In: The New England journal of medicine 383 (19), S. 1813–1826. DOI: 10.1056/NEJMoa2007764.

Beyer, Robert M.; Manica, Andrea; Mora, Camilo (2021): Shifts in global bat diversity suggest a possible role of climate change in the emergence of SARS-CoV-1 and SARS-CoV-2. In: The Science of the total environment 767, S. 145413. DOI: 10.1016/j.scitotenv.2021.145413.

Bilaloglu, Seda; Aphinyanaphongs, Yin; Jones, Simon; Iturrate, Eduardo; Hochman, Judith; Berger, Jeffrey S. (2020): Thrombosis in Hospitalized Patients With COVID-19 in a New York City Health System. In: JAMA 324 (8), S. 799–801. DOI: 10.1001/jama.2020.13372.

Bloyet, Louis-Marie; Schramm, Antoine; Lazert, Carine; Raynal, Bertrand; Hologne, Maggy; Walker, Olivier et al. (2019): Regulation of measles virus gene expression by P protein coiled-coil properties. In: Science advances 5 (5), eaaw3702. DOI: 10.1126/sciadv.aaw3702.

Bolles, Meagan; Deming, Damon; Long, Kristin; Agnihothram, Sudhakar; Whitmore, Alan; Ferris, Martin et al. (2011): A double-inactivated severe acute respiratory syndrome coronavirus vaccine provides incomplete protection in mice and induces increased eosinophilic proinflammatory pulmonary response upon challenge. In: JVI 85 (23), S. 12201–12215. DOI: 10.1128/JVI.06048-11.

Bos, Rinke; Rutten, Lucy; van der Lubbe, Joan E. M.; Bakkers, Mark J. G.; Hardenberg, Gijs; Wegmann, Frank et al. (2020): Ad26 vector-based COVID-19 vaccine encoding a prefusion-

stabilized SARS-CoV-2 Spike immunogen induces potent humoral and cellular immune responses. In: NPJ Vaccines 5, S. 91. DOI: 10.1038/s41541-020-00243-x.

Bourhis, Jean-Marie; Receveur-Bréchot, Véronique; Oglesbee, Michael; Zhang, Xinsheng; Buccellato, Matthew; Darbon, Hervé et al. (2005): The intrinsically disordered C-terminal domain of the measles virus nucleoprotein interacts with the C-terminal domain of the phosphoprotein via two distinct sites and remains predominantly unfolded. In: Protein science : a publication of the Protein Society 14 (8), S. 1975–1992. DOI: 10.1110/ps.051411805.

Brandler, Samantha; Ruffié, Claude; Combredet, Chantal; Brault, Jean-Baptiste; Najburg, Valérie; Prevost, Marie-Christine et al. (2013): A recombinant measles vaccine expressing chikungunya virus-like particles is strongly immunogenic and protects mice from lethal challenge with chikungunya virus. In: Vaccine 31 (36), S. 3718–3725. DOI: 10.1016/j.vaccine.2013.05.086.

Cano, Amanda; Ettcheto, Miren; Chang, Jui-Hsien; Barroso, Emma; Espina, Marta; Kühne, Britta A. et al. (2019): Dual-drug loaded nanoparticles of Epigallocatechin-3-gallate (EGCG)/Ascorbic acid enhance therapeutic efficacy of EGCG in a APPswe/PS1dE9 Alzheimer's disease mice model. In: Journal of controlled release : official journal of the Controlled Release Society 301, S. 62–75. DOI: 10.1016/j.jconrel.2019.03.010.

Carreño, Juan Manuel; Alshammary, Hala; Tcheou, Johnstone; Singh, Gagandeep; Raskin, Ariel J.; Kawabata, Hisaaki et al. (2022): Activity of convalescent and vaccine serum against SARS-CoV-2 Omicron. In: Nature 602 (7898), S. 682–688. DOI: 10.1038/s41586-022-04399-5.

Castilow, Elaine M.; Meyerholz, David K.; Varga, Steven M. (2008): IL-13 is required for eosinophil entry into the lung during respiratory syncytial virus vaccine-enhanced disease. In: Journal of immunology (Baltimore, Md. : 1950) 180 (4), S. 2376–2384. DOI: 10.4049/jimmunol.180.4.2376.

Cathomen, T.; Naim, H. Y.; Cattaneo, R. (1998): Measles viruses with altered envelope protein cytoplasmic tails gain cell fusion competence. In: Journal of virology 72 (2), S. 1224–1234. DOI: 10.1128/jvi.72.2.1224-1234.1998.

Cattaneo, R.; Rebmann, G.; Schmid, A.; Baczko, K.; ter Meulen, V.; Billeter, M. A. (1987): Altered transcription of a defective measles virus genome derived from a diseased human brain. In: The EMBO Journal 6 (3), S. 681–688.

Cele, Sandile; Jackson, Laurelle; Khoury, David S.; Khan, Khadija; Moyo-Gwete, Thandeka; Tegally, Houriiyah et al. (2022): Omicron extensively but incompletely escapes Pfizer BNT162b2 neutralization. In: Nature 602 (7898), S. 654–656. DOI: 10.1038/s41586-021-04387-1.

Chan, Jasper Fuk-Woo; Kok, Kin-Hang; Zhu, Zheng; Chu, Hin; To, Kelvin Kai-Wang; Yuan, Shuofeng; Yuen, Kwok-Yung (2020): Genomic characterization of the 2019 novel human-pathogenic coronavirus isolated from a patient with atypical pneumonia after visiting Wuhan. In: Emerging microbes & infections 9 (1), S. 221–236. DOI: 10.1080/22221751.2020.1719902.

Chatterjee, Srijan; Bhattacharya, Manojit; Nag, Sagnik; Dhama, Kuldeep; Chakraborty, Chiranjib (2023): A Detailed Overview of SARS-CoV-2 Omicron: Its Sub-Variants, Mutations and Pathophysiology, Clinical Characteristics, Immunological Landscape, Immune Escape, and Therapies. In: Viruses 15 (1). DOI: 10.3390/v15010167.

Chen, Ruochan; Huang, Yan; Quan, Jun; Liu, Jiao; Wang, Haichao; Billiar, Timothy R. et al. (2020): HMGB1 as a potential biomarker and therapeutic target for severe COVID-19. In: Heliyon 6 (12), e05672. DOI: 10.1016/j.heliyon.2020.e05672.

Chen, Yuxin; Yin, Shengxia; Tong, Xin; Tao, Yue; Ni, Jun; Pan, Jie et al. (2022): Dynamic SARS-CoV-2-specific B-cell and T-cell responses following immunization with an inactivated COVID-19 vaccine. In: Clinical microbiology and infection : the official publication of the

European Society of Clinical Microbiology and Infectious Diseases 28 (3), S. 410–418. DOI: 10.1016/j.cmi.2021.10.006.

Cheng, Samuel M. S.; Mok, Chris Ka Pun; Leung, Yonna W. Y.; Ng, Susanna S.; Chan, Karl C. K.; Ko, Fanny W. et al. (2022): Neutralizing antibodies against the SARS-CoV-2 Omicron variant BA.1 following homologous and heterologous CoronaVac or BNT162b2 vaccination. In: Nature medicine 28 (3), S. 486–489. DOI: 10.1038/s41591-022-01704-7.

Chiou, Wei-Chung; Chen, Jui-Chieh; Chen, Yun-Ti; Yang, Jinn-Moon; Hwang, Lih-Hwa; Lyu, Yi-Shuan et al. (2021): The inhibitory effects of PGG and EGCG against the SARS-CoV-2 3C-like protease. In: Biochemical and biophysical research communications. DOI: 10.1016/j.bbrc.2020.12.106.

Chourasia, Mukesh; Koppula, Purushotham Reddy; Battu, Aruna; Ouseph, Madhu M.; Singh, Anil K. (2021): EGCG, a Green Tea Catechin, as a Potential Therapeutic Agent for Symptomatic and Asymptomatic SARS-CoV-2 Infection. In: Molecules (Basel, Switzerland) 26 (5). DOI: 10.3390/molecules26051200.

Clausen, Thomas Mandel; Sandoval, Daniel R.; Spliid, Charlotte B.; Pihl, Jessica; Perrett, Hailee R.; Painter, Chelsea D. et al. (2020): SARS-CoV-2 Infection Depends on Cellular Heparan Sulfate and ACE2. In: Cell 183 (4), 1043-1057.e15. DOI: 10.1016/j.cell.2020.09.033.

Colpitts, Che C.; Schang, Luis M. (2014): A small molecule inhibits virion attachment to heparan sulfate- or sialic acid-containing glycans. In: JVI 88 (14), S. 7806–7817. DOI: 10.1128/JVI.00896-14.

Corbett, Kizzmekia S.; Edwards, Darin K.; Leist, Sarah R.; Abiona, Olubukola M.; Boyoglu-Barnum, Seyhan; Gillespie, Rebecca A. et al. (2020): SARS-CoV-2 mRNA vaccine design enabled by prototype pathogen preparedness. In: Nature 586 (7830), S. 567–571. DOI: 10.1038/s41586-020-2622-0.

Cucinotta, Domenico; Vanelli, Maurizio (2020): WHO Declares COVID-19 a Pandemic. In: Acta bio-medica : Atenei Parmensis 91 (1), S. 157–160. DOI: 10.23750/abm.v91i1.9397.

Davis, Hannah E.; McCorkell, Lisa; Vogel, Julia Moore; Topol, Eric J. (2023): Long COVID: major findings, mechanisms and recommendations. In: Nature Reviews. Microbiology, S. 1–14. DOI: 10.1038/s41579-022-00846-2.

Del Valle, Jorge Reyes; Devaux, Patricia; Hodge, Gregory; Wegner, Nicholas J.; McChesney, Michael B.; Cattaneo, Roberto (2007): A vectored measles virus induces hepatitis B surface antigen antibodies while protecting macaques against measles virus challenge. In: Journal of virology 81 (19), S. 10597–10605. DOI: 10.1128/JVI.00923-07.

Denning, Naomi-Liza; Aziz, Monowar; Gurien, Steven D.; Wang, Ping (2019): DAMPs and NETs in Sepsis. In: Frontiers in immunology 10, S. 2536. DOI: 10.3389/fimmu.2019.02536.

Desmyter, Jan; Melnick, Joseph L.; Rawls, William E. (1968): Defectiveness of Interferon Production and of Rubella Virus Interference in a Line of African Green Monkey Kidney Cells (Vero). In: JVI 2 (10), S. 955–961.

Dicks, Matthew D. J.; Spencer, Alexandra J.; Edwards, Nick J.; Wadell, Göran; Bojang, Kalifa; Gilbert, Sarah C. et al. (2012): A novel chimpanzee adenovirus vector with low human seroprevalence: improved systems for vector derivation and comparative immunogenicity. In: PloS one 7 (7), e40385. DOI: 10.1371/journal.pone.0040385.

Dinda, Biswanath; Dinda, Subhajit; Dinda, Manikarna (2023): Therapeutic potential of green tea catechin, (-)-epigallocatechin-3-O-gallate (EGCG) in SARS-CoV-2 infection: Major interactions with host/virus proteases. In: Phytomedicine plus : international journal of phytotherapy and phytopharmacology 3 (1), S. 100402. DOI: 10.1016/j.phyplu.2022.100402.

Dingemans, Jozef; van der Veer, Brian M. J. W.; Gorgels, Koen M. F.; Hackert, Volker; Heijer, Casper D. J. den; Hoebe, Christian J. P. A. et al. (2022): Investigating SARS-CoV-2 breakthrough infections per variant and vaccine type. In: Frontiers in microbiology 13, S. 1027271. DOI: 10.3389/fmicb.2022.1027271.

DiPiazza, Anthony T.; Leist, Sarah R.; Abiona, Olubukola M.; Moliva, Juan I.; Werner, Anne; Minai, Mahnaz et al. (2021): COVID-19 vaccine mRNA-1273 elicits a protective immune

profile in mice that is not associated with vaccine-enhanced disease upon SARS-CoV-2 challenge. In: Immunity 54 (8), 1869-1882.e6. DOI: 10.1016/j.immuni.2021.06.018.

Dörig, Ruth E.; Marcil, Anne; Chopra, Arvind; Richardson, Christopher D. (1993): The human CD46 molecule is a receptor for measles virus (Edmonston strain). In: Cell 75 (2), S. 295–305. DOI: 10.1016/0092-8674(93)80071-l.

Du, Ashuai; Zheng, Rong; Disoma, Cyrollah; Li, Shiqin; Chen, Zongpeng; Li, Sijia et al. (2021): Epigallocatechin-3-gallate, an active ingredient of Traditional Chinese Medicines, inhibits the 3CLpro activity of SARS-CoV-2. In: International journal of biological macromolecules 176, S. 1–12. DOI: 10.1016/j.ijbiomac.2021.02.012.

Dube, Admire; Nicolazzo, Joseph A.; Larson, Ian (2011): Chitosan nanoparticles enhance the plasma exposure of (-)-epigallocatechin gallate in mice through an enhancement in intestinal stability. In: European journal of pharmaceutical sciences : official journal of the European Federation for Pharmaceutical Sciences 44 (3), S. 422–426. DOI: 10.1016/j.ejps.2011.09.004.

Dunkle, Lisa M.; Kotloff, Karen L.; Gay, Cynthia L.; Áñez, Germán; Adelglass, Jeffrey M.; Barrat Hernández, Alejandro Q. et al. (2022): Efficacy and Safety of NVX-CoV2373 in Adults in the United States and Mexico. In: The New England journal of medicine 386 (6), S. 531–543. DOI: 10.1056/NEJMoa2116185.

Durrheim, David N.; Crowcroft, Natasha S.; Strebel, Peter M. (2014): Measles - The epidemiology of elimination. In: Vaccine 32 (51), S. 6880–6883. DOI: 10.1016/j.vaccine.2014.10.061.

Earle, Kristen A.; Ambrosino, Donna M.; Fiore-Gartland, Andrew; Goldblatt, David; Gilbert, Peter B.; Siber, George R. et al. (2021): Evidence for antibody as a protective correlate for COVID-19 vaccines. In: Vaccine 39 (32), S. 4423–4428. DOI: 10.1016/j.vaccine.2021.05.063.

Ebenig, Aileen; Lange, Mona V.; Mühlebach, Michael D. (2022a): Versatility of live-attenuated measles viruses as platform technology for recombinant vaccines. In: NPJ Vaccines 7. DOI: 10.1038/s41541-022-00543-4.

Ebenig, Aileen; Muraleedharan, Samada; Kazmierski, Julia; Todt, Daniel; Auste, Arne; Anzaghe, Martina et al. (2022b): Vaccine-associated enhanced respiratory pathology in COVID-19 hamsters after TH2-biased immunization. In: Cell reports 40 (7), S. 111214. DOI: 10.1016/j.celrep.2022.111214.

Eckerle, Isabella; Müller, Marcel A.; Kallies, Stephan; Gotthardt, Daniel N.; Drosten, Christian (2013): In-vitro renal epithelial cell infection reveals a viral kidney tropism as a potential mechanism for acute renal failure during Middle East Respiratory Syndrome (MERS) Coronavirus infection. In: Virology journal 10, S. 359. DOI: 10.1186/1743-422X-10-359.

ENDERS, J. F.; PEEBLES, T. C. (1954): Propagation in tissue cultures of cytopathogenic agents from patients with measles. In: Proceedings of the Society for Experimental Biology and Medicine. Society for Experimental Biology and Medicine (New York, N.Y.) 86 (2), S. 277–286. DOI: 10.3181/00379727-86-21073.

Escriou, Nicolas; Callendret, Benoît; Lorin, Valérie; Combredet, Chantal; Marianneau, Philippe; Février, Michèle; Tangy, Frédéric (2014): Protection from SARS coronavirus conferred by live measles vaccine expressing the spike glycoprotein. In: Virology 452-453, S. 32–41. DOI: 10.1016/j.virol.2014.01.002.

Europäische Arzneimittel-Agentur (2021a): COVID-19 Vaccine AstraZeneca: benefits still outweigh the risks despite possible link to rare blood clots with low blood platelets. Online verfügbar unter https://www.ema.europa.eu/en/news/covid-19-vaccine-astrazeneca-benefits-still-outweigh-risks-despite-possible-link-rare-blood-clots, zuletzt geprüft am 04.04.2023.

Europäische Arzneimittel-Agentur (2021b): COVID-19 Vaccine AstraZeneca: PRAC investigating cases of thromboembolic events - vaccine’s benefits currently still outweigh

risks - Update. Online verfügbar unter https://www.ema.europa.eu/en/news/covid-19-vaccine-astrazeneca-prac-investigating-cases-thromboembolic-events-vaccines-benefits, zuletzt geprüft am 04.04.2023.

Europäische Arzneimittel-Agentur (2021c): COVID-19 Vaccine AstraZeneca: PRAC preliminary view suggests no specific issue with batch used in Austria. Online verfügbar unter https://www.ema.europa.eu/en/news/covid-19-vaccine-astrazeneca-prac-preliminary-view-suggests-no-specific-issue-batch-used-austria, zuletzt geprüft am 04.04.2023.

Europäische Arzneimittel-Agentur (2021d): COVID-19 Vaccine Janssen: EMA recommendation on booster dose. Online verfügbar unter https://www.ema.europa.eu/en/news/covid-19-vaccine-janssen-ema-recommendation-booster-dose, zuletzt geprüft am 04.04.2023.

Europäische Arzneimittel-Agentur (2023a): Comirnaty. Online verfügbar unter https://www.ema.europa.eu/en/medicines/human/EPAR/comirnaty, zuletzt geprüft am 18.01.2023.

Europäische Arzneimittel-Agentur (2023b): COVID-19 treatments: authorised. Online verfügbar unter https://www.ema.europa.eu/en/human-regulatory/overview/public-health-threats/coronavirus-disease-covid-19/treatments-vaccines/treatments-covid-19/covid-19-treatments-authorised.

Europäische Arzneimittel-Agentur (2023c): COVID-19 Vaccine (inactivated, adjuvanted) Valneva. Online verfügbar unter https://www.ema.europa.eu/en/medicines/human/EPAR/covid-19-vaccine-inactivated-adjuvanted-valneva, zuletzt geprüft am 28.01.2023.

Europäische Arzneimittel-Agentur (2023d): COVID-19 Vaccine Janssen. Online verfügbar unter https://www.ema.europa.eu/en/medicines/human/EPAR/covid-19-vaccine-janssen, zuletzt geprüft am 26.03.2023.

Europäische Arzneimittel-Agentur (2023e): COVID-19 Vaccine Moderna. Online verfügbar unter https://www.ema.europa.eu/en/medicines/human/EPAR/covid-19-vaccine-moderna, zuletzt geprüft am 26.03.2023.

Europäische Arzneimittel-Agentur (2023f): COVID-19 vaccines. Online verfügbar unter https://www.ema.europa.eu/en/human-regulatory/overview/public-health-threats/coronavirus-disease-covid-19/treatments-vaccines/covid-19-vaccines, zuletzt geprüft am 18.01.2023.

Europäische Arzneimittel-Agentur (2023g): EMA recommends approval of VidPrevtyn Beta as a COVID 19 booster vaccine. Online verfügbar unter https://www.ema.europa.eu/en/news/ema-recommends-approval-vidprevtyn-beta-covid-19-booster-vaccine, zuletzt geprüft am 29.01.2023.

Europäische Arzneimittel-Agentur (2023h): Nuvaxovid. Online verfügbar unter https://www.ema.europa.eu/en/medicines/human/EPAR/nuvaxovid, zuletzt geprüft am 28.01.2023.

Europäische Arzneimittel-Agentur (2023i): Nuvaxovid : EPAR - Product information. Online verfügbar unter https://www.ema.europa.eu/documents/product-information/nuvaxovid-epar-product-information_en.pdf, zuletzt geprüft am 04.03.2023.

Europäische Arzneimittel-Agentur (2023j): Vaxzevria (previously COVID-19 Vaccine AstraZeneca). Online verfügbar unter https://www.ema.europa.eu/en/medicines/human/EPAR/vaxzevria-previously-covid-19-vaccine-astrazeneca, zuletzt geprüft am 26.03.2023.

Europäische Arzneimittel-Agentur (2023k): VidPrevtyn Beta. Online verfügbar unter https://www.ema.europa.eu/en/medicines/human/EPAR/vidprevtyn-beta, zuletzt geprüft am 28.01.2023.

Europäische Arzneimittel-Agentur (2023l): VidPrevtyn Beta : EPAR - Risk-management-plan. Online verfügbar unter https://www.ema.europa.eu/documents/rmp-summary/vidprevtyn-beta-epar-risk-management-plan_en.pdf, zuletzt geprüft am 04.03.2023.

European Centre for Disease Prevention and Control (2023): Total vaccines doses distributed to EU Member States by vaccine product as of 2023-03-23. Online verfügbar unter https://vaccinetracker.ecdc.europa.eu/public/extensions/COVID-19/vaccine-tracker.html#distribution-tab, zuletzt aktualisiert am 23.03.2023, zuletzt geprüft am 04.04.2023.

Feng, Shuo; Phillips, Daniel J.; White, Thomas; Sayal, Homesh; Aley, Parvinder K.; Bibi, Sagida et al. (2021): Correlates of protection against symptomatic and asymptomatic SARS-CoV-2 infection. In: Nature medicine 27 (11), S. 2032–2040. DOI: 10.1038/s41591-021-01540-1.

Fidler, David P. (2004): Germs, governance, and global public health in the wake of SARS. In: The Journal of clinical investigation 113 (6), S. 799–804. DOI: 10.1172/JCI21328.

Fisher, Dale; Heymann, David (2020): Q&A: The novel coronavirus outbreak causing COVID-19. In: BMC medicine 18 (1), S. 57. DOI: 10.1186/s12916-020-01533-w.

Folegatti, Pedro M.; Ewer, Katie J.; Aley, Parvinder K.; Angus, Brian; Becker, Stephan; Belij-Rammerstorfer, Sandra et al. (2020): Safety and immunogenicity of the ChAdOx1 nCoV-19 vaccine against SARS-CoV-2: a preliminary report of a phase 1/2, single-blind, randomised controlled trial. In: The Lancet 396 (10249), S. 467–478. DOI: 10.1016/S0140-6736(20)31604-4.

Frantz, Phanramphoei N.; Barinov, Aleksandr; Ruffié, Claude; Combredet, Chantal; Najburg, Valérie; Melo, Guilherme Dias de et al. (2021): A live measles-vectored COVID-19 vaccine induces strong immunity and protection from SARS-CoV-2 challenge in mice and hamsters. In: Nature communications 12 (1), S. 6277. DOI: 10.1038/s41467-021-26506-2.

Gandhi, Shiv; Klein, Jonathan; Robertson, Alexander J.; Peña-Hernández, Mario A.; Lin, Michelle J.; Roychoudhury, Pavitra et al. (2022): De novo emergence of a remdesivir

resistance mutation during treatment of persistent SARS-CoV-2 infection in an immunocompromised patient: a case report. In: Nature communications 13 (1), S. 1547. DOI: 10.1038/s41467-022-29104-y.

Gao, Bo; Gong, Xiaoqian; Fang, Shouguo; Weng, Wenlian; Wang, Huan; Chu, Hongyan et al. (2021): Inhibition of anti-viral stress granule formation by coronavirus endoribonuclease nsp15 ensures efficient virus replication. In: PLoS pathogens 17 (2), e1008690. DOI: 10.1371/journal.ppat.1008690.

Gartlan, Cillian; Tipton, Tom; Salguero, Francisco J.; Sattentau, Quentin; Gorringe, Andrew; Carroll, Miles W. (2022): Vaccine-Associated Enhanced Disease and Pathogenic Human Coronaviruses. In: Frontiers in immunology 13, S. 882972. DOI: 10.3389/fimmu.2022.882972.

Gilbert, Peter B.; Montefiori, David C.; McDermott, Adrian B.; Fong, Youyi; Benkeser, David; Deng, Weiping et al. (2022): Immune correlates analysis of the mRNA-1273 COVID-19 vaccine efficacy clinical trial. In: Science (New York, N.Y.) 375 (6576), S. 43–50. DOI: 10.1126/science.abm3425.

Goldblatt, David; Alter, Galit; Crotty, Shane; Plotkin, Stanley A. (2022): Correlates of protection against SARS-CoV-2 infection and COVID-19 disease. In: Immunological reviews 310 (1), S. 6–26. DOI: 10.1111/imr.13091.

Greinacher, Andreas; Thiele, Thomas; Warkentin, Theodore E.; Weisser, Karin; Kyrle, Paul A.; Eichinger, Sabine (2021): Thrombotic Thrombocytopenia after ChAdOx1 nCov-19 Vaccination. In: The New England journal of medicine 384 (22), S. 2092–2101. DOI: 10.1056/NEJMoa2104840.

Griffin, Diane E. (2018): Measles Vaccine. In: Viral immunology 31 (2), S. 86–95. DOI: 10.1089/vim.2017.0143.

Grifoni, Alba; Sidney, John; Zhang, Yun; Scheuermann, Richard H.; Peters, Bjoern; Sette, Alessandro (2020): A Sequence Homology and Bioinformatic Approach Can Predict

Candidate Targets for Immune Responses to SARS-CoV-2. In: Cell host & microbe 27 (4), 671-680.e2. DOI: 10.1016/j.chom.2020.03.002.

Guryanov, Sergey G.; Liljeroos, Lassi; Kasaragod, Prasad; Kajander, Tommi; Butcher, Sarah J. (2015): Crystal Structure of the Measles Virus Nucleoprotein Core in Complex with an N-Terminal Region of Phosphoprotein. In: JVI 90 (6), S. 2849–2857. DOI: 10.1128/JVI.02865-15.

Guseva, Serafima; Milles, Sigrid; Jensen, Malene Ringkjøbing; Salvi, Nicola; Kleman, Jean-Philippe; Maurin, Damien et al. (2020): Measles virus nucleo- and phosphoproteins form liquid-like phase-separated compartments that promote nucleocapsid assembly. In: Science advances 6 (14), eaaz7095. DOI: 10.1126/sciadv.aaz7095.

Hackbart, Matthew; Deng, Xufang; Baker, Susan C. (2020): Coronavirus endoribonuclease targets viral polyuridine sequences to evade activating host sensors. In: Proceedings of the National Academy of Sciences of the United States of America 117 (14), S. 8094–8103. DOI: 10.1073/pnas.1921485117.

Heath, Paul T.; Galiza, Eva P.; Baxter, David N.; Boffito, Marta; Browne, Duncan; Burns, Fiona et al. (2021): Safety and Efficacy of NVX-CoV2373 Covid-19 Vaccine. In: The New England journal of medicine 385 (13), S. 1172–1183. DOI: 10.1056/NEJMoa2107659.

Heinrich, Bianca S.; Cureton, David K.; Rahmeh, Amal A.; Whelan, Sean P. J. (2010): Protein expression redirects vesicular stomatitis virus RNA synthesis to cytoplasmic inclusions. In: PLoS pathogens 6 (6), e1000958. DOI: 10.1371/journal.ppat.1000958.

Henss, Lisa; Auste, Arne; Schürmann, Christoph; Schmidt, Christin; Rhein, Christine von; Mühlebach, Michael D.; Schnierle, Barbara S. (2021): The green tea catechin epigallocatechin gallate inhibits SARS-CoV-2 infection. In: The Journal of general virology 102 (4). DOI: 10.1099/jgv.0.001574.

Hoffmann, Markus; Krüger, Nadine; Schulz, Sebastian; Cossmann, Anne; Rocha, Cheila; Kempf, Amy et al. (2022): The Omicron variant is highly resistant against antibody-

mediated neutralization: Implications for control of the COVID-19 pandemic. In: Cell 185 (3), 447-456.e11. DOI: 10.1016/j.cell.2021.12.032.

Hogan, John I.; Duerr, Ralf; Dimartino, Dacia; Marier, Christian; Hochman, Sarah E.; Mehta, Sapna et al. (2022): Remdesivir resistance in transplant recipients with persistent COVID-19. In: Clinical infectious diseases : an official publication of the Infectious Diseases Society of America. DOI: 10.1093/cid/ciac769.

Honda-Okubo, Yoshikazu; Barnard, Dale; Ong, Chun Hao; Peng, Bi-Hung; Tseng, Chien-Te Kent; Petrovsky, Nikolai (2015): Severe acute respiratory syndrome-associated coronavirus vaccines formulated with delta inulin adjuvants provide enhanced protection while ameliorating lung eosinophilic immunopathology. In: JVI 89 (6), S. 2995–3007. DOI: 10.1128/JVI.02980-14.

Hong, Seokho; Seo, Sang Hwan; Woo, Sun-Je; Kwon, Yonghoon; Song, Manki; Ha, Nam-Chul (2021): Epigallocatechin Gallate Inhibits the Uridylate-Specific Endoribonuclease Nsp15 and Efficiently Neutralizes the SARS-CoV-2 Strain. In: Journal of agricultural and food chemistry 69 (21), S. 5948–5954. DOI: 10.1021/acs.jafc.1c02050.

Hörner, Cindy; Fiedler, Anna H.; Bodmer, Bianca S.; Walz, Lisa; Scheuplein, Vivian A.; Hutzler, Stefan et al. (2023): A protective measles virus-derived vaccine inducing long-lasting immune responses against influenza A virus H7N9. In: NPJ Vaccines 8 (1), S. 46. DOI: 10.1038/s41541-023-00643-9.

Hörner, Cindy; Schürmann, Christoph; Auste, Arne; Ebenig, Aileen; Muraleedharan, Samada; Dinnon, Kenneth H. et al. (2020): A highly immunogenic and effective measles virus-based Th1-biased COVID-19 vaccine. In: Proceedings of the National Academy of Sciences of the United States of America. DOI: 10.1073/pnas.2014468117.

Hsieh, Ching-Lin; Goldsmith, Jory A.; Schaub, Jeffrey M.; DiVenere, Andrea M.; Kuo, Hung-Che; Javanmardi, Kamyab et al. (2020): Structure-based design of prefusion-stabilized

SARS-CoV-2 spikes. In: Science (New York, N.Y.) 369 (6510), S. 1501–1505. DOI: 10.1126/science.abd0826.

Hu, Ben; Guo, Hua; Zhou, Peng; Shi, Zheng-Li (2020): Characteristics of SARS-CoV-2 and COVID-19. In: Nature Reviews. Microbiology, S. 1–14. DOI: 10.1038/s41579-020-00459-7.

Hu, Biying; Huang, Shaoying; Yin, Lianghong (2021): The cytokine storm and COVID-19. In: Journal of medical virology 93 (1), S. 250–256. DOI: 10.1002/jmv.26232.

Huan, Changchao; Xu, Weiyin; Guo, Tingting; Pan, Haochun; Zou, Hengyue; Jiang, Luyao et al. (2020): (-)-Epigallocatechin-3-Gallate Inhibits the Life Cycle of Pseudorabies Virus In Vitro and Protects Mice Against Fatal Infection. In: Frontiers in cellular and infection microbiology 10, S. 616895. DOI: 10.3389/fcimb.2020.616895.

Hung, Sze Wan; Liang, Bo; Gao, Yating; Zhang, Ruizhe; Tan, Zhouyurong; Zhang, Tao et al. (2021): An In-Silico, In-Vitro and In-Vivo Combined Approach to Identify NMNATs as Potential Protein Targets of ProEGCG for Treatment of Endometriosis. In: Frontiers in pharmacology 12, S. 714790. DOI: 10.3389/fphar.2021.714790.

Iankov, Ianko D.; Federspiel, Mark J.; Galanis, Evanthia (2013): Measles virus expressed Helicobacter pylori neutrophil-activating protein significantly enhances the immunogenicity of poor immunogens. In: Vaccine 31 (42), S. 4795–4801. DOI: 10.1016/j.vaccine.2013.07.085.

Iwata-Yoshikawa, Naoko; Shiwa, Nozomi; Sekizuka, Tsuyoshi; Sano, Kaori; Ainai, Akira; Hemmi, Takuya et al. (2022): A lethal mouse model for evaluating vaccine-associated enhanced respiratory disease during SARS-CoV-2 infection. In: Science advances 8 (1), eabh3827. DOI: 10.1126/sciadv.abh3827.

Iwata-Yoshikawa, Naoko; Uda, Akihiko; Suzuki, Tadaki; Tsunetsugu-Yokota, Yasuko; Sato, Yuko; Morikawa, Shigeru et al. (2014): Effects of Toll-like receptor stimulation on eosinophilic infiltration in lungs of BALB/c mice immunized with UV-inactivated severe

acute respiratory syndrome-related coronavirus vaccine. In: JVI 88 (15), S. 8597–8614. DOI: 10.1128/JVI.00983-14.

Jackson, Lisa A.; Anderson, Evan J.; Rouphael, Nadine G.; Roberts, Paul C.; Makhene, Mamodikoe; Coler, Rhea N. et al. (2020): An mRNA Vaccine against SARS-CoV-2 - Preliminary Report. In: The New England journal of medicine 383 (20), S. 1920–1931. DOI: 10.1056/NEJMoa2022483.

Jaggaiahgari, Shashidhar; Munigela, Apoorva; Mitnala, Sasikala; Gujjarlapudi, Deepika; Simhadri, Venu; D, Nageshwar Reddy (2022): Heterologous Booster Dose with CORBEVAX following Primary Vaccination with COVISHIELD Enhances Protection against SARS-CoV-2. In: Vaccines 10 (12). DOI: 10.3390/vaccines10122146.

Jang, Minsu; Park, Rackhyun; Park, Yea-In; Cha, Yeo-Eun; Yamamoto, Ayane; Lee, Jin I.; Park, Junsoo (2021): EGCG, a green tea polyphenol, inhibits human coronavirus replication in vitro. In: Biochemical and biophysical research communications 547, S. 23–28. DOI: 10.1016/j.bbrc.2021.02.016.

Jang, Minsu; Park, Yea-In; Cha, Yeo-Eun; Park, Rackhyun; Namkoong, Sim; Lee, Jin I.; Park, Junsoo (2020): Tea Polyphenols EGCG and Theaflavin Inhibit the Activity of SARS-CoV-2 3CL-Protease In Vitro. In: Evidence-based complementary and alternative medicine : eCAM 2020, S. 5630838. DOI: 10.1155/2020/5630838.

Johns Hopkins University (2023): COVID-19 Dashboard. Online verfügbar unter https://www.arcgis.com/apps/dashboards/bda7594740fd40299423467b48e9ecf6.

Johnson, Bryan A.; Xie, Xuping; Bailey, Adam L.; Kalveram, Birte; Lokugamage, Kumari G.; Muruato, Antonio et al. (2021): Loss of furin cleavage site attenuates SARS-CoV-2 pathogenesis. In: Nature 591 (7849), S. 293–299. DOI: 10.1038/s41586-021-03237-4.

Johnson, T. R.; Graham, B. S. (1999): Secreted respiratory syncytial virus G glycoprotein induces interleukin-5 (IL-5), IL-13, and eosinophilia by an IL-4-independent mechanism. In: Journal of virology 73 (10), S. 8485–8495. DOI: 10.1128/jvi.73.10.8485-8495.1999.

Jones, Kate E.; Patel, Nikkita G.; Levy, Marc A.; Storeygard, Adam; Balk, Deborah; Gittleman, John L.; Daszak, Peter (2008): Global trends in emerging infectious diseases. In: Nature 451 (7181), S. 990–993. DOI: 10.1038/nature06536.

Joseph, Jeswin; Karthika, T.; Das, V. R. Akshay; Raj, V. Stalin (2021): Epigallocatechin-3-gallate (EGCG): a potential molecule for the development of therapeutics against emerging SARS-CoV-1, MERS-CoV and SARS-CoV-2 coronaviruses. In: Journal of global antimicrobial resistance. DOI: 10.1016/j.jgar.2021.05.005.

Kalnin, Kirill V.; Plitnik, Timothy; Kishko, Michael; Zhang, Jinrong; Zhang, Donghui; Beauvais, Adrien et al. (2021): Immunogenicity and efficacy of mRNA COVID-19 vaccine MRT5500 in preclinical animal models. In: NPJ Vaccines 6 (1), S. 61. DOI: 10.1038/s41541-021-00324-5.

Karlin, David; Ferron, François; Canard, Bruno; Longhi, Sonia (2003): Structural disorder and modular organization in Paramyxovirinae N and P. In: The Journal of general virology 84 (Pt 12), S. 3239–3252. DOI: 10.1099/vir.0.19451-0.

KATZ, S. L.; KEMPE, C. H.; BLACK, F. L.; LEPOW, M. L.; KRUGMAN, S.; HAGGERTY, R. J.; ENDERS, J. F. (1960): Studies on an attenuated measles-virus vaccine. VIII. General summary and evaluation of the results of vaccine. In: The New England journal of medicine 263, S. 180–184. DOI: 10.1056/NEJM196007282630408.

Kawall, Anasha; Lewis, Devin S. M.; Sharma, Avini; Chavada, Krishna; Deshmukh, Rahul; Rayalam, Srujana et al. (2022): Inhibitory effect of phytochemicals towards SARS-CoV-2 papain like protease (PLpro) proteolytic and deubiquitinase activity. In: Frontiers in chemistry 10, S. 1100460. DOI: 10.3389/fchem.2022.1100460.

Kearns, Fiona L.; Sandoval, Daniel R.; Casalino, Lorenzo; Clausen, Thomas M.; Rosenfeld, Mia A.; Spliid, Charlotte B. et al. (2022): Spike-heparan sulfate interactions in SARS-CoV-2 infection. In: Current opinion in structural biology 76, S. 102439. DOI: 10.1016/j.sbi.2022.102439.

Khan, Naghma; Afaq, Farrukh; Saleem, Mohammad; Ahmad, Nihal; Mukhtar, Hasan (2006): Targeting multiple signaling pathways by green tea polyphenol (-)-epigallocatechin-3-gallate. In: Cancer research 66 (5), S. 2500–2505. DOI: 10.1158/0008-5472.CAN-05-3636.

Khoury, David S.; Cromer, Deborah; Reynaldi, Arnold; Schlub, Timothy E.; Wheatley, Adam K.; Juno, Jennifer A. et al. (2021): Neutralizing antibody levels are highly predictive of immune protection from symptomatic SARS-CoV-2 infection. In: Nature medicine 27 (7), S. 1205–1211. DOI: 10.1038/s41591-021-01377-8.

Kim, H. W.; Canchola, J. G.; Brandt, C. D.; Pyles, G.; Chanock, R. M.; Jensen, K.; Parrott, R. H. (1969): Respiratory syncytial virus disease in infants despite prior administration of antigenic inactivated vaccine. In: American journal of epidemiology 89 (4), S. 422–434. DOI: 10.1093/oxfordjournals.aje.a120955.

Kim, You-Me; Shin, Eui-Cheol (2021): Type I and III interferon responses in SARS-CoV-2 infection. In: Experimental & molecular medicine 53 (5), S. 750–760. DOI: 10.1038/s12276-021-00592-0.

Klemm, Theresa; Ebert, Gregor; Calleja, Dale J.; Allison, Cody C.; Richardson, Lachlan W.; Bernardini, Jonathan P. et al. (2020): Mechanism and inhibition of the papain-like protease, PLpro, of SARS-CoV-2. In: The EMBO Journal 39 (18), e106275. DOI: 10.15252/embj.2020106275.

Krishnan, Arunkumar; Hamilton, James P.; Alqahtani, Saleh A.; Woreta, Tinsay A. (2021): COVID-19: An overview and a clinical update. In: World journal of clinical cases 9 (1), S. 8–23. DOI: 10.12998/wjcc.v9.i1.8.

Kwak, Hye Won; Park, Hyo-Jung; Jung, Seo-Yeon; Oh, Eun Young; Park, Sang-In; Kim, Yeonhwa et al. (2023): Recombinant measles virus encoding the spike protein of SARS-CoV-2 efficiently induces Th1 responses and neutralizing antibodies that block SARS-CoV-2 variants. In: Vaccine 41 (11), S. 1892–1901. DOI: 10.1016/j.vaccine.2023.02.005.

Ladner, Jason T.; Henson, Sierra N.; Boyle, Annalee S.; Engelbrektson, Anna L.; Fink, Zane W.; Rahee, Fatima et al. (2021): Epitope-resolved profiling of the SARS-CoV-2 antibody response identifies cross-reactivity with endemic human coronaviruses. In: Cell reports. Medicine 2 (1), S. 100189. DOI: 10.1016/j.xcrm.2020.100189.

Lahaye, Xavier; Vidy, Aurore; Pomier, Carole; Obiang, Linda; Harper, Francis; Gaudin, Yves; Blondel, Danielle (2009): Functional characterization of Negri bodies (NBs) in rabies virus-infected cells: Evidence that NBs are sites of viral transcription and replication. In: JVI 83 (16), S. 7948–7958. DOI: 10.1128/JVI.00554-09.

Lai, Yu-Heng; Sun, Cheng-Pu; Huang, Hsiu-Chen; Chen, Jui-Chieh; Liu, Hui-Kang; Huang, Cheng (2018): Epigallocatechin gallate inhibits hepatitis B virus infection in human liver chimeric mice. In: BMC complementary and alternative medicine 18 (1), S. 248. DOI: 10.1186/s12906-018-2316-4.

Lam, Wai Har; Kazi, Aslamuzzaman; Kuhn, Deborah J.; Chow, Larry M. C.; Chan, Albert S. C.; Dou, Q. Ping; Chan, Tak Hang (2004): A potential prodrug for a green tea polyphenol proteasome inhibitor: evaluation of the peracetate ester of (-)-epigallocatechin gallate (-)-EGCG. In: Bioorganic & medicinal chemistry 12 (21), S. 5587–5593. DOI: 10.1016/j.bmc.2004.08.002.

Lamb, Yvette N. (2021): BNT162b2 mRNA COVID-19 Vaccine: First Approval. In: Drugs 81 (4), S. 495–501. DOI: 10.1007/s40265-021-01480-7.

Lang, Jianshe; Yang, Ning; Deng, Jiejie; Liu, Kangtai; Yang, Peng; Zhang, Guigen; Jiang, Chengyu (2011): Inhibition of SARS pseudovirus cell entry by lactoferrin binding to heparan sulfate proteoglycans. In: PloS one 6 (8), e23710. DOI: 10.1371/journal.pone.0023710.

Launay, Odile; Artaud, Cécile; Lachâtre, Marie; Ait-Ahmed, Mohand; Klein, Jelle; Luong Nguyen, Liem Binh et al. (2022): Safety and immunogenicity of a measles-vectored SARS-CoV-2 vaccine candidate, V591 / TMV-083, in healthy adults: results of a randomized,

placebo-controlled Phase I study. In: EBioMedicine 75, S. 103810. DOI: 10.1016/j.ebiom.2021.103810.

Lazarus, Rajeka; Querton, Benedicte; Corbic Ramljak, Irena; Dewasthaly, Shailesh; Jaramillo, Juan Carlos; Dubischar, Katrin et al. (2022): Immunogenicity and safety of an inactivated whole-virus COVID-19 vaccine (VLA2001) compared with the adenoviral vector vaccine ChAdOx1-S in adults in the UK (COV-COMPARE): interim analysis of a randomised, controlled, phase 3, immunobridging trial. In: The Lancet. Infectious diseases 22 (12), S. 1716–1727. DOI: 10.1016/S1473-3099(22)00502-3.

LeBlanc, Emmanuelle V.; Colpitts, Che C. (2022): The green tea catechin EGCG provides proof-of-concept for a pan-coronavirus attachment inhibitor. In: Scientific reports 12 (1), S. 12899. DOI: 10.1038/s41598-022-17088-0.

Lee, Eunok; Sandgren, Kerrie; Duette, Gabriel; Stylianou, Vicki V.; Khanna, Rajiv; Eden, John-Sebastian et al. (2021): Identification of SARS-CoV-2 Nucleocapsid and Spike T-Cell Epitopes for Assessing T-Cell Immunity. In: JVI 95 (6). DOI: 10.1128/JVI.02002-20.

Lei, Sibei; Chen, Xiaohua; Wu, Jieping; Duan, Xingmei; Men, Ke (2022): Small molecules in the treatment of COVID-19. In: Signal transduction and targeted therapy 7 (1), S. 387. DOI: 10.1038/s41392-022-01249-8.

Letarov, A. V.; Londer, Y. Y.; Boudko, S. P.; Mesyanzhinov, V. V. (1999): The carboxy-terminal domain initiates trimerization of bacteriophage T4 fibritin. In: Biochemistry. Biokhimiia 64 (7), S. 817–823.

Levin, Andrew T.; Owusu-Boaitey, Nana; Pugh, Sierra; Fosdick, Bailey K.; Zwi, Anthony B.; Malani, Anup et al. (2022): Assessing the burden of COVID-19 in developing countries: systematic review, meta-analysis and public policy implications. In: BMJ global health 7 (5). DOI: 10.1136/bmjgh-2022-008477.

Li, Wei; Ashok, Mala; Li, Jianhua; Yang, Huan; Sama, Andrew E.; Wang, Haichao (2007): A major ingredient of green tea rescues mice from lethal sepsis partly by inhibiting HMGB1. In: PloS one 2 (11), e1153. DOI: 10.1371/journal.pone.0001153.

Lin, Wen-Hsuan W.; Pan, Chien-Hsiung; Adams, Robert J.; Laube, Beth L.; Griffin, Diane E. (2014): Vaccine-induced measles virus-specific T cells do not prevent infection or disease but facilitate subsequent clearance of viral RNA. In: mBio 5 (2), e01047. DOI: 10.1128/mbio.01047-14.

Liniger, Matthias; Zuniga, Armando; Tamin, Azaibi; Azzouz-Morin, Teldja N.; Knuchel, Marlyse; Marty, Rene R. et al. (2008): Induction of neutralising antibodies and cellular immune responses against SARS coronavirus by recombinant measles viruses. In: Vaccine 26 (17), S. 2164–2174. DOI: 10.1016/j.vaccine.2008.01.057.

Liu, Jinbiao; Bodnar, Brittany H.; Meng, Fengzhen; Khan, Adil I.; Wang, Xu; Saribas, Sami et al. (2021a): Epigallocatechin gallate from green tea effectively blocks infection of SARS-CoV-2 and new variants by inhibiting spike binding to ACE2 receptor. In: Cell & bioscience 11 (1), S. 168. DOI: 10.1186/s13578-021-00680-8.

Liu, Jinyan; Chandrashekar, Abishek; Sellers, Daniel; Barrett, Julia; Jacob-Dolan, Catherine; Lifton, Michelle et al. (2022a): Vaccines elicit highly conserved cellular immunity to SARS-CoV-2 Omicron. In: Nature 603 (7901), S. 493–496. DOI: 10.1038/s41586-022-04465-y.

Liu, Lihong; Iketani, Sho; Guo, Yicheng; Chan, Jasper F-W; Wang, Maple; Liu, Liyuan et al. (2022b): Striking antibody evasion manifested by the Omicron variant of SARS-CoV-2. In: Nature 602 (7898), S. 676–681. DOI: 10.1038/s41586-021-04388-0.

Liu, Lin; Chopra, Pradeep; Li, Xiuru; Bouwman, Kim M.; Tompkins, Stephen Mark; Wolfert, Margreet A. et al. (2021b): Heparan sulfate proteoglycans as attachment factor for SARS-CoV-2. In: bioRxiv : the preprint server for biology. DOI: 10.1101/2020.05.10.087288.

Logunov, Denis Y.; Dolzhikova, Inna V.; Shcheblyakov, Dmitry V.; Tukhvatulin, Amir I.; Zubkova, Olga V.; Dzharullaeva, Alina S. et al. (2021): Safety and efficacy of an rAd26 and

rAd5 vector-based heterologous prime-boost COVID-19 vaccine: an interim analysis of a randomised controlled phase 3 trial in Russia. In: Lancet (London, England) 397 (10275), S. 671–681. DOI: 10.1016/S0140-6736(21)00234-8.

Logunov, Denis Y.; Dolzhikova, Inna V.; Zubkova, Olga V.; Tukhvatulin, Amir I.; Shcheblyakov, Dmitry V.; Dzharullaeva, Alina S. et al. (2020): Safety and immunogenicity of an rAd26 and rAd5 vector-based heterologous prime-boost COVID-19 vaccine in two formulations: two open, non-randomised phase 1/2 studies from Russia. In: The Lancet 396 (10255), S. 887–897. DOI: 10.1016/S0140-6736(20)31866-3.

Long, Brit; Carius, Brandon M.; Chavez, Summer; Liang, Stephen Y.; Brady, William J.; Koyfman, Alex; Gottlieb, Michael (2022): Clinical update on COVID-19 for the emergency clinician: Presentation and evaluation. In: The American journal of emergency medicine 54, S. 46–57. DOI: 10.1016/j.ajem.2022.01.028.

Lorin, Clarisse; Mollet, Lucile; Delebecque, Frédéric; Combredet, Chantal; Hurtrel, Bruno; Charneau, Pierre et al. (2004): A single injection of recombinant measles virus vaccines expressing human immunodeficiency virus (HIV) type 1 clade B envelope glycoproteins induces neutralizing antibodies and cellular immune responses to HIV. In: Journal of virology 78 (1), S. 146–157. DOI: 10.1128/jvi.78.1.146-157.2004.

Lu, Mijia; Dravid, Piyush; Zhang, Yuexiu; Trivedi, Sheetal; Li, Anzhong; Harder, Olivia et al. (2021a): A safe and highly efficacious measles virus-based vaccine expressing SARS-CoV-2 stabilized prefusion spike. In: Proceedings of the National Academy of Sciences of the United States of America 118 (12). DOI: 10.1073/pnas.2026153118.

Lu, Shuai; Xie, Xi-Xiu; Zhao, Lei; Wang, Bin; Zhu, Jie; Yang, Ting-Rui et al. (2021b): The immunodominant and neutralization linear epitopes for SARS-CoV-2. In: Cell reports 34 (4), S. 108666. DOI: 10.1016/j.celrep.2020.108666.

Makino, S.; Sasaki, K.; Nakagawa, M.; Saito, M.; Shinohara, Y. (1977): Isolation and biological characterization of a measles virus-like agent from the brain of an autopsied case of

subacute sclerosing panencephalitis (SSPE). In: Microbiology and immunology 21 (4), S. 193–205. DOI: 10.1111/j.1348-0421.1977.tb00281.x.

Malczyk, Anna H.; Kupke, Alexandra; Prüfer, Steffen; Scheuplein, Vivian A.; Hutzler, Stefan; Kreuz, Dorothea et al. (2015): A Highly Immunogenic and Protective Middle East Respiratory Syndrome Coronavirus Vaccine Based on a Recombinant Measles Virus Vaccine Platform. In: JVI 89 (22), S. 11654–11667. DOI: 10.1128/JVI.01815-15.

Martin, Arnold; Staeheli, Peter; Schneider, Urs (2006): RNA polymerase II-controlled expression of antigenomic RNA enhances the rescue efficacies of two different members of the Mononegavirales independently of the site of viral genome replication. In: Journal of virology 80 (12), S. 5708–5715. DOI: 10.1128/JVI.02389-05.

McCarthy, Michael (2002): A brief history of the World Health Organization. In: The Lancet 360 (9340), S. 1111–1112. DOI: 10.1016/S0140-6736(02)11244-X.

McGill COVID19 Vaccine Tracker Team (2023): COVID-19 Vaccine Tracker. Online verfügbar unter https://covid19.trackvaccines.org/, zuletzt aktualisiert am 04.03.2023, zuletzt geprüft am 04.04.2023.

McMahan, Katherine; Yu, Jingyou; Mercado, Noe B.; Loos, Carolin; Tostanoski, Lisa H.; Chandrashekar, Abishek et al. (2021): Correlates of protection against SARS-CoV-2 in rhesus macaques. In: Nature 590 (7847), S. 630–634. DOI: 10.1038/s41586-020-03041-6.

McMichael, Anthony J. (2001): Human frontiers, environments, and disease. Past patterns, uncertain futures. Cambridge, New York: Cambridge University Press. Online verfügbar unter http://site.ebrary.com/lib/academiccompletetitles/home.action.

Mercado, Noe B.; Zahn, Roland; Wegmann, Frank; Loos, Carolin; Chandrashekar, Abishek; Yu, Jingyou et al. (2020): Single-Shot Ad26 Vaccine Protects Against SARS-CoV-2 in Rhesus Macaques. In: Nature 586 (7830), S. 583–588. DOI: 10.1038/s41586-020-2607-z.

Mhatre, Susmit; Naik, Shivraj; Patravale, Vandana (2021): A molecular docking study of EGCG and theaflavin digallate with the druggable targets of SARS-CoV-2. In: Computers in biology and medicine 129, S. 104137. DOI: 10.1016/j.compbiomed.2020.104137.

Milewska, Aleksandra; Zarebski, Miroslaw; Nowak, Paulina; Stozek, Karol; Potempa, Jan; Pyrc, Krzysztof (2014): Human coronavirus NL63 utilizes heparan sulfate proteoglycans for attachment to target cells. In: JVI 88 (22), S. 13221–13230. DOI: 10.1128/JVI.02078-14.

Mocroft, A.; Ledergerber, B.; Katlama, C.; Kirk, O.; Reiss, P.; d'Arminio Monforte, A. et al. (2003): Decline in the AIDS and death rates in the EuroSIDA study: an observational study. In: Lancet (London, England) 362 (9377), S. 22–29. DOI: 10.1016/S0140-6736(03)13802-0.

Modrow, Susanne (2021): Molekulare Virologie. 4. Auflage. Heidelberg: Spektrum Akademischer Verlag.

Mosca, J. D.; Pitha, P. M. (1986): Transcriptional and posttranscriptional regulation of exogenous human beta interferon gene in simian cells defective in interferon synthesis. In: Molecular and Cellular Biology 6 (6), S. 2279–2283.

Mühlebach, Michael D.; Mateo, Mathieu; Sinn, Patrick L.; Prüfer, Steffen; Uhlig, Katharina M.; Leonard, Vincent H. J. et al. (2011): Adherens junction protein nectin-4 is the epithelial receptor for measles virus. In: Nature 480 (7378), S. 530–533. DOI: 10.1038/nature10639.

Munoz, Flor M.; Cramer, Jakob P.; Dekker, Cornelia L.; Dudley, Matthew Z.; Graham, Barney S.; Gurwith, Marc et al. (2021): Vaccine-associated enhanced disease: Case definition and guidelines for data collection, analysis, and presentation of immunization safety data. In: Vaccine 39 (22), S. 3053–3066. DOI: 10.1016/j.vaccine.2021.01.055.

Muñoz-Alía, Miguel Á.; Nace, Rebecca A.; Balakrishnan, Baskar; Zhang, Lianwen; Packiriswamy, Nandakumar; Singh, Gagandeep et al. (2022): Surface-modified measles vaccines encoding oligomeric, fusion-stabilized SARS-CoV-2 spike glycoproteins bypass measles seropositivity, boosting neutralizing antibody responses to omicron and historical variants. In: bioRxiv : the preprint server for biology. DOI: 10.1101/2022.12.16.520799.

Muñoz-Alía, Miguel Ángel; Nace, Rebecca A.; Zhang, Lianwen; Russell, Stephen J. (2021): Serotypic evolution of measles virus is constrained by multiple co-dominant B cell epitopes on its surface glycoproteins. In: Cell reports. Medicine 2 (4), S. 100225. DOI: 10.1016/j.xcrm.2021.100225.

Nakagawa, K.; Miyazawa, T. (1997): Chemiluminescence-high-performance liquid chromatographic determination of tea catechin, (-)-epigallocatechin 3-gallate, at picomole levels in rat and human plasma. In: Analytical biochemistry 248 (1), S. 41–49. DOI: 10.1006/abio.1997.2098.

Naniche, D. (2009): Human immunology of measles virus infection. In: Current topics in microbiology and immunology 330, S. 151–171. DOI: 10.1007/978-3-540-70617-5_8.

Naniche, D.; Varior-Krishnan, G.; Cervoni, F.; Wild, T. F.; Rossi, B.; Rabourdin-Combe, C.; Gerlier, D. (1993): Human membrane cofactor protein (CD46) acts as a cellular receptor for measles virus. In: Journal of virology 67 (10), S. 6025–6032. DOI: 10.1128/JVI.67.10.6025-6032.1993.

Naniche, Denise; Garenne, Michel; Rae, Chris; Manchester, Marianne; Buchta, Richard; Brodine, Stephanie K.; Oldstone, Michael B. A. (2004): Decrease in measles virus-specific CD4 T cell memory in vaccinated subjects. In: The Journal of Infectious Diseases 190 (8), S. 1387–1395. DOI: 10.1086/424571.

National Centers for Environmental Information (2023): NOAA National Centers for Environmental Information, State of the Climate: Global Climate Report for Annual 2020. (2021). Online verfügbar unter https://www.ncei.noaa.gov/access/monitoring/products/, zuletzt geprüft am 28.01.2023.

Navaratnarajah, Chanakha K.; Oezguen, Numan; Rupp, Levi; Kay, Leah; Leonard, Vincent H. J.; Braun, Werner; Cattaneo, Roberto (2011): The heads of the measles virus attachment protein move to transmit the fusion-triggering signal. In: Nature structural & molecular biology 18 (2), S. 128–134. DOI: 10.1038/nsmb.1967.

Nemet, Ital; Kliker, Limor; Lustig, Yaniv; Zuckerman, Neta; Erster, Oran; Cohen, Carmit et al. (2022): Third BNT162b2 Vaccination Neutralization of SARS-CoV-2 Omicron Infection. In: The New England journal of medicine 386 (5), S. 492–494. DOI: 10.1056/NEJMc2119358.

Nikolic, Jovan; Le Bars, Romain; Lama, Zoé; Scrima, Nathalie; Lagaudrière-Gesbert, Cécile; Gaudin, Yves; Blondel, Danielle (2017): Negri bodies are viral factories with properties of liquid organelles. In: Nature communications 8 (1), S. 58. DOI: 10.1038/s41467-017-00102-9.

Norris, Michael J.; Husby, Monica L.; Kiosses, William B.; Yin, Jieyun; Saxena, Roopashi; Rennick, Linda J. et al. (2022): Measles and Nipah virus assembly: Specific lipid binding drives matrix polymerization. In: Science advances 8 (29), eabn1440. DOI: 10.1126/sciadv.abn1440.

Noyce, Ryan S.; Bondre, Daniel G.; Ha, Michael N.; Lin, Liang-Tzung; Sisson, Gary; Tsao, Ming-Sound; Richardson, Christopher D. (2011): Tumor cell marker PVRL4 (nectin 4) is an epithelial cell receptor for measles virus. In: PLoS pathogens 7 (8), e1002240. DOI: 10.1371/journal.ppat.1002240.

Ohgitani, Eriko; Shin-Ya, Masaharu; Ichitani, Masaki; Kobayashi, Makoto; Takihara, Takanobu; Kawamoto, Masaya et al. (2021): Significant Inactivation of SARS-CoV-2 In Vitro by a Green Tea Catechin, a Catechin-Derivative, and Black Tea Galloylated Theaflavins. In: Molecules (Basel, Switzerland) 26 (12). DOI: 10.3390/molecules26123572.

Ohishi, Tomokazu; Hishiki, Takayuki; Baig, Mirza S.; Rajpoot, Sajjan; Saqib, Uzma; Takasaki, Tomohiko; Hara, Yukihiko (2022): Epigallocatechin gallate (EGCG) attenuates severe acute respiratory coronavirus disease 2 (SARS-CoV-2) infection by blocking the interaction of SARS-CoV-2 spike protein receptor-binding domain to human angiotensin-converting enzyme 2. In: PloS one 17 (7), e0271112. DOI: 10.1371/journal.pone.0271112.

Oran, Daniel P.; Topol, Eric J. (2021): The Proportion of SARS-CoV-2 Infections That Are Asymptomatic: A Systematic Review. In: Annals of Internal Medicine. DOI: 10.7326/M20-6976.

Our World in Data (2023): Coronavirus (COVID-19) Vaccinations. Online verfügbar unter https://ourworldindata.org/covid-vaccinations, zuletzt aktualisiert am 04.04.2023, zuletzt geprüft am 04.04.2023.

Ovsyannikova, Inna G.; Dhiman, Neelam; Jacobson, Robert M.; Vierkant, Robert A.; Poland, Gregory A. (2003): Frequency of measles virus-specific CD4+ and CD8+ T cells in subjects seronegative or highly seropositive for measles vaccine. In: Clinical and diagnostic laboratory immunology 10 (3), S. 411–416. DOI: 10.1128/CDLI.10.3.411-416.2003.

Pallesen, Jesper; Wang, Nianshuang; Corbett, Kizzmekia S.; Wrapp, Daniel; Kirchdoerfer, Robert N.; Turner, Hannah L. et al. (2017): Immunogenicity and structures of a rationally designed prefusion MERS-CoV spike antigen. In: Proceedings of the National Academy of Sciences of the United States of America 114 (35), E7348-E7357. DOI: 10.1073/pnas.1707304114.

Pape, Kathryn A.; Catron, Drew M.; Itano, Andrea A.; Jenkins, Marc K. (2007): The humoral immune response is initiated in lymph nodes by B cells that acquire soluble antigen directly in the follicles. In: Immunity 26 (4), S. 491–502. DOI: 10.1016/j.immuni.2007.02.011.

Paranjape, Neha; Husain, Mir; Priestley, Jennifer; Koonjah, Yashila; Watts, Christopher; Havlik, Joseph (2021): Early Use of Remdesivir in Patients Hospitalized With COVID-19 Improves Clinical Outcomes: A Retrospective Observational Study. In: Infectious diseases in clinical practice (Baltimore, Md.) 29 (5), e282-e286. DOI: 10.1097/IPC.0000000000001023.

Park, Rackhyun; Jang, Minsu; Park, Yea-In; Park, Yeonjeong; Jung, Woochul; Park, Jayhyun; Park, Junsoo (2021): Epigallocatechin Gallate (EGCG), a Green Tea Polyphenol, Reduces Coronavirus Replication in a Mouse Model. In: Viruses 13 (12). DOI: 10.3390/v13122533.

Parks, C. L.; Lerch, R. A.; Walpita, P.; Wang, H. P.; Sidhu, M. S.; Udem, S. A. (2001a): Analysis of the noncoding regions of measles virus strains in the Edmonston vaccine lineage. In: Journal of virology 75 (2), S. 921–933. DOI: 10.1128/JVI.75.2.921-933.2001.

Parks, C. L.; Lerch, R. A.; Walpita, P.; Wang, H. P.; Sidhu, M. S.; Udem, S. A. (2001b): Comparison of predicted amino acid sequences of measles virus strains in the Edmonston vaccine lineage. In: Journal of virology 75 (2), S. 910–920. DOI: 10.1128/JVI.75.2.910–920.2001.

Patton, J. T.; Davis, N. L.; Wertz, G. W. (1984): N protein alone satisfies the requirement for protein synthesis during RNA replication of vesicular stomatitis virus. In: Journal of virology 49 (2), S. 303–309. DOI: 10.1128/jvi.49.2.303-309.1984.

Patz, Jonathan A.; Daszak, Peter; Tabor, Gary M.; Aguirre, A. Alonso; Pearl, Mary; Epstein, Jon et al. (2004): Unhealthy landscapes: Policy recommendations on land use change and infectious disease emergence. In: Environmental health perspectives 112 (10), S. 1092–1098. DOI: 10.1289/ehp.6877.

Pavan Kumar, Nathella; Moideen, Kadar; Nancy, Arul; Selvaraj, Nandhini; Renji, Rachel Mariam; Munisankar, Saravanan et al. (2022): Enhanced SARS-CoV-2-Specific CD4+ T Cell Activation and Multifunctionality in Late Convalescent COVID-19 Individuals. In: Viruses 14 (3). DOI: 10.3390/v14030511.

Pedenko, Borys; Sulbaran, Guidenn; Guilligay, Delphine; Effantin, Gregory; Weissenhorn, Winfried (2023): SARS-CoV-2 S Glycoprotein Stabilization Strategies. In: Viruses 15 (2). DOI: 10.3390/v15020558.

Peiris, Joseph S. M.; Yuen, Kwok Y.; Osterhaus, Albert D. M. E.; Stöhr, Klaus (2003): The severe acute respiratory syndrome. In: The New England journal of medicine 349 (25), S. 2431–2441. DOI: 10.1056/NEJMra032498.

Piccoli, Luca; Park, Young-Jun; Tortorici, M. Alejandra; Czudnochowski, Nadine; Walls, Alexandra C.; Beltramello, Martina et al. (2020): Mapping Neutralizing and

Immunodominant Sites on the SARS-CoV-2 Spike Receptor-Binding Domain by Structure-Guided High-Resolution Serology. In: Cell 183 (4), 1024-1042.e21. DOI: 10.1016/j.cell.2020.09.037.

Pitsillou, Eleni; Liang, Julia; Ververis, Katherine; Hung, Andrew; Karagiannis, Tom C. (2021): Interaction of small molecules with the SARS-CoV-2 papain-like protease: In silico studies and in vitro validation of protease activity inhibition using an enzymatic inhibition assay. In: Journal of molecular graphics & modelling 104, S. 107851. DOI: 10.1016/j.jmgm.2021.107851.

Plumet, Sébastien; Duprex, W. Paul; Gerlier, Denis (2005): Dynamics of viral RNA synthesis during measles virus infection. In: Journal of virology 79 (11), S. 6900–6908. DOI: 10.1128/JVI.79.11.6900-6908.2005.

Polack, Fernando P.; Thomas, Stephen J.; Kitchin, Nicholas; Absalon, Judith; Gurtman, Alejandra; Lockhart, Stephen et al. (2020): Safety and Efficacy of the BNT162b2 mRNA Covid-19 Vaccine. In: The New England journal of medicine 383 (27), S. 2603–2615. DOI: 10.1056/NEJMoa2034577.

Portnoy, Allison; Jit, Mark; Ferrari, Matthew; Hanson, Matthew; Brenzel, Logan; Verguet, Stéphane (2019): Estimates of case-fatality ratios of measles in low-income and middle-income countries: a systematic review and modelling analysis. In: The Lancet Global Health 7 (4), e472-e481. DOI: 10.1016/S2214-109X(18)30537-0.

Premkumar, Lakshmanane; Segovia-Chumbez, Bruno; Jadi, Ramesh; Martinez, David R.; Raut, Rajendra; Markmann, Alena et al. (2020): The receptor binding domain of the viral spike protein is an immunodominant and highly specific target of antibodies in SARS-CoV-2 patients. In: Science immunology 5 (48). DOI: 10.1126/sciimmunol.abc8413.

Radecke, F.; Spielhofer, P.; Schneider, H.; Kaelin, K.; Huber, M.; Dötsch, C. et al. (1995): Rescue of measles viruses from cloned DNA. In: The EMBO Journal 14 (23), S. 5773–5784.

Ramsauer, Katrin; Schwameis, Michael; Firbas, Christa; Müllner, Matthias; Putnak, Robert J.; Thomas, Stephen J. et al. (2015): Immunogenicity, safety, and tolerability of a recombinant measles-virus-based chikungunya vaccine: a randomised, double-blind, placebo-controlled, active-comparator, first-in-man trial. In: The Lancet. Infectious diseases 15 (5), S. 519–527. DOI: 10.1016/S1473-3099(15)70043-5.

Rauch, Susanne; Jasny, Edith; Schmidt, Kim E.; Petsch, Benjamin (2018): New Vaccine Technologies to Combat Outbreak Situations. In: Frontiers in immunology 9, S. 1963. DOI: 10.3389/fimmu.2018.01963.

Reisinger, Emil C.; Tschismarov, Roland; Beubler, Eckhard; Wiedermann, Ursula; Firbas, Christa; Loebermann, Micha et al. (2018): Immunogenicity, safety, and tolerability of the measles-vectored chikungunya virus vaccine MV-CHIK: a double-blind, randomised, placebo-controlled and active-controlled phase 2 trial. In: The Lancet 392 (10165), S. 2718–2727. DOI: 10.1016/S0140-6736(18)32488-7.

Rey-Jurado, Emma; Tapia, Felipe; Muñoz-Durango, Natalia; Lay, Margarita K.; Carreño, Leandro J.; Riedel, Claudia A. et al. (2018): Assessing the Importance of Domestic Vaccine Manufacturing Centers: An Overview of Immunization Programs, Vaccine Manufacture, and Distribution. In: Frontiers in immunology 9, S. 26. DOI: 10.3389/fimmu.2018.00026.

Rodrigues, Charlene M. C.; Plotkin, Stanley A. (2020): Impact of Vaccines; Health, Economic and Social Perspectives. In: Frontiers in microbiology 11, S. 1526. DOI: 10.3389/fmicb.2020.01526.

Sadoff, Jerald; Le Gars, Mathieu; Shukarev, Georgi; Heerwegh, Dirk; Truyers, Carla; Groot, Anne M. de et al. (2021): Interim Results of a Phase 1-2a Trial of Ad26.COV2.S Covid-19 Vaccine. In: The New England journal of medicine. DOI: 10.1056/NEJMoa2034201.

Sahin, Ugur; Muik, Alexander; Vogler, Isabel; Derhovanessian, Evelyna; Kranz, Lena M.; Vormehr, Mathias et al. (2020): BNT162b2 induces SARS-CoV-2-neutralising antibodies and T cells in humans.

Sahin, Ugur; Muik, Alexander; Vogler, Isabel; Derhovanessian, Evelyna; Kranz, Lena M.; Vormehr, Mathias et al. (2021): BNT162b2 vaccine induces neutralizing antibodies and poly-specific T cells in humans. In: Nature 595 (7868), S. 572–577. DOI: 10.1038/s41586-021-03653-6.

Schmit, J. C.; Cogniaux, J.; Hermans, P.; van Vaeck, C.; Sprecher, S.; van Remoortel, B. et al. (1996): Multiple drug resistance to nucleoside analogues and nonnucleoside reverse transcriptase inhibitors in an efficiently replicating human immunodeficiency virus type 1 patient strain. In: The Journal of Infectious Diseases 174 (5), S. 962–968. DOI: 10.1093/infdis/174.5.962.

Schneider, H.; Spielhofer, P.; Kaelin, K.; Dötsch, C.; Radecke, F.; Sutter, G.; Billeter, M. A. (1997): Rescue of measles virus using a replication-deficient vaccinia-T7 vector. In: Journal of virological methods 64 (1), S. 57–64. DOI: 10.1016/s0166-0934(96)02137-4.

Schneider, Urs; Naegele, Melanie; Staeheli, Peter; Schwemmle, Martin (2003): Active Borna Disease Virus Polymerase Complex Requires a Distinct Nucleoprotein-to-Phosphoprotein Ratio but No Viral X Protein. In: JVI 77 (21), S. 11781–11789. DOI: 10.1128/JVI.77.21.11781-11789.2003.

Schultz, Nina H.; Sørvoll, Ingvild H.; Michelsen, Annika E.; Munthe, Ludvig A.; Lund-Johansen, Fridtjof; Ahlen, Maria T. et al. (2021): Thrombosis and Thrombocytopenia after ChAdOx1 nCoV-19 Vaccination. In: The New England journal of medicine 384 (22), S. 2124–2130. DOI: 10.1056/NEJMoa2104882.

Scully, Marie; Singh, Deepak; Lown, Robert; Poles, Anthony; Solomon, Tom; Levi, Marcel et al. (2021): Pathologic Antibodies to Platelet Factor 4 after ChAdOx1 nCoV-19 Vaccination. In: The New England journal of medicine 384 (23), S. 2202–2211. DOI: 10.1056/NEJMoa2105385.

Shi, He-Xin; Yang, Kai; Liu, Xing; Liu, Xin-Yi; Wei, Bo; Shan, Yu-Fei et al. (2010): Positive regulation of interferon regulatory factor 3 activation by Herc5 via ISG15 modification. In: Molecular and Cellular Biology 30 (10), S. 2424–2436. DOI: 10.1128/MCB.01466-09.

Shiffman, Mitchell L. (2014): Hepatitis C virus therapy in the direct acting antiviral era. In: Current opinion in gastroenterology 30 (3), S. 217–222. DOI: 10.1097/MOG.0000000000000062.

Shiliaev, Nikita; Lukash, Tetyana; Palchevska, Oksana; Crossman, David K.; Green, Todd J.; Crowley, Michael R. et al. (2021): Natural and Recombinant SARS-CoV-2 Isolates Rapidly Evolve In Vitro to Higher Infectivity through More Efficient Binding to Heparan Sulfate and Reduced S1/S2 Cleavage. In: JVI 95 (21), e0135721. DOI: 10.1128/JVI.01357-21.

Shin, Donghyuk; Mukherjee, Rukmini; Grewe, Diana; Bojkova, Denisa; Baek, Kheewoong; Bhattacharya, Anshu et al. (2020): Papain-like protease regulates SARS-CoV-2 viral spread and innate immunity. In: Nature 587 (7835), S. 657–662. DOI: 10.1038/s41586-020-2601-5.

Shrestha, Dhan Bahadur; Budhathoki, Pravash; Syed, Nawazish-I-Husain; Rawal, Era; Raut, Sumit; Khadka, Sitaram (2021): Remdesivir: A potential game-changer or just a myth? A systematic review and meta-analysis. In: Life sciences 264, S. 118663. DOI: 10.1016/j.lfs.2020.118663.

Singh, M.; Cattaneo, R.; Billeter, M. A. (1999): A recombinant measles virus expressing hepatitis B virus surface antigen induces humoral immune responses in genetically modified mice. In: Journal of virology 73 (6), S. 4823–4828. DOI: 10.1128/JVI.73.6.4823-4828.1999.

Singh, Satyam; Sk, Md Fulbabu; Sonawane, Avinash; Kar, Parimal; Sadhukhan, Sushabhan (2021): Plant-derived natural polyphenols as potential antiviral drugs against SARS-CoV-2 via RNA-dependent RNA polymerase (RdRp) inhibition: an in-silico analysis. In: Journal of biomolecular structure & dynamics 39 (16), S. 6249–6264. DOI: 10.1080/07391102.2020.1796810.

Solbach, Philipp; Wedemeyer, Heiner (2015): The New Era of Interferon-Free Treatment of Chronic Hepatitis C. In: Viszeralmedizin 31 (4), S. 290–296. DOI: 10.1159/000433594.

Su, Justin M.; Wilson, Maxwell Z.; Samuel, Charles E.; Ma, Dzwokai (2021): Formation and Function of Liquid-Like Viral Factories in Negative-Sense Single-Stranded RNA Virus Infections. In: Viruses 13 (1). DOI: 10.3390/v13010126.

Suryadevara, Naveenchandra; Shrihari, Swathi; Gilchuk, Pavlo; VanBlargan, Laura A.; Binshtein, Elad; Zost, Seth J. et al. (2021): Neutralizing and protective human monoclonal antibodies recognizing the N-terminal domain of the SARS-CoV-2 spike protein. In: Cell 184 (9), 2316-2331.e15. DOI: 10.1016/j.cell.2021.03.029.

Swaim, Caleb D.; Canadeo, Larissa A.; Monte, Kristen J.; Khanna, Swati; Lenschow, Deborah J.; Huibregtse, Jon M. (2020): Modulation of Extracellular ISG15 Signaling by Pathogens and Viral Effector Proteins. In: Cell reports 31 (11), S. 107772. DOI: 10.1016/j.celrep.2020.107772.

Swart, Rik L. de; Kuiken, Thijs; Timmerman, Helga H.; van Amerongen, Geert; van den Hoogen, Bernadette G.; Vos, Helma W. et al. (2002): Immunization of macaques with formalin-inactivated respiratory syncytial virus (RSV) induces interleukin-13-associated hypersensitivity to subsequent RSV infection. In: Journal of virology 76 (22), S. 11561–11569. DOI: 10.1128/JVI.76.22.11561-11569.2002.

Tahara, Maino; Takeda, Makoto; Yanagi, Yusuke (2007): Altered interaction of the matrix protein with the cytoplasmic tail of hemagglutinin modulates measles virus growth by affecting virus assembly and cell-cell fusion. In: Journal of virology 81 (13), S. 6827–6836. DOI: 10.1128/JVI.00248-07.

Tai, Wanbo; Zhang, Xiujuan; Yang, Yang; Zhu, Jiang; Du, Lanying (2022): Advances in mRNA and other vaccines against MERS-CoV. In: Translational research : the journal of laboratory and clinical medicine 242, S. 20–37. DOI: 10.1016/j.trsl.2021.11.007.

Tatsuo, H.; Ono, N.; Tanaka, K.; Yanagi, Y. (2000): SLAM (CDw150) is a cellular receptor for measles virus. In: Nature 406 (6798), S. 893–897. DOI: 10.1038/35022579.

Tchesnokov, Egor P.; Feng, Joy Y.; Porter, Danielle P.; Götte, Matthias (2019): Mechanism of Inhibition of Ebola Virus RNA-Dependent RNA Polymerase by Remdesivir. In: Viruses 11 (4). DOI: 10.3390/v11040326.

Teijaro, John R.; Farber, Donna L. (2021): COVID-19 vaccines: modes of immune activation and future challenges. In: Nature reviews. Immunology 21 (4), S. 195–197. DOI: 10.1038/s41577-021-00526-x.

The Novel Coronavirus Outbreak: What We Know and What We Don't (2020). In: Cell 180 (6), S. 1034–1036.

Thuluva, Subhash; Paradkar, Vikram; Gunneri, Subba Reddy; Yerroju, Vijay; Mogulla, Rammohan; Turaga, Kishore et al. (2022): Evaluation of safety and immunogenicity of receptor-binding domain-based COVID-19 vaccine (Corbevax) to select the optimum formulation in open-label, multicentre, and randomised phase-1/2 and phase-2 clinical trials. In: EBioMedicine 83, S. 104217. DOI: 10.1016/j.ebiom.2022.104217.

Tseng, Chien-Te; Sbrana, Elena; Iwata-Yoshikawa, Naoko; Newman, Patrick C.; Garron, Tania; Atmar, Robert L. et al. (2012): Immunization with SARS coronavirus vaccines leads to pulmonary immunopathology on challenge with the SARS virus. In: PloS one 7 (4), e35421. DOI: 10.1371/journal.pone.0035421.

U. S. National Library of Medicine (2020): Previfenon® as Chemoprophylaxis of COVID-19 in Health Workers (HERD). Online verfügbar unter https://clinicaltrials.gov/ct2/show/NCT04446065, zuletzt geprüft am 21.07.2023.

Ujike, Makoto; Huang, Cheng; Shirato, Kazuya; Makino, Shinji; Taguchi, Fumihiro (2016): The contribution of the cytoplasmic retrieval signal of severe acute respiratory syndrome coronavirus to intracellular accumulation of S proteins and incorporation of S protein into

virus-like particles. In: The Journal of general virology 97 (8), S. 1853–1864. DOI: 10.1099/jgv.0.000494.

United States National Library of Medicine (2012): Study to Evaluate the Dosage and Safety of Two Intramuscular Injections of an Investigational Clade B HIV Vaccine. Online verfügbar unter https://www.clinicaltrials.gov/study/NCT01320176?term=NCT01320176&rank=1, zuletzt aktualisiert am 14.02.2012, zuletzt geprüft am 29.08.2023.

United States National Library of Medicine (2022a): A Trial to Evaluate the Optimal Dose of MV-LASV (V182-001). Online verfügbar unter https://www.clinicaltrials.gov/study/NCT04055454?term=NCT04055454&rank=1, zuletzt aktualisiert am 24.01.2022, zuletzt geprüft am 29.08.2023.

United States National Library of Medicine (2022b): Zika-Vaccine Dose Finding Study Regarding Safety, Immunogenicity and Tolerability (V186-001). Online verfügbar unter https://www.clinicaltrials.gov/study/NCT02996890?term=NCT02996890&rank=1, zuletzt aktualisiert am 18.08.2022, zuletzt geprüft am 29.08.2023.

Uschner, Diane; Bott, Matthew; Lagarde, William H.; Keating, Joseph; Tapp, Hazel; Berry, Andrea A. et al. (2022): Breakthrough SARS-CoV-2 Infections after Vaccination in North Carolina. In: Vaccines 10 (11). DOI: 10.3390/vaccines10111922.

van Doremalen, Neeltje; Lambe, Teresa; Spencer, Alexandra; Belij-Rammerstorfer, Sandra; Purushotham, Jyothi N.; Port, Julia R. et al. (2020): ChAdOx1 nCoV-19 vaccine prevents SARS-CoV-2 pneumonia in rhesus macaques. In: Nature 586 (7830), S. 578–582. DOI: 10.1038/s41586-020-2608-y.

VanBlargan, Laura A.; Errico, John M.; Halfmann, Peter J.; Zost, Seth J.; Crowe, James E.; Purcell, Lisa A. et al. (2022): An infectious SARS-CoV-2 B.1.1.529 Omicron virus escapes neutralization by therapeutic monoclonal antibodies. In: Nature medicine 28 (3), S. 490–495. DOI: 10.1038/s41591-021-01678-y.

Vanhoutte, Frédéric; Liu, Wen; Wiedmann, Richard T.; Haspeslagh, Liesbeth; Cao, Xin; Boundy, Keith et al. (2022): Safety and immunogenicity of the measles vector-based SARS-CoV-2 vaccine candidate, V591, in adults: results from a phase 1/2 randomised, double-blind, placebo-controlled, dose-ranging trial. In: EBioMedicine 75, S. 103811. DOI: 10.1016/j.ebiom.2021.103811.

Vogel, Annette B.; Kanevsky, Isis; Che, Ye; Swanson, Kena A.; Muik, Alexander; Vormehr, Mathias et al. (2021): BNT162b vaccines protect rhesus macaques from SARS-CoV-2. In: Nature 592 (7853), S. 283–289. DOI: 10.1038/s41586-021-03275-y.

Volz, Asisa; Kupke, Alexandra; Song, Fei; Jany, Sylvia; Fux, Robert; Shams-Eldin, Hosam et al. (2015): Protective Efficacy of Recombinant Modified Vaccinia Virus Ankara Delivering Middle East Respiratory Syndrome Coronavirus Spike Glycoprotein. In: JVI 89 (16), S. 8651–8656. DOI: 10.1128/JVI.00614-15.

Voysey, Merryn; Clemens, Sue Ann Costa; Madhi, Shabir A.; Weckx, Lily Y.; Folegatti, Pedro M.; Aley, Parvinder K. et al. (2021): Safety and efficacy of the ChAdOx1 nCoV-19 vaccine (AZD1222) against SARS-CoV-2: an interim analysis of four randomised controlled trials in Brazil, South Africa, and the UK. In: The Lancet 397 (10269), S. 99–111. DOI: 10.1016/S0140-6736(20)32661-1.

Walsh, Edward E.; Frenck, Robert W.; Falsey, Ann R.; Kitchin, Nicholas; Absalon, Judith; Gurtman, Alejandra et al. (2020): Safety and Immunogenicity of Two RNA-Based Covid-19 Vaccine Candidates. In: The New England journal of medicine 383 (25), S. 2439–2450. DOI: 10.1056/NEJMoa2027906.

Wang, H.; Bloom, O.; Zhang, M.; Vishnubhakat, J. M.; Ombrellino, M.; Che, J. et al. (1999): HMG-1 as a late mediator of endotoxin lethality in mice. In: Science (New York, N.Y.) 285 (5425), S. 248–251. DOI: 10.1126/science.285.5425.248.

Wang, Ying-Qi; Li, Qing-Sheng; Zheng, Xin-Qiang; Lu, Jian-Liang; Liang, Yue-Rong (2021): Antiviral Effects of Green Tea EGCG and Its Potential Application against COVID-19. In: Molecules (Basel, Switzerland) 26 (13). DOI: 10.3390/molecules26133962.

Watanabe, Rie; Sawicki, Stanley G.; Taguchi, Fumihiro (2007): Heparan sulfate is a binding molecule but not a receptor for CEACAM1-independent infection of murine coronavirus. In: Virology 366 (1), S. 16–22. DOI: 10.1016/j.virol.2007.06.034.

Weltgesundheitsorganisation (2002): Global public goods for health. The report of Working Group 2 of the Commission on Macroeconomics and Health. Geneva: World Health Organization.

Weltgesundheitsorganisation (2023): Measles. Online verfügbar unter https://www.who.int/news-room/fact-sheets/detail/measles, zuletzt aktualisiert am 20.03.2023, zuletzt geprüft am 05.04.2023.

Weltgesundheitsorganisation; MI4A (2020): GLOBAL MARKET STUDY MEASLES-CONTAINING VACCINES (MCV). Online verfügbar unter https://cdn.who.int/media/docs/default-source/immunization/mi4a/measles_containing_vaccines_market_study_public_summary_july2020.pdf?sfvrsn=7c7527a_6&download=true, zuletzt geprüft am 04.04.2023.

Wertz, G. M.; Howard, M. B.; Davis, N.; Patton, J. (1987): The switch from transcription to replication of a negative-strand RNA virus. In: Cold Spring Harbor symposia on quantitative biology 52, S. 367–371. DOI: 10.1101/SQB.1987.052.01.042.

Westerhof, Lotus M.; McGuire, Kris; MacLellan, Lindsay; Flynn, Ashley; Gray, Joshua I.; Thomas, Matthew et al. (2019): Multifunctional cytokine production reveals functional superiority of memory CD4 T cells. In: European journal of immunology 49 (11), S. 2019–2029. DOI: 10.1002/eji.201848026.

World Health Organization: Prioritizing diseases for research and development in emergency contexts. Online verfügbar unter https://www.who.int/activities/prioritizing-diseases-for-research-and-development-in-emergency-contexts.

World Health Organization (2016): An R&D Blueprint for Action to Prevent Epidemics. Plan of Action May 2016. World Health Organization. Online verfügbar unter https://www.who.int/docs/default-source/blue-print/an-randd-blueprint-for-action-to-prevent-epidemics.pdf?sfvrsn=f890ab4e_1&download=true.

World Health Organization (2020a): Statement on the second meeting of the International Health Regulations (2005) Emergency Committee regarding the outbreak of novel coronavirus (2019-nCoV). Online verfügbar unter https://www.who.int/news/item/30-01-2020-statement-on-the-second-meeting-of-the-international-health-regulations-(2005)-emergency-committee-regarding-the-outbreak-of-novel-coronavirus-(2019-ncov).

World Health Organization (2020b): The top 10 causes of death. Online verfügbar unter https://www.who.int/news-room/fact-sheets/detail/the-top-10-causes-of-death, zuletzt geprüft am 15.03.2023.

World Health Organization (2020c): World health statistics 2020: monitoring health for the SDGs, sustainable development goals: World Health Organization.

World Health Organization (2023): Draft landscape and tracker of COVID-19 candidate vaccines. Online verfügbar unter https://www.who.int/publications/m/item/draft-landscape-of-covid-19-candidate-vaccines, zuletzt geprüft am 21.01.2023.

Wrapp, Daniel; Wang, Nianshuang; Corbett, Kizzmekia S.; Goldsmith, Jory A.; Hsieh, Ching-Lin; Abiona, Olubukola et al. (2020): Cryo-EM structure of the 2019-nCoV spike in the prefusion conformation. In: Science (New York, N.Y.) 367 (6483), S. 1260–1263. DOI: 10.1126/science.abb2507.

Yang, Huan; Ochani, Mahendar; Li, Jianhua; Qiang, Xiaoling; Tanovic, Mahira; Harris, Helena E. et al. (2004): Reversing established sepsis with antagonists of endogenous high-mobility

group box 1. In: Proceedings of the National Academy of Sciences of the United States of America 101 (1), S. 296–301. DOI: 10.1073/pnas.2434651100.

Yang, Jingyun; Wang, Wei; Chen, Zimin; Lu, Shuaiyao; Yang, Fanli; Bi, Zhenfei et al. (2020): A vaccine targeting the RBD of the S protein of SARS-CoV-2 induces protective immunity. In: Nature 586 (7830), S. 572–577. DOI: 10.1038/s41586-020-2599-8.

Yi, Seonju; Choe, Young June; Kim, Jia; Kim, Yoo-Yeon; Kim, Ryu Kyung; Jang, Eun Jung et al. (2022): SARS-CoV-2 Breakthrough Infections after introduction of 4 COVID-19 Vaccines, South Korea, 2021. In: Emerging infectious diseases 28 (3), S. 753–756. DOI: 10.3201/eid2803.212210.

Zhang, Dingqi; Hamdoun, Sami; Chen, Ruihong; Yang, Lijun; Ip, Chi Kio; Qu, Yuanqing et al. (2021a): Identification of natural compounds as SARS-CoV-2 entry inhibitors by molecular docking-based virtual screening with bio-layer interferometry. In: Pharmacological research 172, S. 105820. DOI: 10.1016/j.phrs.2021.105820.

Zhang, Naru; Shang, Jian; Li, Chaoqun; Zhou, Kehui; Du, Lanying (2020): An overview of Middle East respiratory syndrome coronavirus vaccines in preclinical studies. In: Expert review of vaccines 19 (9), S. 817–829. DOI: 10.1080/14760584.2020.1813574.

Zhang, Zhichao; Zhang, Xiangchun; Bi, Keyi; He, Yufeng; Yan, Wangjun; Yang, Chung S.; Zhang, Jinsong (2021b): Potential protective mechanisms of green tea polyphenol EGCG against COVID-19. In: Trends in food science & technology 114, S. 11–24. DOI: 10.1016/j.tifs.2021.05.023.

Zhong, Baisen; Peng, Weiyu; Du, Shan; Chen, Bingyi; Feng, Yajuan; Hu, Xinfeng et al. (2022): Oridonin Inhibits SARS-CoV-2 by Targeting Its 3C-Like Protease. In: Small science 2 (6), S. 2100124. DOI: 10.1002/smsc.202100124.

Zhou, Yuyong; Gammeltoft, Karen Anbro; Ryberg, Line Abildgaard; Pham, Long V.; Tjørnelund, Helena Damtoft; Binderup, Alekxander et al. (2022): Nirmatrelvir-resistant SARS-CoV-2

variants with high fitness in an infectious cell culture system. In: Science advances 8 (51), eadd7197. DOI: 10.1126/sciadv.add7197.

Zhu, Feng-Cai; Li, Yu-Hua; Guan, Xu-Hua; Hou, Li-Hua; Wang, Wen-Juan; Li, Jing-Xin et al. (2020a): Safety, tolerability, and immunogenicity of a recombinant adenovirus type-5 vectored COVID-19 vaccine: a dose-escalation, open-label, non-randomised, first-in-human trial. In: The Lancet 395 (10240), S. 1845–1854. DOI: 10.1016/S0140-6736(20)31208-3.

Zhu, Na; Zhang, Dingyu; Wang, Wenling; Li, Xingwang; Yang, Bo; Song, Jingdong et al. (2020b): A Novel Coronavirus from Patients with Pneumonia in China, 2019. In: The New England journal of medicine 382 (8), S. 727–733. DOI: 10.1056/NEJMoa2001017.

Zhu, Shu; Li, Wei; Ward, Mary F.; Sama, Andrew E.; Wang, Haichao (2010): High mobility group box 1 protein as a potential drug target for infection- and injury-elicited inflammation. In: Inflammation & allergy drug targets 9 (1), S. 60–72.

9. Abkürzungsverzeichnis

2P	2-Prolin-Substitution
3CLpro	*3C-like protease*, 3C-ähnliche Proteinase
6P	6-Prolin-Substitution
Ab	*antibody*, Antikörper
ACE2	*Angiotensin-converting enzyme 2*
Ad26	Adenovirus Serotyp 26
Alum	Aluminiumhydroxid
APC	*antigen-presenting cell*, antigenpräsentierende Zelle
ATU	*additional transcription unit*, zusätzliche Transkriptionseinheit
bAb	*binding antibodies*, bindende Antikörper
BDV	Borna Disease-Virus
CCL11	CC-chemokine ligand 11
CD	*cluster of differentiation*
CDV	*canine distemper virus*, Hundestaupevirus
CH	*central helix*, zentrale Helix
CHIKV	Chikungunya-Virus
CTD	C-terminale Domäne
Cys	Cystein
COVID-19	*Coronavirus disease 2019*
d	*day(s)*, Tag(e)
DAMP	*damage-associated molecular patterns*, Schaden-assoziierte molekulare Muster
DFurin	Deletion der Furinspaltstelle
DNA	*deoxyribonucleic acid*, Desoxyribonukleinsäure
DZIF	Deutsches Zentrum für Infektionsforschung
EGCG	Epigallocatechingallat

EMA	*European Medicines Agency*, Europäische Arzneimittelagentur
ERRS	*endoplasmic reticulum retention signal*, Signalsequenz für das Endoplasmatische Retikulum
EU	Europäische Union
F	Fusionsprotein
F&E	Forschung und Entwicklung
FRET	Förster-Resonanzenergietransfer
g	Gramm
H	Hämagglutinin
HBV	Hepatitis B-Virus
His	Histidin
HIV	Humanes Immundefizienz-Virus
HMGB1	*high mobility group box 1*
HR1	*heptad repeat 1*, Heptad-Wiederholung 1
HS	Heparansulfat
IC_{50}	*half maximal inhibitory concentration*, mittlere inhibitorische Konzentration
IFN	Interferon
IFNAR	Interferon-α/β-Rezeptor
IgG	Immunglobulin G
IL	Interleukin
IRF3	Interferon-responsiver Faktor 3
ISG	Interferon-stimuliertes Gen
kb	Kilobase
kg	Kilogramm
l	Liter
L	*large protein*

LLPS	*liquid-liquid phase separation*, Flüssig-Flüssig-Phasentrennung
LNP	Lipid-Nanopartikel
LPS	Lipopolysaccharide
LV	Lentivirus
M	Matrixprotein
MA	Maus-adaptiert
mg	Mikrogramm
mM	Mikromolar
MERS-CoV	*Middle East respiratory syndrome-related coronavirus*
MeV	*measles virus*, Masernvirus
MHC	*major histocompatibility complex*, Haupthistokompatibilitätskomplex
MHV	Maus-Hepatitisvirus
ml	Milliliter
MR	*Moraten Resurfaced*
mRNA	*messenger ribonucleic acid*
MVA	Modifiziertes Vacciniavirus Ankara
N	Nukleoprotein
nAb	*neutralizing antibodies*, neutralisierende Antikörper
NAP	Neutrophilen-aktivierendes Protein
nm	Nanometer
Nsp	Nichtstrukturprotein
NT_{50}	neutralisierende Titer 50
NTD	N-terminale Domäne
P	Phosphoprotein
PAMP	*pathogen-associated molecular patterns*, Pathogen-assoziierte molekulare Muster
PBMC	*peripheral blood mononuclear cells*, mononukleäre Zellen des peripheren Blutes

PFU	*plaque forming units*
PLGA	*poly(lactic-co-glycolic acid)*, Poly(laktid-co-glykolid)
PLpro	*papain-like protease*, Papain-ähnliche Protease
pp	Polyprotein
PRNT	Plaque-Reduktion-Neutralisationstest
PRR	*pattern recognition receptors*, Mustererkennungsrezeptoren
PsV	Pseudovirus
R_0	Basisreproduktionszahl
RBD	Rezeptorbindedomäne
RdRp	*RNA-dependent RNA-polymerase*, RNA-abhängige RNA-Polymerase
rMeV	rekombinantes Masernimpfvirus
RNA	*ribonucleic acid*, Ribonukleinsäure
RNP	Ribonukleoproteinkomplex
RSV	Respiratorisches Synzytial-Virus
S	Spikeprotein
SARS-CoV	*Severe acute respiratory syndrome-related coronavirus*
SARS-CoV-2	*Severe acute respiratory syndrome-related coronavirus 2*
SFC	*spot forming cells*, Spot-bildende Zellen
SLAM	*signaling lymphocytic activation molecule*
$TCID_{50}$	*tissue culture infection dose 50*, Zellkultur-Infektionsdosis 50
Th	T-Helferzelle
TLR	Toll-like-Rezeptor
TMD	Transmembrandomäne
TNF	Tumornekrosefaktor
tPA	*tissue plasminogen activator*, gewebespezifischer Plasminogenaktivator
TTS	Thrombosen mit Thrombozytopenie-Syndrom

TTU EI	*Thematic Translational Unit Emerging Infections*
VAERD	*Vaccine Associated Enhanced Respiratory Disease*
VNT	Virusneutralisationstest
vRNA	virale RNA
VSV	Vesikuläre Stomatitis-Virus
WHO	*World Health Organization*, Weltgesundheitsorganisation

10. Danksagung

Allen voran möchte ich mich bei PD Dr. Michael Mühlebach bedanken, der in meine Fähigkeiten vertraute und mir damit überhaupt erst ermöglichte an diesen Forschungsthemen zu arbeiten. Ich bin dankbar für die Investition von so viel Zeit im Rahmen von regelmäßigen Terminen und Korrekturrunden, durch die ich langsam, aber stetig das wissenschaftliche Arbeiten lernen konnte.

Ich bedanke mich posthum bei Prof. Dr. Sutter für die Betreuung und bei den weiteren Gutachtenden für die Beurteilung dieser Arbeit.

Alle Mitglieder meines Thesis-Komitees halfen mir in der Spur in Richtung Dissertation zu bleiben, indem sie wissenschaftlich-beratend zur Seite standen. Ich danke Prof. Dr. Christian Buchholz, Prof. Dr. Zoe Waibler, Prof. Dr. Sutter, aber vor allem Prof. Dr. Veronika von Messling.

Bei Bevan bedanke ich mich für seine großartige Unterstützung im BSL-3-Labor und wie er unseren Alltag mit unvergesslichen Pecan Pies, Pavlovas und seinem Humor versüßte.

Ich möchte mich bei allen Ehemaligen der 4/3 bedanken, vor allem bei Cindy, Christoph, Bianca und Antonia. Wir waren ein so wunderbares Team, weil wir immer füreinander und nie gegeneinander arbeiteten.

In der Nachfolge-Gruppe der 4/3 sind es Carina, Aileen und Mona, bei denen ich mich für ihre andauernde Unterstützung bedanken möchte.

Wann war die Stimmung in der „Gemeinschaft Doktorandenbüro“ nicht gut? Ich weiß es nicht, bin dankbar für die liebevolle Aufnahme und denke dabei an Kristin, Lisa, Kevin, Oliver, Mareike, Rebecca und Yvonne.

Eine virologische Fernbeziehung in die alte Heimat München prägte meine Doktorandenzeit. Die moralische Unterstützung begann schon an einem Lagerfeuer-Abend in Kanada. Ich danke Hendrik, dass er mich auf diesem Weg begleitete.

Weil er schon früh half, bestimmte Weichen richtig zu stellen und mir bis heute als Vorbild dient danke ich meinem Bruder Torben.

Meiner Mutter Inge danke ich, weil sie mir immer bedingungslos zur Seite steht, egal welche Wendung mein Leben nimmt.

Sie hört zu, fiebert mit und motiviert mich. Ich danke meiner lieben Caro, dass sie mir all die Unterstützung gab, die ich brauchte auf dem Weg zur Promotion.